



Mitchell, Kevin J. (2020) *Laser beam shaping: properties and applications*. PhD thesis.

<https://theses.gla.ac.uk/81263/>

Copyright and moral rights for this work are retained by the author

A copy can be downloaded for personal non-commercial research or study, without prior permission or charge

This work cannot be reproduced or quoted extensively from without first obtaining permission from the author

The content must not be changed in any way or sold commercially in any format or medium without the formal permission of the author

When referring to this work, full bibliographic details including the author, title, awarding institution and date of the thesis must be given

Enlighten: Theses  
<https://theses.gla.ac.uk/>  
[research-enlighten@glasgow.ac.uk](mailto:research-enlighten@glasgow.ac.uk)

# Laser beam shaping: properties and applications

Kevin J. Mitchell

Submitted in fulfilment of the requirements for the degree of  
Doctor of Philosophy

School of Physics and Astronomy  
College of Science and Engineering  
University of Glasgow



University  
of Glasgow

April 2020

# Abstract

The field of laser beam shaping advances the study of optics by pushing the limits of structured light and its applications. This thesis aims to exploit classical optical theory using state of the art structuring techniques to introduce two novel demonstrations: (1) high-speed digital micro-mirror device (DMD) light shaping and (2) broadband dual spatial light modulator (SLM) *arbitrary vector beam shaping*. These shaping techniques are also employed to demonstrate the fundamental group delay of structured light in free space, for Bessel and focused Gaussian beams.

Motivation for the structuring of light in both scalar and vector regimes is explained for a wide range of applications, from optical fibre communications and microscopy, through to computational imaging and micro-manipulation. The thesis continues by providing an in-depth background to the relevant principles of optical wave theory, and provides an overview of holographic beam modulating techniques to be used thereafter.

The first key result in this thesis is the high-speed (4 kHz) generation of arbitrary vector beams using a DMD, by way of tuning the intensity, phase and polarisation of the light. Widely used vector profiles such as radial, azimuthal, uniformly circular polarisations and Poincaré beams are characterised using spatially-resolved Stokes parameters. The intention is to promote the DMD as a cost-effective SLM which provides a switching rate that is up to  $\sim 2$  orders of magnitude faster than competing liquid crystal (LC-)SLMs. Extended details into the practical considerations of using a DMD as a diffractive optical element are discussed.

The second result in this thesis is the broadband (100 nm) generation of arbitrary vector beams using a pair of LC-SLMs in tandem. The wavelength-dependent dispersion of diffractive optics is a major issue in the beam shaping of broadband light; the

system presented in this thesis employs a second dispersion-correcting SLM within a Sagnac interferometer. The vector beam profiles from the previous result above are reproduced across four wavebands within the 100 nm range. Furthermore, the effects of chromatic dispersion in both DMDs and LC-SLMs are investigated, as is the use of in-situ wavefront correction in beam shaping systems.

In the final investigation reported in this thesis, the fundamental group velocity delay of structured light in free space is demonstrated in a classical interferometer. An elegant and novel approach is presented, which interferes one Gaussian beam with another which has, at some point in its propagation, been structured and then destructured by two LC-SLMs in tandem. The associated reduction of group velocity arises from the free space boundary conditions associated with structured beams, which in turn affects their wavevectors; this effect is demonstrated for Bessel beams and focused Gaussian beams using a simple interferometric approach. The delays detected are on the order of  $1\text{ }\mu\text{m}$  over 10 cm. Furthermore, the structuring and destructuring of beams with many constituent wavevectors (c.f. optical speckle) is presented, and its delay is theorised in anticipation of future studies.

It is intended that this thesis serves as a comprehensive account of the practicalities of vector beam shaping in different regimes for potential applications, bolstered by meaningful investigations to unearth the true nature of structured light and its properties.

# Contents

<b>Abstract</b>	<b>i</b>
<b>Contents</b>	<b>iii</b>
<b>List of Figures</b>	<b>vii</b>
<b>Image credits</b>	<b>x</b>
<b>Acknowledgements</b>	<b>xi</b>
<b>Declaration of Authorship</b>	<b>xiii</b>
<b>Publications</b>	<b>xiv</b>
<b>1 General introduction</b>	<b>1</b>
1.1 Introduction to optical beam shaping . . . . .	1
1.2 Scalar and vectorial structuring of light . . . . .	2
1.3 Applications of structured light . . . . .	3
1.3.1 Communications . . . . .	3
1.3.2 Microscopy . . . . .	6
1.3.3 Computational imaging . . . . .	8
1.3.4 DMD technologies . . . . .	9
1.3.5 Optical micro-manipulation . . . . .	10
1.3.6 Other applications . . . . .	10
<b>2 Background theory</b>	<b>13</b>
2.1 Wave theory . . . . .	13
2.1.1 A brief history . . . . .	13
2.1.2 Fundamental wave theory . . . . .	14
2.1.3 Interference of quasi-monochromatic waves . . . . .	15
2.1.4 Coherence . . . . .	18
2.1.5 Interferometry in practice . . . . .	19
2.1.6 Chromatic dispersion . . . . .	22
2.1.7 Optical speckle . . . . .	23

2.2	Polarisation . . . . .	24
2.2.1	Linear polarisers . . . . .	25
2.2.2	Wave retardance . . . . .	26
2.2.3	Polarising optics . . . . .	27
2.2.4	Characterising polarisation . . . . .	29
2.2.5	Polarisation ellipse . . . . .	29
2.2.6	Stokes parameters . . . . .	31
2.3	Laser modes . . . . .	32
2.3.1	Gaussian beam . . . . .	33
2.3.2	Hermite-Gaussian modes . . . . .	34
2.3.3	Laguerre-Gaussian modes . . . . .	35
2.4	Fourier optics . . . . .	36
2.4.1	Fourier transforming with a lens . . . . .	36
2.4.2	The 4- $f$ imaging system . . . . .	37
2.5	Holographic beam modulation . . . . .	37
2.5.1	Liquid crystal SLMs and dynamic modulation . . . . .	40
2.5.2	Mirror-based SLMs . . . . .	42
2.5.3	Computer-generated holograms . . . . .	45
<b>3</b>	<b>High-speed spatial control of the intensity, phase and polarisation of vector beams using a digital micro-mirror device</b>	<b>48</b>
3.1	Introduction to DMD vector beam shaping . . . . .	48
3.2	Light as a vector . . . . .	50
3.3	State of the art in beam shaping . . . . .	50
3.3.1	Scalar complex beam shaping techniques . . . . .	51
3.3.2	Vector beam shaping techniques . . . . .	52
3.3.3	DMDs: superfast beam shaping . . . . .	53
3.4	Using a DMD as a diffractive optic . . . . .	54
3.5	DMD vector beams: experimental setup . . . . .	60
3.5.1	DMD vector beams: setup intricacies . . . . .	64
3.6	DMD vector beams: hologram design . . . . .	66
3.6.1	Binary transmittance function . . . . .	66
3.6.2	Target beam definition . . . . .	68
3.6.3	DMD vector beams: hologram design intricacies . . . . .	69
3.7	DMD vector beams: results . . . . .	74
3.7.1	Uniform polarisation vector beams . . . . .	76
3.7.2	Vector vortex beams with spatially varying polarisation . . . . .	76
3.7.3	High speed DMD operation . . . . .	78
3.7.4	Higher order vector beams . . . . .	84
3.7.5	Quantifying vector beams . . . . .	84
3.8	DMD vector beams: discussion and conclusion . . . . .	88

3.8.1	Accuracy of vector beams . . . . .	88
3.8.2	High speed vector beams . . . . .	89
3.8.3	Spatial mode generation . . . . .	90
3.8.4	Diffraction efficiency . . . . .	91
<b>4</b>	<b>Polarisation structuring of broadband light</b>	<b>92</b>
4.1	Introduction to broadband beam shaping . . . . .	92
4.1.1	Wavelength dependence in beam shaping . . . . .	93
4.1.2	State of the art in broadband beam shaping . . . . .	94
4.2	Considerations in broadband beam shaping . . . . .	95
4.2.1	Chromatic dispersion in SLMs . . . . .	95
4.2.2	Coherence revisited . . . . .	99
4.3	Broadband vector beams: experimental setup . . . . .	102
4.4	Broadband vector beams: hologram design . . . . .	107
4.4.1	Lookup table . . . . .	110
4.4.2	In situ wavefront correction . . . . .	110
4.5	Broadband vector beams: results . . . . .	115
4.5.1	Coherence time of broadband vector beams . . . . .	120
4.6	Broadband vector beams: discussion and conclusion . . . . .	123
4.6.1	Evaluating the setup and design . . . . .	123
4.6.2	Operational bandwidth . . . . .	124
4.6.3	On correcting the angular dispersion . . . . .	125
4.6.4	Non-correctable wavelength dependence . . . . .	126
<b>5</b>	<b>Group velocity delay of structured light: Bessel beams</b>	<b>127</b>
5.1	Structured light delay: introduction . . . . .	127
5.1.1	Group velocity delay in a medium . . . . .	128
5.1.2	Group velocity delay in free space . . . . .	129
5.2	Structured light delay: theory . . . . .	131
5.2.1	Group delay of Bessel beams . . . . .	131
5.2.2	Measuring the $v_g$ delay in interferometry . . . . .	134
5.3	Structured light delay: experimental setup . . . . .	137
5.3.1	Structured light delay: interference system . . . . .	139
5.3.2	Beam collimation . . . . .	141
5.3.3	Beam alignment techniques . . . . .	142
5.3.4	Laser characteristics . . . . .	146
5.3.5	Interference visibility testing . . . . .	149
5.4	Structured light delay: hologram design . . . . .	155
5.4.1	Axicon lens optimisation . . . . .	157
5.5	Structured light delay: results . . . . .	159
5.5.1	Qioptiq source delay testing . . . . .	160
5.5.2	Broadband $v_g$ delay in Bessel beams . . . . .	164

5.6	Structured light delay: discussion and conclusion . . . . .	170
5.6.1	Evaluating the setup and design . . . . .	170
5.6.2	Sources of error . . . . .	171
5.6.3	Future work . . . . .	172
<b>6</b>	<b>Group velocity of structured light: further studies</b>	<b>174</b>
6.1	Further studies: introduction . . . . .	174
6.2	$v_g$ delay of a confocal telescope . . . . .	175
6.3	(De)structuring optical speckle . . . . .	184
6.3.1	In-situ wavefront correction revisited . . . . .	188
6.3.2	Microscanning wavefront correction . . . . .	190
6.3.3	Optical speckle down a single mode fibre . . . . .	191
6.3.4	High order optical speckle destructuring using a speckle basis . . . . .	193
6.4	Further studies: conclusion . . . . .	195
<b>7</b>	<b>Conclusion</b>	<b>197</b>
7.1	Chapters 1 and 2 . . . . .	197
7.2	Chapter 3 . . . . .	198
7.3	Chapter 4 . . . . .	199
7.4	Chapters 5 and 6 . . . . .	202
7.5	Final remarks . . . . .	204
<b>A</b>	<b>Relating phase and group velocities in a waveguide</b>	<b>205</b>
<b>B</b>	<b>Expectation value of <math>r^2</math> for a Gaussian beam</b>	<b>206</b>
<b>C</b>	<b>SLD Bessel beam delay with improved alignment</b>	<b>208</b>
<b>D</b>	<b>SLD lens delay with Gaussian apertures</b>	<b>211</b>
	<b>Bibliography</b>	<b>213</b>

# List of Figures

1.1	Mode division multiplexing . . . . .	5
1.2	Multimode fibre imaging . . . . .	7
1.3	Computational imaging: single pixel camera . . . . .	9
1.4	White light vector vortex beams . . . . .	12
2.1	The oscillatory propagation of the electric field . . . . .	15
2.2	The superposition of quasi-monochromatic light . . . . .	16
2.3	Division of wavefront: Young's double slits . . . . .	20
2.4	Division of amplitude: interferometer variations . . . . .	21
2.5	Optical speckle in lab environments . . . . .	24
2.6	Wave retardance with conventional optics . . . . .	26
2.7	Polarising optics . . . . .	28
2.8	The polarisation ellipse and Poincaré sphere . . . . .	30
2.9	Gaussian-like modes . . . . .	35
2.10	Fourier transforming with a lens . . . . .	37
2.11	4- $f$ imaging system . . . . .	38
2.12	Recording and reconstructing a transmitting hologram . . . . .	40
2.13	LC-SLM design . . . . .	41
2.14	DMD design . . . . .	44
2.15	Comparing modulators . . . . .	45
2.16	LG mode generation with SLM Fourier holography . . . . .	46
3.1	DMD diffraction orders and blazing . . . . .	56
3.2	Observing DMD diffraction . . . . .	57
3.3	DMD orders up close . . . . .	58
3.4	Experimental setup . . . . .	61
3.5	Experimental setup photographs . . . . .	62
3.6	Displacement of vector modes . . . . .	63
3.7	DMD hologram design . . . . .	70
3.8	Global relative intensity . . . . .	70
3.9	Global relative phase . . . . .	71
3.10	DMD hologram control . . . . .	72
3.11	DMD experimental hologram . . . . .	73
3.12	Stokes measurement sequence . . . . .	75
3.13	Experimental uniform polarisation beams . . . . .	77

3.14	Experimental vector beams with spatially varying polarisation	79
3.15	Stokes and ellipse parameters of a radial vector beam . . . . .	80
3.16	Stokes and ellipse parameters of a Poincaré beam . . . . .	81
3.17	High speed DMD beam shaping . . . . .	82
3.18	Vector beam rotation . . . . .	83
3.19	Higher order polarisation shaping . . . . .	85
3.20	Image subtraction in DMD vector beams . . . . .	86
4.1	Source spectra . . . . .	96
4.2	Fourier holographic imaging test . . . . .	97
4.3	DMDs vs LC-SLMs in broadband holographic beam shaping	98
4.4	Wollaston prism interference test . . . . .	99
4.5	Broadband interferograms in OPL matching test . . . . .	101
4.6	Experimental setup . . . . .	103
4.7	Supercontinuum spectrum . . . . .	104
4.8	DSLR photo of experimental setup . . . . .	105
4.9	Dual hologram design . . . . .	108
4.10	SLM2 hologram argument . . . . .	109
4.11	LC-SLM Lookup table . . . . .	111
4.12	In-situ wavefront correction . . . . .	113
4.13	Experimental vector beams of uniform polarisation . . . . .	116
4.14	Ellipticity and orientation . . . . .	117
4.15	Experimentally generated broadband radial and azimuthally polarised vector beams . . . . .	117
4.16	Fourier planes . . . . .	118
4.17	Broadband Poincaré beams . . . . .	119
4.18	Image subtraction in broadband beams . . . . .	121
4.19	Higher order vector beams . . . . .	122
4.20	Image plane test . . . . .	123
5.1	Propagation down a hollow waveguide . . . . .	130
5.2	Refractive vs diffractive optics . . . . .	133
5.3	Bessel beam delay . . . . .	134
5.4	Visibility in low coherence beams . . . . .	136
5.5	Experimental setup . . . . .	137
5.6	Photo of experimental setup . . . . .	138
5.7	Interferometer configurations . . . . .	140
5.8	Beam collimation and aberration correction . . . . .	142
5.9	Centering the beam on SLM1 . . . . .	143
5.10	Structured beam alignment . . . . .	144
5.11	Photo of LC-SLM beam structuring . . . . .	145
5.12	Superluminescent diode spectra . . . . .	147
5.13	Number of fringes in interferogram . . . . .	148
5.14	Secondary interference visibility . . . . .	150

5.15	Michelson interferometer coherence . . . . .	151
5.16	Arm B self interference . . . . .	153
5.17	Holographic aberration correction . . . . .	155
5.18	$\alpha_2$ optimisation . . . . .	158
5.19	Axicon strength at a fixed distance . . . . .	159
5.20	Axicon lens delay holograms . . . . .	160
5.21	Bessel beam visibility pixel shift . . . . .	161
5.22	Qioptiq Bessel beam $v_g$ delay . . . . .	163
5.23	Bessel beam delay vs. axicon alignment . . . . .	164
5.24	Adjusted SLD visibility envelope . . . . .	166
5.25	SLD Bessel beam $v_g$ delay . . . . .	167
6.1	Confocal telescope delay . . . . .	175
6.2	Confocal lens phase holograms . . . . .	176
6.3	Confocal lens delay test 1 . . . . .	178
6.4	Confocal lens delay test 2 . . . . .	179
6.5	Beam waist fitting . . . . .	180
6.6	Exposure and beam convergence . . . . .	181
6.7	Generating holographic optical speckle . . . . .	185
6.8	Speckle field photos . . . . .	187
6.9	Spherical wavefront correction . . . . .	189
6.10	Microscanning wavefront correction . . . . .	190
6.11	Wavefront correction for optical speckle and focusing lens . . . . .	192
6.12	Speckle basis correction . . . . .	193
7.1	DMDs vs LC-SLMs . . . . .	200
C.1	Optimising $\alpha_2$ revisited . . . . .	209
C.2	Bessel delay with equal $\alpha$ . . . . .	210
D.1	Confocal lens delay with Gaussian apertures . . . . .	212

# Image credits

The figures below contain material obtained from external sources, used for context only:

[1.2\(b\)](#): Multimode fibre imaging, Turtaev *et al.* (2018) [[1](#)]

[1.3\(b\)](#): Single pixel camera result, Edgar *et al.* (2015) [[2](#)]

[1.4\(a\)](#): Fresnel cone, A. Selyem (2017)

[2.5\(c\)](#): Optical speckle, O'Holleran *et al.* (2008) [[3](#)]

[2.14](#)(lower right): DMD mirrors, Mignardi (2016) [[4](#)]

[5.4](#) (insets): Interferometric visibility, Mandel *et al.* (1965) [[5](#)]

The remaining material is my own; figures drawn with explicit reference to external sources will include a reference in the caption.

The figures containing spatial beam profiles were generated using the *WaveTrace* development library- a toolkit of LabVIEW Virtual Instruments (VIs) for scalar optical modelling, provided by Johannes Courtial (University of Glasgow).

# Acknowledgements

The completion of this thesis and the projects therein would not be possible without the guidance and support of a select group of people, whose impact on my personal and professional growth cannot be overstated. This work was also made possible by funding from the European Research Council (ERC).

Firstly, I would like to express my deepest gratitude to my supervisor, Miles Padgett. After three undergraduate projects and two summer internships with Miles, I surprised no one by asking to stay and embark on a PhD. Suffice to say that the optics group has been a home to me for almost 7 years now, and I graciously thank Miles for each and every opportunity. Thank you for providing such an expansive window into the scientific community; for equipping me with the tools that will allow me to pursue any and every future challenge with confidence and drive. I also wish to give thanks to Sonja Franke-Arnold for her counsel over many years; for proof-reading, guiding me through my progression and for expert advice and guidance that transcends the formalities of the process and puts my interests first.

To David Phillips, I express my sincere thanks for your daily tutelage over the three years we collaborated. Your unwavering commitment to excellence through understanding and perseverance has set a high standard, which I will strive to uphold going forward. To Daan Stellinga, I am truly grateful for your mentorship throughout my final project; your breadth of knowledge is only matched by your generosity to share it, and your calming influence throughout this endeavour has been most welcome.

To the veterans of the Glasgow university optics group with whom I have collaborated, Matt Edgar, Neal Radwell and Graham Gibson: your research prowess speaks for itself, and your insights into your careers has been invaluable. Matt and Neal both relished doing an honest day's work with high spirits and an appreciation of the work-life balance. In my time, Graham has been my most trusted source of technical support and banter, which I appreciate immensely.

I also wish to acknowledge the Optics group as a whole, past and present; a workplace that is congenial and brings joy is not a given, and I appreciate the sense of belonging instilled in me by everyone. My thanks go to Rebecca Hay for looking out for me throughout the first few years, and keeping me on the right track as I progressed. To Sara Restuccia, my heartfelt thanks for being a world-class conversationalist over the years; I hold your friendship and alignment skills in equally high esteem. The optics laboratory environment is a testing one; working in complete darkness, particularly through the winter months, is enough to drive you mad... but I'll tell you a secret – all the best people are.

There exists many avenues of support to aid a PhD student in their work, but the steadfast support of a good friend is singular in its worth. Special thanks to Fraser Graham for his friendship through it all. My lasting connection with you and your family has been a major source of encouragement and gives me respite and a fresh perspective when I need it most; long may it continue.

My family do not understand laser beam shaping – apart from my brother, who teaches physics, and my niece, who knows everything. What they do understand is the commitment they have made to support me in all my endeavours; to encourage me to press through the bad times and celebrate the good. I am indebted to all of my family for being there for me throughout my studies; trust that this marks the beginning of my repayment.

# Declaration of Authorship

I hereby declare that this thesis is the result of my own work, except where explicit reference is made to the work of others, and has not been presented in any previous application for a degree at this or any other institution.

Kevin J. Mitchell

# Publications

What follows is a list of papers written during my PhD which have either been published, or are currently in preparation.

1. K. J. Mitchell, S. Turtaev, M. J. Padgett, T. Čižmár and D. B. Phillips, “High-speed spatial control of the intensity, phase and polarisation of vector beams using a digital micro-mirror device,” *Opt. Express* **24** (25), 29269–29282 (2016).
2. K. J. Mitchell, N. Radwell, S. Franke-Arnold, M. J. Padgett and D. B. Phillips, “Polarisation structuring of broadband light,” *Opt. Express* **25** (21), 25079–25089(2017).
3. S. Turtaev, I. T. Leite, K. J. Mitchell, M. J. Padgett, D. B. Phillips and T. Čižmár, “Comparison of nematic liquid-crystal and DMD based spatial light modulation in complex photonics,” *Opt. Express*, **25** (24), 29874-29884 (2017).

The content of my first publication (1) is detailed in chapter 3, whilst the content of my second publication (2) contributes to chapter 4. The third publication (3) is largely unrelated to this thesis, however the results have been used to better inform conclusions reached in the first publication. Chapters 5 and 6 feature results which are yet to be published. In addition, the work in chapters 3 and 4 were presented at the CLEO conference in San Jose, USA (May 2017):

K. J. Mitchell, S. Turtaev, M. J. Padgett, T. Čižmár and D. B. Phillips, “High-speed polarisation shaping of arbitrary vector beams using a digital micro-mirror device,” CLEO: Science and Innovations, STu4O.2

To my parents,

Carol and Billy Mitchell

*“I have heard articulate speech produced by sunlight! I have heard a ray of the sun laugh and cough and sing! The dream of the past year has become a reality – the “photophone” is an accomplished fact.”*

Alexander Graham Bell, in a letter to his father. 26<sup>th</sup> February 1880

# Chapter 1

## General introduction

### 1.1 Introduction to optical beam shaping

Our curiosity with the nature of light and its fundamental properties is innate, and as such has permeated through all of human history. Reflections in still water and polished metal; imaging through pinholes and polished glass. From prehistory through to antiquity and across all major civilisations since, a collective evolution in the understanding of these phenomena and more has led to the field of optics we recognise today. We are indebted to those that have come before us for the breadth of knowledge attained so far; this includes the principles, technologies and applications born as humble ideas, which have since graduated from the scrutiny of the scientific method to become ubiquitous. It is therefore our duty to continue this ancient study into the fundamental properties of light and its structure, to harness its potential in the real-world applications of today and of the days still to come.

Optical beam shaping, according to [6], refers to the manipulation of a light source in terms of its fundamental properties of intensity, phase, polarisation and wavelength in order to produce custom structured light fields. The ability to detect and analyse light with structure was first achieved in the 1800s, with the birth of photography (Niepce, 1827 among others) and communication via amplitude-modulated sunlight in the form of the “photophone” (Bell, 1880) [7]. In the mid 1900s, a surge of interest in optics and electronics led to the invention of holography (Gabor, 1947) and the laser (Maiman, 1960). By the 1980s a new era of coherent light sources and ever-shrinking technologies led to the emergence of micro-opto-electro-mechanical

systems (MOEMs); these included the Liquid Crystal on Silicon Spatial Light Modulator (LCoS SLM) and Digital Micromirror Device (DMD), the latter being a subset of SLM. With the continued development of such technologies, the growing list of applications for these devices promises substantial benefits in real-world environments.

The work presented in this thesis concerns the use of several novel methods of arbitrary vector beam shaping: firstly, a DMD is used to generate *high-speed* vector beams with a switching rate of up to 4 kHz, which compares favourably to most liquid crystal SLMs (LC-SLMs) (by several orders of magnitude, when comparing devices of a similar price). Secondly, a pair of these LC-SLMs are used in tandem to generate dispersion-free *broadband* vector beams with a bandwidth of 100 nm. Lastly, the phenomenon of group velocity ( $v_g$ ) delay of structured light in free space is demonstrated in a classical interferometer; specifically, beams of Bessel and focused Gaussian profiles.

The use of such devices is now standard practice in many optical laboratories around the world, where they are used to structure light in phase and amplitude, in both the *scalar* and *vector* regimes. The following chapter defines these regimes explicitly; a comprehensive overview of the current applications of shaped light follows, with emphasis on the applicability of high-speed and broadband vector beam shaping in research and industry.

## 1.2 Scalar and vectorial structuring of light

Whilst the fundamental properties of light are inherent (albeit randomised and incoherent in most cases), we reserve the term *structured light* for that which has been deliberately shaped in amplitude, phase, polarisation or a combination of the three. As discussed by Rosales-Guzmán *et al.* (2018) [8], *scalar* beams may be defined as those with a uniform polarisation across their profile – in practice, the polarisation may only be tuned for maximal efficiency in polarisation-sensitive apparatus. For example, intensity-only masks in early forms of holography were used to modulate scalar beams [9].

Whilst *unpolarised* light fields still have an E field orientation (though time-varying and incoherent), the expression *vector beam* is henceforth used to refer to a light field whose transverse polarisation distribution is *not* homogeneous (c.f. polarisation

in only one direction in linearly polarised light) [8]. This difference manifests when viewing the respective beam types through a linear polariser: on rotation of the polariser, a scalar beam whose polarisation is uniform will only change in intensity, whereas a beam of structured polarisation will alter its spatial profile (e.g. a radially polarised vector vortex beam will become an  $\text{HG}_{10}$  mode) [8, 10].

Diffractive optics have been used for many years to structure scalar light fields; treating the fields vectorially was only applied when controlling features  $< \lambda$  [8]. However, there has been increasing research interest in using diffractive optics and polarisation-varying vector beams with this extra degree of freedom to exploit [11, 12]. Such beam structures are already well established, with their usage in conical diffraction and anisotropic crystals among others [13, 14]. However, the advent of cost-effective dynamic beam shaping has led to a wealth of tools and techniques to generate and measure vector beams. With these advances has come a surge of interest in the research community, and the applications, both proven and potential, continue to grow year upon year.

## 1.3 Applications of structured light

The major advances in beam shaping technology in the last 30 years are largely due to the realised potential of structured light; both as scalar and vector fields, for static and dynamic regimes. There is a myriad of current real-world applications to provide the motivation to continue the progress already made, with vector beam shaping due to make a significant impact in the decades to come. In the following sections I will highlight some of these exciting applications which benefit from state of the art beam shaping technology and practices.

### 1.3.1 Communications

The *information age* as we know it today is made possible by a globalised telecommunications network, with light-carrying fibre optics at its heart. From undersea cabling between continents to domestic broadband services in the home, optical fibres and their accompanying source and detection infrastructure support an unprecedented bandwidth of data to maintain and improve our communication channels. Whilst we

may nowadays be familiar with *Google fiber* and broadband speeds of up to 1Gbit/s, optical fibre has long been embedded into the phone networks of many countries; medium to large scale institutions such as banks and universities make use of localised intranets. In these applications, fibre technology is lauded for its reliability, security and data transfer rates [15].

Modern communications demands, such as more bandwidth for 4k and 8k video streaming and broadcasting, video conferencing, 5G mobile networks and the rise of big data in tech, science and industry have put a real strain on existing physical communications networks. The stability of these communication channels is now inherently tied to the global economy, security and prosperity, and so it is imperative that government and industry collaborate to design the future of communication to avoid a “capacity crunch” [16–18].

With the threat of such a bandwidth crisis on the horizon, much research has been invested in trying to identify the next generation of fibre optics solutions, largely centred around the concept of *division multiplexing*. This term is used to describe the separation of the total bandwidth of a transmission medium into discrete information-carrying channels for simultaneous transmission. This can occur in several regimes, or “bases” whose individual channels are orthogonal to one another; a common example is Wavelength Division Multiplexing (WDM). This technique encodes information in neighbouring wavelengths, which can all be sent along the same optical fibre link, hence multiplying the bit rate transfer by the number of distinct wavelength channels [19]. Space division multiplexing (SDM) describes the use of multiple spatial channels, e.g. fibres with multiple single mode cores and the means to steer individual pulses down each channel [20]. Such techniques are limited by the wavelength-dependency of the system, and the maximum rates of the optical switching respectively.

A subset of SDM, known as Mode Division Multiplexing (MDM), instead uses multimode fibres (MMF) with the capacity to transmit many orthogonal spatial modes simultaneously. A factor 2 increase in transmission rate is achieved by combining orthogonal polarisations as individual channels (polarisation division multiplexing (PDM)). Of great potential is the use of a multimode fibre with a mode capacity in the thousands, which has the means to provide a significantly higher capacity [21–28].

In [29], WDM and MDM are combined using different OAM (Orbital Angular Momentum) modes (modes with varying degrees of spin or helicity) over multiple wavelengths to transmit light down a low dispersion fibre to achieve 1.6 Tb/s. One of the most recent demonstrations of high capacity data transfer was conducted by Putnam et al [30], whereby PDM was used in conjunction with 16-QAM (Quadrature Amplitude Modulation) to achieve a record 715Tb/s transfer across a fibre of length 2000 km. Notably, the fibre used was an Erbium doped multi-core of few-mode fibres.

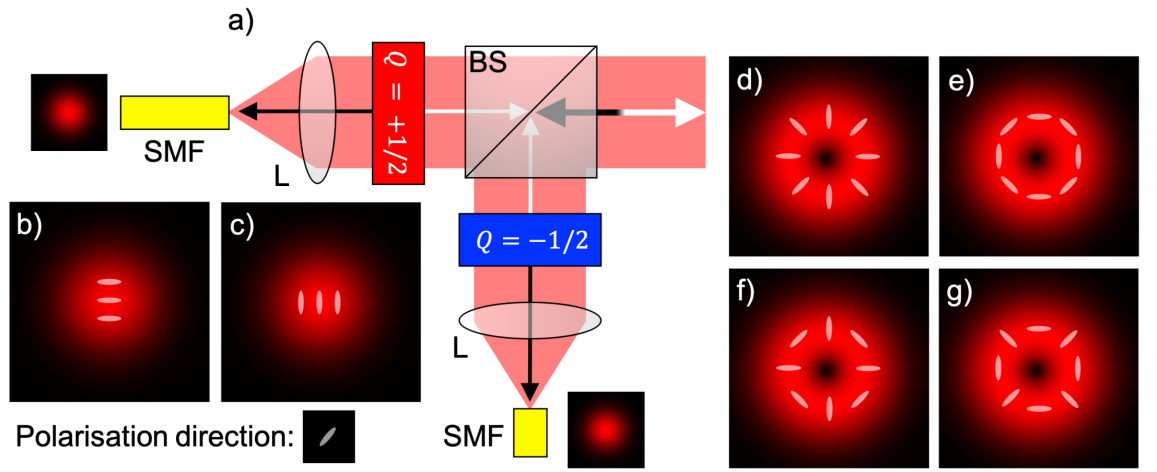


FIGURE 1.1: **Vector beam mode division multiplexing in free space** Reproduced from Milione *et al.* (2014) [31]. (a) a vector mode (de)multiplexer used to transmit a signal containing 4 vector beams a distance 1 m in free space. Orthogonally polarised Gaussian beams (b,c) are combined and sent down both the single mode fibres (SMF); the beams are collimated by lenses L and phase modulated by custom “q-plates” ( $q = \pm 1/2$ ) designed such that vector beams (d,e) emerge from  $q = +1/2$  and beams (f,g) emerge from  $q = -1/2$ . The beams propagate in free space some distance as one channel to the receiver, which demultiplexes the beam into constituent signals. The authors reported that each vector beam supports a 20 Gbit/s signal. Propagation direction is marked with a white arrow for multiplexing and a black arrow for de-multiplexing, while the local linear polarisation across each beam profile is marked in white.

The same principles can be applied to free-space communication, whereby the transmission and detection occurs at two different locations that are e.g. buildings/cities apart. As in the fibre case, polarisation, spatial modes and orbital angular momentum are used to increase the bit rate of a single pulse, although the distortion to contend with is not dispersion but atmospheric turbulence [32–34]. In figure 1.1 (Milione *et al.* (2015) [31]), custom  $q$ -plates were used to (de)multiplex a single pulse of 4 vector beams over a metre.

### 1.3.2 Microscopy

The structuring of light by SLMs on the scale of microns is of particular relevance to the fields of imaging and microscopy – such devices can be readily inserted into bench-based optical systems such as microscopes, cameras and projectors (indeed this is why SLMs were invented [35]).

Vector vortex beam structures are well established in the field of microscopy – their properties are used to increase the resolution achievable beyond the diffraction limit. In conventional stimulated emission depletion (STED) microscopy, an initial beam excites a fluorescent sample, before a circularly polarised “*doughnut*” beam with a phase singularity stimulates emission and therefore depletes the fluorophores in the surrounding area. This leads to a measured fluorescence of the remaining region within the ring which is smaller than a diffraction limited spot [36–39] – this is therefore a functional approach to super-resolution. The properties of these beam profiles have also been exploited in confocal microscopy [40].

Structured illumination microscopy (SIM) is a wide-field imaging technique which instead makes use of a dynamic diffraction grating in the path of the excitation beam to build up a super-resolution image; the superposition of the sample with several gratings results in a set of moiré patterns, which are more easily resolved by the objective lens [41–45].

There exists environments where reactive structuring is required to counteract existing structuring, e.g. transmission through turbid media: when a well-defined beam propagates through a scattering medium the rays are scattered in a largely random process, such that it is unfeasible to determine the propagation matrix of the scattering medium *a priori*. This applies in biomedical imaging, where endoscopy is used to image into tissues of live samples [1]. The imaging depth is limited by this scatter effect, which varies according to its speckle decorrelation time ( $\sim$ ms). Specifically, this is the time taken for an initial wavefront to lose correlation with subsequent wavefronts due to turbulence from sources like Brownian motion or motion in the living body [46]. It follows that we must correct for this turbulence on the same time-scale as this motion occurs.

The “transmission matrix method” is the means by which a previously unknown turbid medium can be characterised: by dividing an incident beam into individual

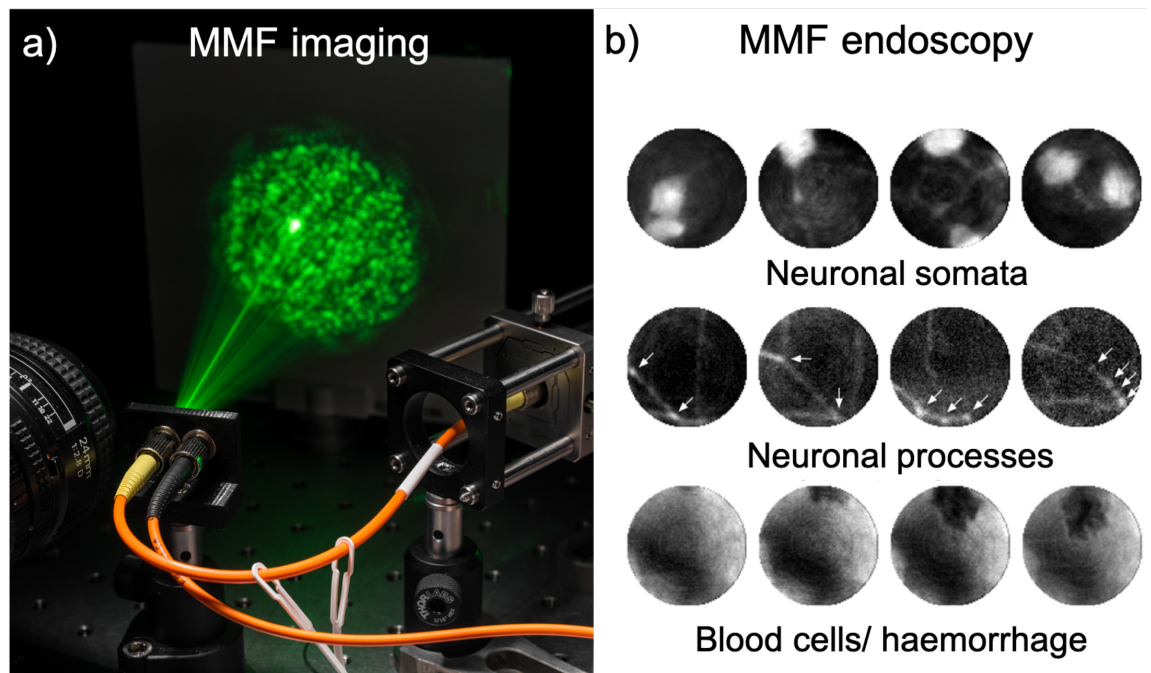


FIGURE 1.2: **Turbid media: multimode fibre imaging:** (a) Time-of-flight imaging down a Multimode fibre (MMF) by Stellinga *et al.* (2018) [47]: by first probing the propagation of some mode basis down an MMF, an incident beam may be pre-structured to exit the distal end of the fibre with most of the power concentrated within a single mode for scanning. (b) Vector beams produced with a high-speed DMD can be used to calculate the transmission matrix for “deep-brain in vivo imaging” of biological samples – pictured are images of a mouse brain by Turtaev *et al.* (2018) (reproduced from [1]).

eigen-modes of the medium and observing how they propagate through this medium, it is possible to construct a complex transmission matrix of the medium at that moment in time [22]. It is then possible to use matrix inversion to pre-modulate a beam such that it will propagate through the medium and focus as a well defined mode, such as a focused spot for raster scan imaging, as seen in figure 1.2(a) [48–53]. In [1, 54], this concept was applied to correct for the inherent mode dispersion in multimode fibres (MMF), and produce an imaging system the width of a single multimode fibre, whose resolution is tied to the number of fibre eigen-modes (figure 1.2(b)). The dynamic regime of this technique requires an SLM with an extremely fast switching rate, to achieve real-time matrix characterisation and raster scanning of an object.

### 1.3.3 Computational imaging

The recent rise in single-photon, simultaneous multi-spectral and time-resolved imaging requires the use of highly specialised equipment including avalanche photodiodes (single photon SPADs and APDs), photodiodes with different semiconductor substrates, triggering and high-performance processing power [6, 55].

“Ghost imaging” is a technique used to construct an image with photons which have never encountered the object, and are merely correlated with those which have. As discussed in [6], spatially entangled photon pairs are generated from a nonlinear crystal; whilst one photon in the pair is used to illuminate the object or be collected by a bucket detector, the other is detected by a camera [56, 57]. Whilst the photons from the crystal are said to be spatially entangled in the quantum regime, only their spatial correlation is applied in the image acquisition. Correlated-photon imaging is an established means to explore single photon imaging, which is difficult with conventional imaging due to inescapable noise levels and dark counts. By only using photons that are proven to be coincident with the illumination, it is possible to form images with only  $< 0.2$  photons per pixel ( $\sim 10,000$  photons) [58].

From the exploration of a paradoxical phenomenon to imaging with very few photons, the correlation lies with the photon source. In the field of computational ghost imaging (CGI), the same principles have been applied to structured light generation and detection. In CGI, an LC-SLM is used to generate incoherent randomised intensity holograms, which shape the plane wave illumination light into a set of structured light fields [59]; here the correlation is between the illumination beam post-object and the set of holograms generated by the computer. Each structured light field illuminates the object, and the backscattered reflectance is detected by a single pixel (photodiode). Each field is then weighted with the intensity of the reflectance signal, and summed to obtain the final image [60].

In recent years, the CGI process has been reversed to introduce a novel offshoot – the single pixel camera (SPC), as shown in figure 1.3. Whereas before the object was illuminated by pre-structured light fields, the SPC post-modulates the incoming scene of the object using a DMD [61]. The operation of the SPC transfers the responsibility of mapping the spatial structure of an image from the detector array to the DMD; this is particularly useful for developing multi-spectral cameras, as the cost of single

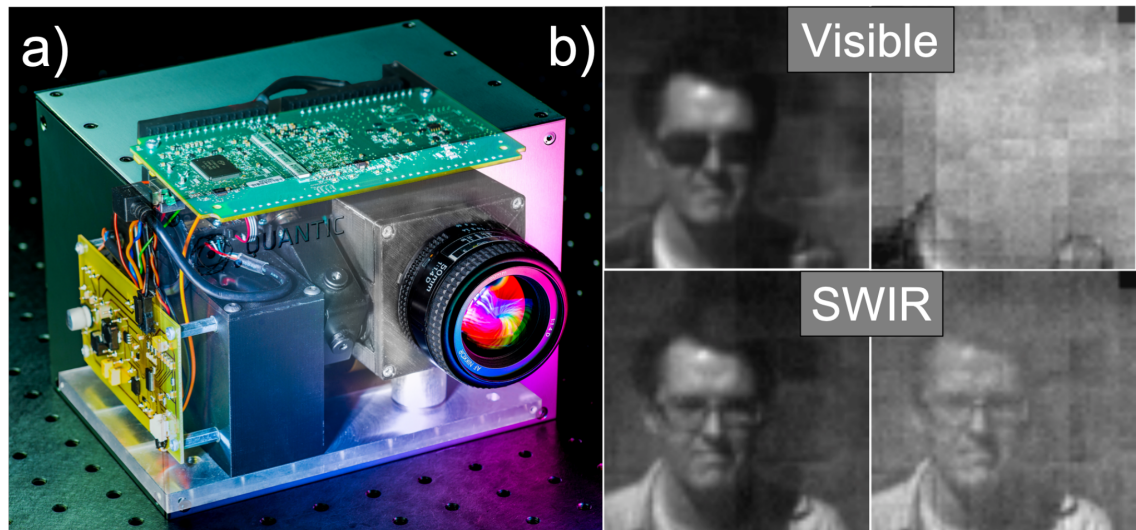


FIGURE 1.3: **Computational imaging: seeing through smoke with a single pixel camera (SPC):** Reproduced from Edgar *et al.* (2015) [2]. (a) A single pixel camera, developed by the University of Glasgow and QuantIC. Built from a DMD and a pair of cheap photodiodes, the device is able to simultaneously capture low resolution images in two different wavebands using structured light. For example, (b) shows the SPC imaging in the visible and short wave infrared, with (right) and without (left) viewing through smoke.

pixel detectors (photodiodes) are far cheaper than their many-pixel counterparts (e.g. CMOS) at every waveband [2, 62].

### 1.3.4 DMD technologies

In 1987, Texas Instruments developed the first DMD modulator to revolutionise the functionality and capability of MOEM devices by coupling micro-optics and electro-mechanics [63]. The device has since come to be ubiquitous as the projection unit in almost all digital projectors in classrooms and theatres [35]. However, the advantages of the device over liquid crystal SLMs has led to an exciting array of opportunities including high-speed beam shaping, adaptive optics, single-pixel imaging and most recently LiDAR (light detection and ranging) [64–66]. The device has also been employed in the “world’s fastest camera” which can reportedly achieve 10 trillion frames per second using passive compressed ultrafast photography, dubbed “T-CUP” [67].

### 1.3.5 Optical micro-manipulation

Customised light fields have been used for decades in the field of micro-manipulation. For 50 years, microscopes have been adapted using structured laser light to form *optical traps* – an umbrella term which includes tweezers, spanners, sorting and confinement. As discussed in [6], the original optical tweezer principle was outlined in 1970 by Ashkin *et al.* [68], and involved the use of a focused laser to trap and relocate particles such as dielectric spheres. Gaussian laser light focused from a microscope objective onto the sample plane exerts a net scattering force along the direction of propagation, as well as a restoring gradient force which is directed towards the centre of the beam. The result is a trapping force acting on the sample on the order of pN to objects which are in the nm to mm range. In the decades since, the principle has been applied to a vast array of samples, including atoms, DNA, living cells, bacteria, viruses and metallic objects [69–72].

The introduction of advanced light structuring using affordable spatial light modulation has extended the applications of optical trapping considerably; instead of using a single Gaussian trap, a holographic optical tweezer (HOT) can diffract the incident laser light into many traps simultaneously, and can be steered in realtime to move, sort, track and measure these same samples with great accuracy. This flexibility was demonstrated to great effect by Curtis *et al.* (2002) [69]; samples may also be rotated (optical spanner) and trapped in 3D space using holograms of defocusing lenses. More exotic beam profiles and polarisations can be used e.g. the Laguerre-Gaussian “doughnut” beam, in order to exploit its optical vortex and orbital angular momentum [73–76]. Optical traps have also been used to measure the forces of molecular motors and the elasticity of DNA [6].

### 1.3.6 Other applications

The major applications of vector vortex beams and structured light in general has led to the adoption of such technologies in other areas, such as in manufacturing and quantum experiments.

Firstly, full control of the intensity, phase and polarisation of light is an attractive prospect in the laser machining industry; the properties of various beam profiles are advantageous for different processes, including cutting, drilling and welding [77]. For

systems with a high numerical aperture ( $NA > 1.5$ ), a radially polarised vector vortex beam which is focused down produces a sharper focus due to a large on-axis E field component – this is useful for laser cutting at high speed and precision [78–81]. For beams with a flat top profile and a longer depth of focus, the ratio of cutting depth:width is useful when considering the absorption characteristics of the materials being machined [82]. Note that as well as exploiting the various properties of transverse polarisation-shaped vector beams (radial, azimuthal, circular etc.) focusing down a radially polarised beam through a lens of a high enough NA will also produce a longitudinal component of polarisation, resulting in arbitrary 3D polarisation shaping [83–85].

Next, the same entangled photon pairs discussed in section 1.3.3 are also used to test the Einstein-Podolsky-Rosen paradox by violating Bell inequalities – this has been shown for photon pairs exhibiting several types of entanglement, e.g. spin, polarisation and OAM [57, 86–88]. This reinforces the non-classical nature of quantum mechanics and paves the way for real-world quantum technologies, such as quantum key distribution [89–91], which provides secure communication channels.

Lastly, the field of *ultrafast* photonics is so named because of the pulsed laser sources used – each pulse is a wave packet of some short coherence length  $l_c$ , which is a byproduct of having a broad bandwidth. As such, spatial and temporal beam shaping is a novel method of producing scalar and vector beams useful in both ultrafast photonics and white light beam shaping.

Specialised dispersion-compensating broadband beam shaping techniques give rise to the generation of tailored ultrashort pulses in either the pico or femtosecond range [92–96]. The nature of the pulse packets formed from a spread of wavelengths has been used for pulsed WDM and time-division multiplexing (TDM) using spectral phase encoding [97, 98]. Ultrafast pulses are also used in biomedical imaging, specifically for rapid time delay scanning in optical coherence tomography, as well as multi-photon confocal microscopy [99–101].

The ability to uniformly shape a large bandwidth beam without dispersion is of particular use for applications which exploit white light sources. Using a supercontinuum source, transmission down a waveguide can be probed in multiple wavelengths with low-coherence interferometry – this allows the dispersion behaviour and any manufacturing flaws to be measured with great precision [103]. In biomedical imaging,

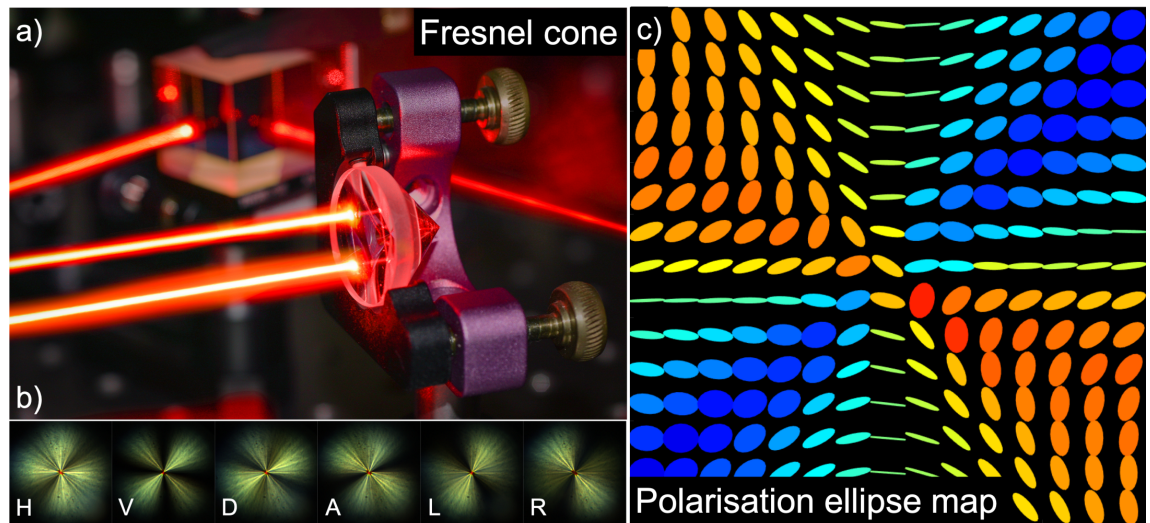


FIGURE 1.4: **White light vector vortex beams using a Fresnel cone:** Reproduced from Radwell *et al.* (2016) [102] (photo credit: Adam Selyem). (a) total internal reflection from a glass Fresnel cone is a novel method for generating achromatic vector vortex beams. For a polarised source, reflection from the cone imparts a phase tilt which varies angularly, such that the outgoing beam contains a range of polarisations. (b) images of the white light degenerate polarisation states (see section 2.2). These states are used to produce the polarisation ellipse map depicted in (c), where handedness is represented by colour. This setup, combined with circularly polarised light, can also produce beams of radial and azimuthal polarisation.

there are sometimes specimens which need to be illuminated by multiple wavelengths – by analysing samples using structured beams which may contain any number of wavelengths, broadband beam shaping negates the need for the combining of multiple sources in separate shaping systems [100, 102, 104–106]. A low coherence source is also the primary means to achieve optical coherence tomography [107].

Figure 1.4, adapted from Radwell *et al.* (2016), depicts the use of an achromatic glass Fresnel cone to generate white light vector vortex beams; (c) the polarisation ellipse map (defined in chapter 2) is an intuitive means to display the local polarisations within a given beam profile. The orientation and ellipticity of each ellipse defines the polarisation, and handedness is shown as colour.

# Chapter 2

## Background theory

The following chapter is devoted to introducing the fundamental wave theory that makes up the prerequisite knowledge for the beam shaping investigations that follow. Furthermore, I will introduce the optical elements and devices central to beam shaping, their attributes and mechanics which will inform many of the decisions made during their use.

### 2.1 Wave theory

#### 2.1.1 A brief history

The structuring of light fields in scalar and vector regimes is reliant on wave theory, which has a rich history. As described by Hecht (2002) [10], the wave-like nature of light was first hypothesised in the mid 1600s, when Robert Hooke (1635–1703) proposed that “the condition associated with the emission of light by a luminous body is a *rapid vibratory motion*” and that every vibration of this body propagates in every direction through a homogeneous medium “like rays from the centre of a sphere” [108]. The first mathematical theory of light was introduced in the same period by Christiaan Huygens (1629–1695), who in 1690 published his *Treatise on light* [109]. In it he sought to introduce the concept of light propagating as wavefronts in the “luminiferous aether,” whereby every point along the wavefront is itself the origin of new spherical waves; with this treatment of light rays, he was able to account for the

behaviour of light in geometric optical phenomena, such as refraction, reflection and polarisation. For the next century, the wave theory of light was largely overtaken by the prominence of the corpuscular (particle) theory, formalised by Sir Isaac Newton (1642–1727). However, this theory did not fully explain the results obtained for interference and diffraction [10].

Leading against the tide of opinion that had arisen, Thomas Young (1773–1829) presented his famous double slits experiment, which identified the interference of light waves from two separated sources of sunlight, in much the same way as water waves ripple and interfere [110]. Augustin-Jean Fresnel (1788–1827) confirmed and expanded upon the wave nature of light in diffraction and interference, by combining his own findings with Huygens' principle. By the early 19th century, light was firmly established as exhibiting properties consistent with a transverse wave. It was not until the birth of quantum theory in the 20th century before the particle nature of light was incorporated to fully describe the now accepted wave-particle duality of light [10].

### 2.1.2 Fundamental wave theory

Consider light as a transverse electromagnetic (E,B) field induced by moving charges. Within a vacuum, the orthogonal components of this field are related by the speed of light  $c$ , such that  $E = cB$  (expanded upon in section 3.2). In the first instance, the transverse electric field may be simply defined as a sinusoidal relation. According to Collett (2005) [111], Fresnel argued that this field could be fully characterised by the orthogonal components  $E_x$  and  $E_y$  such that they can be written as the wave equations

$$\frac{\partial^2 E_x(\mathbf{r}, t)}{\partial x^2} = \frac{1}{v^2} \frac{\partial^2 E_x(\mathbf{r}, t)}{\partial t^2}, \quad (2.1)$$

$$\frac{\partial^2 E_y(\mathbf{r}, t)}{\partial y^2} = \frac{1}{v^2} \frac{\partial^2 E_y(\mathbf{r}, t)}{\partial t^2}. \quad (2.2)$$

Here,  $E_{x,y}(\mathbf{r}, t)$  are the field components, as depicted in figure 2.1(a);  $\mathbf{r}$  is the radius vector and  $v$  is the velocity at time  $t$ . The wave number is defined as  $k = 2\pi/\lambda$  for some wavelength  $\lambda$ . By convention, the field propagates along the  $z$  direction, such that the displacement of the electric field in the transverse plane has solution

$$\mathbf{E}(\mathbf{r}, t) = E_0 \cos(\omega t - \mathbf{k} \cdot \mathbf{r} + \delta) \quad (2.3)$$

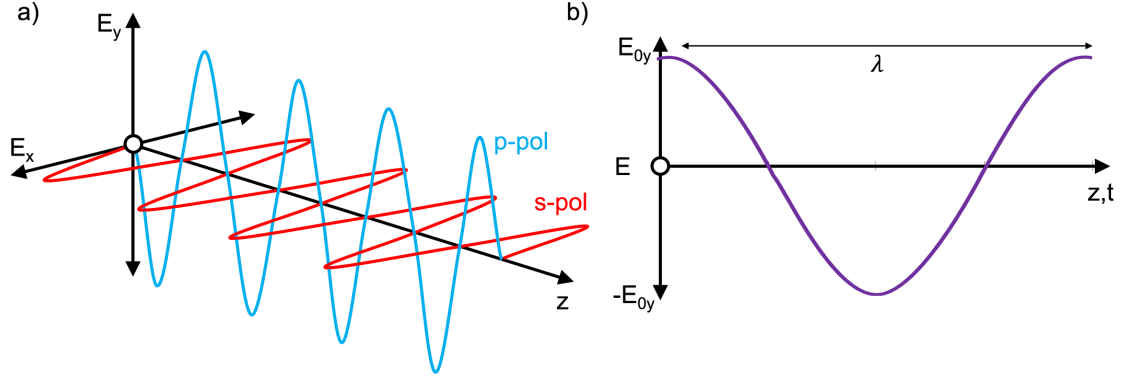


FIGURE 2.1: **The oscillatory propagation of the electric field:**(a) the field is comprised of orthogonal components. A linear vibration along the  $y$ -axis  $E_y$  (in the plane of the paper) is defined as the  $p$  polarisation component; along the  $x$ -axis  $E_x$  and perpendicular to the plane of the paper is the  $s$  polarisation component. (b) a solution of the wave equation  $\nabla^2 E_y(\mathbf{r}, t)$  traces out a sinusoidal wave of peak amplitude  $E_{0y}$  with periodicity  $\lambda$  along direction  $z$ .

The angular frequency of this sinusoidal relation, shown in figure 2.1(b), is defined as  $\omega = 2\pi f$ , whilst  $E_0$  is the maximal amplitude and  $\delta$  is some arbitrary phase. Converting to polar complex form, we may rewrite the solutions of the wave equation as:

$$E_{x,y}(z, t) = E_{0x,y} e^{i\theta_{x,y}}, \quad (2.4)$$

where  $\theta_{x,y} = \omega t - \mathbf{k} \cdot \mathbf{r} + \delta_{x,y}$  [112–114].

### 2.1.3 Interference of quasi-monochromatic waves

The mathematical description introduced in section 2.1.2 is a second order homogeneous partial differential equation, and therefore the combination of two similar fields may be investigated by using the *superposition principle*. That is, as defined in Hecht (2002) [10], the resultant intensity when two or more fields combine is not the scalar sum but the vector sum of the individual fields themselves. This is the basis for *optical interference*, a phenomenon that is the mechanism behind diffractive vector beam shaping. Fundamentally, the interference of two plane waves with some angle between their optic axes results in consecutive regions of constructive and destructive intensity fringes – this “interferogram” also depends on the orientation of the local polarisation direction between the two waves.

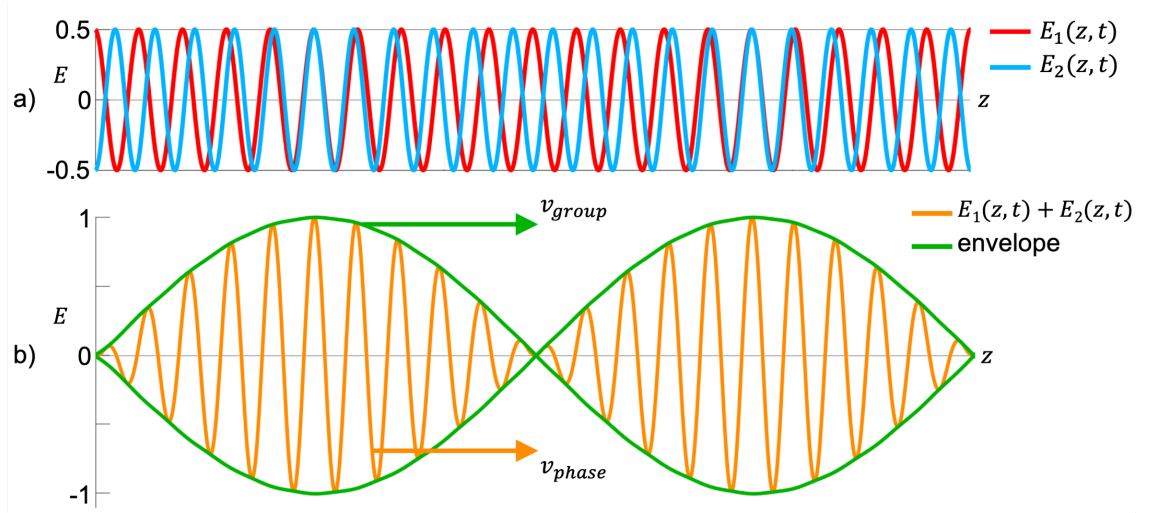


FIGURE 2.2: **The superposition of quasi-monochromatic light:** (a) comparing two waves of similar but unequal wavelength  $E_{1,2}(z, t)$  where ( $k_1 > k_2$ ,  $\omega_1 > \omega_2$ ). Successive instances of total constructive and destructive interference form *beats*. (b) the sum of the two fields  $E_1(z, t) + E_2(z, t)$  therefore shows a high frequency carrier wave of frequency  $\bar{\omega}$  modulated by a cosine envelope function  $\omega_m$ . Whilst the carrier wave propagates as  $v_p$ , the envelope itself moves with  $v_g$ , and not always in the same direction.

The investigations to follow are dependent on the interferometric superposition of two light fields which share the same source but travel through different optical paths before recombination. In the ideal case, such fields would be purely monochromatic and have a wavetrain which is infinitely long. For chapters 4 and 5 we must consider the quasi-monochromatic case, where light from a laser has a limited coherence length with a sizeable bandwidth (spread) of wavelengths,  $\Delta\lambda$ . To characterise the physical variables to be accounted for, consider figure 2.2(a) – as introduced in [10], the superposition of two fields of slightly different wave number and angular frequency ( $k_1 > k_2$ ,  $\omega_1 > \omega_2$ ) such that:

$$E_1(z, t) = E_{01} \cos(\omega_1 t - k_1 z) \quad (2.5)$$

$$E_2(z, t) = E_{01} \cos(\omega_2 t - k_2 z) \quad (2.6)$$

For simplicity, the fields share the same amplitude and are initially in phase. The addition of the two fields becomes

$$E = E_{01} [\cos(\omega_1 t - k_1 z) + \cos(\omega_2 t - k_2 z)]. \quad (2.7)$$

We can define the average of  $\omega, k$  such that  $\bar{\omega} = (\omega_1 + \omega_2)/2$  and  $\bar{k} = (k_1 + k_2)/2$ ; also, let  $\omega_m = (\omega_1 - \omega_2)/2$  and  $k_m = (k_1 - k_2)/2$  be the modulation parameters. Including these terms, whilst simplifying by using the product-sum identity, we find that

$$E = 2E_{01} \cos(\omega_m t - k_m z) \cos(\bar{\omega} t - \bar{k} z). \quad (2.8)$$

By defining the modulation envelope amplitude  $E_0(z, t) = 2E_{01} \cos(\omega_m t - k_m z)$ , we may say that the superposition of these fields is another field of frequency  $\bar{\omega}$ , namely

$$E(z, t) = E_0(z, t) \cos(\bar{\omega} t - \bar{k} z). \quad (2.9)$$

It follows that the intensity  $E_0^2(z, t) = 2E_{01}^2 [1 + \cos(2\omega_m t - 2k_m z)]$  oscillates between  $2E_{01}^2$  with a *beat frequency*  $(\omega_1 - \omega_2)$ . The oscillating field propagates with phase velocity  $v_p$ , which in a vacuum is

$$v_p = \frac{\bar{\omega}}{\bar{k}} = \frac{c}{n} \quad (2.10)$$

So far we have been concerned with the superposition of ideal monochromatic light. The output of a laser may also be considered a broadband superposition of light waves within a narrow frequency band. An *envelope* then modulates the average of the individual waves with some group velocity  $v_g$  [10]. In figure 2.2(b),  $\omega_m$  is the frequency of the carrier wave which undergoes a cosine modulation. For dispersive media, (assuming a small  $\Delta\omega$ ), we may define the group velocity as the rate of change of the phase velocity, indicating the propagation of the modulating function itself:

$$v_g = \frac{\omega_m}{k_m} = \frac{\Delta\omega}{\Delta k} = \frac{d\omega}{dk_{\bar{\omega}}}. \quad (2.11)$$

Generally, the optical refractive index  $n$  decreases with increasing wavelength for visible light. As discussed in [115], the group velocity inside a material is related to this refractive index by

$$v_g = \frac{d\omega}{dk} = \frac{c}{n - \lambda \frac{dn}{d\lambda}}. \quad (2.12)$$

It is important to note that light in a vacuum propagates at a constant velocity  $c = 299792458 \text{ ms}^{-1}$ , in which case  $v_p = v_g = c$ . However, in dispersive media with refractive indices  $n$  that are not unity, both  $v_p > v_g$  when  $\frac{dn}{d\lambda} > 0$  and  $v_p < v_g$  when  $\frac{dn}{d\lambda} < 0$  are possible. It is also possible to have  $v_{p,g} > c$ , however superluminal

information exchange remains outside the realm of possibility as it violates causality [10, 116]. This concept can also be applied to the deliberate delaying of  $v_g$  by transmission through dispersive media or waveguides (as demonstrated in chapter 5).

### 2.1.4 Coherence

The above definitions for the superposition of waves with differing  $\lambda$  may also inform our understanding of the *coherence* of quasi-monochromatic light. A pair of light fields  $E_{1,2}$  which interfere are deemed to be *spatially* coherent when the phase difference of two points along the same wavefront  $\Delta\phi = \text{constant}$ , and the waves oscillate in step with one another [10]. The coherence length  $\ell_c$  of a given source tells us the optical path difference ( $\Delta\text{OPL}$ ) over which the two fields can no longer be interfered, i.e. when the visibility of fringes becomes zero. This will be of particular use in chapters 4 and 5, where the use of sources of finite coherence in an interferometric system must be accounted for to successfully path length match two separated components from a single beam.

Within a typical quasi-monochromatic light source, the excited atoms radiate photons independently as a stream of finite photon wavetrains. The timescale over which electrons transition between energy levels is on the order of 10 ns. The coherence time is therefore the duration over which the phase of the wavetrain remains predictable, and the oscillation is sinusoidal; *temporal* coherence arises when  $\Delta\phi = \text{constant}$  between points radiating out from the same axis of the source. Temporal coherence is a measure of the spectral purity of the light source, and is intrinsic to the bandwidth  $\Delta\lambda$ . An ideal monochromatic beam would have an infinitely long coherence time [10, 113].

For a source of quasi-monochromatic light, we may define the coherence length – that is, the longitudinal length over which the phase remains predictable, given that our laser emits waves with wavelength  $\lambda_0$  and bandwidth  $\Delta\lambda$ . Recall figure 2.2(a): a consecutive pair of wavetrains  $E_{1,2}$  with wavelength  $\lambda_0$  and  $\lambda_0 + \Delta\lambda$  respectively will at some point interfere constructively, then destructively interfere after some path length – the coherence length  $\ell_c$ . As described in [117], the coherence length of a quasi-monochromatic laser with a Gaussian profile is defined as

$$\ell_c = \sqrt{\frac{2\ln 2}{\pi}} \frac{\lambda_0^2}{\Delta\lambda}. \quad (2.13)$$

The coherence time is then  $\tau_c = \ell_c/c$ . For some stabilised He-Ne lasers, the operating wavelength  $(\lambda, \Delta\lambda)$  is  $(632.8, 1 \times 10^{-6})$  nm, for a coherence length of  $\approx 400$  m. In contrast, mercury lamps, historically used as near-white light sources, produce  $(546.1, 1)$  nm for a coherence length of 0.03 cm [10].

### 2.1.5 Interferometry in practice

When discussing interference patterns made from a pair of fields, we require them to share a similar wavelength  $\lambda$ . As Hecht (2002) [10] explains, interfering beams of considerably different  $\lambda$  results in a  $\Delta\phi$  that varies greatly over time; this causes the quantifiable interference to average to zero over any meaningful detection time. In the event that these sources have large  $\Delta\lambda$  (e.g. white light) the resultant interferograms are the superposition of the interferogram of each constituent  $\lambda$ . Beams of equivalent amplitudes produce the largest contrast range between bright and dark fringes, and  $\Delta\phi$  should be constant with spatial and temporal coherence. Together, these are the conditions that make optical interference possible – before the invention of monochromatic laser sources, some ingenuity was required to observe the phenomenon.

The principle of interference by the *division of a wavefront* was famously demonstrated by Young’s double slits experiment [110]. As described in [10], Young used the sun as a single incoherent wavefront, which illuminated a pinhole. This in turn generated a spatially coherent sunbeam, which was then incident on a pair of pinholes equidistant from the first. Young observed the resulting bright and dark fringes as the first observation of interference fringes. In the modern interpretation, we may instead consider incident plane waves of wavelength  $\lambda$  on a pair of parallel narrow slits  $A$  and  $B$ . Each slit then becomes a secondary coherent source, this time of cylindrical wavelets which are in phase at the plane of the slits. The slits are separated by distance  $d$ , and the wavelets propagate a distance  $D$  ( $D \gg d$ ) before interfering at the screen to produce fringes. This requires that  $\Delta\text{OPL} < \ell_c$ .

From Young’s setup (see figure 2.3), we can derive the grating equation for constructive interference, as detailed in [113]: firstly, consider the optical path between the rays from each slit:  $\Delta\text{OPL} = p_1 - p_2 = d \sin \theta \approx d\theta$ . From the diagram we can infer that the diffraction angle with respect to the origin is  $\theta \approx y/D$ , where  $y$  is the transverse distance from the zero fringe. The approximation  $p_1 - p_2 \approx dy/D$  therefore

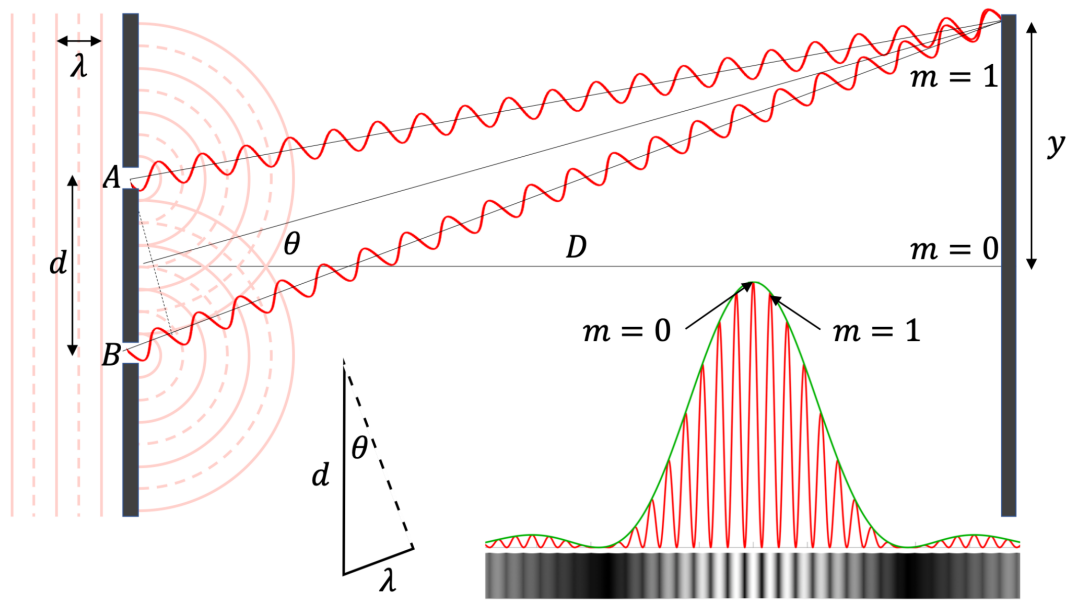


FIGURE 2.3: **Division of wavefront: Young's double slits.** An idealised plane wave source incident on a pair of identical slits results in interference in the far field. (inset) whilst the transverse interference fringe locations are dictated by slit separation  $d$  and  $\lambda$  by the diffraction equation 2.14 (red), the shape of the slits creates a modulating sinc envelope which reduces the interference to zero (green).

occurs at  $p_1 - p_2 = m\lambda$  where  $m$  is the interference order. The distance to the  $m^{\text{th}}$  constructive interference fringe  $y_m$  is then  $y_m \approx \frac{Dm\lambda}{d}$  or angular position  $\theta_m = m\lambda/d$ . Finally, we may define the condition for constructive interference for the  $m^{\text{th}}$  fringe

$$d \sin \theta = m\lambda. \quad (2.14)$$

The second class of interferometry to consider is that which operates as a *division of amplitude*, as explained in [10, 113]: when a beam is incident on a semi-transparent mirror tilted with respect to the axis of propagation, the beam is split into two different components of the same wavefront travelling in different directions. That is, the wavefront remains intact in each new direction, however the original amplitude is shared between them. Instead of interference from adjacent slits, the beams are purposefully steered with mirrors to interfere, with the resultant fringes easily detected on camera. As was the case before, interference is only possible when the path difference between the two beams after the split is less than the coherence length. If instead  $\Delta\text{OPL} > l_c$ , the wavefronts interfered will belong to the wrong wavetrains, and lack a stable  $\Delta\phi$ , resulting in washed out or absent fringes. We now discuss

the various interferometric devices that can be built to study and exploit optical interference, which will be used in chapters 4,5.

Consider figure 2.4(a): in a Michelson interferometer, a beam enters a beamsplitter (e.g. a non-polarising cube NPBS) at a  $45^\circ$  angle. The beam is simultaneously transmitted/reflected along orthogonal paths of similar length, before being reflected by perpendicular mirrors  $M_{1,2}$ . Upon returning to the beamsplitter, the two beams are instead reflected/transmitted in the same direction and interfere. Note that one beam traverses the beamsplitter medium more than the other for a larger OPL (dependent on refractive index  $n$ ) – this is rectified by inserting a compensator plate (C) of the same optical thickness in the other arm to equalise the two. By using this plate, the effects of chromatic dispersion are minimised, such that the system can be used with broadband sources. Should the interfering beams be co-propagating and coincident, the fringes will be circular; slight changes in mirror orientation will instead produce straight or even parabolic fringes. The Michelson interferometer is widely used to measure lengths with superlative accuracy, by correlating the longitudinal movement of mirror  $M_2$  with the number of fringes which pass a point on the detector. This design is the basis for the LIGO gravitational wave detectors [10].

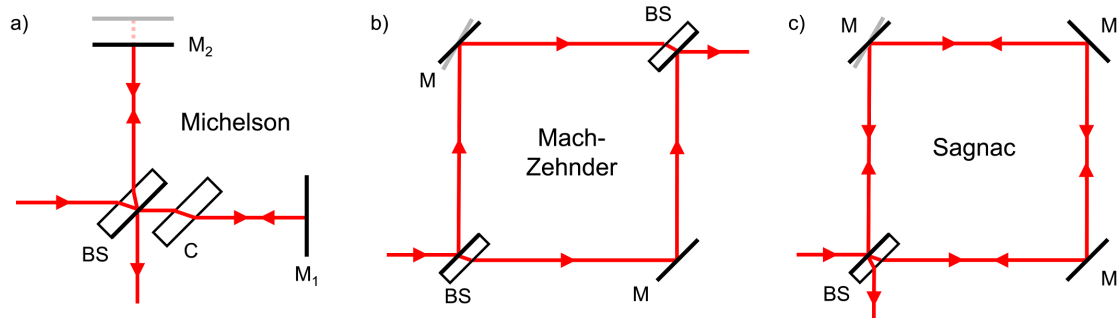


FIGURE 2.4: **Division of amplitude: interferometer variations** (a) A Michelson interferometer compares the OPLs of two distinct beam paths often using circular interference fringes. (b) A Mach-Zehnder interferometer uses a pair of beamsplitters to divide and then recombine the beams using mirrors with fine control. (c) A Sagnac interferometer replaces the second BS in the previous design to cause the beams to take equal but opposite paths around the system in a closed loop.

Another variation is the Mach-Zehnder interferometer (figure 2.4(b)), which comprises two beamsplitters and two mirrors. As before, the incident beam is split into two by a beamsplitter; however this time, the mirrors are oriented at  $45^\circ$  to the beam path. A second beamsplitter is positioned at the convergence of the two beams,

where they are transmitted/reflected in the same direction to interfere. The OPL can be adjusted by slight changes in mirror and beamsplitter orientation. This design has found use in electron interference and gas-flow density variations in wind tunnels [10].

Lastly, the second beamsplitter in the previous case can be replaced by a mirror to form a Sagnac Interferometer (figure 2.4(c)), which allows the beams to travel along identical but opposing paths in a closed loop [118]. Here the beams exit together via the initial beamsplitter. The fact that both beams travel along the same paths using the same optical elements means that it is a particularly stable design, especially when combating thermal drift and environmental vibrations. This arrangement can be used to form a ring laser gyroscope to measure rotational velocity .

### 2.1.6 Chromatic dispersion

Chromatic dispersion is the variation of optical properties with wavelength, e.g. white light through a triangular prism. In fibre optic communications, dispersion of different wavelengths causes pulse broadening based on the different paths each wavelength component takes through the waveguide. Provided such dispersion is compensated for, broadband sources such as white light can still be useful, e.g. mode-locked lasers for ultra-fast pulses. This dispersion fundamentally stems from the frequency dependence of dielectric susceptibility – specifically the polarisation density of a dielectric material features a frequency-dependent susceptibility in the frequency domain. To better illustrate this dispersion, consider the optical spectral phase as described by Thompson *et al.* (2013) [119] – the phase of the  $E$  field in the frequency domain. For a medium of length  $L$ , the optical phase is defined as

$$\varphi(\omega) = \frac{n_0(\omega)\omega L}{c} \quad (2.15)$$

where the frequency dependent refractive index  $n_0(\omega)$  comes from the real part of the dielectric susceptibility. By performing a Taylor expansion of the spectral phase

$$\varphi(\omega) = \varphi(\omega_0) + (\omega - \omega_0) \left. \frac{d\varphi}{d\omega} \right|_{\omega_0} + \frac{1}{2}(\omega - \omega_0)^2 \left. \frac{d^2\varphi}{d\omega^2} \right|_{\omega_0} + \dots \quad (2.16)$$

the individual dispersive effects can be isolated. The first term  $\varphi(\omega_0)$  simply denotes a change of total carrier phase on traversing a medium. The second term defines a

linear phase ramp in frequency which delays a broadband pulse in time. The third term, however, is a quadratic that defines the group delay dispersion (variation of group delay with frequency/wavelength) and actually reshapes the beam pulse with an added linear chirp – a time-varying change in the instantaneous optical frequency across the pulse [115].

There are several forms of dispersion: linear material dispersion arises from the refractive index of the bulk material. Modal dispersion arises from the confinement of light traversing a waveguide (e.g. optical fibre: figure 2.5(a)). Finally, geometrical dispersion is caused by a diffractive optical element whose angular response depends on the incident bandwidth of light (diffractive and refractive optics) [115]. The chromatic dispersion displayed by these components can be negated by using a corrective setup, e.g. a double pass Brewster-angled pair of triangular prisms [120].

### 2.1.7 Optical speckle

The spatial coherence of light can be visualised in everyday use of monochromatic and quasi-monochromatic sources. When coherent laser light is scattered from a diffuse or rough surface (such as a piece of card or a ground glass diffuser), the reflected light takes on a granular cross-sectional intensity, known as *optical speckle*. The disk of illumination is filled with a stationary interference pattern of grains and phase singularities. As described in [10], for every angle to the surface, the speckle-like field viewed is a superposition of a large number of scattered wavelets, which have a constant relative phase given by the OPL from the surface to the plane imaged. The spatial size of the individual granules is dependent on the distance to the screen, such that they appear to grow with increasing distance [121]. In practice, optical speckle can be synthesised in the laboratory by creating holograms comprised of many randomly oriented plane waves of comparable intensity, as will be demonstrated in section 6.3. Speckle phase singularities have been identified as the same optical vortices [122] that can be found in the centre of Laguerre-Gaussian beams (see section 2.3) – in a 3D mapping, the optical vortices permeate along the propagation of the speckle in complex paths, forming loops and knots along the  $z$ -direction (figure 2.5(c)) [3, 123]. In general, optical speckle is one of the most common forms of spatial structuring of light, however in a research environment it is usually considered as background noise, e.g. in holography.

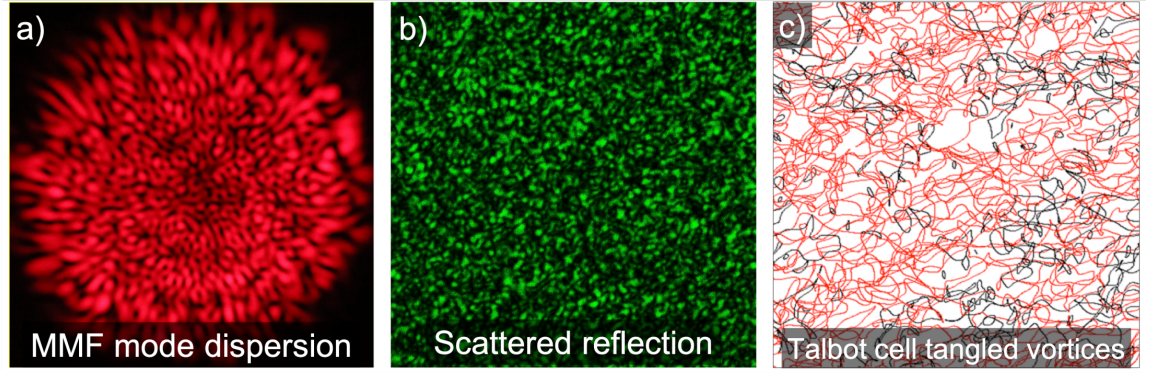


FIGURE 2.5: **Optical speckle in laboratory environments** (a) a Gaussian beam propagating through a multimode fibre (MMF) will disperse into the various eigen-modes of the fibre, such that the light exiting the distal end is scrambled into a radially varying speckle. (b) reflection from a diffuse surface (i.e. microscopically textured) such as a metal plate produces uniform granules. (c) Within a Talbot cell, speckle can be analysed as having vortex loops (black) and tangled “spaghetti-like” vortices along its propagation (source: [3]).

## 2.2 Polarisation

As an electromagnetic field propagates through space, the orthogonal components oscillate with a particular orientation at some instance in time. The magnitude and orientation of this oscillation is known as the *polarisation*. In general a natural incoherent light source, e.g. the sun is comprised of a large collection of randomly oriented atoms. As described by [10], photons are emitted on timescales of  $\approx 10^{-8}$  s due to electron energy level transitions. In this timeframe, each atom radiates a polarised wave. The combination of multiple atoms radiating differing polarisations constantly produces new wavetrains, which in turn results in no net polarisation in time. This is unpolarised light [113, 114].

In the event that the field vector of a light ray undergoes a linear vibration upon propagation, such that the orientation remains the same, then this light is linearly polarised. There exist distinct *degenerate polarisation states*, according to [111], defined by the relationship between the  $E_x, E_y$  components, their rotation angle  $\theta$

and phase offset  $\delta$ :

$$\text{Horizontal :} \quad E_{0y} = 0 \quad (2.17)$$

$$\text{Vertical :} \quad E_{0x} = 0 \quad (2.18)$$

$$+45^\circ : \quad E_{0x} = E_{0y} = \frac{1}{\sqrt{2}} E_0 \quad \delta = 0 \quad (2.19)$$

$$-45^\circ : \quad E_{0x} = E_{0y} = \frac{1}{\sqrt{2}} E_0 \quad \delta = \pi \quad (2.20)$$

$$\text{Right circular :} \quad E_{0x} = E_{0y} = \frac{1}{\sqrt{2}} E_0 \quad \delta = \frac{\pi}{2} \quad (2.21)$$

$$\text{Left circular :} \quad E_{0x} = E_{0y} = \frac{1}{\sqrt{2}} E_0 \quad \delta = \frac{-\pi}{2} \quad (2.22)$$

In the first four linear states, the E-field traces out a straight line in the transverse plane; in the circular states, the E-field instead traces out a circle. More generally, the field is described as elliptically polarised when  $E_{0x} \neq E_{0y}$  or  $\delta \neq \pi/2$ .

### 2.2.1 Linear polarisers

In the case of an ideal monochromatic laser, the field is a plane wave with an infinitely long wavetrain. The orthogonal components share the same frequency and are coherent – i.e. the beam is polarised. In reality, however, natural light and laser light is often only partially polarised, and we must introduce the means to polarise it.

This can be achieved by using an element which exploits asymmetry in its structure to select a single polarisation from the incident field. Commercial polarisers, explains [10], make use of mechanisms such as *dichroism* (selective absorption), *reflection* off a dielectric medium and *birefringence* (dual refractive indices). Dichroic polarisers, such as wire-grid designs and dichroic crystals like tourmaline, make use of the anisotropic structure of the material to promote selective absorption. An incident field parallel to the wires/long-axis of the crystal lattice will drive the conduction electrons along the full length and induce a current – this in turn transfers the energy from the field to the lattice atoms. It follows that only the field component that is parallel to the optic axis of the material (and orthogonal to the absorbed axis above) will pass through largely unchanged.

### 2.2.2 Wave retardance

The first step towards manipulating the polarisation of light fields to generate vector beams is to utilise the common methods of polarisation control in beam optics. These include polarisers and wave retardance plates, the most common of which are demonstrated in figure 2.6. Waveplates, or wave retarders, are widely used planar

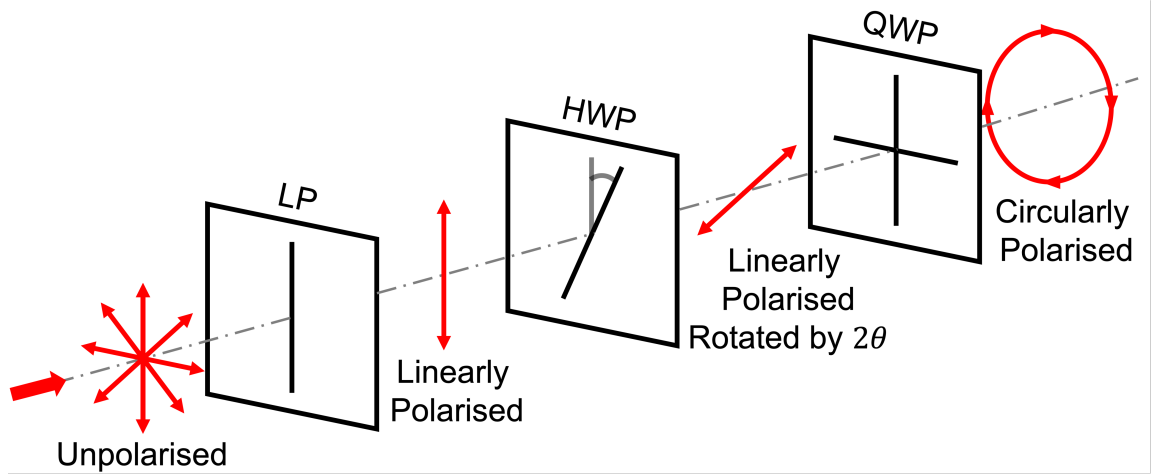


FIGURE 2.6: **Wave retardance with conventional optics** Initially unpolarised light will pass through only one field component through a linear polariser (LP), along the direction of its optic axis. An HWP will rotate a single polarisation by  $2\theta$  about its optic axis, whilst a QWP converts linearly polarised light to circular, when oriented  $45^\circ$  to the polarisation orientation.

optical components, manufactured from a birefringent medium. The thickness of the plate is such that light passing through normal to the surface will experience a phase delay between its orthogonal components (ordinary and extraordinary), resulting in a shift of polarisation state. In a positive uniaxial material,  $n_e > n_o$  and the phase velocity of light polarised along the slow  $n_e$  axis is  $v = c/n_e$ . For a beam with components in both orthogonal orientations e.g.  $45^\circ$  from the crystal axes, this results in a phase shift between the fast and slow components, which represents an altered polarisation. Given some propagation thickness  $t$  of material, [124] refers to the relative phase retardance as  $\Gamma = 2\pi(n_e - n_o)t/\lambda$ , i.e. a given waveplate will exhibit a wavelength-dependent retardance.

Quarter-wave and half-wave retardance can be readily achieved with two thicknesses of birefringent material, and can be defined for an incident linearly polarised beam

that possesses components  $E_e\hat{e}$  in the slow axis and  $E_o\hat{o}$  in the fast axis to form

$$E(z, t) = (E_o\hat{o} + E_e\hat{e})e^{i(\omega t - kz)}. \quad (2.23)$$

A material thickness and birefringence for a given  $\lambda$  that results in a quarter-wave of phase retardance  $\Gamma = \pi/2$  radians) is known as a quarter-wave plate. Adding this as a factor  $e^{i\Gamma} = e^{i\pi/2} = i$ , the outgoing field becomes

$$E(z, t) = (E_o\hat{o} + iE_e\hat{e})e^{i(\omega t - kz)}. \quad (2.24)$$

Should the incident plane polarised beam be angled at  $45^\circ$  to both the birefringence axes, then  $E_o = E_e$  and the field is converted to become circularly polarised – as such we use quarter-wave plates to convert from linear to circular polarisation.

By instead selecting a waveplate that exhibits  $\Gamma = \pi$  for a given incident  $\lambda$ , the same procedure gives us a phase offset of  $e^{i\delta} = e^{i\pi} = -1$ . For some beam polarised along direction  $\hat{d}$  at  $\theta$  to the fast axis, we may define

$$\mathbf{E}(z, t) = Ee^{i(\omega t - kz)} = E(\cos\theta\hat{o} + \sin\theta\hat{e})e^{i(\omega t - kz)}. \quad (2.25)$$

Propagation through a half-wave plate therefore results in an outgoing field

$$E(\cos\theta - \sin\theta)e^{i(\omega t - kz)} = E[\cos(-\theta) + \sin(-\theta)]e^{i(\omega t - kz)}. \quad (2.26)$$

The shift in orientation of the polarisation from  $\theta$  to  $-\theta$  indicates that the action of a half-wave plate is to rotate an incident linear polarisation by  $2\theta$  in the direction of the fast axis.

### 2.2.3 Polarising optics

In the following investigations, the ability to discriminate between different polarisations to generate polarised light is dependent on the polarising optics used. The following is a short summary of the optical elements used, and their physical mechanisms. Firstly, the most common method to split unpolarised light into corresponding  $s$  and  $p$  state (horizontal and vertical) fields is by using a polarising beamsplitter cube, shown in figure 2.7(a). This is formed by combining two right-angle prisms of

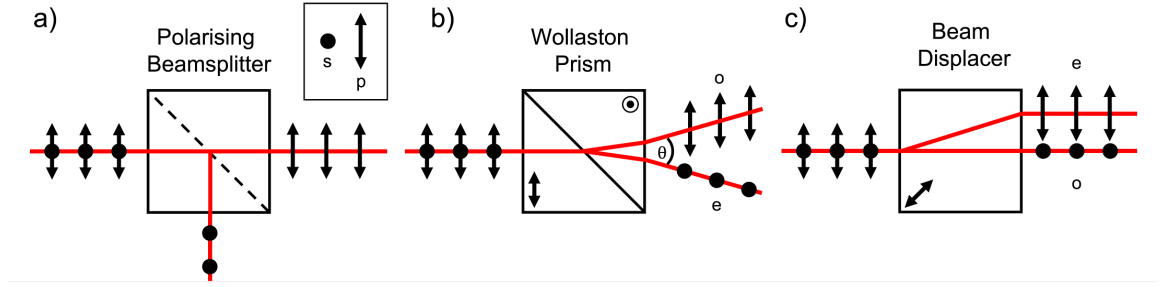


FIGURE 2.7: **Polarising optics:** (a) in a beamsplitter cube, two glass prisms set with dielectric film can be used to split incoming light based on its polarisation, by reflecting (transmitting) the  $s$  ( $p$ ) component. (b) two birefringent crystals combined with orthogonal optic axes make up a Wollaston prism, which transmits the  $(o, e)$  components of the beam, separated with an angle  $\theta$  between them. (c) shows a beam displacer: a single cut of crystal with optic axis oriented diagonally will instead displace only the  $e$  components of the incident beam, and the two components exit normal to the surface of the crystal.

crown glass with a multi-layered transparent dielectric film in between. Under similar electron-oscillation behaviours as in section 2.2.1 and applying Brewster's law, the  $s$  component is reflected whilst  $p$  is allowed to transmit, thereby separating the orthogonal states by  $90^\circ$  [10, 113].

A birefringent medium (e.g. calcite or quartz) may be cut and recombined to have orthogonal optic axes, such that it refracts the ordinary and extra-ordinary components with different angles. This is the *double refraction* famously associated with calcite crystals. Within a Wollaston prism (figure 2.7(b)) there exists two refractive indices  $n_e < n_o$ ; once the prism-prism boundary is traversed and the optic axis rotates, the ordinary and extra-ordinary rays switch, causing a refraction towards and away from the surface normal respectively. This results in the  $s, p$  states emerging at some wedge angle  $\theta$  [10].

Lastly, a single birefringent crystal can be cut into a rhomb such that the optic axis lies through the diagonal, e.g. a calcite beam displacer 2.7(c) [125]. A plane which incorporates the optic axis is known as a principal section. Initially unpolarised light incident normal to the facet of this rhomb will refract in different directions – components perpendicular to the principle section will propagate unhindered ( $o$ -ray), whilst components parallel to the principle section ( $e$ -ray) will refract based on the birefringence  $\Delta n$  [10]. Significantly, both components exit normal to the crystal surface, but with a lateral displacement; this component will be used in the work detailed in chapter 3.

### 2.2.4 Characterising polarisation

From the definitions in section 2.2, we have established the general case of polarised light being an electromagnetic field, with field vector  $E_{x,y}(z, t)$  and exhibiting some variation of elliptical polarisation. Whilst the electric field traces out this ellipse as it propagates, the period of this trace is much too small to measure accurately. As a consequence, it is pertinent to consider a time-independent measurement to characterise the polarisation of a given light field. The following is a brief introduction to calculating the intuitive *polarisation ellipse* and its relation to the commonly used *Poincaré sphere* to characterise polarised light [10].

### 2.2.5 Polarisation ellipse

The polarisation ellipse can be derived by manipulating a time-independent form of equation 2.4. Following the procedure used in Collett (2005) [111], let  $\omega t - kz = \eta$ , whilst each orthogonal field component has a corresponding additional phase shift  $\delta_{x,y}$  such that:

$$E_x(z, t) = E_{0x} \cos(\eta + \delta_x) \quad (2.27)$$

$$E_y(z, t) = E_{0y} \cos(\eta + \delta_y). \quad (2.28)$$

By some manipulation, including using the double angle formula, it can be shown that

$$\frac{E_x(z, t)^2}{E_{0x}^2} + \frac{E_y(z, t)^2}{E_{0y}^2} - 2 \frac{E_x(z, t)}{E_{0x}} \frac{E_y(z, t)}{E_{0y}} \cos(\delta) = \sin^2(\delta), \quad (2.29)$$

where  $\delta = \delta_y - \delta_x$ . This maps out the equation of an ellipse – the *polarisation ellipse*, as depicted in figure 2.8(a). Note that whilst we have eliminated the time-space propagator, the electric field remains time-space dependent. The constants  $E_{0x,y}$  and phase  $\delta$  imply that the ellipse is unchanged on propagation.

For the purposes of plotting polarisation with cartesian axes, we only need to consider two angles: the orientation  $\Psi$  ( $0 \leq \Psi \leq \pi$ ), and ellipticity  $\chi$  ( $-\frac{\pi}{4} < \chi \leq \frac{\pi}{4}$ ). These can be combined with the above field components to produce an entirely trigonometric form, provided  $\alpha = \tan^{-1}(E_{0y}/E_{0x})$ . In terms of the parameters  $(\Psi, \delta)$ :

$$\tan 2\Psi = \frac{2E_{0x}E_{0y}}{E_{0x}^2 - E_{0y}^2} \cos \delta = (\tan 2\alpha) \cos \delta, \quad (2.30)$$

$$\sin 2\chi = \frac{2E_{0x}E_{0y}}{E_{0x}^2 + E_{0y}^2} \sin \delta = (\sin 2\alpha) \sin \delta, \quad (2.31)$$

which is true given  $0 \leq \alpha \leq \pi/2$  and  $0 \leq \delta < 2\pi$  [111].

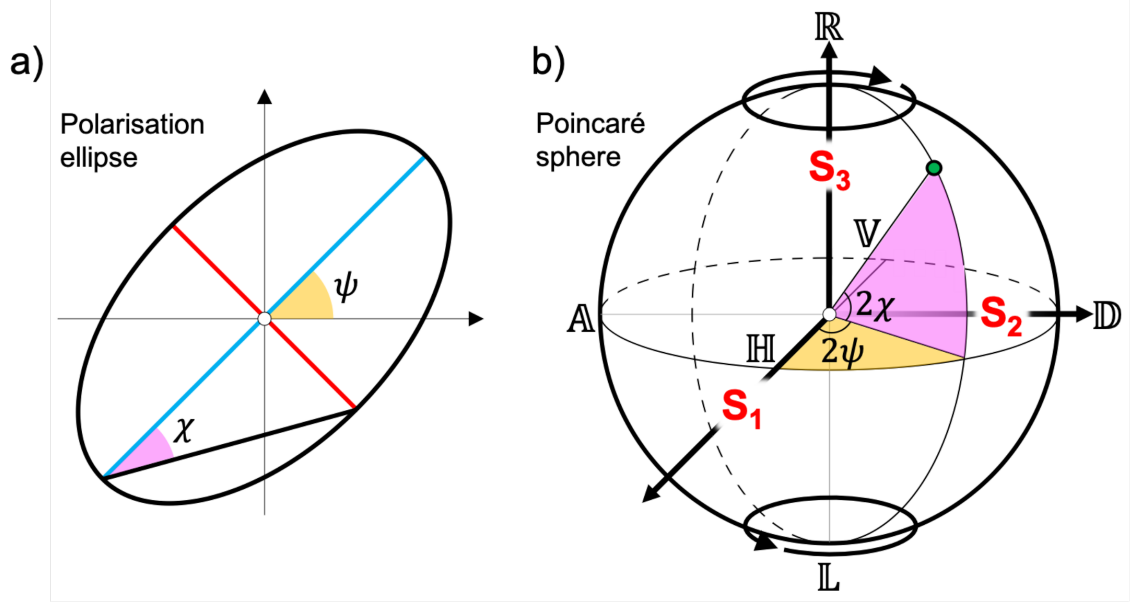


**FIGURE 2.8: The polarisation ellipse and Poincaré sphere for characterising polarisation states:** Adapted from [111]. (a) the average polarisation state of a point in a field may be represented by an ellipse in cartesian co-ordinates by determining the orientation  $\Psi$  and ellipticity  $\chi$ . The former describes the orientation of the polarisation state, whilst the latter describes the relative lengths of the major (blue) and minor (red) axes. (b) These angles can be used to plot the polarisation state on the surface  $(2\Psi, 2\chi)$  of the Poincaré sphere, whose 3D axes represent the latter three Stokes parameters.

In (1892) the French mathematician Henri Poincaré (1852–1912) devised a method of representing polarisation by mapping the same ellipse parameters onto the surface of a sphere. This is useful to contextualise the polarisation ellipse within the wider beam shaping community, and thus is defined here for reference.

The overall polarisation state is defined as a point located on the surface at  $(2\Psi, 2\chi)$ ; the above cartesian co-ordinates are then related to their spherical counterparts by

$$x = \cos(2\chi) \cos(2\Psi), \quad 0 \leq \Psi < \pi, \quad (2.32)$$

$$y = \cos(2\chi) \sin(2\Psi), \quad -\pi/4 < \chi \leq \pi/4, \quad (2.33)$$

$$z = \sin(2\chi), \quad (2.34)$$

which results in a sphere of unit radius  $x^2 + y^2 + z^2 = 1$ . Notably, the pure degenerate polarisation states in section 2.2 are found at the orthogonal axes – e.g. horizontal  $(0, 0)$ ,  $+45^\circ$  diagonal at  $(90, 0)$  and left circular at  $(0, -90)$  (all measured in degrees). In general, partial polarised states lie within the unit sphere, with the length of the state vector proportional to the degree of polarisation. The special cases are pure linear states, which are confined to the sphere equator, whilst left/right circular are found on the poles [111].

### 2.2.6 Stokes parameters

Whilst the Poincaré sphere and polarisation ellipse are valuable depictions of polarisation state, it remains the case that they are instantaneous snapshots, and measuring angles  $\Psi$  and  $\chi$  directly (and accurately) is not practical under laboratory conditions. Instead, we need to define the polarisation state using physical observables that can be measured in real-time. [10] describes that in 1852, G.G. Stokes developed the eponymous Stokes parameters – four parameters which are calculated by measuring only the irradiance of a light field under various conditions. These parameters are capable of succinctly defining the polarisation state, quantifying the extent of polarisation in each of the aforementioned degenerate states.

The procedure, discussed in [10, 111] and utilised in [102], is as follows: in the first instance, a set of polarising filters are used alongside a detector such as a diode or camera. The first filter used is isotropic, i.e. all polarisations pass through freely with maximal irradiance ( $I_0$ ); the second is a linear polariser with an axis along the horizontal s-state ( $I_1$ ). Next, the polariser is oriented along the diagonal  $+45^\circ$  state ( $I_2$ ). Finally, the polariser and quarter-wave plate are combined to probe the left circular polarisation state ( $I_3$ ). The Stokes parameters are therefore defined by the deviation of these observables from the maximal irradiance ( $I_0$ ):

$$\mathcal{S}_0 = 2I_0 \tag{2.35}$$

$$\mathcal{S}_1 = 2I_1 - 2I_0 \tag{2.36}$$

$$\mathcal{S}_2 = 2I_2 - 2I_0 \tag{2.37}$$

$$\mathcal{S}_3 = 2I_3 - 2I_0. \tag{2.38}$$

Using these relations,  $\mathcal{S}_0$  is known as the incident irradiance. The sense of the remaining Stokes parameters indicates the hemisphere of each polarisation state on the Poincaré sphere – specifically,  $\mathcal{S}_1 > 0$  denotes horizontal polarisation, whereas  $\mathcal{S}_1 < 0$  is vertical. As described in [111, 126], we can identify the relation between these parameters and the electric field by considering the time-averaged form of the electric field, which in turn allows us to define the Stokes parameters in terms of the time-averaged electric field components:

$$\mathcal{S}_0 = \langle E_{0x}^2 \rangle_T + \langle E_{0y}^2 \rangle_T \quad (2.39)$$

$$\mathcal{S}_1 = \langle E_{0x}^2 \rangle_T - \langle E_{0y}^2 \rangle_T \quad (2.40)$$

$$\mathcal{S}_2 = \langle 2E_{0x}E_{0y} \cos \epsilon \rangle_T \quad (2.41)$$

$$\mathcal{S}_3 = \langle 2E_{0x}E_{0y} \sin \epsilon \rangle_T. \quad (2.42)$$

In the ideal case of a purely monochromatic beam,  $E_{0x,y}$  are time-independent. It also follows that

$$\mathcal{S}_0^2 = \mathcal{S}_1^2 + \mathcal{S}_2^2 + \mathcal{S}_3^2. \quad (2.43)$$

By virtue of the fact that  $\mathcal{S}_0$  is the maximal irradiance, we can normalise the Stokes parameters to simplify the form and view them as a vector; this leads to a powerful tool in calculating the cumulative effect of different polarisation optics. In this regime, unpolarised light can be written as Stokes vector  $(1, 0, 0, 0)$ ; when a beam is completely horizontally/vertically polarised,  $\mathcal{S}_1 = \pm 1$  and the vector becomes  $(1, \pm 1, 0, 0)$ . In this notation the equations from 2.39 onward remain valid. Written as Stokes vectors, we may combine different fields simply by summing the matching vector elements, e.g. the resultant polarisation formed from  $(1, -1, 0, 0) + (2, 0, 0, -2) = (3, -1, 0, -2)$ . This formalism extends further for polarising components by the introduction of Jones calculus, which defines a polarising optical element with a Jones matrix – by finding the product of the incident light Stokes vector and the Jones matrix of some optic, the resultant polarisation can be determined. [10].

## 2.3 Laser modes

The beam shaping techniques outlined in chapters 3 and 4 involve the decomposition of a desired vector beam into orthogonally polarised field components which can

be independently generated by diffraction of a Gaussian beam from a spatial light modulator. In particular, radially and azimuthally polarised vector vortex beams (theorised in section 3.6) can be decomposed into a pair of Hermite-Gaussian modes of opposite mode indices. It is therefore appropriate to introduce the most common mode bases as solutions to the wave equation in various symmetries [127, 128].

Within the optical resonator of a laser, photons are produced and amplified through stimulated emission via the gain medium. These photons reflect between the mirrors of the resonator over many round trips before transmission – as such, all but a few propagation orientations and frequencies survive. The most reproducible patterns over successive round trips are the most stable over time, and represent the natural fields of the resonator – the resonator eigen-modes.

We may now define a laser mode as an optical field which remains self-consistent in shape throughout its propagation through some propagating medium e.g. a resonator or waveguide. That is, the cross-sectional intensity profile maintains the same structure along the optic axis; this is a consequence of the boundary conditions placed on a light field by the propagating medium, and are solutions to Maxwell's equations. Lasers are conventionally designed to operate with paraxial modes – in general, however, we can define both a transverse and longitudinal mode: a *transverse* mode is one whose transverse field cross-section remains the same during propagation, unless the amplitude is multiplied by a complex factor.

Should this field also gain an integer  $m$  multiple of  $2\pi$  in phase after a round trip/propagation through the medium, this mode is also longitudinal (i.e. the above factor must be a real and positive eigenvalue, with the optical path length of the resonator  $\text{OPL} = m \lambda/2$ ) [128].

### 2.3.1 Gaussian beam

The simplest mode of a stable canonical resonator is the fundamental Gaussian field, or  $TEM_{00}$  mode (transverse electro-magnetic). According to [127], the complex field in cylindrical co-ordinates  $(r, z)$  is defined by:

$$u(r, z) = i \frac{U_0}{z_R} \exp[i(kz - \omega t)] \frac{w_0}{w(z)} \exp\left[-\frac{r^2}{w(z)^2}\right] \exp\left[i\frac{kr^2}{2R(z)}\right] \exp[-i\alpha(z)]. \quad (2.44)$$

Here,  $\exp[i(kz - \omega t)]$  is the plane wave propagation, whilst  $\exp[-r^2/w(z)^2]$  is the Gaussian profile of the intensity in the transverse plane. The spot size  $w(z) = w_0\sqrt{1 + (z/z_R)^2}$  becomes the beam waist  $w(z) = w_0$  when  $z = 0$ . The Rayleigh range  $z_R$  is defined as the distance along the propagation at which  $w(z_R) = \sqrt{2}w_0$ .  $U_0$  is the field amplitude at  $t = 0$ , whilst the radius of curvature  $R(z) = z[1 + (z/z_R)^2]$ . Finally, the curvature of the wavefront and Gouy phase shift are represented by  $\exp[ikr^2/2R(z)]$  and  $\exp[-i\alpha(z)]$  respectively, whilst  $\alpha(z) = \tan^{-1}(z/z_R)$ .

Gaussian beams are the paraxial limit of spherical waves from a complex source, and are one of the solutions to the paraxial wave equation. For a standard laboratory laser, the fundamental Gaussian field is both a transverse and longitudinal mode of the optical resonator. It is possible to induce higher orders of modes within a laser resonator by altering the symmetry of the cavity itself; for instance, by adjusting the alignment of the laser output coupler or introducing an intracavity cross-wire [129]. In doing so, we may introduce different polynomial sets to solve the paraxial wave equation in these new symmetries.

### 2.3.2 Hermite-Gaussian modes

As defined by Hooker and Webb (2010) [127], Hermite-Gaussian (HG) modes are a complete set of solutions to the paraxial wave equation with rectangular symmetry, which use Hermite polynomials  $H_{m,n}(x)$ . We may define the complex amplitude of HG beams as

$$\begin{aligned} \text{HG}_{m,n}(r, z) = & i \frac{U_0}{z_R} \exp[i(kz - \omega t)] \frac{w_0}{w(z)} \exp\left[-\frac{r^2}{w(z)^2}\right] \times H_m\left[\frac{\sqrt{2}x}{w(z)}\right] H_n\left[\frac{\sqrt{2}y}{w(z)}\right] \\ & \exp\left[i\frac{kr^2}{2R(z)}\right] \times \exp[-i(m+n+1)\alpha(z)]. \end{aligned} \quad (2.45)$$

Here, the integers  $(m, n)$  define the HG mode indices, which correspond to horizontal and vertical axis intensity nodes respectively to produce unique HG modes. Each combination of these mode orders  $(m, n)$  is distinct and orthogonal, such that they form a complete basis set. The fundamental HG modes are shown in the top row of figure 2.9; note that each field comprises of lobes, whose amplitude are equal but

opposite in sign to neighbouring lobes with a  $\pi$  phase shift. Note that the fundamental Gaussian mode is also the fundamental HG mode,  $\text{HG}_{00}$ .

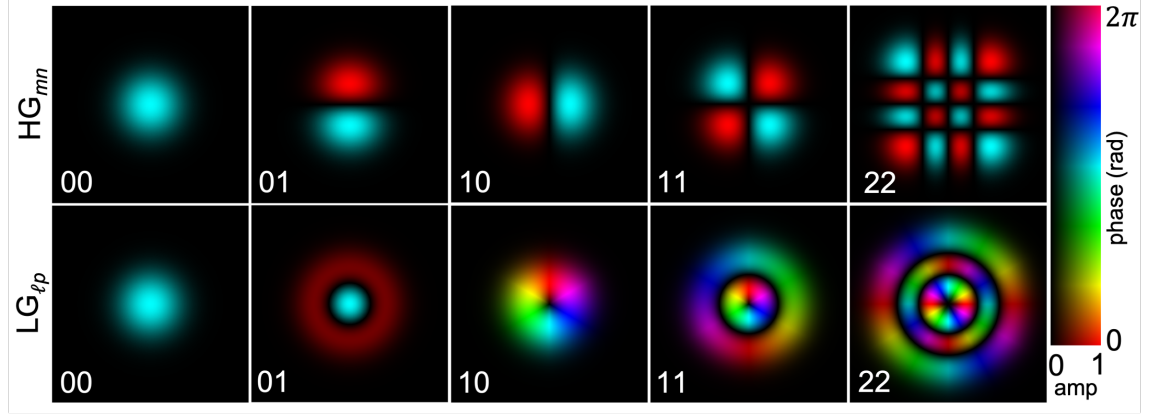


FIGURE 2.9: **Hermite and Laguerre Gaussian mode bases.** Solutions of the fundamental wave equation with rectangular and cylindrical symmetry – the lowest order Hermite (top) and Laguerre (bottom) Gaussian mode sets. HG beams have a mode index of  $(m, n)$ , whilst Laguerre Gaussian beams use  $(\ell, p)$ , where  $\ell$  is the azimuthal index for OAM. When the mode indices are zero, both solutions are Gaussian profiles.

### 2.3.3 Laguerre-Gaussian modes

Should the laser cavity be cylindrically symmetric, we may instead use associated Laguerre polynomials  $L_p^{|\ell|}(x)$  to generate the Laguerre-Gaussian (LG) mode set. Shown in figure 2.9 (bottom), these are rotationally symmetric beams with a “doughnut” intensity and a helical phase; specifically, the integer  $\ell$  is the azimuthal index, which provides an orbital angular momentum (OAM) of  $\ell\hbar$  per photon, and  $p$  is the radial node index ( $p \in \mathbb{W}$ ) [123, 128, 130]. A consequence of helical phase is that such beams have an optical vortex singularity in the centre [131]. As in [123], we may define these modes with a complex field distribution:

$$\text{LG}_{p\ell}(r, z) = \sqrt{\frac{2p!}{\pi(p + |\ell|)!}} \frac{1}{w(z)} \left[ \frac{r\sqrt{2}}{w(z)} \right]^{|\ell|} \exp\left[ \frac{-r^2}{w(z)^2} \right] L_p^{|\ell|}\left( \frac{2r^2}{w(z)^2} \right) \exp[i\ell\phi] \exp\left[ \frac{ik_0 r^2 z}{2(z^2 + z_R^2)} \right] \exp\left[ -i(2p + |\ell| + 1)\tan^{-1}\left( \frac{z}{z_R} \right) \right]. \quad (2.46)$$

Within this profile,  $L_p^{|\ell|}(z)$  is an associated Laguerre polynomial;  $w(z) = w(0)\sqrt{(z^2 + z_R^2)/z_R^2}$  is the beam radius at  $1/e$  the peak intensity.

## 2.4 Fourier optics

The superposition principle may be combined with harmonic analysis to characterise the behaviour of quasi-monochromatic waves on propagation through a holographic system. We must therefore consider the relevant Fourier optics. Following the argument defined by Saleh and Teich (1991) [132], an arbitrary function  $f(x, y)$  can be represented as a sum of harmonic functions that contain unique spatial frequencies and complex amplitudes:

$$f(x, y) = \int_{-\infty}^{\infty} \int_{-\infty}^{\infty} \mathcal{F}(\nu_x, \nu_y) \exp[-i2\pi(\nu_x x + \nu_y y)] d\nu_x d\nu_y \quad (2.47)$$

i.e. a superposition of harmonic functions of  $(x, y)$ . Here, the complex amplitude  $\mathcal{F}(\nu_x, \nu_y)$  contains variables  $(\nu_x, \nu_y)$ , which are the spatial frequencies in the Fourier plane (FP). For some plane wave  $U(x, y) = A \exp[-i(k_x x + k_y y)]$ , we may convert this to Fourier space terms  $U(x, y) = A \exp[-i2\pi(\nu_x x + \nu_y y)]$  such that  $\nu_x \Leftrightarrow k_x/2\pi$  and  $\nu_y \Leftrightarrow k_y/2\pi$ . By this logic we may define the behaviour of some arbitrary propagating wave  $U(x, y)$  as the superposition of a set of individual plane waves. These harmonic functions  $\mathcal{F}(\nu_x, \nu_y)$  are known as the Fourier components.

### 2.4.1 Fourier transforming with a lens

Next, we consider the propagation of waves through optical elements in terms of their Fourier components – firstly note that transmission of a plane wave through said elements can be used to decompose the corresponding Fourier components resulting from  $f(x, y)$ . This can be achieved through applying the Fraunhofer approximation, which determines behaviour in the far field. Instead, we will consider the *Fourier transform* by propagation through a simple lens, which for some incident wave brings the far field to the focal length  $f$  of the lens. For example, in figure 2.10, we see the propagation of an ideal plane wave through a convex lens – the wavefront components are directed onto a focused point in the small angle case. In other words, the propagation direction  $(\theta_x, \theta_y)$  is mapped onto the point  $(x, y) = (\theta_x f, \theta_y f)$  – figure 2.10 shows this transform in  $x$  only. In the 2D case, the amplitude of a wave travelling at  $(\theta_x, \theta_y)$  is proportional to the Fourier transform  $\mathcal{F}(\nu_x, \nu_y)$  where the mapping is found to be  $(\theta_x, \theta_y) = (\lambda \nu_x, \lambda \nu_y)$  [132].

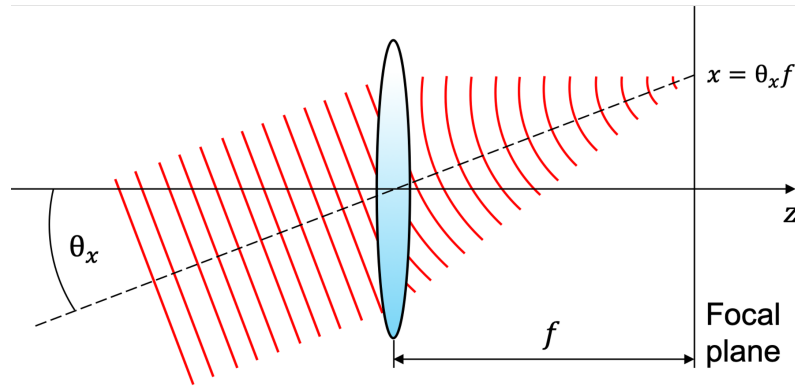


FIGURE 2.10: **Fourier transforming with a lens:** Adapted from [132]. An idealised plane wave incident on a convex lens (focal length  $f$ ) at some  $\theta_x$  to the optic axis is focused to a diffraction limited spot at a transverse distance  $x$  in the lens focal plane. This is equivalent to bringing the far-field to the back focal plane of the lens, i.e. performing a Fourier transform.

### 2.4.2 The $4-f$ imaging system

In chapters 3, 4 and 5, I will use the Fourier transforming properties of a convex lens by employing them in a  $4-f$  (two lens) imaging system. Recall that upon traversing a lens, an object with amplitude transmittance  $f(x, y)$  will be split into its constituent spatial frequencies in the Fourier plane. In the case of holographic beam modulation, this is significant because we may diffract light into transverse spatial modes with high accuracy in the Fourier plane via a lens. However, it is possible to image the object plane itself by using consecutive lenses spaced apart by the sum of their focal lengths. Consider the process described in [10, 132] and depicted in figure 2.11: the first lens  $L_1$  transforms the object plane into the FP, before  $L_2$  inverse Fourier transforms the beam back into  $(x, y)$  components as an image. Magnification of the object can be achieved by combining two lenses of differing focal lengths. Notably, an aperture placed in the FP of  $L_1$  will act as a *spatial filter* – this includes either optical high/low pass filters, depending on which transverse regions (and therefore spatial frequencies) are blocked from propagating further.

## 2.5 Holographic beam modulation

Light scatters or radiates from objects in all three co-ordinates of the vector electric field, i.e. with an associated amplitude  $A$  and phase  $\phi$ ; however we will restrict the

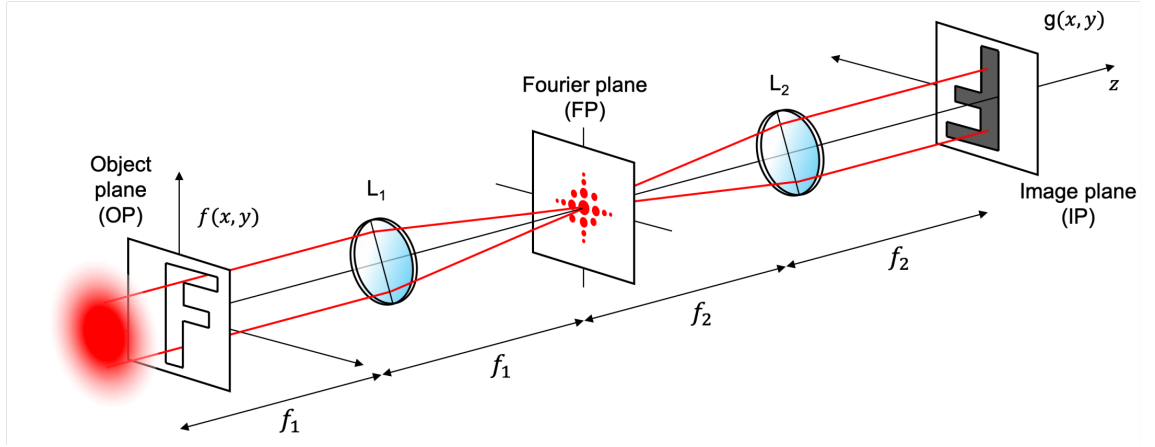


FIGURE 2.11: **4- $f$  imaging system:** Adapted from [132]. For a collimated incident beam amplitude masked by an object  $f(x, y)$ , the far-field is collected in the back focal plane of lens  $L_1$  in the Fourier plane (FP) by Fourier transform. Further projection through a lens  $L_2$  inverse Fourier transforms the beam, such that the image plane of object  $f(x)$ ,  $(g(x))$  is found a distance  $(f_1) + (f_1 + f_2) + (f_2)$  from the object. The FP is mapped into  $k$ -space such that a pinhole or annular filter at this plane can be used to filter out the high/ low frequency components of the object respectively.

following arguments to scalar fields for simplicity. In conventional imaging, a detector such as a CCD is used to capture the intensity ( $\propto A^2$ ), but cannot record the phase of the light at any given transverse location. The resultant image has therefore lost the phase information of the incident light to the detector, in the mapping from 3D to 2D. However, reasoned Dennis Gabor (1900–1979) [133], if there was a way to record both the amplitude and phase of the original light, it would lead to the creation of images which are indistinguishable to viewing the original object at the time of recording. In 1948, Gabor introduced the concept for spherical lens corrections in electron microscopy – by interfering a coherent reference wave with the scattered electron wavefronts, he was able to capture the 3D object information within an interference pattern. This would come to be known as a *hologram*.

The classic holographic technique, discussed in [10], is as follows: firstly, a coherent incident plane wave of wavelength  $\lambda$  is split using e.g. a beamsplitter, into two identical fields. The first beam is used to illuminate the object to be captured, whilst the second is the reference beam, used to illuminate the recording medium (usually photographic film or plates). Light which coincidentally scatters from the object and strikes the recording medium interferes with the reference wave; this interferogram is exposed onto film and developed as a hologram. In this way, both the

amplitude and the phase of the light scattered is captured in the interference pattern. The holographic image of the object is reconstructed, by illuminating the hologram with the same  $\lambda$  and the same angle of incidence as the original reference beam. This diffracts beams of the real and virtual (true) image, which exactly resembles the object and (in the virtual case) is located where the original object used to be. More specifically, the reconstruction beam incident on the hologram produces a superposition of three waves – the direct wave (zeroth order), object wave (first order virtual image that reconstructs object) and the conjugate wave (real image with negative phase angle).

Since the object wave is the only wave which perfectly recreates the object, it is common to use an off-axis hologram to prevent the three beams from overlapping [134]. The principle is depicted in figure 2.12 for the general case of Fourier holography using a transmitting hologram (e.g. photographic film). The recording process is marked in blue, whilst the reconstruction is in green. Here, the interference of the Fourier plane of the off-axis object  $f(x, y)$  (produced by lens  $L$ ) and planar reference wave  $U_r$  generates a hologram with a complex amplitude transmittance  $\mathcal{F}$ . With the removal of this object, the hologram can be illuminated with the same reference wave to generate object, direct and conjugate waves. By placing lens  $L$  at  $f$  from the hologram plane, object  $f(x, y)$  will be reconstructed in the FP of  $L$  with the same angular separation  $\theta$  from the direct (zero order) wave.

In a simple example, if the reference beam is a plane wave and is used to create a converging (focusing) beam hologram, then subsequent re-illumination of this hologram with the same reference wave will produce a converging beam. By this method a hologram can replicate refractive optics.

Over the last 50 years, the field has evolved substantially. Holograms of purely hypothetical objects can be designed by calculating the intensity distribution of the light scattered from an object if the incident illumination is known. The emergence of spatial light modulators in the late 20th century has heralded in a new era of holography – whereby computer generated holograms (CGHs) are used to shape light in realtime with a number of attributes not possible with photographic film [10, 127, 135].

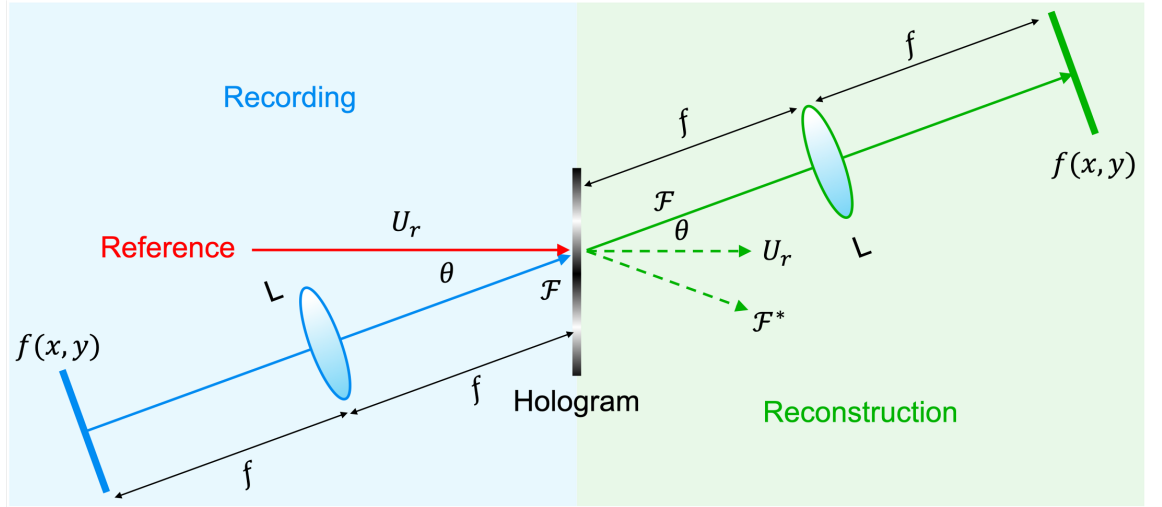


FIGURE 2.12: **Recording and reconstructing a transmitting hologram in the FP of a lens:** Adapted from [132]. The recording (blue) and reconstruction (green) of a traditional hologram. The FP of object  $f(x,y)$  is projected in the back focal plane of the hologram medium, such that an incident reference beam will interfere with it from an angle  $\theta$  to the object. This interference pattern (grating) is recorded on e.g. photographic film. In the physical absence of the object, its hologram may be recovered by illuminating the hologram with the original source from the same angle, which diffracts light into several orders. The direct (reference beam  $U_r$ ) and conjugate  $F^*$  beams are ignored in favour of the object beam, formed in the back focal plane of lens  $L$  from the hologram. This is analogous to the  $-1, 0, +1$  beam orders discussed in later sections.

### 2.5.1 Liquid crystal SLMs and dynamic modulation

The origins of the Liquid Crystal Spatial light modulators (LC-SLMs) used in this research lie in the discovery of the liquid crystal state of matter itself. As documented in [10], in 1888, Austrian-born botanist Friedrich Reintzer observed that when heated, the organic chemical cholesteryl benzoate underwent two separate transitions. When heated sufficiently, the chemical would melt into a cloudy liquid, however with further heating the substance became transparent. Although the implications were unclear at the time, this is now considered a new state of matter – a liquid of crystals which flow as a fluid yet can exhibit structural properties synonymous with solids. Within a given liquid crystal layer, there are elongated *cigar-shaped* molecules which are free to move as in other fluids. However, these individual molecules can interact with one another enough to emulate a solid crystalline structure with a well-defined common orientation among molecules [10].

There are various phases of liquid crystal phase identified at different temperatures

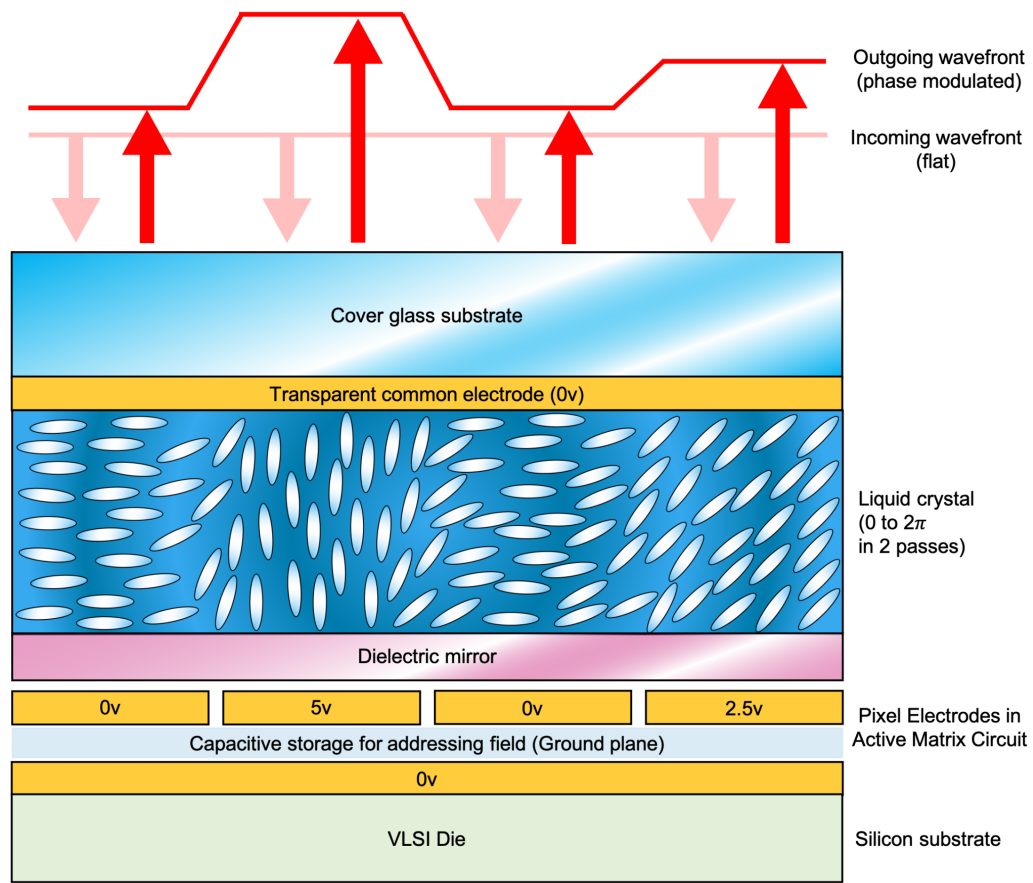


FIGURE 2.13: **LC-SLM design:** Adapted from [136]. Applying a voltage across the electrode produces a perpendicular electric field within each pixel of the LC-SLM. This in turn produces dipoles which apply a torque on the liquid crystals to re-orientate them in the direction of the field. This direction represents the slow axis of the liquid crystal medium; light incident on these pixels will then encounter a phase retardance based on the voltage across the pixel, within a typical range of  $[0 : 2\pi]$  radians.

with differing molecular alignments – namely nematic, smectic and cholesteric. We consider only the nematic phase, which is the most common and relevant one to LC-SLM design. Within the nematic phase, the molecules are aligned with their major axes facing the same direction, whilst located randomly within the cell.

A parallel nematic liquid crystal cell is formed using a pair of glass plates coated with a conductive transparent indium tin oxide layer; the first plate is known as a common electrode, whilst the second can be subdivided into individual pixels. The base electrode is set on a capacitive storage layer for digital addressing, which in turn is set in a silicon substrate. The internal plate surfaces are both carefully

grooved along the length of the cell. A nematic liquid crystal, such as 4-Cyano-4'-pentylbiphenyl ( $C_{18}H_{19}N$ ) is then inserted between the electrodes [137]. The grooves are quickly filled with long LC molecules, which are fixed in place naturally with their major axis along the length of the grooves; the remaining molecules are free to move. In this context the liquid crystal cell can be treated as an anisotropic dielectric which exhibits positive uniaxial birefringence [10].

Upon applying some voltage across the electrodes, an E field is established perpendicular to the plates; in turn, electric dipoles are formed, and the fixed molecules within the grooves apply a torque to neighbouring molecules, and gradually apply a common major-axis alignment with the E field across all molecules in the LC between electrodes. The common direction of molecule alignment now doubles as the extra-ordinary (slow) axis of the birefringent cell. Incident light polarised with the same orientation will then experience a retardance (similar to birefringent crystals 2.2.3), by changing the phase relative to a planar mirror reflection. The birefringence of the LC is then a function of the voltage  $V$  across the cell [10].

The maximum phase delay of the light is achieved with  $V = 0$  such that  $\Delta\phi = \pi$ ; when the voltage across the cell is increased, the unfixed molecules rotate their axes towards the E field for minimum retardance. Extended across all pixels, this concept is known as a phase-only Liquid crystal on Silicon Spatial Light Modulator (LCoS-SLM, shortened to LC-SLM hereafter). Note that for extra diffraction efficiency, an optional dielectric mirror is placed above the pixel electrodes. The LC-SLM is used primarily as a phase modulator, and operates by displaying a user-encoded phase hologram onto the LC pixels, with a typical switching rate of 60 – 200Hz [138]. The LC-SLM has become prevalent in scientific research and industry where highly precise and efficient modulation is required. This includes the aforementioned fields of spatial and temporal beam shaping, adaptive optics and micro-manipulation [136].

### 2.5.2 Mirror-based SLMs

Light steering by way of fast-switching planar mirrors is well established in optics; this includes heliographic communication, single lens reflex (SLR) cameras, optical choppers, deflectors and scanners [10]. As discussed in section 1.3.1, global telecommunications networks have been gradually updated from electrical signalling to optical fibre. Optical switches are generally cheaper and have an improved form factor

over their electrical counterparts, as well as maintaining ultra high speeds. One such optical switch technique makes use of Micro-Opto-Electro-Mechanical Systems (MOEMS) in the form of digital micro-mirror devices (DMD) which are arrays of independently programmable micron-sized planar mirrors which pivot between binary states [10].

The DMD was developed in the late 1980s by Larry J. Hornbeck of Texas Instruments (TI), with a U.S. patent filed in 1990 [139]. The brief was to design a MEMS device that could steer light, using existing semiconductor and electronics knowledge [4].

The following describes in detail the operation of a typical DMD with  $\pm 12^\circ$  tilt angle, as shown in figure 2.14: each micro-mirror is formed using a reflective aluminium surface attached using a “via” to a hidden torsional hinge. On pivoting from the surface normal, the mirror makes contact with spring tips at either side. Lastly, two electrodes are used to electrostatically attract and lock the mirror into its binary  $\pm 12^\circ$  positions. By redirecting light incident on the mirror, the DMD is technically a subset of SLM. By convention, the beam formed by all mirrors in the  $+12^\circ$  “on” state is the beam which reflects closest to the input, whilst the other beam is the  $-12^\circ$  “off” state [35, 63, 139].

Each mirror pixel has its own memory cell, comprised of two CMOS (Complementary metal-oxide semiconductor) memory elements – when one element is of logical value 1, the other is 0 and vice versa. TI DMD units are all fitted with internal RAM (DDR SDRAM), which allows a finite number of preloaded patterns to be displayed at the highest switching rate possible without an HDMI link [140, 141].

In the time since the first DMD was developed, the speed and resolution has been drastically increased. As of 2019, TI now offers DMD chipsets capable of switching rates up to 32.5 kHz (1-bit binary patterns- DLP7000) and 4K UHD micromirror arrays for 4K UHD projection (DLP660TE). Companies such as Vialux offer these chipsets (capped at 22.7 kHz) with upgraded controllers for larger RAM, e.g. the *V-7001* has 60GB of RAM, allowing a storage of 87,000 binary patterns. DLP products are now ubiquitous around the world, dominating the market of digital projection for entertainment, education and in the workspace. The technology is also used in portable spectrometers and head-up displays in vehicles [64]. The table in figure 2.15 compares the specifications of several options for liquid crystal and micromirror modulation technologies, from cheap mass production to the top of the

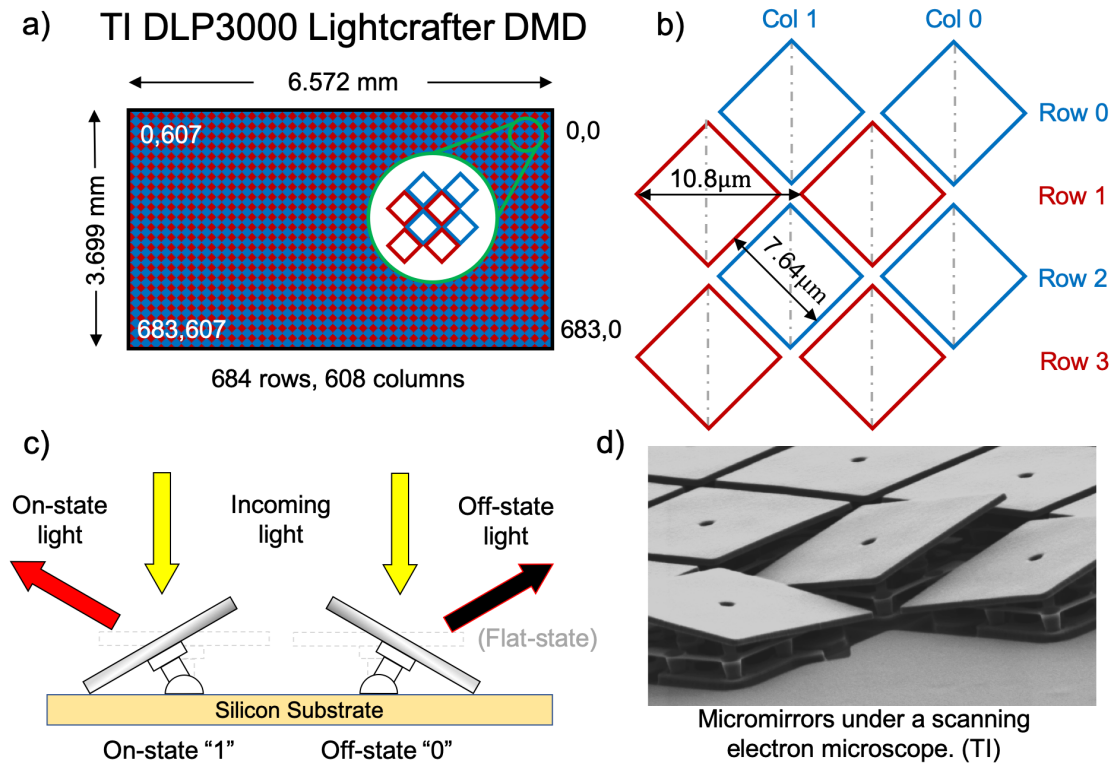


FIGURE 2.14: **DMD design: TI Lightcrafter DLP3000** The DMD chipset used in chapter 3 is an evaluation module designed for custom digital light projection applications. (c) Each pixel is a polished micromirror on a hinge, such that it has binary positions – the “on” state at  $+12^\circ$  tilt and the “off” state at  $-12^\circ$ . Whilst this is a binary amplitude modulator, greyscale projection is achieved by rapid switching of these micromirrors. The DLP3000 mirrors rotate about the vertical, and are therefore arranged in a checkerboard pattern (a). As a consequence, the rows and columns are not spaced equally (b), which must be addressed when encoding holograms to the device. (d) DMD micromirrors under a scanning electron microscope (source: [4]).

line for scientific use. The specification details are based on the sales quote received from each manufacturer, with the exception of the Optoma mini projector (PC World) and the Nokia 3310 display conversion [142].

There exists other MOEMS devices whose applicability overlaps that of the above devices. The Deformable Mirror Array (DMA) is an SLM comprised of independently addressable segments (pixels) which have multiple degrees of freedom to alter the wavefront of incoming light. DMAs are produced either as segmented hexagonal mirrors or as a continuous silver-coated cellulose membrane, which use actuators to activate a “piston-tip-tilt” movement of each segment/membrane region. The DMAs available today are capable of similar speeds to DMDs ( $\sim 10$  kHz) [143]. DMAs are

	Commercial		LC-SLM		DMD		
	LC-SLM	DMD	LC-SLM		DMD		
Manufacturer	Nokia	Optoma	Cambridge Correlators	Meadowlark Optics	Texas Instruments		Vialux
Model	3310 phone LCD	LV130 projector	SDE1024	512x512 series	Lightcrafter 3000 6500		V-7000
Price (£)	< 70	180	1000	17500	500	1693	7500
Resolution (pixels)	84x48	854x480	1024x768	512x512	608x684	1920x1080	1024x768
Pitch ( $\mu\text{m}$ )	~500	5.4	9	15	7.6	7.6	13.7
Switching (Hz)	<10	120	60	200	4000	9523	22700
Phase stroke	-	-	$0.5\pi$	$>3\pi$	-	-	-
Greyscale	Binary	Binary	8 bit	8/16-bit	Binary		
+1 Diffraction efficiency (%)	<50	-	50	95	~5 Array diff. : 86		
Buffer (1-bit)	-	-	-	-	96	400	43690

FIGURE 2.15: **Comparing specifications of LC-SLMs and DMDs:** Both types of modulators are mass produced, as liquid crystal phone displays and digital projectors- such products can be modified to achieve beam shaping on a budget [142]. LC-SLMs are characterised by their phase bit depth ( $\sim 2\pi$ ) and high diffraction efficiency, whilst DMDs are able to achieve particularly high switching rates, made possible with an onboard memory buffer to store patterns. Most of the prices listed are accurate to the time of purchase by Glasgow University optics group (c.2013-2019).

capable of high-speed and efficient adaptive optics, and are currently used for scaled modelling of the James Webb Space Telescope [144–146].

### 2.5.3 Computer-generated holograms

In preparation for chapters 3 and 4, which utilise Fourier transform holography, I present an operation that is ubiquitous in the field of beam shaping: the generation of laser modes in the FP of the SLM. Consider the fields, modelled in *Wavetrace* (cited in the *Image credits*) and presented in figure 2.16: to generate a mode from an SLM, we first illuminate the hologram with an incident gaussian beam, with amplitude and phase shown in (a,b). The hologram is composed of the amplitude and phase of the object we wish to create (in this case an  $\text{LG}_{1,0}$  mode) in (c,d), combined with the phase tilt grating necessary to separate out the zero and higher orders; shown in (e), this is the interference of a hypothetical incident plane wave and the back-projected

desired beam path. Note that deviation from an ideal collimated Gaussian input beam may be considered when determining the hologram, as will be discussed in section 4.4 [147].

As explained further in [123], the resultant hologram to be displayed (f) constitutes a forked grating (necessary to impart a phase singularity) with a doughnut amplitude modulation, tilted away from the zero-order angular position by  $(N_{cyc,x}, N_{cyc,y})$  blazed phase cycles. Here, a blazed grating refers to the “sawtooth” phase profile used to efficiently steer light into a particular order; we generally wish to maximise the power in the +1 order [148, 149]. By placing a lens of focal length  $f$  away from the SLM and observing the plane a further  $f$  from the lens, we can image the FT of the hologram (g) – in the ideal case, we see  $\pm 1, 2, 3\dots$  diffraction orders tilted away from the zero order. The following investigations will strictly concern the +1 order, whose efficiency can be optimised by use of an SLM look-up table and custom amplitude modulation.

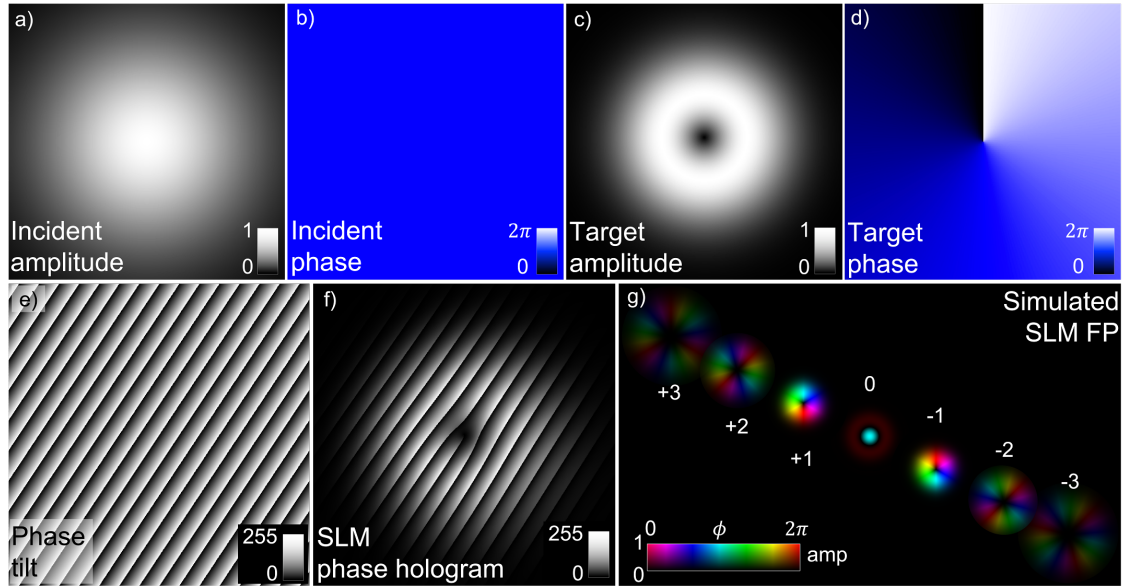


**FIGURE 2.16: Simulation of LG mode generation using an SLM in Fourier holography:** To generate a target beam e.g.  $LG_{1,0}$ , a plane wave (amplitude (a), phase (b)) is incident on the SLM window. The target beam of amplitude (c), phase (d) is also encoded. The phase tilt added to the hologram is the interference of the incident beam with the a modelled back-projection of the desired beam path (e). The hologram to be displayed is then the complex addition of the phase tilt with the target beam, and is scaled with the bit depth of the SLM (e.g. 8-bits [0:255]). The simulated field in the FP of the hologram features the non-diffractive zero order, as well as the target beam located at the  $\pm 1$  order, and unwanted higher orders.

In learning to design amplitude and phase holograms, I made some initial observations about the beam shaping characteristics of DMDs with respect to LC-SLMs. In the latter, the phase of the hologram modelled is taken directly as the phase of the hologram to be displayed; for amplitude modulation, the contrast of the hologram is varied (e.g. across an 8-bit scale). However, the binary mirrors on a DMD cannot implement a full  $2\pi$  phase modulation, and so the phase is locally adjusted by a lateral pixel shift (see [150]). To modulate the amplitude, the duty cycle is adjusted, where the maximum amplitude is achieved with a 50:50 on:off ratio. It is important to note that the amplitude modulation resolution for both modulator designs cannot exceed the tilt grating used to diffract light away from the zero order.

## Chapter 3

# High-speed spatial control of the intensity, phase and polarisation of vector beams using a digital micro-mirror device

### 3.1 Introduction to DMD vector beam shaping

The following chapter presents my own work, which aims to use the DMD from a relatively low-cost Texas Instruments (TI) development kit to produce numerous vector beams which can be generated with a switching rate of at least 4 kHz. To the best of my knowledge, this is the first instance of a DMD being used in the diffractive regime to generate *arbitrary* vector beams; note that the current maximum switching rate of the more expensive DMDs (Vialux V7000) can outperform similarly-priced LC-SLMs by a factor of 100.

The project arose from initial talks held between myself, my supervisors Miles J. Padgett (University of Glasgow) and David B. Phillips of the University of Exeter (formerly Glasgow) alongside collaborators Tomáš Čížmár and Sergey Turtaev, of the Leibniz Institute of Photonic Technology, (formerly the University of Dundee). The project was led by Prof. Padgett, with Prof. Čížmár and Dr. Turtaev providing

advice and proof-reading. The experimental procedure, hologram design, data acquisition and analysis were all performed by myself, with guidance from Dr. Phillips. The work was then published in Optics Express [151] and presented by myself at CLEO:2017 (San Jose, USA) [152].

Advancements in the availability and performance of spatial light modulators in the research and industry sectors has led to a wealth of interest in dynamic shaping of light in not only amplitude and phase, but in polarisation. Vector beams, as defined in section 3.2, offer an extra degree of freedom beyond scalar beams, and as such can be tailored to possess an array of attributes to be exploited in different applications, such as multiplexing in communications, STED microscopy and fibre imaging (section 1.3). The following chapter is the culmination of my own work on the shaping of monochromatic light into vector beams of arbitrary amplitude, phase and polarisation.

The project was initially conceived as a means to developing vector beams for a real-time multimode fibre (MMF) imaging system in collaboration with Prof. Čižmár, expanding on his previous work in Plöschner *et al.* (2015) [54]. Within this publication, among others (see section 1.3.2), the concepts of transmission matrix calculation and propagation invariant modes were employed. In particular, an LC-SLM was used to raster scan a diffraction-limited spot on the proximal end of an MMF – one of the main limiting factors was indeed the switching rate of the LC-SLM, and so this characterisation of propagation was only valid for a fibre whose degree of movement, bend radius and temperature were static; the system was not fast enough for dynamic imaging.

The aim was therefore to evaluate the potential of DMDs as a diffractive optical element (DOE), namely for shaping the amplitude and phase, such that it can be incorporated into systems which require either orthogonal or spatially-varying polarisations. This includes the possibility of varied structured light fields for quantum Bell experiments in future [87, 153]. The following section outlines the current state of the field of beam shaping, specifically to produce both scalar and vector fields. Thereafter, the motivation for high-speed vector beam shaping is discussed.

## 3.2 Light as a vector

Following on from the definitions in section 1.2, the electromagnetic theory of light (developed in the 18th and 19th centuries by Green, Maxwell and Thomson among others), makes clear that the fields which make up electromagnetic waves are *vectors*. That is,  $\mathbf{E}$  and  $\mathbf{B}$  have both magnitude and direction – an intrinsic structure of light. As explained in [8], a time-varying  $\mathbf{E}(\mathbf{B})$  field gives rise to a perpendicular  $\mathbf{B}(\mathbf{E})$  field, and together they propagate along direction  $\mathbf{k}$  as the electromagnetic field.  $\mathbf{k}$  is orthogonal to both  $\mathbf{E}$  and  $\mathbf{B}$ ; the Poynting vector (direction of energy flux) is defined as  $\mathbf{S} = (1/\mu_0) \mathbf{E} \times \mathbf{B}$ , where  $\mu_0$  is the vacuum permeability.

Despite the orthogonality constraint, the transverse components of either field have no such limitations on their scalar value. In calculating the flux density of each field, it can be shown that  $E_x = cB_y$  and  $E_y = -cB_x$ ; that is, the in-phase transverse components only differ by the scalar  $c$  – the speed of light in a vacuum. This indicates that the transverse components of the  $\mathbf{E} = (E_x, E_y)$  are not bound by one another, and can support *independent* scalar values perpendicular to the propagation direction.

From Maxwell's equations in free space,  $\nabla \cdot \mathbf{E} = 0$  is only existent in the transverse plane. It follows that to properly define a propagating wave, the instantaneous orientation of this field in the transverse plane must be determined, i.e. its polarisation. We can manipulate polarisation by way of combining field components of different amplitudes and phases; the unit vector of  $\mathbf{E}$  can then be considered as the polarisation state. By considering the spatial transverse profile of  $\mathbf{E}$  we can also identify propagation modes with intensity proportional to  $E^2$  [8].

## 3.3 State of the art in beam shaping

In chapter 1, the real-world applications and future potential of shaping light into scalar and vector beams were presented, whilst section 2.5 has detailed the evolution of holography and an in-depth look at how beam modulation devices operate. In general, there is no one modulation technique which is optimal for all applications, however it is pertinent to consider which modulation attributes will be sought after in technologies of the near future, and to identify novel methods which tailor to such technologies.

### 3.3.1 Scalar complex beam shaping techniques

Scalar beam shaping has an extensive role in state of the art computer generated holography, which must be appreciated before considering the demands for the future and what advancements can be made.

There are circumstances in which a beam can be sufficiently shaped in phase alone: for instance, the diffracted light formed by a Gaussian beam incident on a forked phase hologram is a superposition of LG modes with the same OAM index  $\ell$ , which lends itself to optical trapping and OAM multiplexing (recall section 2.3.3). In this case, the FT of the hologram is sufficient to recover the target beam. In general, the optimum hologram is represented by the complex far-field diffraction of the target beams, which considers both phase and amplitude [123]. LC-SLMs are, by their very nature, phase-only spatial modulators; DMDs, in contrast, are natural binary amplitude modulators. Nevertheless, there already exists a wealth of studies demonstrating combined phase *and* amplitude shaping using the former device [45, 69, 72, 154, 155].

A critical attribute of DOEs like the LC-SLM is that the blazing function of the grating displayed directly affects the efficiency of the light sent into the fundamental diffraction orders. In [154, 156, 157] this was exploited by purposefully reducing the phase depth from the rated maximum depth ( $\phi_{depth} < 2\pi$ ), which in turn altered the distribution of total power into the zero and first orders. A local change in phase depth in the hologram results in local intensity variations – when combined with the correct phase distributions from the FT of the desired diffraction pattern, the result is full complex modulation. Determining the most appropriate amplitude shaping algorithm (for efficiency or otherwise) remains an open question, which depends largely on the application [147].

In [69] and [158], an iterative algorithm known as the Gerchberg-Saxton (G-S) algorithm ([159]) was used to determine the phase required, when the desired amplitude mask (kinoform) was known. The former investigation used an SLM in an optical tweezers microscope setup to produce a  $20 \times 20$  array of optical traps which could be manipulated in 3 dimensions. The latter employed an SLM with a pair of phase holograms – the first hologram using the G-S algorithm before the second corrected the phase to that of the target beam.

### 3.3.2 Vector beam shaping techniques

By combining the above principles for phase and amplitude structuring with careful manipulation of the polarisation of the resulting diffracted light, it is possible to configure all three variables to generate light whose cross-section exhibits spatially varying polarisation. This can either be using a static diffractive optical element for fixed polarisations or by way of an SLM for dynamic control. The following outlines the state of the art in vector beam shaping, which makes clear the opportunity for high speed DMD vector beams.

Vector beams may be generated in a variety of novel ways. For instance, in figure 1.4 [102] a solid glass cone was used to convert circularly polarised light into beams with OAM and radial polarisation. This was achievable because light internally reflected from the vertex of the glass cone imparts an angular phase tilt on the incident light based both on the cylindrical symmetry of the cone and the incident polarisation of the beam.

The q-plate (see figure 1.1) is a well-established hologram design, introduced in 2006 to capitalise on the Spin-to-Orbital Angular Momentum (SAM-OAM) conversion possible with anisotropic and inhomogeneous DOEs like liquid crystal SLMs [160]. Analogous to a half-wave plate with a spatially varying optic axis, the q-plate works by way of computing an azimuthally-varying hologram of known charge  $q$ , which converts e.g. L/R circularly polarised light into OAM beams of  $\ell = \pm 2q\hbar$  per photon, where  $q$  is the topological charge of the singularity [161]. The work of [162] uses a pair of q-plates inside a laser cavity to induce pure OAM beams and create vector vortex beams of any state on the higher-order Poincaré sphere.

True arbitrary vector beams are those whose polarisation can theoretically take any degree of orientation, ellipticity and handedness at any point in the transverse field. The use of LC-SLMs to create arbitrary polarisations, by individually modulating the amplitude and phase of two orthogonal components (e.g. horizontal and vertical) before recombination of the beam interferometrically, has been successfully reported in a number of studies. For instance, in [163] it is demonstrated that a radially/azimuthally polarised doughnut beam is attainable by the interferometric addition of two HG modes (as discussed further in section 3.6). In [164] and [165], a Wollaston prism is used to spatially separate beams of orthogonal polarisation before diffraction from an LC-SLM. The latter cleverly makes use of a split-screen LC-SLM to

display the combined appropriate amplitude, phase and grating hologram to eventually overlap the beams upon re-entry back into the prism, providing a high efficiency. A similar hologram arrangement was used in [166], however this time using a pair of polarising beamsplitters (PBS) and a right-angle prism to enable a double-pass of the split LC-SLM. In [167], the incident light is diffracted from an LC-SLM into two +1 orders of the same polarisation orientation, before a pair of half-wave plates create the orthogonality required.

### 3.3.3 DMDs: superfast beam shaping

The LC-SLM has been successfully used to create tailored fields in a variety of conditions, for a range of applications. However, there may yet be conditions for which the use of a DMD could prove advantageous, particularly given the major differences in operation between the devices. One such scenario is when the aforementioned beams of arbitrary intensity, phase and polarisation require *high-speed* hologram switching, often for computationally intensive and time-varying optical systems. Of great interest in recent years is the measurement-intensive characterisation of turbid media, which requires many measurements to build a complex transmission matrix that defines the media in orthogonal polarisations [22, 49, 51, 52]. Furthermore, many telecommunications applications revolve around data transfer speeds, which is directly impacted by the switching rates at e.g. fibre-to-fibre terminals (section 1.3.1).

The typical operating speeds of the current DMDs available (4 – 32.5 kHz) significantly outperform the rates of typical nematic LC-SLMs of a similar resolution due to LC viscosity ( $\sim 200$  Hz). As discussed in section 2.5.2, DMDs are manufactured as binary amplitude modulators owing to their binary mirror states, although there are methods to combine the amplitude with phase by other means, provided that efficiency is not paramount [168]. In the last 10 years, with the introduction of modular development kits it has become readily accessible and cost-effective (in comparison to LC-SLMs of the same resolution) to shape arbitrary scalar light fields with a DMD SLM [48, 150, 169–172].

There is now great interest in the beam shaping community to fully establish the intricacies and algorithms for optimal complex beam shaping with a DMD device, to complement and in some applications rival the mainstay of beam shaping in the 21st century – the LC-SLM [173, 174]. The following work seeks to advance the

operational potential of the DMD device towards arbitrary vector beam shaping by using a TI Lightcrafter DMD kit and the interferometric principles outlined above in section 3.3.2 to produce an array of fields with well-defined and useful transverse polarisations. I will demonstrate the super-fast switching speeds possible, whilst also giving a rigorous account of the subtleties one can consider when using a DMD in the laboratory.

### 3.4 Using a DMD as a diffractive optic

The DMD has been critical to the widespread and longstanding success of Texas Instrument’s Digital Light Projection (DLP) system, which until recently was largely for amplitude-only spatial light modulation e.g. cinema projectors. However, the last decade has seen a shift in the potential use of the device. With the introduction of development kits such as the DLP Light Commander [175], researchers have been able to repurpose the DMD and controller for use with light sources other than proprietary LEDs (Light emitting diodes).

Whilst the DMD can indeed be used with a laser source in the same manner as an LC-SLM, the inherent geometry of the micro-mirror arrays (with periodicity and tilt axes) is responsible for several diffractive effects which must be accounted for to maximise device efficiency. The argument, theorised in the Texas Instruments white paper (2008) [141], is as follows: first consider the simplest form of diffraction grating – transmission from a single narrow slit onto a far-field screen. For some plane wave of wavelength  $\lambda$  incident on the slit of width  $a$  at incident angle  $\theta_i \neq 0$ , the intensity is

$$I(\theta) = \text{sinc}^2 \left[ \pi \frac{a}{\lambda} (\sin \theta - \sin \theta_i) \right]. \quad (3.1)$$

The peak intensity of the  $\text{sinc}^2$  profile will therefore occur at  $\theta = -\theta_i$ . For multiple slits of separation (pitch)  $d$ , the diffracted light is further constrained into defined diffraction orders, specifically:

$$\sin \theta = m \frac{\lambda}{d} - \sin \theta_i. \quad (3.2)$$

Here,  $m \in \mathbb{Z}$  is the mode order. The combination of these constraints results in a profile whose relative intensity is in the shape of a single slit, but only at the angular

positions of the diffraction orders in equation 3.2, as depicted for two slits in figure 2.3. For transmissive multiple-slit diffraction gratings, the incident angle of light controls both the  $\text{sinc}^2$  profile and sinusoidal order position in unison – the position of the peak of the former and the zero order of the latter are coincident, resulting in a zero order with maximal intensity with respect to the higher orders [141].

Diffraction from a 2D micro-mirror array behaves similarly to the 1D transmissive case above, however light is now reflected from the mirror gratings, such that  $\theta_r = -\theta_i$ . When the slit aperture is replaced with a tilting micro-mirror, one must consider the consequences for this tilt on the reflected diffraction orders. For instance, the diffraction order positions in the far field still depend on  $(\theta_i, d, \lambda)$ , such that they diffract about the zero order position, which is itself simply the specular reflection  $\theta_r$ . In contrast, the introduction of mirror arrays which are tilted away from the surface of the grating causes the previously linked orders and intensity profile to be dissociated from each other. The envelope occurs at the angle of reflectance about the mirror normal, and not the reflectance from the grating normal as was previously the case. Note that whilst the peak of the envelope profile varies with the incident angle combined with the fixed mirror tilt, the minima of the envelope profile depend on mirror width  $a$  and  $\lambda$  [141].

*Blazed* gratings are tailored diffraction gratings used to diffract the maximal amount of power into a chosen non-zero diffraction order. This is in contrast to e.g. a binary grating whose slit profile appears as a step function. This tailoring is strictly wavelength-dependent: for a given  $\lambda$ , the slits are spaced  $d$  apart with a sawtooth profile whose angle from the grating plane is blazing angle  $\phi_{Blaze}$ . The notable effect with such a diffraction grating is that any specular reflection now stems from  $\phi_{Blaze}$ , and not the surface normal of the grating plane. This implies that diffraction efficiency is now dependent on  $\phi_{Blaze}$ .

DMD mirrors have only binary states – a  $\pm 12^\circ$  tilt. In effect, a DMD with all mirrors in the “on” state is a fixed blazed grating with  $\phi_{Blaze} = 12^\circ$ . Should the incident angle be chosen such that the  $\text{sinc}^2$  peak happens to be coincident with a non-zero diffraction order, this is known as a *blazed* order, and only occurs for a single wavelength. This provides maximum diffracted intensity into this order; it follows then that in an *off-blaze* position, the opposite is true, and the efficiency of the desired diffractive order is lower.

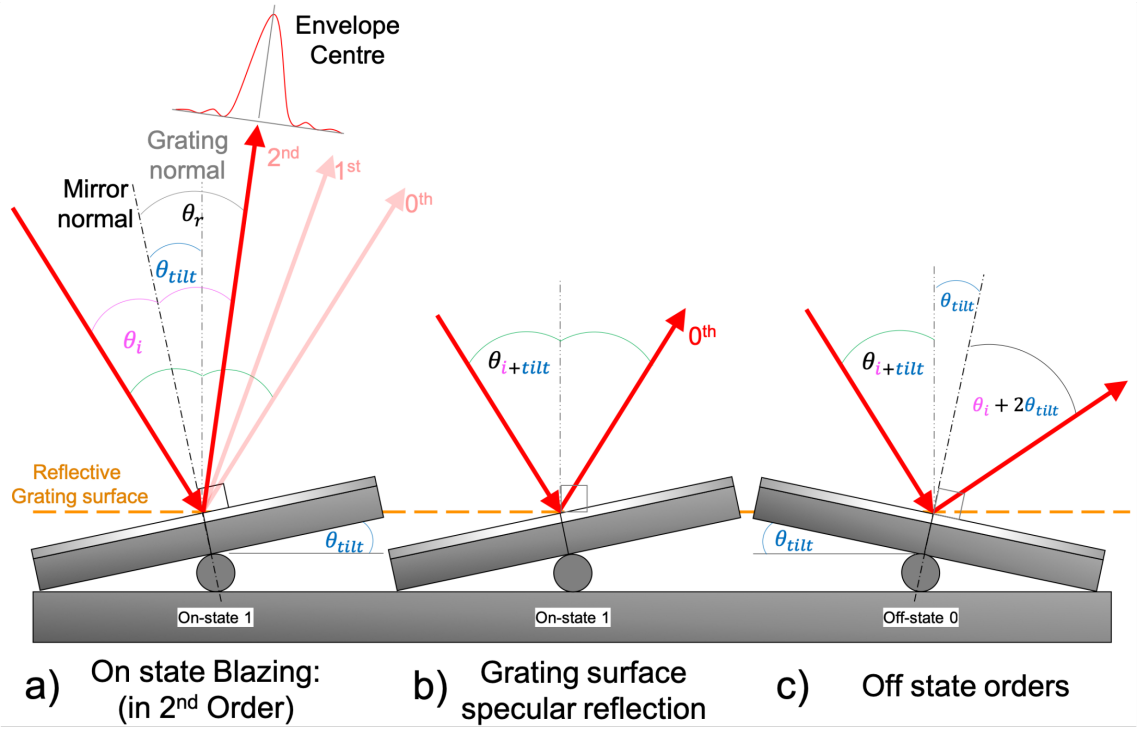


**FIGURE 3.1: DMD diffraction orders and blazing:** Adapted from [141]. (a) the blaze condition for some “on” state diffraction order occurs when the incident angle  $\theta_i$  in conjunction with the fixed mirror tilt angle  $\theta_{tilt} = +12^\circ$  cause the  $\text{sinc}^2$  grating envelope centre to fall on that order for maximum power. (b) the micromirror array has a 92% fill factor – the remaining light is sent into a zeroth order at  $\theta_i + \theta_{tilt}$  from the grating surface normal as specular reflection. (c) “off” state diffraction orders, whose mirrors are angled at  $\theta_{tilt} = -12^\circ$ , are formed at  $\theta_i + 3\theta_{tilt}$  from the grating normal – these resemble “negative” holograms.

Crucially, whilst the zero order and envelope peak move together with incident angle whilst offset from one another, the higher orders are equally spaced by  $m\lambda/d$  such that for  $\pm 12^\circ$  tilting DMDs,  $\theta_i$  can be tuned until the envelope falls on e.g. the +1 order. This is depicted in figure 3.1 for the +2 order – the mirror spacing and tilt angle  $\theta_{tilt}$  are constant, which generates an envelope centred on the diffraction angle  $\theta_r = -\theta_i$ . Part (a) shows the  $\theta_i$  necessary for a blazed second order from an “on” state mirror. Part (b) depicts the specular reflection off the grating plane, which reflects off at angle  $\theta_i + \theta_{tilt}$ . Lastly, the “off” state mirrors contribute to an entirely different set of diffraction orders diffracted at  $\theta_i + 3\theta_{tilt}$  to the grating plane normal. All three of these order subsets feature in the bench photo, figure 3.2, with an on-axis close up in figure 3.3.

A DMD is a 2D diffraction grating – as such it is pertinent to expand this theory to the 2D case. Here, the orders are not angles from a 1D grating, but are instead

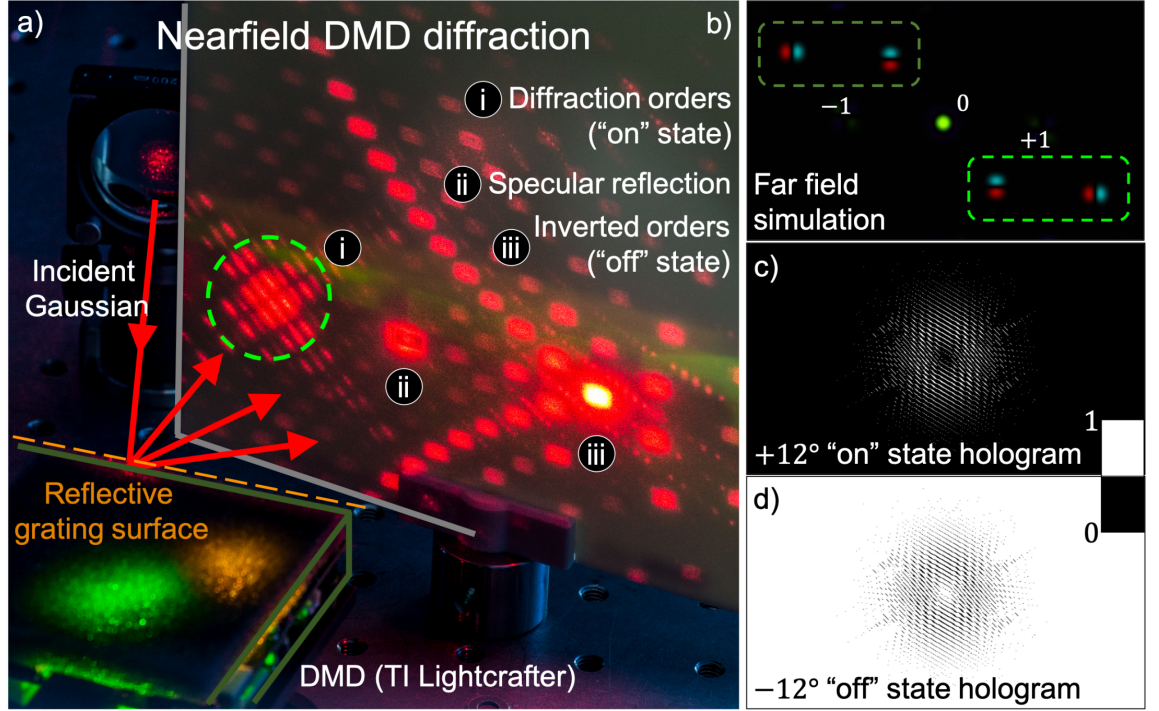


FIGURE 3.2: **Observing DMD diffraction:**(a) to demonstrate the nuances of the DMD as a DOE, a collimated laser is incident on a TI Lightcrafter DMD with some angle  $\theta_i$ . To produce a beam comprising of HG beams in the +1 diffractive order (b), a binary hologram of the vector sum of two gratings is displayed on the DMD (c). By placing a screen immediately after, a great number of diffracted beams are realised. Most notably (i), the target “on” state orders (in green), (ii) the wasted specular reflection and (iii) the inverted orders from the “off” state mirrors produced by the corresponding negative hologram (d).

angular co-ordinates which direct the diffraction orders from both horizontal (m) and vertical (n) gratings onto positions in the far field. Such orders are located at  $[\frac{m\lambda}{d_x}, \frac{n\lambda}{d_y}]$ . The intensity profile envelope, diffracted at  $\theta_r$  relative to the mirror tilt is

$$I(\theta_{x,y}) \propto \text{sinc}^2 \left[ \pi \frac{a}{\lambda} (\sin \theta_x - \sin \theta_{xi}) \right] \text{sinc}^2 \left[ \pi \frac{a}{\lambda} (\sin \theta_y - \sin \theta_{yi}) \right]. \quad (3.3)$$

The DMD mirrors in this case are square, such that  $a_x = a_y$  and  $d_x = d_y$ ; they also tilt about an axis which runs along the diagonal of the mirrors, shown in figure 2.14. As such, the only orders which can be blazed satisfy  $m = n$ , such that the 2D intensity envelope satisfies a  $\text{sinc}^4$  profile.

We can therefore say that a blazed order can be induced along the (n,n) direction, with the correct incident angle for some wavelength. The  $\text{sinc}^4$  blazed order profile shown above is a direct consequence of the square mirrors, and implies that there is a

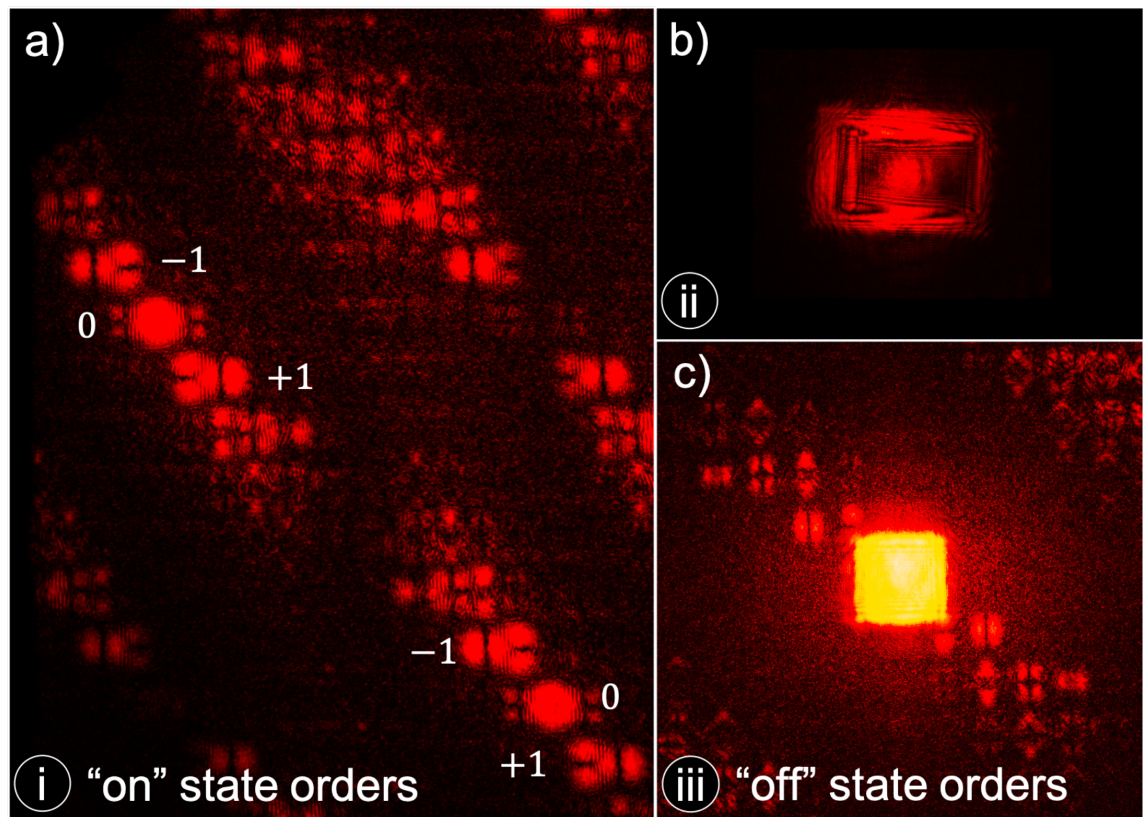


FIGURE 3.3: **DMD near-field diffraction orders up close:** (a) the “on” state orders manifest as 4 (two shown) identical diffraction order sets, based on the symmetry of the square mirrors. Within each set is a zero order reflection from the mirror faces, as well as the  $\pm 1, 2$  orders generated by the HG hologram displayed. (b) a close up of the specular reflection from the reflective grating surface – note that the majority of the intensity is in the border of the DMD window which acts as a reflective aperture edge. (c) the inverted diffraction orders from the “off” state mirrors – for this particular hologram, the majority of the mirrors are “off” which sends most of the light into this region. The zero order appears square due to the relatively large angle of reflection from the rectangular DMD.

high extinction ratio between “on” and “off” mirrors. The diagonal orders caused by these mirrors are also linked, such that one cannot be minimised without minimising the rest [141]. Note that as shown in figure 3.3(a), the micromirror geometry results in 4 individual diffraction order groupings, (only two are visible). This is perhaps due to diffraction from the 4 edges of the micromirrors; the grouping of orders ultimately chosen was that which maintained the propagating beam height.

In summary, the DMD presents some unique diffractive effects when used with a monochromatic coherent source such as a laser, which can be exploited to maximise

the efficiency and discretisation of diffraction orders. By being confined to the diagonal of the 2D sinc profile, the useful orders of the DMD are better discretised from each other and offer high extinction ratios between binary tilt states. This manifests as a relatively high fidelity when compared to comparable LC-SLM modulated beams [176].

### 3.5 DMD vector beams: experimental setup

The experimental setup for DMD vector beam generation is shown in figure 3.4. Its design was adapted from the system described in the supplementary material from our collaborators [54]. In order to gain access to the full set of polarisations necessary to generate vector beams, I used the overlap of two beams within the +1 DMD diffraction order carrying orthogonal polarisation states to produce a vector sum of polarisations across the beam profile. As such, the superposition combining the global relative phase and intensity between the two beams resulted in tunable polarisation orientation and ellipticity (discussed at length in section 3.6). After careful consideration of factors including cost and efficiency, I chose this design based on its stability – the two individual beams share all but one of the optics (HWP1), which helps to minimise the drift experienced between their relative path lengths.

What follows is a full description of the beam path: firstly, the incident beam is a horizontally polarised Zeeman-stabilised He-Ne laser with a waist of  $\sim 2\text{mm}$ . Note that the polarisation of the light incident on a DMD mirror array should be oriented along (or orthogonal to) the axis of rotation of those mirrors. This is due to the threat of polarisation ellipticity which can be induced when differences in the Fresnel coefficients of the mirrors (which are polarisation dependent) cause path length changes across the beam. In anticipation of overfilling the DMD, I then expanded the beam with a 2F telescope using convex lenses F1 and F2. This beam was then incident on the DMD, where the flattest part of the Gaussian profile of the beam filled the active area of the DMD chip.

Next I chose a hologram to display on the DMD to diffract the incident beam into two distinct locations in the +1 order, with their own tilt angles, to separate them from the reflected zero order. These beams will henceforth be referred to as beams A and B. Additionally, the hologram can be tuned to vary the local intensity and phase across beams A and B (for full details, see section 3.6). Upon diffraction from the DMD, I placed a lens F3 to send the light in A and B into the Fourier plane of the DMD, followed by a square aperture (APT) to block all other diffraction orders (section 2.4.2). HWP1 was then inserted into the path of beam B only, such that the polarisation of beam B could be rotated orthogonal to beam A.

Orthogonally polarised and spatially separated, the beams were displaced onto a common axis. The birefringent calcite beam displacers (recall section 2.2.3) used

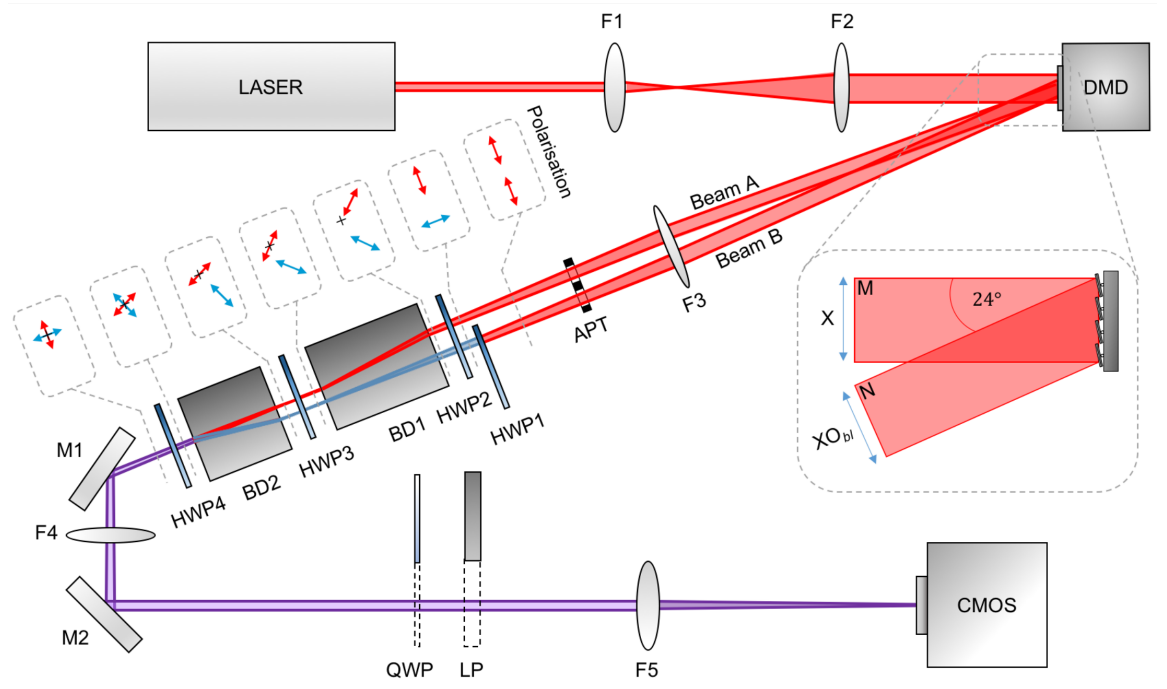


FIGURE 3.4: **Experimental setup:** From our publication, [151]. A monochromatic Zeeman stabilised HeNe laser (Neoark Neo-262) is expanded to overfill the DMD using lenses  $F1 = 40$  mm,  $F2 = 160$  mm. A TI Lightcrafter DMD with 0.3 WVGA chipset is used to diffract the incident beam into a +1 order comprising two orthogonal modes. Fourier lens  $F3 = 300$  mm and aperture APT are used to transform and isolate these modes in the far field. HWP1-4 are zero order half-wave plates. BD1 and BD2 are Thorlabs calcite beam displacers which displace the extra-ordinary ray by 4.25 mm and 2.9 mm respectively. A telescope with  $F4 = 200$  mm and  $F5 = 150$  mm and Mirrors M1,2 are used to demagnify and relay the FP of the DMD onto the camera (Prosilica GC660 or high-speed Mikrotron EoSens CL MC1362). The distribution of polarisation was characterised by inserting the optional QWP and LP before F5. Inset are the relative polarisations of beams A and B at each stage (left), as well as the geometry demonstrating the obliquity factor for reflected light after normal incidence to the grating (right).

to achieve this were purchased in two sizes – BD40 and BD27 which displace the extraordinary ray by  $a = 4.25$  mm and  $b = 2.9$  mm (when  $\lambda = 633$  nm) from the ordinary ray respectively. In this context the ordinary ray is the ray whose polarisation is along the fast axis of the beam displacer. The beam displacers were placed in the path of the diffracted beam in the region of the Fourier plane of lens F3. My aim was to efficiently displace beams A and B onto the same axis such that they overlap at a transverse location marked “X”, and travel as one co-propagating collinear beam. Since beam displacers only act upon one component of polarisation, two were used in series; the first for beam A, and a second for beam B. Note that only one displacer may be used if the separation of the beams in the FP  $c$  matches the displacement

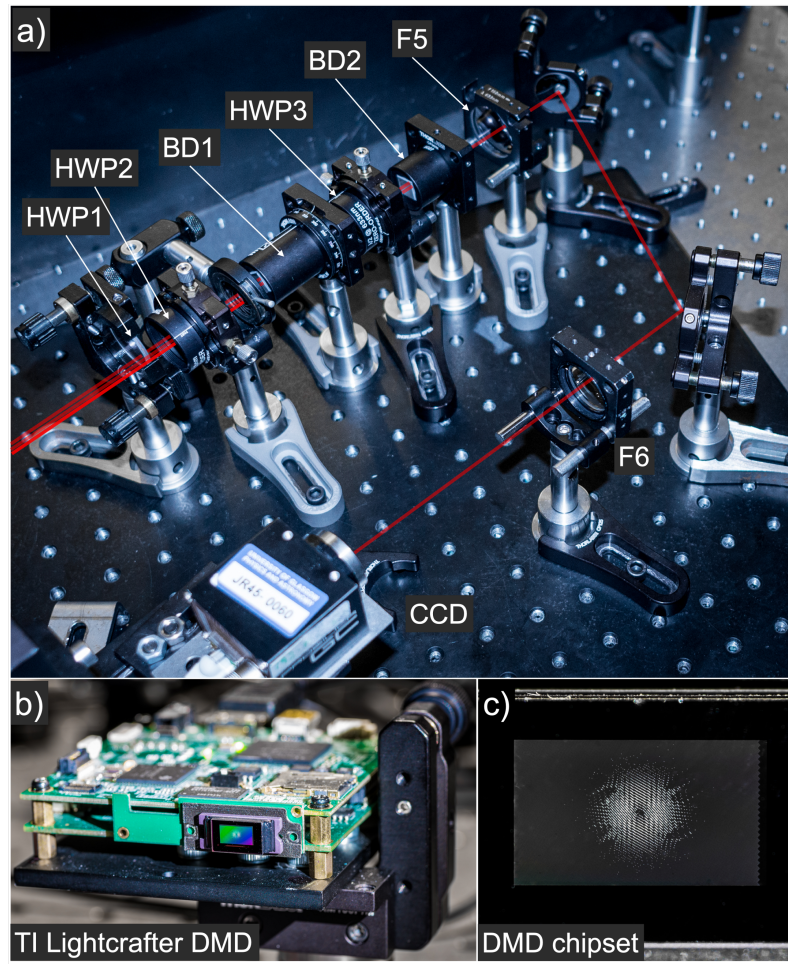


FIGURE 3.5: **Experimental setup photographs:** (a) beams A and B are orthogonalised in polarisation and overlapped in the FP of the DMD. In practice, BD1,2 were aligned in isolation, before the HWP2-4 were inserted sequentially. (b) the Texas Instruments Lightcrafter DMD projector evaluation module without a light engine, attached to an XY stage. (c) a macro image of the DMD window along the “on” state direction, displaying a dual grating hologram for vector beam generation.

(here *a* or *b*).

Firstly, the initially vertically polarised beam B hologram was turned off, such that beam displacer BD1(40) could be rotated to displace beam A into a position roughly half way between the original lateral positions of the two beams (figure 3.6(b)). In general, the beam displacer will displace only the component of polarisation parallel to its fast axis which leads to two beams being formed on exiting the beam displacer. It is for this reason that HWP2 is placed before BD1 – to be rotated until the unwanted ordinary ray of beam A is minimised in intensity, as ideally all the light is displaced onto the overlap position X.

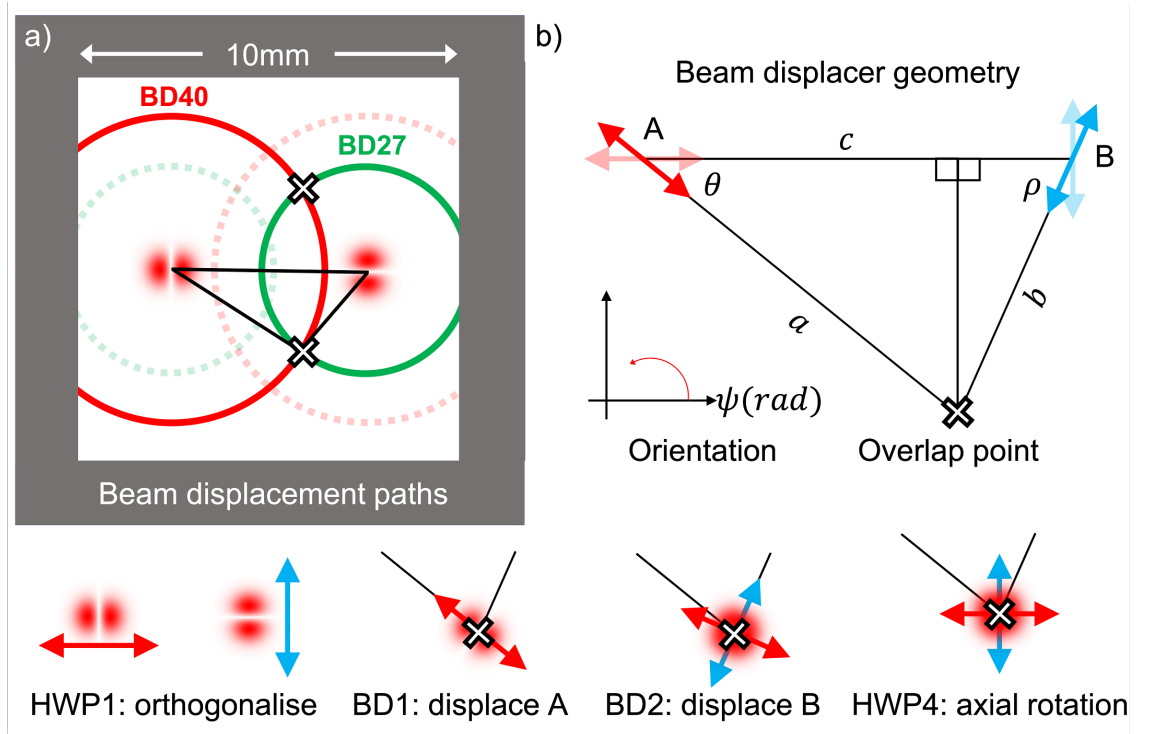


FIGURE 3.6: **Displacement of vector modes:** (a) the beam displacement locations in the FP of the DMD. Beams A and B enter the calcite crystal of side 10 mm; BD1 ( $a = 4$  mm) displaces beam A (red) and BD2 ( $b = 2.7$  mm) displaces beam B (green). This setup allows for unrestricted overlapping of the beams in the centre of the crystal; alternative configurations are shown with dotted lines. (b) The overlapping location(s) are marked with an X; the orientations of each BD and HWP can be determined with simple geometry. For a beam A polarised  $\psi_{off}$  from the horizontal and orthogonal to beam B, the transverse overlap location is related to  $(\theta, \rho)$ , the orientations required to displace each beam towards X.  $c$  is the initial beam separation in the FP.

After this stage, the same process was applied to beam B, albeit initially vertically polarised. Note that because both beams share a common path through the optics after HWP1, beams A and B remain orthogonally polarised.

Lastly, HWP4 was placed after BD2(27) to rotate both A and B together until they were approximately horizontal/vertical polarisations again. This matches the tilt axis of the mirrors M1 and M2 in the system, and so any slight path length changes between the two polarisations on reflecting from the mirrors can be corrected via the hologram.

The exact orientations of each optic can be modelled, provided the incident beam polarisation and separation of beams A and B in the FP of lens F3 is known. In the case of horizontally polarised light from the DMD, and FP beam separation

$c = 4.5$  mm, the simple trigonometric argument outlined in figure 3.6(b) shows that:

$$\cos \theta = \frac{a^2 + c^2 - b^2}{2ac}, \quad (3.4)$$

$$\cos \rho = \frac{b^2 + c^2 - a^2}{2bc}, \quad (3.5)$$

where  $\theta$  and  $\rho$  are the relative angles required to displace beams A and B onto the X position shown. A similar geometry can be used for different combinations of displacers. At  $\lambda = 633$  nm, the displacers are specified as  $a = 4.25$  mm and  $b = 2.9$  mm. It follows that for beams A and B with original polarisation offset  $\psi_{off}$  radians from the horizontal:

$$\Psi_{HWP1} = \psi_{off} + \frac{\pi}{4} \quad (3.6)$$

$$\Psi_{HWP2} = \psi_{off} + \frac{\pi}{2} - \frac{\theta}{2} \quad (3.7)$$

$$\Psi_{BD1} = \psi_{off} + 2\pi - \theta \quad (3.8)$$

$$\Psi_{HWP3} = \psi_{off} + \frac{\rho}{2} \quad (3.9)$$

$$\Psi_{BD2} = \psi_{off} + \rho + \pi \quad (3.10)$$

$$\Psi_{HWP4} = \psi_{off} + \frac{\rho}{2} + \frac{\pi}{4}. \quad (3.11)$$

The Fourier plane of F3 occurs within the beam displacement section – this is required to avoid clipping the displacer edges; consequently, this plane was re-imaged onto a CMOS camera/CCD using a demagnifying telescope (F4 and F5). At this stage, fine tuning of the overlap between beams A and B was achieved by adjusting the number of cycles in the DMD hologram grating. Also included in the setup figure are the components necessary to measure spatially resolved Stokes parameters of the various types of vector beams generated – the linear polariser (LP) and quarter-wave plate (QWP) pictured are not necessary for generating the vector beams themselves.

### 3.5.1 DMD vector beams: setup intricacies

It is prudent to explain the micro-alignment of the two orthogonally polarised beams through the system: in order to better align beams A and B on top of one another, I viewed the re-imaged Fourier plane of lens F3 onto a CCD. From this plane I could rotate both beam displacers until their respective extraordinary beams were collinear.

I was then able to change the DMD tilt angle of one beam with respect to the other until, to within the nearest few pixels, the beams were overlapped on the camera.

The square aperture APT was placed beyond lens F3, as close to the Fourier plane of the DMD as possible, taking into consideration the displacement optics. It was useful to define the region in the transverse plane beams A and B could occupy, by filtering out the intense zero order and unwanted higher orders, as described in section 2.4.2. It was also critical for distinguishing between the stray orders which could enter the beam displacers, and the desired first order beams A and B. Once alignment was complete, however, I found it acceptable to remove APT as the final vector beam was spatially separated enough and I wanted to be sure that no unoptimised spatial filtering affected the final result.

The setup shown was also adapted to measure the quality of beam produced in the *image plane* of the DMD – another convex lens  $F6 = 150$  mm was placed at  $F5 + F6$  away from lens F5 and the CCD was moved to the Fourier plane of this new lens, which is also the image plane of the DMD. Note that the resultant image was the holographic grating, so it was necessary to spatially filter the beam with a pinhole in the original camera plane (back focal plane of F5) giving smooth intensity profiles and accurate phases.

Unlike an LC-SLM, where the zero order reflects at the same angle (relative to the surface normal) as the incident beam, the mirrors of a DMD pivot by  $\pm 12^\circ$ . Due to the diagonal mirror layout of the TI Lightcrafter, this is about the vertical. A beam incident at a  $0^\circ$  angle (ie normal to the DMD plane) will reflect off at  $24^\circ$  along direction N, as depicted in figure 3.1(a). This in turn causes a lateral compression of the entire beam along the horizontal by an obliquity factor  $O_{bl} \approx \cos(24) \approx 0.91$ . During the experiment, this was solved by pre-stretching the beam along the affected direction by  $1/O_{bl}$ . Note that in general,  $O_{bl}(\theta) \approx \cos(\theta + 24)$  where  $\theta$  is the incident angle of the collimated beam along direction M. An alternative would be to change the angle of incidence to  $-24^\circ$ , which would cause the diffracted orders to transmit normal to the DMD screen giving  $O_{bl} \approx 1$ .

Lastly, the mirror geometry described in section 3.4 has a subtle additional effect on the transverse position of the beams. Each component of the incident beam striking an individual mirror along the horizontal axis will travel a slightly different path length, by virtue of the finite width of the mirrors. As such, an extra phase step is

added to each of these components with increasing magnitude – it is in effect an extra angular tilt, which causes the final beam tilt to deviate from its intended transverse position slightly, and alters the expected obliquity factor. This effect is negligible using monochromatic sources, however it appears to become a substantial issue with broadband light (see section 4.2.1).

## 3.6 DMD vector beams: hologram design

I designed a hologram control program using National Instruments LabVIEW software to meet the requirements of the setup and give me the flexibility to arbitrarily shape diffracted beams A and B. What follows is a detailed description of the hologram used to structure the input light, when the spatial light modulator is a binary state DMD. The result is the production of vector beams in the Fourier plane of the DMD with arbitrary amplitude, phase and polarisation.

Since the mid 1950's, it has been shown that binary amplitude masks can modulate not just the intensity of light, but also the phase [168]. Moreover, the introduction of computer generated holograms has led to the real-time creation of 1st order diffraction beams loaded with the intended amplitude and phase profile [177]. As in the case of the more conventional liquid crystal SLMs, the spacing between grating fringes (known as the pitch) determines the angle of diffraction into distinct orders.

### 3.6.1 Binary transmittance function

The technique used to encode complex holograms on a 2D binary grating has previously been theorised by [150]: by modelling the grating as a periodic rectangular function, it is possible to determine the first order diffraction as the coefficient of the appropriate Fourier series. Within this first order relation are two unitless quantities, given here as  $(p, q)$ ; in communication theory, tuning of these terms results in pulse position and width modulation. Specifically, the spatial intensity of the output +1 order can be controlled by locally varying the duty cycle (width,  $q$ ) of the diffraction grating displayed; that is, the effective on:off ratio made up of mirrors within the grating apertures. Also, a locally-varying phase is achieved by offsetting the lateral position ( $p$ ) of the relevant parts of the binary hologram, e.g. two regions

of the beam will be modulated  $\pi$  out of phase with one another if the "on" grating apertures within the first section of grating lines up with the "off" positions of the second section. Combined, these processes modulate the complete intensity and optical phase of the output +1 order.

These physical characteristics can be defined mathematically in the form of the binary transmittance function  $T(x, y)$ , which aims to incorporate into the first order the desired locally varying intensity and phase found in the target field  $\mathbb{S}(x, y) = S(x, y)e^{i\phi_S}$ . Following the conventions described by Mirhosseini *et al.* (2013) [150]:

$$T(x, y) = \frac{1}{2} + \frac{1}{2}\text{sgn}[\cos(p(x, y)) - \cos(q(x, y))], \quad (3.12)$$

where:

$$p(x, y) = \phi_S(x, y) + \phi_{\text{tilt}}(x, y), \quad (3.13)$$

$$q(x, y) = \arcsin(S(x, y)/S_{\text{max}}). \quad (3.14)$$

Note that in the above definitions,  $(x, y)$  defines the Cartesian axes centred on the DMD face. In equation 3.12, the sign function "sgn" returns either a  $\pm 1$  resulting in binary states  $[1, 0]$ . Term  $p(x, y)$  considers the phase, specifically that of the target scalar field  $\phi_S(x, y)$  and the base linear tilt of the first order from the DMD  $\phi_{\text{tilt}} = 2\pi(u_0x + v_0y)$ . The constants  $u_0$  and  $v_0$  simply define the number of  $2\pi$  phase cycles in each axis producing the chosen gradients. Term  $q(x, y)$  considers the normalised amplitude of the target field defined above  $S(x, y)$ .

As with other modulation techniques, the binary transmittance function  $T(x, y)$  produces countless higher diffraction orders (figure 3.2), which serve no useful purpose in this regime and in fact may interfere with the first order; therefore the spatial frequencies contained within the target field  $\mathbb{S}(x, y)$  should be limited to  $(u_0^2 + v_0^2)^{\frac{1}{2}}$ . Note that in the configuration described in section 3.5, the scalar components of the transmitted modes are propagation invariant, such that their profile is preserved in both the image and Fourier plane, with only a magnification and additional phase term to distinguish between the two [178]. Following the relations above, the target field  $\mathbb{S}(x, y)$  is encoded into the image plane of the DMD, provided the extraneous orders are blocked in the Fourier plane. Furthermore, the target beam may be encoded into the Fourier plane if the target holographic field is defined by the Fourier transform of the target beam.

### 3.6.2 Target beam definition

Now that we have defined the binary transmittance function for some target field  $\mathbb{S}(x, y)$ , it is prudent to consider the specific vector beam that can be generated with the setup described. The theoretical argument has been proposed for LC-SLMs by Maurer *et al.* (2007) [165]: for arbitrary manipulation of the intensity, phase and polarisation, consider the field  $\mathbf{E}(x, y)$  where

$$\mathbf{E}(x, y) = \begin{bmatrix} E_A(x, y)e^{i\phi_A} \\ E_B(x, y)e^{i\phi_B} \end{bmatrix}. \quad (3.15)$$

In this definition,  $E_A(x, y)e^{i\phi_A}$  and  $E_B(x, y)e^{i\phi_B}$  represent beams A and B, which are *scalar* beams whose linear polarisations are orthogonal to one another. Here, the tunable intensities and phases are defined as  $E_{A,B}^2$  and  $\phi_{A,B}$  respectively.

Next, we must define a binary transmittance function which produces beams A and B in different lateral positions in the Fourier plane, which is simply achieved by using separate linear tilt gratings for each. Recall that since the initial input beam to the DMD is horizontally polarised, the diffracted +1 order beams A and B will both also be horizontally polarised. Beam B is then rotated to become vertically polarised using a half-wave plate, such that the beams are orthogonally polarised, before being displaced onto a common collinear axis and imaged onto the camera. In general, the independent scalar fields diffracted by the DMD are defined as  $\mathbb{A}(x, y) = A(x, y)e^{i(\phi_A + \phi_{A,tilt})}$  and  $\mathbb{B}(x, y) = B(x, y)e^{i(\phi_B + \phi_{B,tilt})}$ . Here  $\phi_{A,tilt}$  and  $\phi_{B,tilt}$  are the linear diffraction gratings used to generate beam A and B in turn. The function  $T(x, y)$  (equation 3.12) sent to the DMD is therefore the weighted complex interferometric sum of  $\mathbb{A}$  and  $\mathbb{B}$ :

$$\mathbb{S}_{dual} = S_{dual}(x, y)e^{i\phi_{S,dual}(x, y)} = W_{rel}e^{i\phi_{global}}\mathbb{A} + (1 - W_{rel})\mathbb{B}. \quad (3.16)$$

Here,  $W_{rel} \in [0 : 1]$  is the fraction of power designated to beams A and B, such that if  $W_{rel} = 0.5$  then the two beams have an equal power.  $\phi_{global}$  is then the global phase of beam B with respect to beam A. Finally, for a binary transmittance function  $T(x, y)$  with dual beam control, we can define  $p(x, y) = \phi_{S,dual}(x, y)$  and  $q(x, y) = \arcsin(S_{dual}(x, y)/S_{dual,max})$ .

### 3.6.3 DMD vector beams: hologram design intricacies

Let us consider the intricacies of the hologram to be used: within equation 3.16, the functions  $\mathbb{A}$  and  $\mathbb{B}$  are found by the decomposition of the target vector field into two linearly polarised fields which are orthogonal to one another.

For the general case of an arbitrarily polarised vector beam, the polarisation state at any given location throughout the profile of the beam can be represented as a polarisation ellipse. Here, it is the phase difference between the electric fields of the orthogonally polarised beams A and B at that location which defines the local polarisation of the resultant vector beam. In the simplest case, when  $\Delta\phi = n\pi$  rad [ $n = 0, 1, 2, \dots$ ] defines a linearly polarised state, whilst  $\Delta\phi = \pi/2$  is circularly polarised; the values in between these cases are then elliptically polarised.

The orientation of the ellipse major axis is controlled by the local relative phase and amplitude of beams A and B. Therefore in the dual beam generation above, the key parameters (intensity, phase and polarisation) are all dependent on one another – however, as in the case of [165], the method outlined above still enables total control of the phase and polarisation separately. This is due to the transmittance function parameters allowing arbitrary control of not only i) the relative phase of the oscillating E field between neighbouring locations in the transverse profile, but also ii) the relative phase of the E field between the orthogonal polarisations.

Figure 3.7(d) demonstrates the transmittance function required on the DMD to generate a vector beam that is *radially* polarised [179]. This particular beam displays a helical *Pancharatnam-Berry* phase with OAM of  $\ell = 1$  [130] – a geometric phase formed by the rotating local polarisation as the beam axis is orbited [160, 180]. To demonstrate the decomposition of some arbitrary vector beam into programmable components, consider the radial vector beam: such a beam can be decomposed into linear but orthogonally polarised beams, A and B. For radially polarised beams, A and B are defined as Hermite-Gaussian  $\text{HG}_{10}$  and  $\text{HG}_{01}$  spatial modes whose lobes are  $\pi$  out of phase (as shown in figure 3.7(a)) [181].

Lastly, the ratio of the respective amplitudes ( $W_{rel}$ ) and global relative phase ( $\phi_{global}$ ) provide the end user with dynamic fine control of the hologram to provide the optimal beam parameters at whichever plane is under investigation. In the first instance,  $W_{rel}$  was used to correct for the differing diffraction efficiency for the two angles of beams

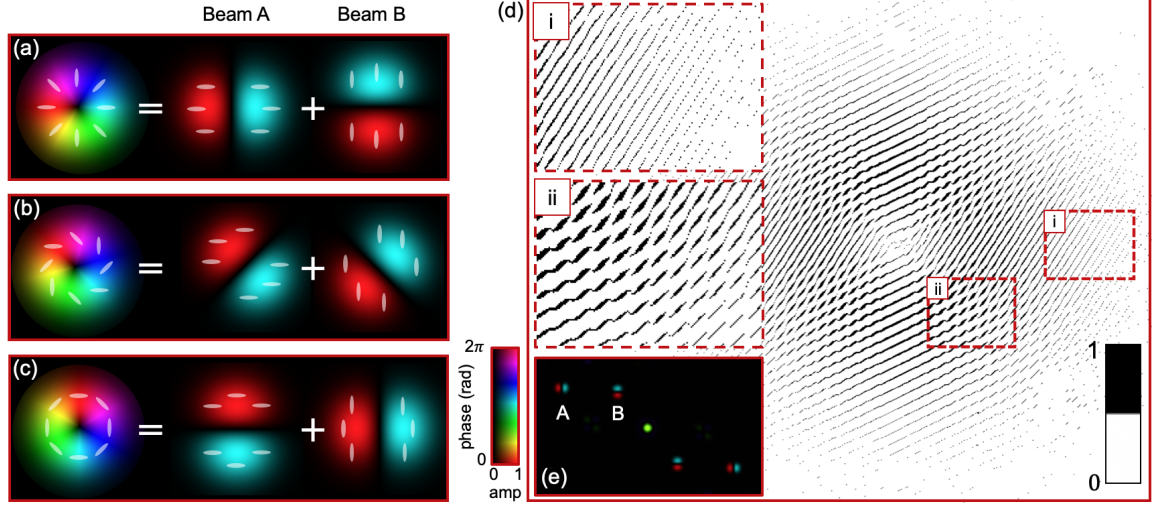


FIGURE 3.7: **DMD hologram design:** From our publication, [151]. (a) the interferometric sum of a horizontally polarised  $HG_{10}$  (A) and vertically polarised  $HG_{01}$  (B) produces a radially polarised vector vortex beam with an  $LG_{10}$  intensity. (b) by rotating each HG mode by  $\pi/4$  (with orthogonal polarisations), the resultant polarisation becomes chiral. (c) At  $\pi/2$  rotation (or by switching the polarisation of mode orders in part (a)), the resultant vector vortex beam is azimuthally polarised. Inverted for clarity, (d) details the binary transmittance function associated with the beam in (a); this includes two different phase tilts to steer light into the two beams within the +1 order. Specifically, part (i) diffracts light only into beam A, and (ii) diffracts light into both beam A and B. (e) shows the simulated FP of this transmittance function, with beams A and B spatially separated and independently controllable.

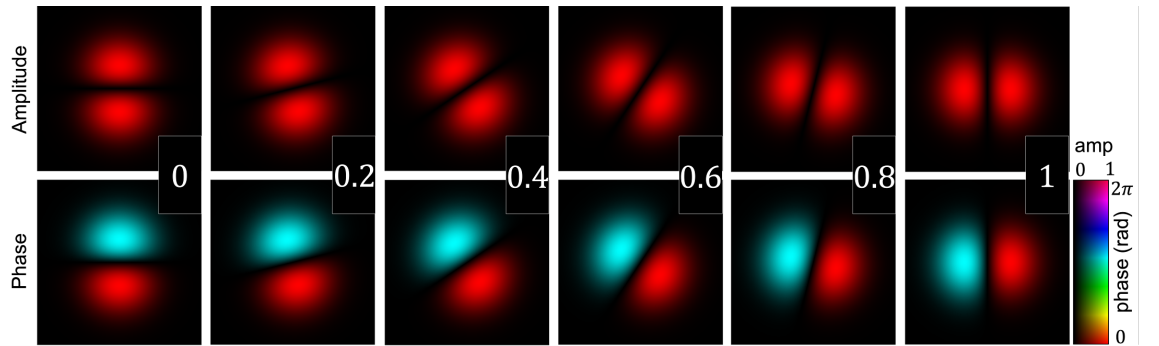


FIGURE 3.8: **Global relative intensity:** Varying  $W_{rel} \in [0 : 1]$  affects the vector contribution from beams A and B (shown here with  $(\phi_{global} = 0)$ ). When  $W_{rel} = 0.5$ , the power directed to each beam of the hologram is equal. In practical terms this was used to correct for the variation of diffraction efficiency with distance from the zero order, by placing an LP at  $H\alpha + 45^\circ$  and adjusting  $W_{rel}$  until exactly  $45^\circ$  HG lobes were observed.

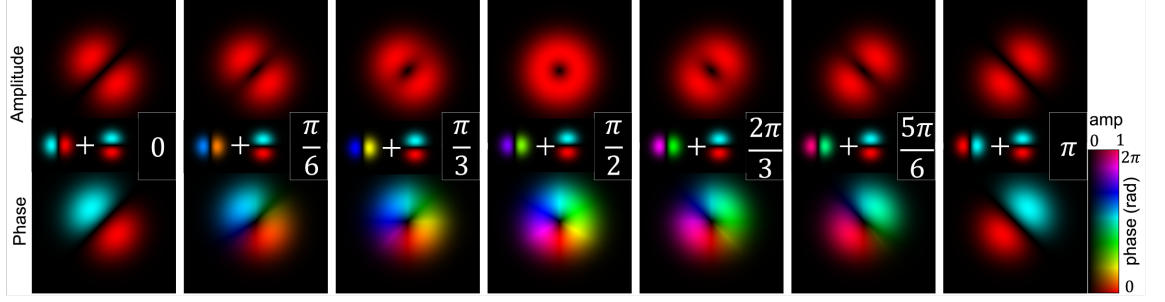


FIGURE 3.9: **Global relative phase:** Once  $W_{rel}$  was optimised, the global relative phase  $\phi_{global} \in [0 : 2\pi]$  was fine-tuned to produce maximally distinct  $45^\circ$  HG lobes when filtered through a  $45^\circ$  LP (e.g. shown here for  $\phi_{global} = 0, \pi$ ). This infers that adding  $\pi/2$  radians to the optimal  $\phi_{global}$  will produce a uniform vector vortex “doughnut” beam.

A and B (figure 3.8) (where beams diffracted at greater angles have reduced power due to the envelope function of the grating) and  $\phi_{global}$  effectively counteracts the different path lengths of beams A and B (figure 3.9), provided the coherence length is long enough (see section 4.2.2). The obliquity factor  $O_{bl}$  was used to deskew the vector beam in the presence of an incident angle onto the DMD not equal to  $2 * \text{mirror tilt} = 24^\circ$

Figure 3.10 depicts the individual binary gratings used to generate beams A and B. The superposition of the two gratings is fine-tuned by adjusting variables ( $W_{rel}, \phi_{global}$ ) (c,d). Figure 3.11(a) presents the actual hologram and parameter settings used in the generation of radially polarised vector beams. (b,c) are wavefront correction phase maps generated for beams A and B in turn, using the techniques described in detail in section 4.4.2 – note that relative optical flatness of these results led us to conclude that this particular DMD required no aberration correction for the final results.

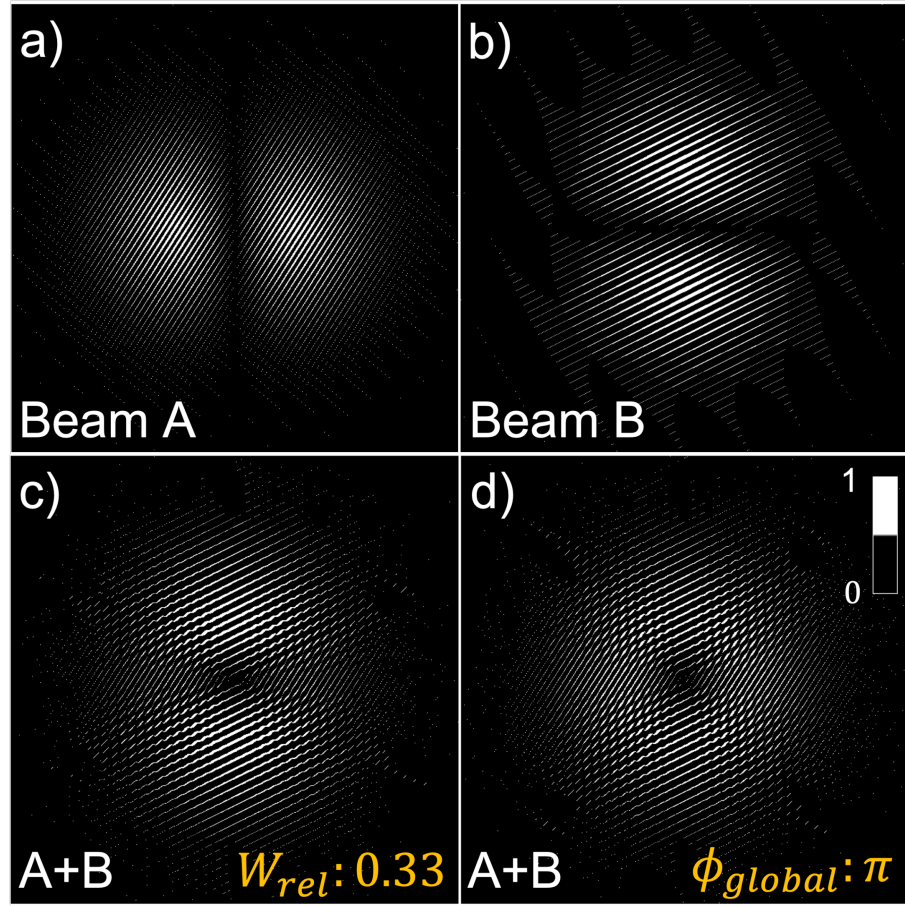


FIGURE 3.10: **DMD hologram control:** (a,b) beams A and B are initially two distinct holograms with differing grating periods in the (x,y) axes which control the phase tilts and direction of diffraction. In these binary holograms, the on state ( $+12^\circ$ ) mirrors are in white, whilst the remaining off state ( $-12^\circ$ ) mirrors are in black. (c,d) the vector sum of these holograms produces a +1 diffraction order containing both beams; the parameters  $W_{rel}$  and  $\phi_{global}$  are instrumental for accurate vector beam generation, as they correct the amplitude and phases of the two beams relative to each other.

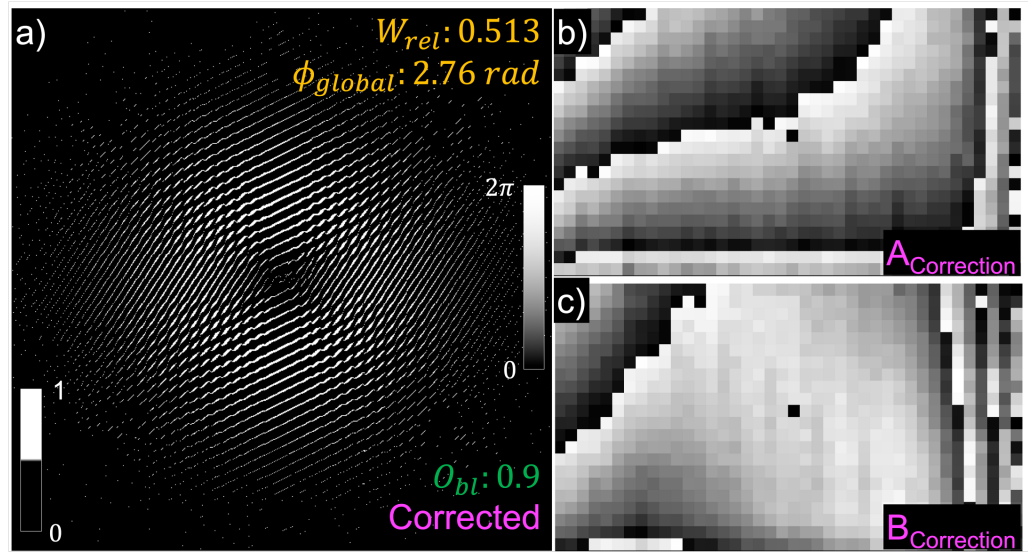


FIGURE 3.11: **DMD experimental hologram:** (a) the final hologram used to generate radially polarised vector vortex beams (in section 3.7.2). (b,c) are the phase correction maps generated via wavefront correction, explained in detail in chapter 4. These corrections maps illustrate that the aberrations in the system are slowly-varying, and the micro-mirror array is largely optically flat. These corrections were observed to have little influence on the quality of the polarisation maps obtained, and so were not applied to the hologram in the results to follow.

### 3.7 DMD vector beams: results

In order to assess the applicability of this system, the Stokes parameters of a wide selection of beams were measured and compared to their theoretical equivalents. As was mentioned in section 3.5, the inclusion of a linear polariser (LP) and quarter waveplate (QWP) before the camera are the only necessary physical changes to the system for characterisation. Note that these additional optics were placed in front of focusing lens F5, before the vector beam is demagnified.

The polarisation state of each beam can be defined by calculating the Stokes parameters of the beam, as defined in section 2.2.4. In practice, this is performed by taking a sequence of CCD images of the intensity of the beam when filtered through the LP, oriented in the position of each axis of the Poincaré sphere. The sequence was as follows: the first image to be taken was the original unfiltered vector beam, which provides the total beam intensity without a LP. Images 2 and 3 are the vertical and horizontal orientations with E field ( $|E_v|^2$ ) and ( $|E_h|^2$ ). Measurements 4 and 5 are the diagonal ( $|E_d|^2$ ) and anti-diagonal ( $|E_a|^2$ ) orientations, achieved by rotating the polariser to  $\pm 45^\circ$  from the horizontal polarisation position of the LP. Lastly, measurements 6 and 7 determine the components of the beam found in the left and right-handed circular polarisations, ( $|E_-|^2$ ) and ( $|E_+|^2$ ) respectively. Note that these two require the use of a QWP before the LP, in order to convert the circular polarisation components of the beam into linearly polarisations for measurement. For reference, figure 3.12 compares a selection of the experimental image sets for various beams with their simulated counterpart.

In order to interpret these Stokes measurements, the polarisation characterisation detailed in [102] was implemented to generate the corresponding polarisation states. By using the following set of equations, it is possible to convert the raw images into spatial polarisation maps – that is, using the intensity of each pixel within the 7 images to define an ellipse, with the result being a 2D array of ellipses showing the polarisation across the beam profile. Using simple geometry, each ellipse in the map can be computed by the magnitude of its major and minor axes, defined here as ( $P_{major}$ ) and ( $P_{minor}$ ) respectively; furthermore, the orientation ( $\theta$ ) of these axes and

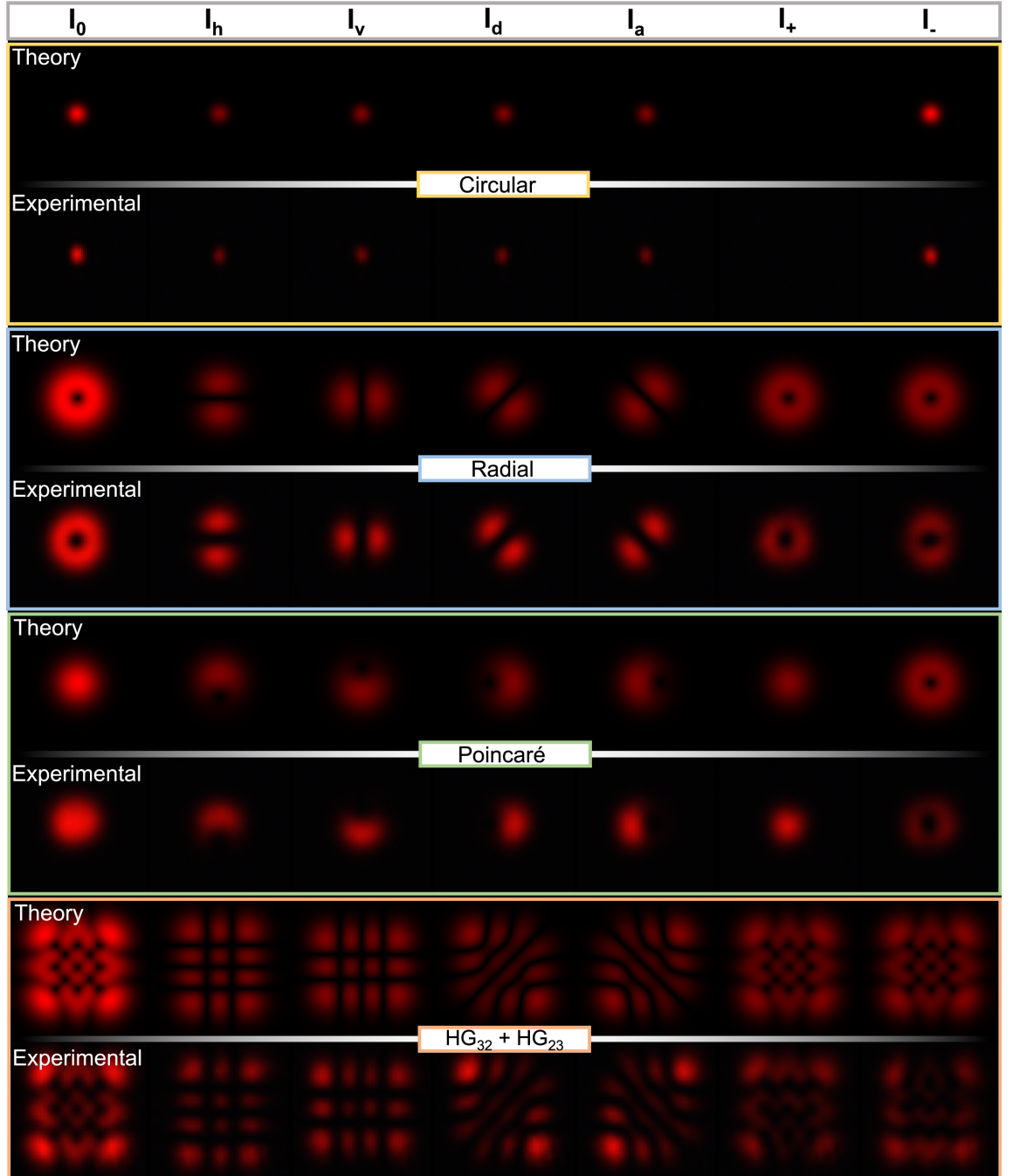


FIGURE 3.12: **Stokes measurement sequence: theory vs experiment** The Stokes parameters were determined by using a QWP and LP to capture a sequence of 6 polarisation states, shown here for a selection of different vector beams. Here  $I_0$  is the unfiltered intensity,  $I_{h,v}$  are the horizontal and vertical states,  $I_{d,a}$  are the  $45^\circ$  states and  $I_{\pm}$  are the circular states. Generally this illustrates a strong accuracy, with discrepancies occurring in the circular polarisation states. More complex profiles such as the  $HG_{32} + HG_{23}$  beam show discrepancies in the intensity profile, which will manifest as slightly incorrect polarisations (see figure 3.19).

the handedness ( $h$ ). Specifically:

$$P_{major} = \left[ \frac{1}{2}(I_p + |L|) \right]^{\frac{1}{2}}, \quad P_{minor} = \left[ \frac{1}{2}(I_p - |L|) \right]^{\frac{1}{2}}, \quad \theta = \frac{1}{2}\arg(L), \quad h = \text{sgn}(S_3), \quad (3.17)$$

when:

$$I_p = \left[ (|E_v|^2 - |E_h|^2)^2 + (|E_a|^2 - |E_d|^2)^2 + (|E_-|^2 - |E_+|^2)^2 \right]^{\frac{1}{2}}, \quad (3.18)$$

$$L = (|E_v|^2 - |E_h|^2)^2 + i(|E_a|^2 - |E_d|^2)^2. \quad (3.19)$$

Note that when generating the following polarisation maps, I used the total intensity from measurement 1 to scale the major axis, such that the ellipse would be reduced in size in the locations of relatively low light, e.g. within vortices.

### 3.7.1 Uniform polarisation vector beams

Firstly, to demonstrate simple polarisation control, I applied phase-only gratings to beams A and B, which fills the entire DMD window with a hologram of uniform intensity; this resulted in both beams combining in a diffraction limited spot in the DMD Fourier plane. Depicted in figure 3.13(a,c), a  $\phi_{global}$  which gives a phase offset between beams A and B of  $n\pi$ , [ $n \in \mathbb{Z}$ ] produces beams of uniform 45° linear polarisation; a  $\pi/2$  shift produces beams of uniform circular polarisation. By placing an aperture at the CCD (FP) and an additional Fourier lens thereafter, these uniform vector beams were also produced in the image plane of the DMD (b,d) – it is clear that the polarisation maintains its form, whilst the intensity profile of the beams are constrained by the edge of the DMD window (recall the overfilling incident Gaussian illumination).

### 3.7.2 Vector vortex beams with spatially varying polarisation

Increasing in complexity but also applicability, I proceeded to apply the binary holograms depicted in figure 3.7 to generate vector beams whose polarisation varied across the transverse profile. To begin with, I compared the experimentally produced radial vector beam in the Fourier/ image plane, with its simulated equivalent (shown

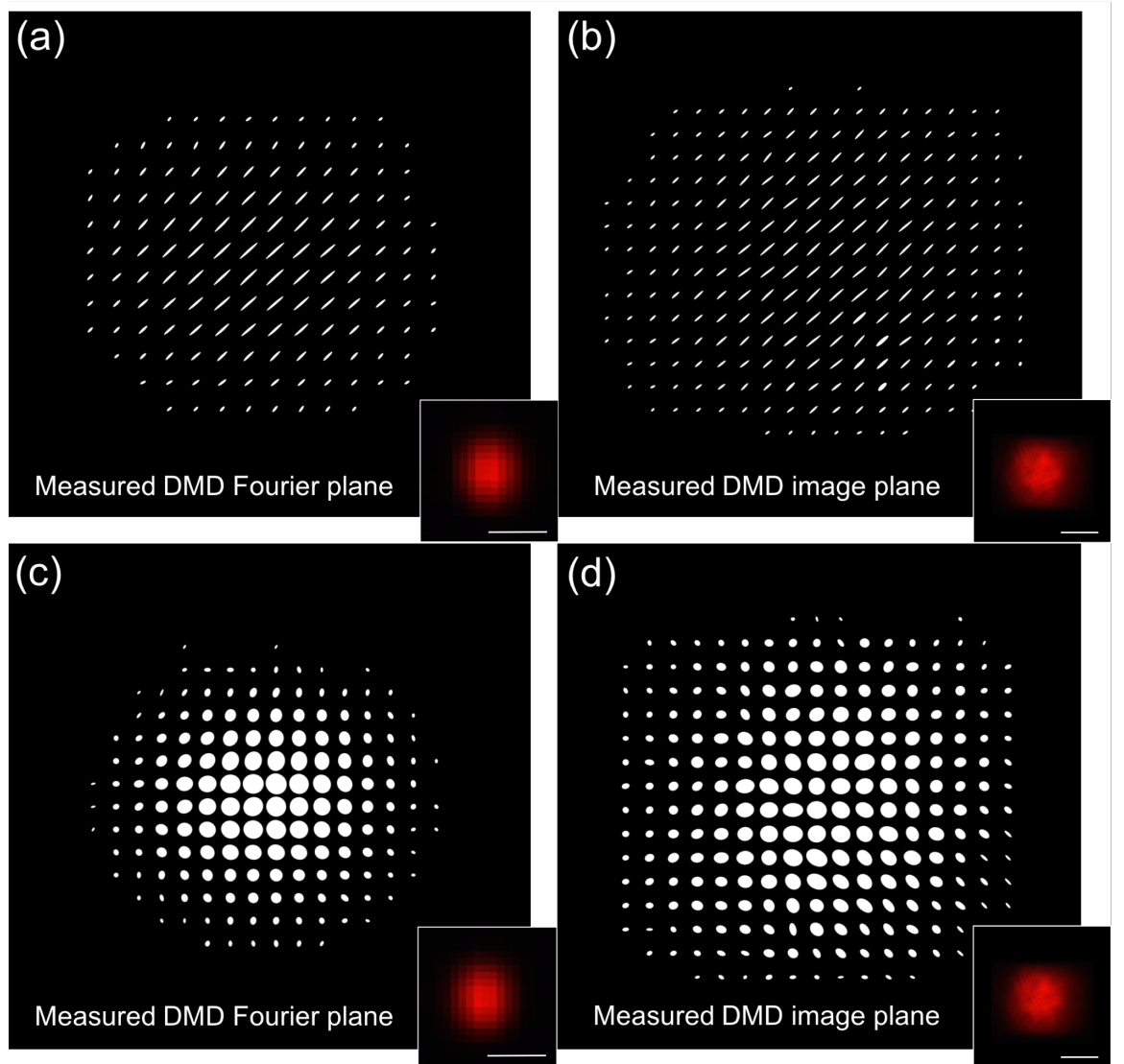


FIGURE 3.13: **Experimental vector beams with uniform polarisation:** From our publication, [151]. A diffraction limited spot produced when the entire DMD array is in the “on” state, observed in the (a,c) Fourier plane (scale bar:  $50\mu\text{m}$ ) and (b,d) image plane of the DMD (scale bar: 1mm). In the top row, beams A and B are balanced in power, with  $\phi_{\text{global}}$  tuned to produce zero phase difference; this results in a uniform  $45^\circ$  diagonal linear polarisation state. In the bottom row, the  $\phi_{\text{global}}$  is tuned to produce a phase difference of  $\pi/2$  radians, resulting in beams of circular polarisation.

in figure 3.14(a,b,c)). The Stokes parameter maps for this vector vortex beam are depicted in the top half of the figure, with each map normalised to  $S_0$ . The script written to produce this map applied equations 3.17 and 3.19 to generate a 2D array of polarisation parameters (bottom). Care was taken to centre-align the images, as the beam was susceptible to lateral displacement when using an LP. The Stokes and ellipse parameters were visualised as 2D maps; (figure 3.15) made clear the relative success of any particular data acquisition.

Next, I inverted the HG modes on beams A and B to produce azimuthally polarised vector beams, with all polarisations perpendicular to the central vortex (figure 3.14(d,g)). Note that the intensity of radially and azimuthally polarised vector beams are indistinguishable from one another.

In an effort to showcase the near-arbitrary control of the polarisation, I present the generation of Poincaré beams – beams whose polarisation states span the entirety of the Poincaré sphere [182]. In accordance with [183], these beams were formed by applying a superposition of  $LG_{\ell,p}$  modes to both beams A and B individually; the resultant combined beam possesses a fundamental Gaussian-like intensity profile. Firstly, the ‘lemon’ Poincaré beam is shown in figure 3.14(e,h): this is produced by  $LG_{1,0}+LG_{0,0}$  modes on beam A, combined with  $LG_{1,0}e^{i\pi}+LG_{0,0}$  on beam B. Similarly, the ‘star’ Poincaré beam (f,i) is made from summing  $LG_{1,0}+LG_{0,0}$  on beam A with  $LG_{1,0}+LG_{0,0}e^{i\pi}$  on beam B. The polarisation of the Poincaré beam is especially interesting: a central core of circular polarisation, encircled by polarisations which gradually alter in ellipticity, orientation and handedness simultaneously in the shape of either a lemon or 3-pointed star; the Stokes and ellipse parameters of the latter are depicted in figure 3.16. The experimental polarisation profiles reveal that there is excellent agreement with the theoretical depiction.

### 3.7.3 High speed DMD operation

The primary aim of this investigation was to demonstrate the generation of arbitrary vector beams using a DMD modulator that is capable of high speed switching. To fulfil this aim, I ran a series of tests using a set of binary patterns preloaded onto the DMD on-board memory (in contrast to the normal 60 Hz HDMI screen link). In this experiment, the DMD ran through a set of 10 holograms, each comprised of a combination of beam A and B rotated by  $\pi/10$  per iteration. When passed through

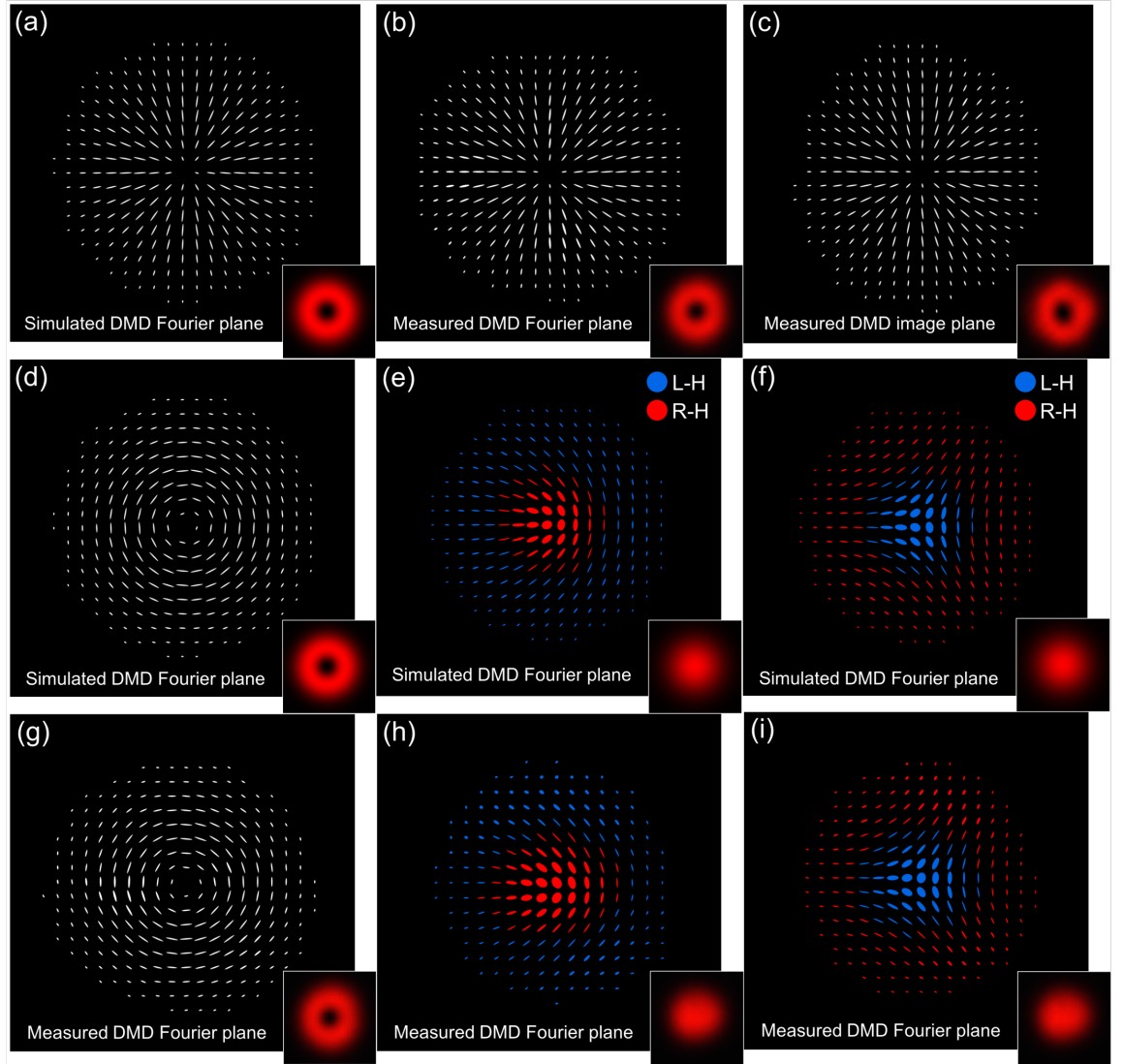


FIGURE 3.14: **Comparison of simulated and experimental vector beams with spatially varying polarisation:** From our publication, [151]. (top row) (a) simulated and experimental polarisation ellipse maps in the (b) FP and (c) image plane of the DMD. (middle row) the simulated maps for an azimuthally polarised vector vortex beam, Poincaré “lemon” and “star” beam profiles in the FP, the latter with handedness denoted in colour. (bottom row) the corresponding experimental maps of (d-f). Inset within each image is the unfiltered  $S_0$  intensity (photo 1:  $I_0$ ).

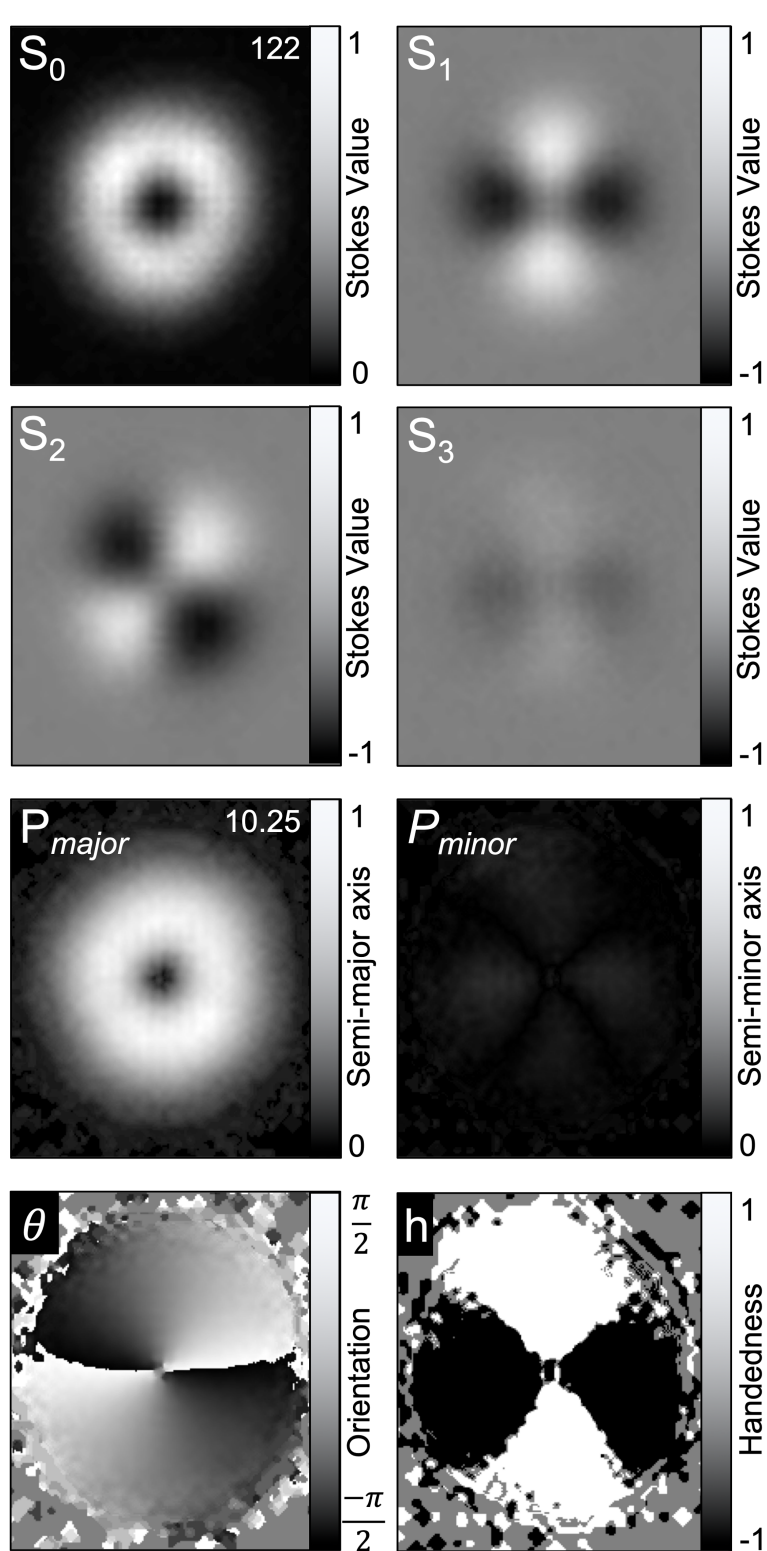


FIGURE 3.15: **Stokes and ellipse parameters of a radially polarised vector beam:** The CCD images in figure 3.12 were used to generate the Stokes parameters ( $S_0, S_1, S_2, S_3$ ) which in turn produce terms  $I_p, L$ . Each pixel location in the image then corresponds to a polarisation ellipse, with major and minor ellipse axes  $P_{major,minor}$ , orientation  $\theta$  and handedness  $h$ . The Stokes fields are normalised to  $S_0$  ( $pixel_{max} = 122$ ), whilst  $P_{major,minor}$  are normalised to the maximum  $P_{major}$  value. For a radial vector beam,  $S_3 \rightarrow 0$ , with a minimised  $P_{minor}$  as it is only linearly polarised.

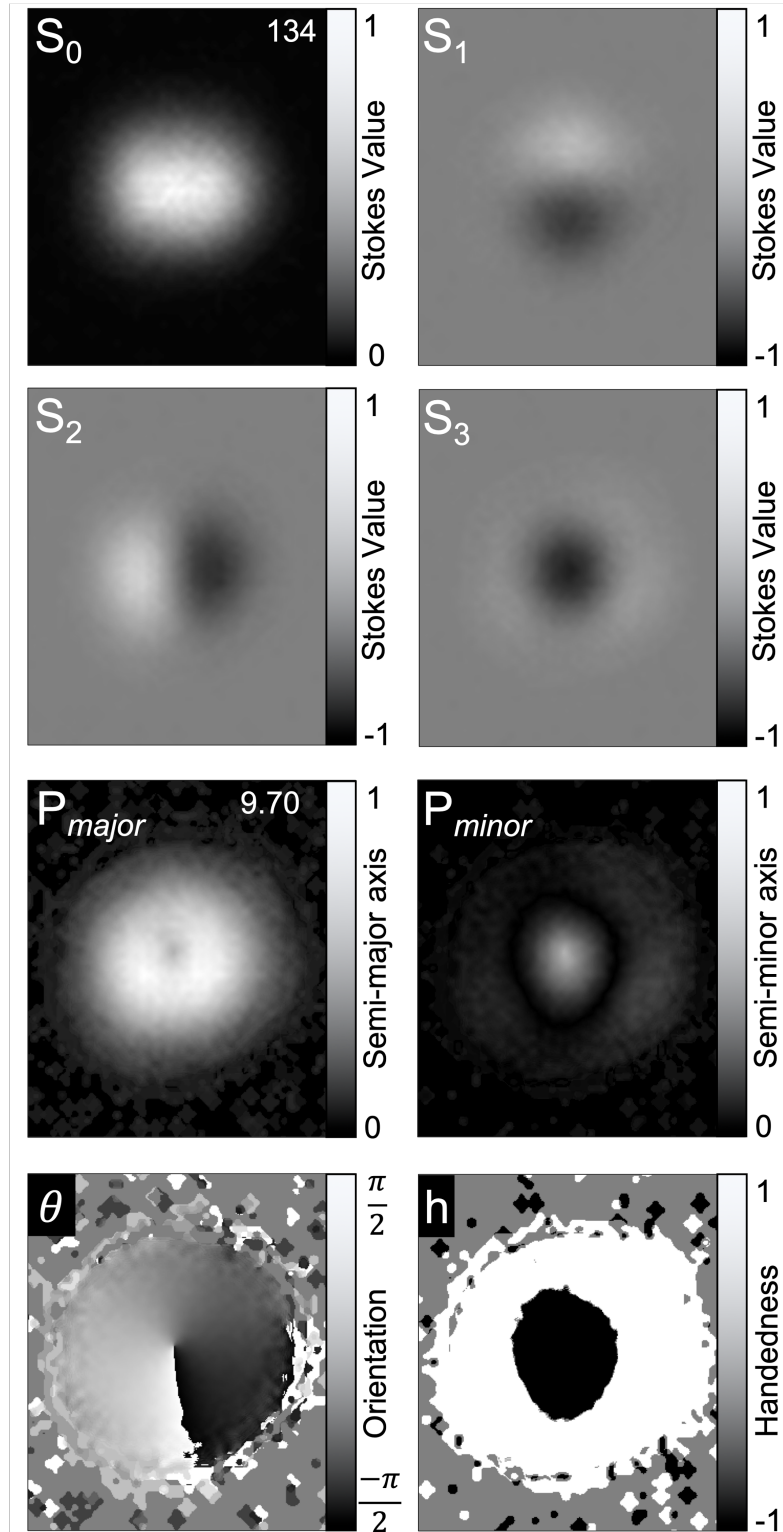


FIGURE 3.16: **Stokes and ellipse parameters of a Poincaré "star" beam:** The Stokes parameters ( $S_0, S_1, S_2, S_3$ ) for a Poincaré "star" beam, which reveal different characteristics to the radially polarised parameters – notably,  $S_3$  illustrates the difference between circular states  $I_{\pm}$  which are a Gaussian and ring profile respectively. Furthermore, the handedness  $h$  varies with radial distance within the beam profile.

a static LP at the camera, these produced vector beams of radial and azimuthal polarisation, with chiral polarisations in between. The TI Lightcrafter DMD used is capable of switching the patterns at a maximum of 4 kHz, whilst the high speed Mikrotron CMOS detector had a low-resolution frame rate of  $\sim 7.7$  kHz. This resulted in the frames recorded demonstrating pattern switching almost every 2 frames (figure 3.17). The accompanying Stokes polarisation maps were made individually for each hologram outside of the fast operation.

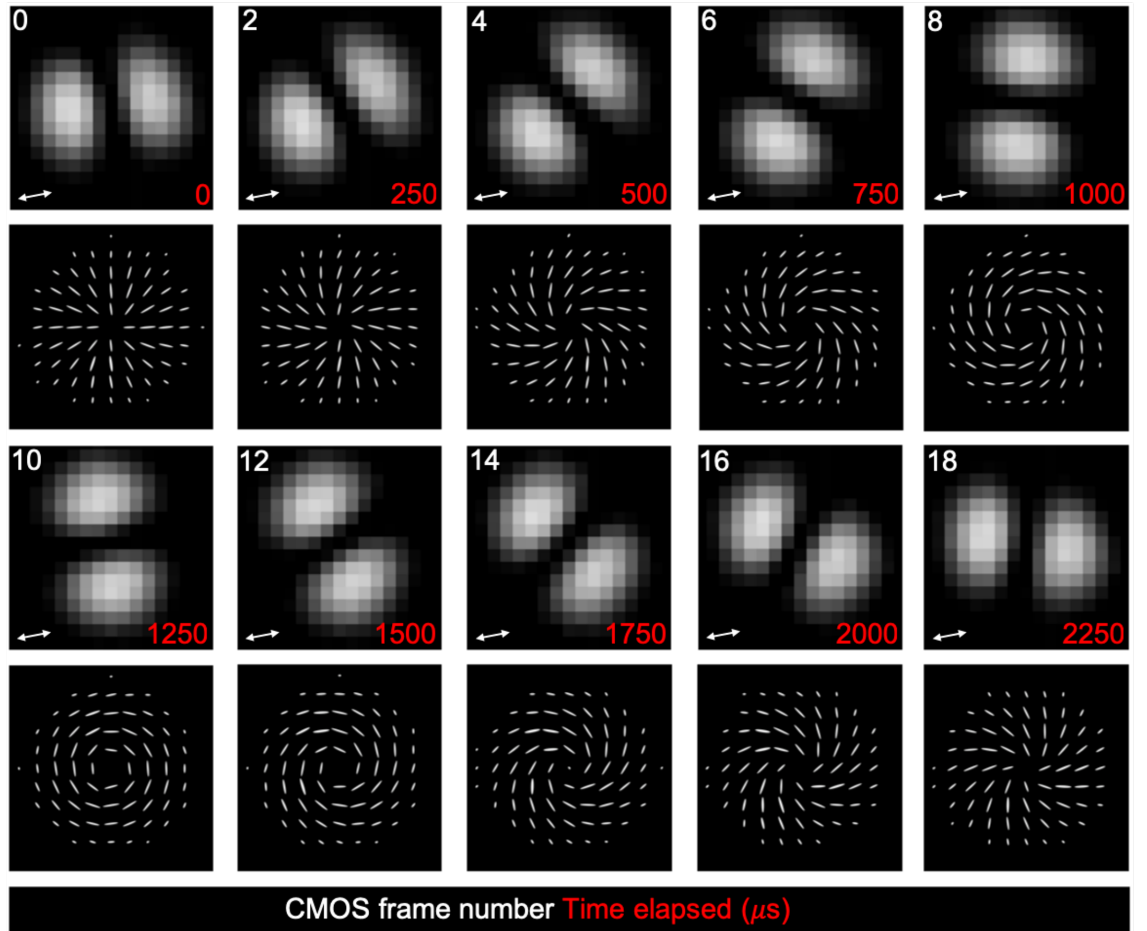


FIGURE 3.17: **High speed DMD beam shaping:** From our publication, [151]. A set of 10 holograms displaying vector vortex beams with varying relative phase  $\phi_{global}$  were preloaded onto the DMD. (lower panels) the associated polarisation maps reveal linearly polarised states transforming between radial, chiral and azimuthal vector profiles. On rifting between these holograms at a rate of 4 kHz and filtering with a fixed LP (orientation marked with white arrow), a high-speed Mikrotron camera ( $\sim 7$ k)Hz reveals a rotating  $HG_{10}$  mode in every second camera frame.

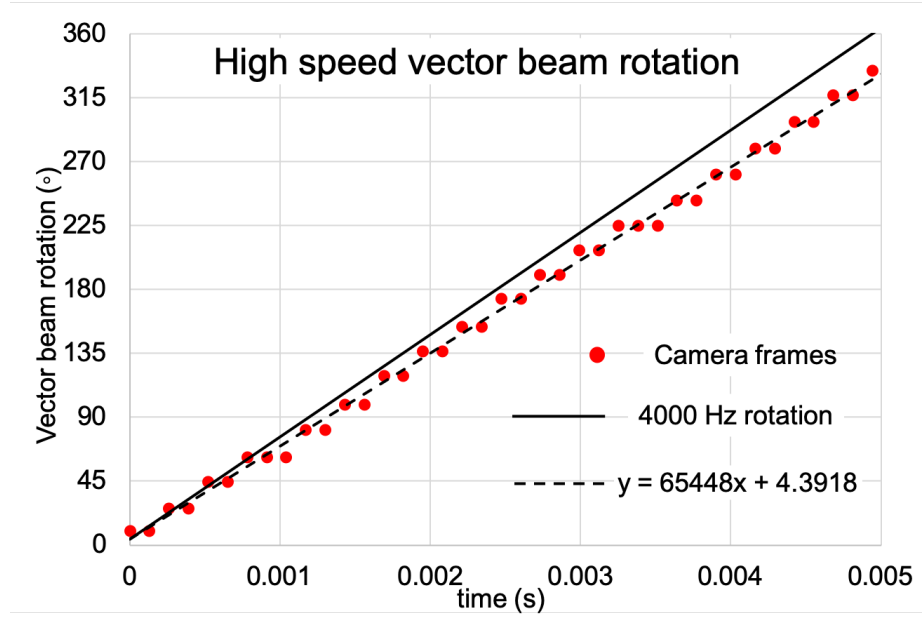


FIGURE 3.18: **Vector beam rotation:** The total frames captured from the Mikrotron camera are measured in terms of their HG<sub>10</sub> lobe orientation in time. The frames shown in figure 3.17 are then a subset of this. The Lightcrafter DMD is rated to switch at a maximum rate of 4 kHz, which corresponds to a gradient of 72,000 (solid black trend); a lack of precision in the measurements and no camera triggering may account for the offset seen in the experimental result (dashed trend).

To better demonstrate the switching rate of the Lightcrafter DMD, figure 3.18 presents the orientation of the spinning lobes from figure 3.17 as it changes in time. The orientation of the lobes was measured approximately for each frame, and plotted at time intervals based on the noted camera frame rate, 7692 kHz. With each  $n$  pattern displayed,  $\phi_{global}$  is altered by  $n\pi/10$ , as shown in figure 3.17; this implies that a full  $2\pi$  rotation is achieved using  $r = 20$  (*patterns/rot*). The gradient of the trend shown is the rotation rate  $m$  ( $^{\circ}s^{-1}$ ) which may be written as  $m/360$  (*rot s<sup>-1</sup>*). Requiring a total  $r$  patterns to achieve one revolution means that the measured frame rate  $F = m/360 * r$  i.e. (*rot s<sup>-1</sup>*) \* (*patterns/rot*) in units of *frames s<sup>-1</sup>* i.e. Hz. For  $m = 65448$  and  $r = 20$ , we find the measured DMD switching rate to be 3636 Hz; this is believed to be offset from the rated 4000 Hz due to the relatively low accuracy in measuring lobe orientation with low resolution images, and through not using an external triggering signal to ensure the Mikrotron captures at a stable frame rate.

### 3.7.4 Higher order vector beams

In order to extend the limit on vector beam feature resolution, I produced beams which comprised of mode orders higher than the HG and LG beams already demonstrated. Firstly, I combined HG<sub>32</sub> and HG<sub>23</sub> into a vector beam whose polarisation orientations repeat in a complex radial pattern at multiple points, whilst the central region features 13 vortices (figure 3.19(a,b)). Also presented are more complicated vector beam combinations (c,d) – note that the intensity across these higher order beams decreases in the central regions – this could be due to slight inaccuracies due to the departure from a Gaussian incident beam profile, or the nature of the amplitude modulation.

### 3.7.5 Quantifying vector beams

The polarisation ellipse maps depicted in the previous subsections are informative and intuitive methods of depicting the quality of the vector beams produced; however, in the interest of comparing results, it was pertinent to quantify the vector beams.

The beams of 45° linear and circular polarisation, as shown in figure 3.13, are uniformly polarised; as such, they are theoretically defined by a single value of the ellipse parameters ( $P_{maj}, P_{min}, \theta, h$ ). It is therefore straightforward to take a cross-sectional average of these parameters to quantify the accuracy of the polarisation ellipticity and orientation achieved. Note that within this measurement, the region of interest was clipped to the full width at half maxima of the  $P_{maj}$  value for all parameters – this ensured that the result was not skewed by the outer regions where there is no light.

To evaluate the 45° beam profiles, we expect the average of the parameters ( $|P_{maj}/P_{min}|, \theta$ ) to be (0, 45°); for the Fourier plane case, we measure an average of  $(0.07 \pm 0.03, 43.74 \pm 2.3)$ , which indicates a reasonable accuracy and uniformity. In the image plane equivalent, we find  $(0.07 \pm 0.06, 47.6 \pm 3)$ ; this slight inaccuracy and increase in spread  $\sigma$  is expected considering the residual non-uniformity in the intensity of the image plane beams, which is caused by interference with the zero order when not spatially filtered enough. The circular polarisation beams can also be expressed in terms of their average ( $|P_{maj}/P_{min}|$ ), which we expect to be unity. For the Fourier plane case,

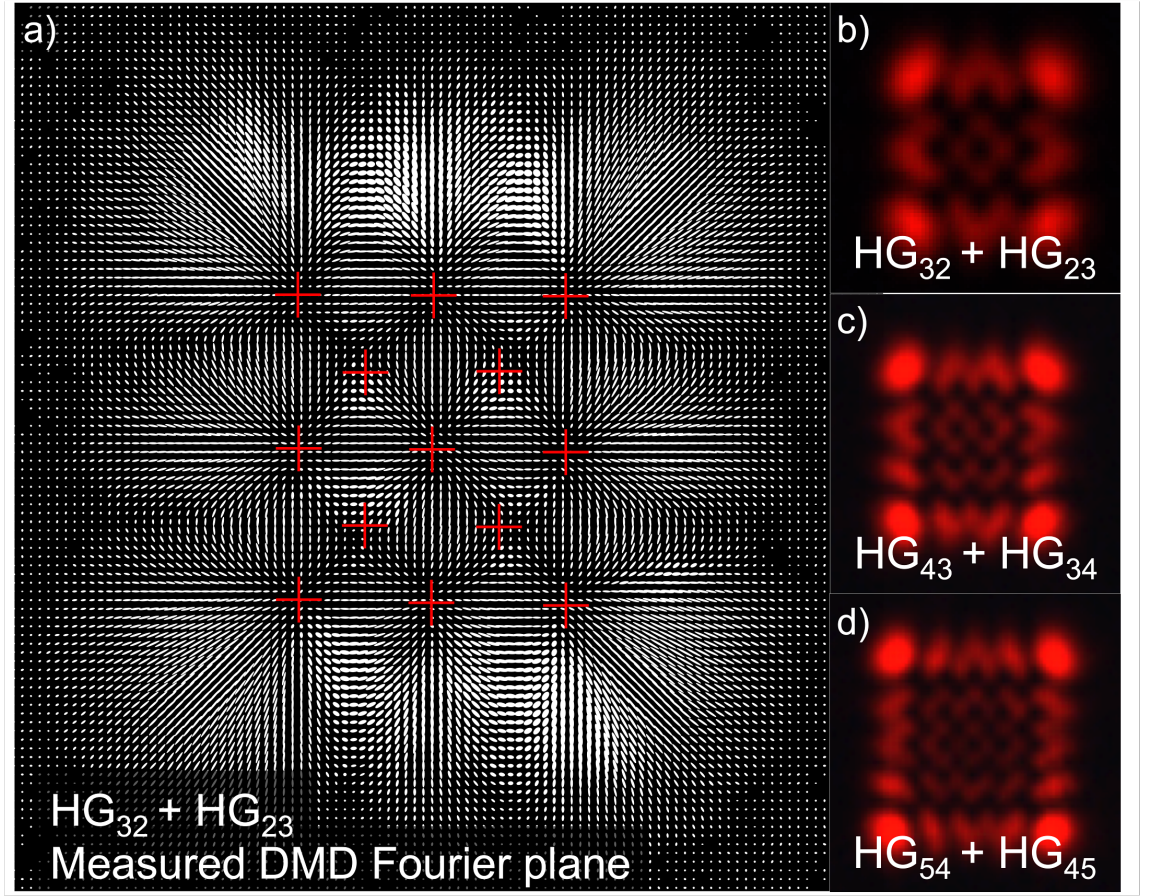


FIGURE 3.19: **Higher order polarisation shaping:** When the mode orders of the HG modes applied to beams A and B are increased from the simplest profiles, a complex linearly polarised vector beam can be formed. (a,b) are the polarisation map and  $S_0$  intensity when beam A is an  $HG_{3,2}$  and beam B is an  $HG_{2,3}$ ; there are 13 optical vortices formed in the beam centre (red crosses), with the surrounding polarisation either radial or resembling a 4-pointed star. (c,d)  $S_0$  images which demonstrate that as the mode numbers increase, the amplitude shaping within the beam centre degrades ( $HG_{43} + HG_{34}$  and  $HG_{54} + HG_{45}$ ).

we find  $(0.89 \pm 0.05)$ , and for the image plane case,  $(0.80 \pm 0.11)$ . Again, this discrepancy is due to the spatial filtering involved with image plane beams. The above results will also feature in figure 4.14 of chapter 4.

In order to quantify the accuracy of the spatially varying vector beams, the Stokes measurement photos shown in figure 3.12 were normalised and subtracted from the theoretical profiles. The resultant subtraction was averaged to produce a “likeness” deviation factor  $L_d \in [0 : 1]$  which effectively describes the intensity match to the theoretical Stokes measurements, and in turn, the accuracy of the overall polarisation shaping. This analysis compliments the Stokes parameter maps in figure 3.15 and

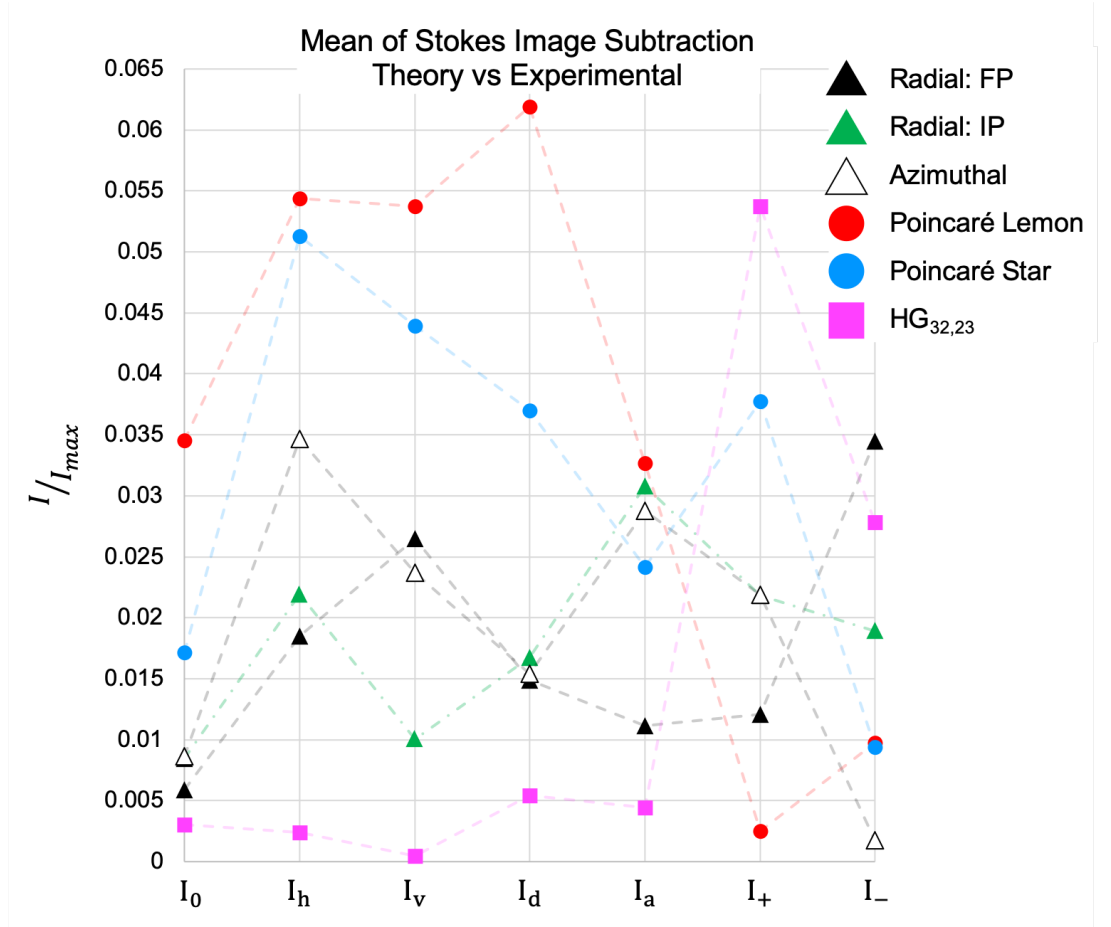


FIGURE 3.20: **Image subtraction in DMD vector beams:** The Stokes measurements in figure 3.12 can be normalised to 1 and compared with (subtracted from) their theoretical counterparts. This results in an average “likeness” deviation from 0 (identical). The first column shows the raw beam intensity likeness deviation  $L_{d,0}$ , when no polariser is used-  $L_{d,avg}$  is then the average of all columns.

3.16, and allows us to quickly compare the various vector beams generated here. For posterity, the camera images in figure 3.12 were cropped, resized and aligned with their theoretical counterparts using Matlab’s “Imregister” tool.

Figure 3.20 compares the image subtraction likeness of the vector vortex beams, Poincaré beams and the higher order vector beam discussed in section 3.7.4. Each column represents an individual Stokes measurement from figure 3.12; the first column,  $I_0$ , is the raw intensity of the vector beam. Each image was normalised to 1, such that  $L_d = 1$  denotes maximal difference and  $L_d = 0$  denotes identical normalised intensities. For reference,  $L_d = 0.01$  is the equivalent of 1% of pixels being the opposite intensity (e.g. normalised intensity  $I/I_{max} = 1$  in a zero array) with a 99%

match.  $L_d = 0.001$  could also be written as 0.1% pixels which deviate maximally, with a 99.9% match.

For radial and azimuthal vector vortex beams, we find that the raw intensity ( $I_0$ ) and average across the 7 Stokes measurements gives ( $L_{d,0} < 0.01$ ,  $L_{d,avg} = 0.02$ ) respectively. This indicates a strong match with the theoretical model, and results in associated polarisation maps which resemble highly linear radial and azimuthal polarisations, as shown in 3.14. In comparison, the Poincaré lemon (0.035, 0.036) and star (0.017, 0.032) are slightly weaker matches, in part due to the crescent shaped Stokes measurements formed from a combination of 4 LG modes which are more complicated to modulate. Finally, the HG<sub>32,23</sub> vector beam was found to have (0.003, 0.014); this strong fit is perhaps unsurprising given that beams A and B are just higher orders of the radial modes (HG<sub>10,01</sub>), with reduced image subtraction background noise given the increased size of the modes.

## 3.8 DMD vector beams: discussion and conclusion

The aim of this investigation was to advocate the use of a DMD binary amplitude modulator for low-cost high speed vector beam shaping, with user control over not just the intensity, but the phase and polarisation across the generated beam's profile. The setup presented uses the DMD to generate a pair of spatially separated orthogonally polarised beams, before a set of HWPs and calcite displacers re-align the beams such that they are collinear in propagation. Additional control between the two modes is achieved by fine tuning the hologram grating, relative phase and intensity to produce accurate vector beam profiles. With the exception of the first HWP in arm B, the common path through the remaining bench optics promotes strong stability, such that any vibrations or thermal drift generally occur to both arms simultaneously, and cancel out the effect on the path length between A and B.

### 3.8.1 Accuracy of vector beams

Firstly, the beams with one polarisation ( $45^\circ$  linear and circular) demonstrate the excellent uniformity achievable when the arms A and B are tuned relative to one another – particularly as a diffraction limited spot in the Fourier plane, the ellipticity in the central regions of figure 3.13(a,c) are near perfect examples of linear and circular polarisation, with  $(|\frac{P_{maj}}{P_{min}}|, \theta)$  of  $(0.07 \pm 0.03, 43.74 \pm 2.3)$ . However, the set of polarisation ellipses found in the image plane of these beams is not as clean; the orientation and ellipticity in (b) show slight irregularities, whilst the ellipticity in (d) has some more elliptical polarisations across the beam face, without any locations achieving the same approximate circular polarisations as its FP counterpart. This results in parameters  $(0.07 \pm 0.06, 47.6 \pm 3)$ , which possesses a slight increase in spread  $\sigma$ . These may be understood when considering the possibility of unwanted orders bleeding into the final beam at the additional aperture. This resulted in a field which was the image plane of the DMD window, and as such took on a similar intensity profile to that of the incident beam on the DMD, but with areas of non-gaussian irregular intensity. It is this which makes fine-tuning the beams accurately rather problematic, resulting in a loss of accuracy with polarisation orientation and ellipticity when compared with the results in the FP.

Figures 3.14(a-c) focused on the combination of both HG and LG modes to produce vector beams whose polarisation varied radially. It is clear that once again, the FP result is virtually indistinguishable from the theory, whilst the image plane result shows a slightly irregular radial intensity distribution, however this does not affect the linearity or orientation of polarisation achieved. Each of these results falls within a ( $L_{d,0} < 0.01$ ,  $L_{d,avg} = 0.02$ ), such that the deviation from theory amounts to (1%, 2%) for the  $I_0$  state and average across the measurements respectively.

Next, images 3.14(d-i) also agree very well with the theoretical maps; the azimuthally polarised beam has only slight elliptical polarisation regions (on par with radial likeness). In obtaining the Poincaré beam Stokes measurements, there was a risk of not choosing the centre of the beam for the various asymmetric intensity maps recorded (see figure 3.16). As such, the regions of left and right handedness have slight discrepancies with the theory, with the general deviations equalling (0.035, 0.036), i.e. 3.6% deviation from theory. In summary, the vector vortex beams generated by the DMD show strong agreement.

### 3.8.2 High speed vector beams

With the aforementioned beams providing a proof of concept, it was a straightforward route to demonstrating the same beams at high speed. In order to capture the maximum switching rate the TI Lightcrafter is capable of, the resolution of the high speed Mikrotron CMOS detectors was reduced to  $130 \times 24$ ; this allowed for a maximum camera frame rate of 7.69 kHz. Given that the system optics were kept identical throughout the FP measurements for continuity, the pixel pitch of the sensor resulted in considerably lower resolution images; nevertheless, there is a clear stepped rotation of the  $HG_{10}$  mode when a set of rotationally offset holograms are used along with a LP. The rate of switching was measured to be  $\sim 3.6$  kHz, whilst the polarisation maps confirm the nature of the beams achieved.

The switching rate possible with this system is only limited by the specification of the DMD used; e.g. whilst the TI Lightcrafter is a cheap alternative (up to 4 kHz), the TI DLP7000 can achieve speeds of up to 32.5 kHz, using the same 1bit patterns as this investigation [2]. Compared with the current generation of commercial phase-only LC-SLMs on offer ( $\sim 120$ -1000 Hz dependent on bit depth) this is an improvement of up to  $\sim 2$  orders of magnitude. The benefits of using the TI Lightcrafter are the low

cost (being  $\sim 10\times$  less than an LC-SLM with similar resolution), the capability of pre-loading patterns and the option to operate as a standard digital light projector, using the light engine provided. Furthermore, the DMD produces an output trigger for synchronising with a detector, which is highly relevant for high speed data acquisition.

### 3.8.3 Spatial mode generation

When using the system for vector spatial mode generation, it is pertinent to approximate the total number of independent modes that can be produced. Note that the DMD modulator is interchangeable with an LC-SLM, and so the capacity of both can be determined and compared. Our publication [151] describes in detail the approximation: if we define the transverse region of the back focal plane of lens  $f = F3$  with height  $Y$  and width  $X$ , the largest possible gratings on an SLM may be steered into the region bounded by  $X, Y = (\lambda_0 f)/(2p_{x,y})$ . Here,  $\lambda_0$  is the wavelength and  $p_{x,y}$  is the pixel pitch in each direction. Theoretically, for an LC-SLM of  $N$  pixels, this corresponds to  $N$  independent spatial modes within area  $XY$ ; in practice, this is not feasible due to the non-uniform efficiency of higher order modes, and coupling between pixels.

In the case of a binary DMD, the  $\pm 1$  mode pair receives equal power (see figure 3.1(c)(i,iii)) which halves the total number of addressable modes. Furthermore, we require zero overlap between orders; the argument in [151] describes segmenting the FP of the DMD into individual active regions for beams A and B. Given the extreme case of the smallest slit separation for the highest tilt angle achievable (i.e. 2 mirrors), the number of non-overlapping diffraction-limited spots in the FP can be estimated via the numerical aperture of the system; each spot may have a width  $d \sim 2.4\lambda f/D$ , with  $D$  being the diameter of the Fourier lens. In the simplified case of a  $512 \times 512$  DMD, we estimate up to 8192 vector spatial modes for beam A and B combined, in the absence of any aberrations. Realistically, this result does not take into consideration the pulse position and width modulation of the binary grating, which requires multiple neighbouring mirrors to contribute to the amplitude and phase shaping. As such, the range of tilts achievable with a DMD for complex modulation are more narrow. Nonetheless, DMDs have already been proven to generate large sets of spatial modes [172].

### 3.8.4 Diffraction efficiency

Whilst the DMD offers substantially faster switching rates, this attribute comes at a price; the efficiency of beams produced in first order diffraction is substantially lower than that of the typical LC-SLM. In order to estimate this diffraction efficiency, it is reasonable to treat the DMD as a filter of the incident beam: we can use the overlap integral between this incident beam and the target vector beam at the DMD plane (should the target vector beam be back-propagated through the setup to the DMD) [184]. As calculated in our publication [151], the normalised efficiency of a radially polarised vector vortex beam was found to be 2-5% for a DMD. This is in stark comparison to the equivalent diffraction efficiency of an LC-SLM ( $\sim 83\%$ ) for the same hologram – even so, the loss in power can nowadays be overcome with the use of higher powered laser sources and detectors of greater sensitivity.

In some applications there is no workaround for switching rate; there is currently growing worldwide interest in characterising diffusive media, in order to determine the transmission matrix detailing how light propagates e.g. multimode silica fibres and turbid media in biomedical applications [50, 54]. In the work published by our collaborators [176], it has been shown that in the cases of wavefront correction, focusing light through scattering media and imaging through a multimode fibre, a DMD has an increased beam shaping *fidelity* compared to LC-SLMs. This was found to be independent of the degree of scattering experienced. In short, LC-SLMs experience a considerable amount of scattering from the liquid crystals – this manifests as a slight background signal which cannot be suppressed, and which washes out the region of interest. Furthermore, LC-SLMs may experience “phase flicker” which hampers the precision in the wavefront correction procedure, which can be mitigated with increased measurements at the detriment of speed.

With the ever-continuing development of DLP technology, I believe that the use of DMDs for the high speed generation of vector beams is an exciting and viable option for researchers today and in the coming years.

# Chapter 4

## Polarisation structuring of broadband light

### 4.1 Introduction to broadband beam shaping

The following chapter presents my own work, which aims to expand upon extending the range of arbitrary vector beam shaping of light, from monochromatic (in chapter 3) to *broadband* sources. Specifically, I demonstrate the vector shaping of light across a bandwidth of 100 nm, which is limited only by the spectrum of the laser source used. In order to achieve dispersion compensation, I use a pair of LC-SLMs in tandem – one to shape the beams as before and the other placed in a Sagnac interferometer. This is to both overlap the beams and diffract them once more to actively reverse the dispersion.

This proof-of-concept is demonstrated experimentally by generating broadband versions of the beams presented in chapter 3, notably the vector vortex beams and Poincaré beams. Once again, the results will be displayed by way of polarisation ellipse maps, although the Stokes measurements will now be spectrally resolved for 4 wavebands across the chosen 100 nm range. Finally, optimisation and limitations of the technique will be discussed, with a note on beam efficiency and fidelity.

The project arose from feasibility studies in converting my system presented in chapter 3 to shape broadband light. The project was led by my supervisor Prof. Padgett, with general advice and proofreading from Prof. Sonja Franke-Arnold (University of

Glasgow). The experimental setup, hologram design, data acquisition and analysis was performed by myself under supervision from Dr Phillips. Dr Neal Radwell (University of Glasgow) provided useful contributions to the writing of the publication. This investigation was published in Optics Express [185], with the results presented at CLEO: 2017 in San Jose (USA).

#### 4.1.1 Wavelength dependence in beam shaping

Over the last 30 years, the combined efforts of commercial entities and the global research community has led to the innovation and ubiquity of light modulation technology in a wealth of applications. As discussed in section 2.5.1, this versatile technology allows for arbitrary amplitude and phase shaping [154, 173]. The techniques introduced in chapter 3.3 can be extended from scalar beam shaping (at most uniformly polarised) to generating vector beams of arbitrary local polarisation [165, 186–189]. Recall from section 3.3.2 that this is typically achieved using an SLM to diffract light into two distinct regions within the +1 order, encoded with the correct relative amplitude and phase such that giving these beams orthogonal polarisations and overlapping them forms the target vector beam [151, 165].

Holography is inherently wavelength dependent. In my overview of holography in section 2.5, I described the off-axis hologram, where a grating is necessary to tilt the object wave away from the unmodulated direct wave and into the first order position to prevent interference of these waves. We must also take into consideration that SLMs are physical devices with a finite phase modulation depth. In the manufacturing process, the  $(2\pi)$  phase modulation/ blazing is determined for a single wavelength,  $\lambda_0$ . The perceived phase modulation changes for neighbouring wavelengths where  $\lambda \neq \lambda_0$ . These characteristics cause LC-SLMs (and DMDs) to be wavelength dependent, such that any incident beam with a significant bandwidth  $\Delta\lambda_0$  will be diffracted into a spread of angles, i.e. displaying *chromatic dispersion* (section 2.1.6). Till now the scope has been confined to monochromatic sources such as the HeNe laser, which typically has a negligibly small  $\Delta\lambda_0$ .

### 4.1.2 State of the art in broadband beam shaping

There exist specialist fields in research and industry which utilise broader bandwidth light sources which pose a strong argument for the extension of beam shaping capabilities to include broadband light, described in section 1.3.6. Numerous studies have looked to adapt the standardised diffractive optical elements (DOE) for use with near-white light sources – this involves the clever use of SLMs, prisms and custom DOEs to compensate for dispersion. A recent innovation is the use of a Fresnel glass cone to impart an angularly-varying phase on a circularly polarised beam via total internal reflection (recall figure 1.4) [102, 106]. This has the ability to produce vector vortex beams possessing OAM with no dispersion using a white light source. Studies have also considered the  $\lambda$  independence inside the central regions of white light Bessel beams formed from an axicon lens [190, 191].

Another solution is to develop a custom DOE such as an  $s$  or  $q$  plate (figure 1.1) [192, 193]; in [192], an  $s$ -waveplate was used to convert an incident white light Gaussian beam into a vortex beam with spectrally-varying contrast (due to a wrongly-polarised Gaussian background); by using a QWP and polarising BS (PBS) as a polarisation filter, the optimum contrast for the entire bandwidth can be retrieved. Furthermore, a pair of prisms can be used in tandem to produce a zero dispersion condition [120, 194]. In [195], a prism was placed after the SLM in the image plane such that the individual spectral components are tilted back by varying degrees into a co-axial propagation, with all wavelengths co-incident as before diffraction.

Lastly, to compensate for the chromatic effects of a diffraction grating, we can intuitively consider the use of a second equal but opposite diffraction grating [96, 99]. In [196], the LC-SLM window was split into two – a Bessel beam was encoded onto the first half of the LC-SLM, whilst a compensation grating of the same magnitude was encoded onto the second. By using a double-pass geometry, the compensated co-axial wavelength components of a white light Bessel beam could be passed out. Other 2D LC-SLM divisions exist which seek to split the LC-SLM up into horizontal bands, and impart locally varying phases to the incident beam [92, 93, 95].

Given the wavelength dependency of SLMs which make arbitrary modulation possible, it is important to consider a solution which can interfere two orthogonally polarised diffraction orders – simultaneously compensating for the inherent chromatic dispersion of both beams, and maintaining the orthogonality [120, 195]. In order

to build a solution that achieves these aims, it was important to answer the following questions: how does the behaviour of LC-SLMs and DMDs compare when using broadband light? Also, what optical geometries can be used to adapt the work in chapter 3 to produce *arbitrary broadband* vector beams?

## 4.2 Considerations in broadband beam shaping

When considering the amplitude and phase shaping of broadband light in the diffractive regime, it is pertinent to understand the implications of using wavelength-dependent grating holograms, and subsequently note the constraints of coherence length  $l_c$  on vector beam generation. The following section highlights these constraints when using LC-SLMs and DMDs in the diffractive regime.

### 4.2.1 Chromatic dispersion in SLMs

The previous experiment was conducted using a Zeeman-stabilised Neo-ark 262 HeNe laser ( $\lambda = 632.8$  nm); we now introduce a comparatively broadband source, the Qioptiq diode laser with specification iFLEX2000-P-1-640-FCP8-50-NP (642.79 nm). On switching out the HeNe source for the Qioptiq laser in the previous beam shaping system, I found that beams A and B possessed chromatic dispersion in the Fourier plane of the DMD. Notably, this effect disappeared when the DMD was replaced by an LC-SLM. However, whilst the LC-SLM-generated beams were well defined, adjusting the relative phase between the beams no longer had any effect on their interference. That is, at no  $\phi_{global}$  could an LP oriented at  $H_z + 45^\circ$  (before the CCD) produce a  $45^\circ$  HG<sub>10</sub> mode, nor would rotation of the LP result in spinning lobes. This was because the  $\Delta OPL > l_c$ , and the corresponding wavetrains of each beam no longer interfered together after traversing their respective paths through the system.

To further characterise the differences between the two modulators, I extended this study to include multiple diffraction angles and introduced a substantially broadband source – the Thorlabs superluminescent diode (SLD) (in figure 4.1(b)) SLD830S-A20 ( $\lambda = 832.36$ ,  $\Delta\lambda = 18.5$  nm). The spectra of the three lasers are compared in figure 4.1. The spectrometer used was an Ocean Optics USB4000; in spite of sub-wavelength data points, the similar widths of the spectra in (a) suggest this spectrometer has

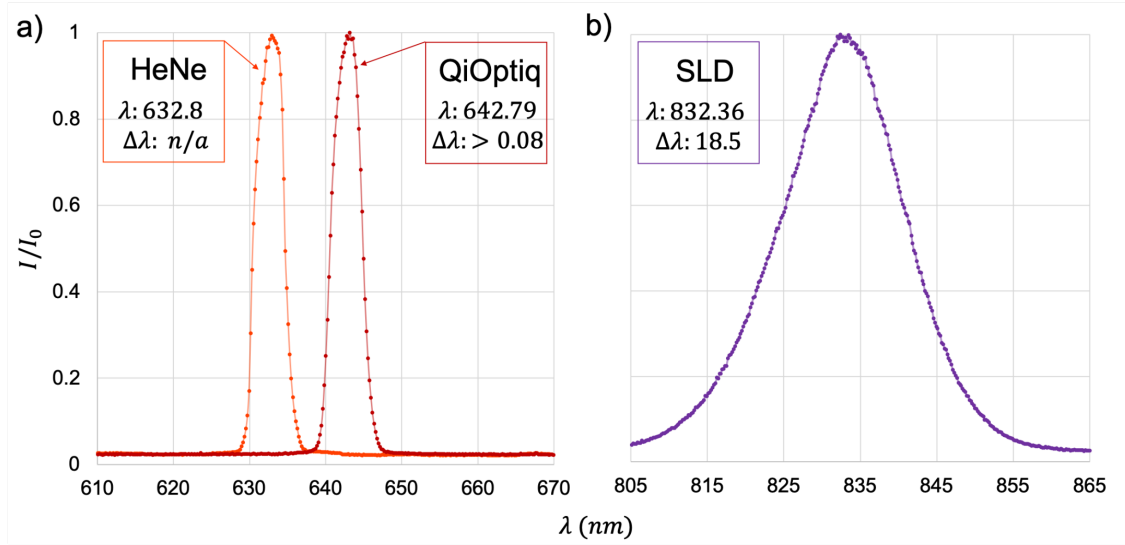


FIGURE 4.1: **Source spectra:** A comparison of the spectrum of each of the laser sources used in the testing of this investigation. The full width at half maximum (FWHM) of the HeNe and Qioptiq source is too small to be resolved by the spectrometer, an Ocean Optics USB4000. The Qioptiq laser is specified to be  $640 \pm 5$  nm but is known to possess lower coherence properties ( $\Delta\lambda > 0.08$  nm), particular when used in interferometry with mismatched path lengths. The SLD operates mostly in the near infrared (NIR), and exhibits a much larger FWHM ( $\Delta\lambda \approx 20$  nm).

a spectral resolution of only  $\sim 1$  nm. Figure 4.2 shows a simplified version of the previous setup in chapter 3, imaging the FP of an SLM with no beam displacement.

In figure 4.3, we see a direct comparison of diffractive beam shaping using a DMD versus an LC-SLM. For reference, part (a) shows the effect of setting all mirrors to the “on” state to produce a diffraction limited spot. In the case of the HeNe source, the typical artefacts of blooming and a slight granular background are visible. However, in the case of the Qioptiq, these artefacts are spread out along an axis some  $10^\circ$  from the horizontal. This dispersion is then extremely prominent in the SLD source, to the extent that a larger sensor was required (N.B. the inset of each image has a 0.5 mm scale bar). In this case the diffraction limited spot is dispersed into a streak with the granulation effect becoming fringes emanating from the central streak.

In part (b), the DMD is encoded with an HG mode pair and a low-angle phase tilt such that the higher order modes are diffracted diagonally from the zero order. The same modes were generated using an LC-SLM with similar tilted gratings, and imaged

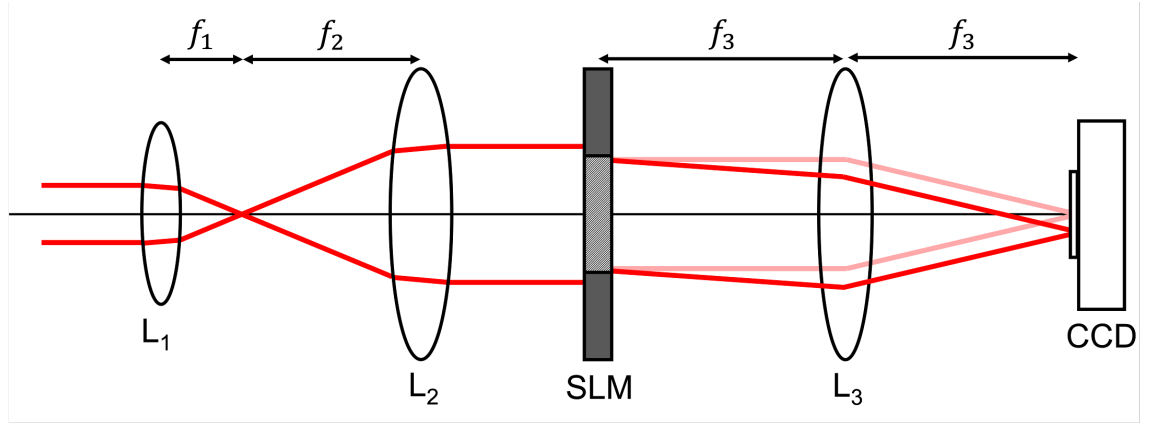
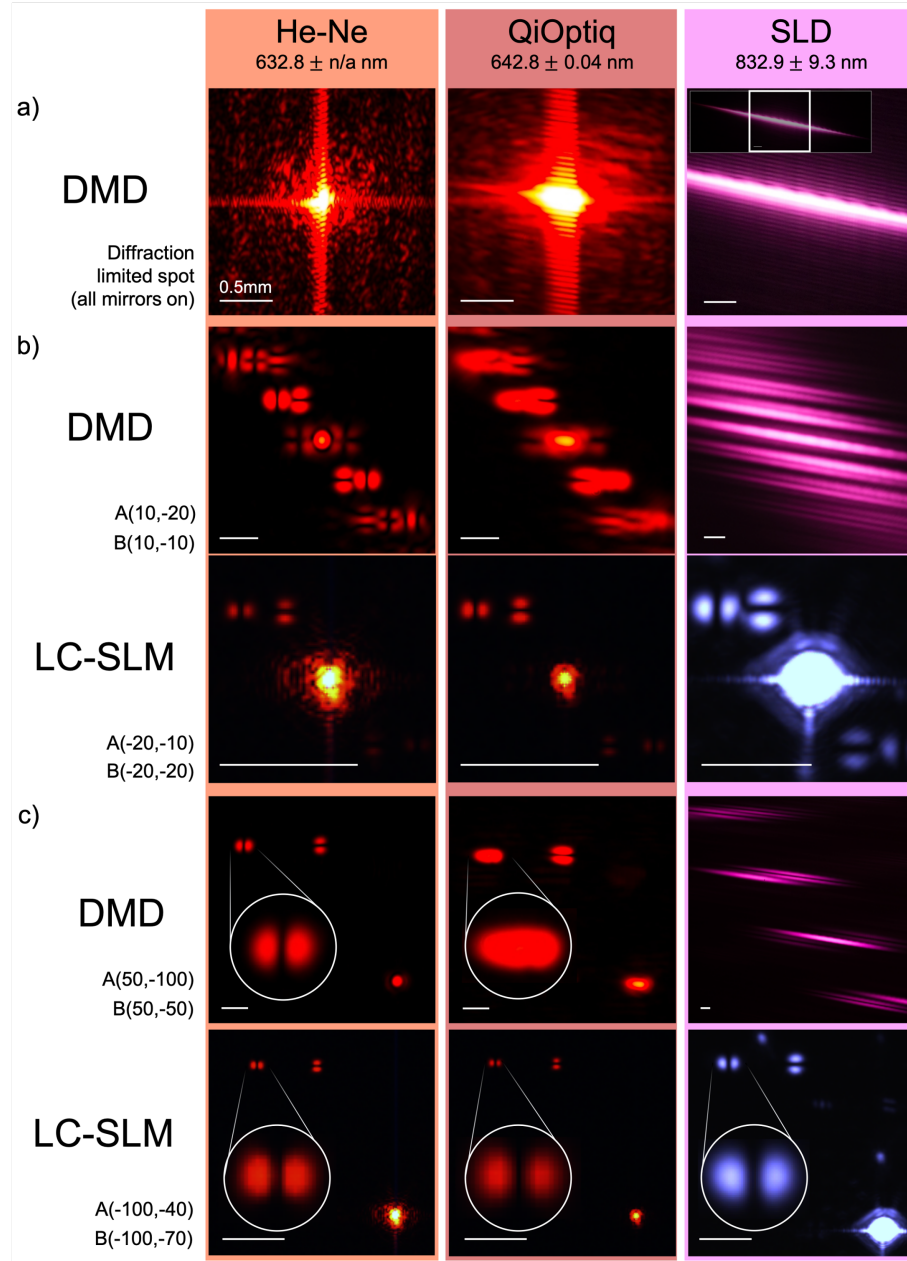


FIGURE 4.2: **Fourier holographic imaging test:** The setup in section 3.5 was simplified to image the zero (faint red) and higher order (red) diffracted modes using a collimated expanded incident Gaussian beam. The reflective LC-SLM is shown in transmission to emphasise the diffraction of the higher orders. With this simple setup we can rule out the influence of other optical components necessary for beam shaping, such as birefringent media.

on a CCD. We observe several features worth noting: for one, both SLMs shape well-defined modes using a monochromatic source. However, in the broadband regimes, the modes are dispersed along the same axis as before, compromising the intensity profile of the mode. Notice that the zero order in the LC-SLM is substantially more intense relative to the modes than in the DMD case – this is evidence of both the higher efficiency of liquid crystal modulation and the importance of correctly blazed gratings in LC-SLMs.

In part (c) a greater tilt angle (resembling that used in chapter 3) is applied, alongside a magnified view of the  $HG_{10}$  mode; the results from (a) and (b) hold, and the only well-defined modes are those produced by the LC-SLM. Note that in the case of the SLD source with the DMD, the dispersion is in 2 directions – the  $\approx 10^\circ$  tilt also found in (a) and the diagonal direction of the tilt hologram – in this test they are not in the same orientation, and so this dispersion cannot be compensated with e.g. a single prism.

Whilst a pair of DMDs were originally considered for *high speed* broadband vector beam shaping, this test is evidence that a DMD is physically disadvantaged for shaping broadband light compared to an LC-SLM. Whilst a DMD and its mirrors are inherently achromatic for amplitude masking in digital light projection (RGB LEDs), the same cannot be said for the diffractive regime. Here we must acknowledge that between each mirror in the DMD array is a step change in path length that



**FIGURE 4.3: DMDs vs LC-SLMs in broadband holographic beam shaping:** (a) diffraction-limited spot dispersion from a DMD. (b,c) the three sources were all used to generate a pair of +1 order  $HG_{10,01}$  mode sets – the basis for vector vortex beams. The number of phase cycles within each beam in  $(x, y)$  is labelled on the left. A monochromatic HeNe source shows zero chromatic dispersion, regardless of the modulator or the tilt angle. With short coherence sources (Qioptiq and SLD), the extended range  $\Delta\lambda$  is diffracted into a spread of angles in the FP; the resultant modes are then smeared out in the transverse plane. This dispersion appears to be significantly worse with a DMD, in part due to the interplay between the 2D binary-state mirror array and the diffraction angle encoded on neighbouring wavelengths.

acts on neighbouring wavelengths differently – this causes an additional stepped tilt grating to act on the beam, which results in a non-blazed wavelength-dependent shift that can disperse the hologram tilt at broad bandwidths. The following investigation therefore makes use of a pair of LC-SLMs.

### 4.2.2 Coherence revisited

To examine the effects of temporal coherence, I compared the self-interference of the HeNe and Qioptiq sources. Whilst the spectra in figure 4.1 do not resolve the differences in bandwidth, we can deduce a lower bound for the Qioptiq by use of a shearing interferometer. With such a device, self-interference is only visible if the coherence length is greater than the thickness of the glass, i.e.  $l_c > \Delta\text{OPL}_{\text{shear}}$ . The Qioptiq was found to produce no visible fringes for  $\Delta\text{OPL}_{\text{shear}} \approx 2.5$  mm, which infers a bandwidth of  $\Delta\lambda > 0.083$  nm. Whilst a HeNe source is often coherent over metres (or greater), broader bandwidth sources such as the Qioptiq must be path length matched. For example, the optical path difference in chapter 3 comprises of the thickness of HWP1 ( $\approx 2$ mm) and the difference in extraordinary ray path inside the beam displacers.

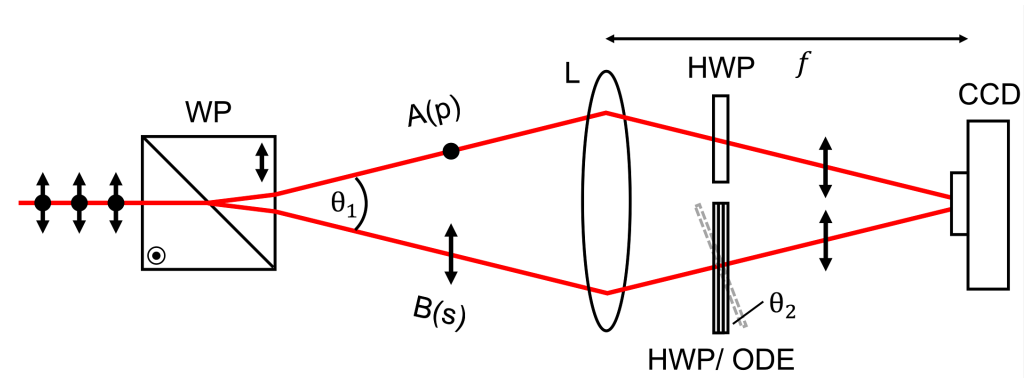


FIGURE 4.4: **Wollaston prism interference test:** A  $45^\circ$  linearly polarised beam is incident on a Wollaston prism (optical axes marked), such that equal components are refracted by the ordinary and extra-ordinary refractive indices. The beams exit at angle  $\theta_1$  to one another. A lens is placed sufficiently close such that the beams interfere on the camera at distance  $f$ . By placing birefringent elements in the back focal plane of the lens, the impact of an OPL mismatch can be probed. Adjusting the perpendicularity of these elements by angle  $\theta_2$  can adjust the  $\Delta\text{OPL}$  with  $\mu\text{m}$  precision.

Figure 4.4 shows a simple test to characterise the effect of optical path length (OPL) matching using the Qioptiq source: after propagation through a Wollaston prism and lens, orthogonally polarised beams A and B interfered in the plane of the camera. The camera image detected for each scenario is shown in figure 4.5, with the corresponding row averaged interferometric visibility  $\mathcal{V} \in [0 : 1]$  which quantifies the contrast. In (a), both beams passed through a HWP in the back-focal plane of the lens to interfere with the same polarisation; one HWP can be oriented with some angle to the other such that the effective OPL of the medium is increased. The result is a subtle control of the path length, and the interference fringes lose 50% visibility at  $\theta_2 > 45^\circ$ . In (b) this HWP was replaced with a set of plane glass optical delay elements (ODEs), specifically microscope slides and cover slips – clearly the path difference is only within the coherence length when thickness  $d \approx 2$  mm to match the HWP. Finally, the role of polarisation-matching was tested (c): in short, the maximum visibility of fringes still occurs when the path lengths are matched. The transmission through the waveplates is maximal when the polarisations of beams A and B are oriented in the same direction – this parameter appears to only constrain the energy in the interferogram, and has little effect on the peak visibility between fringes.

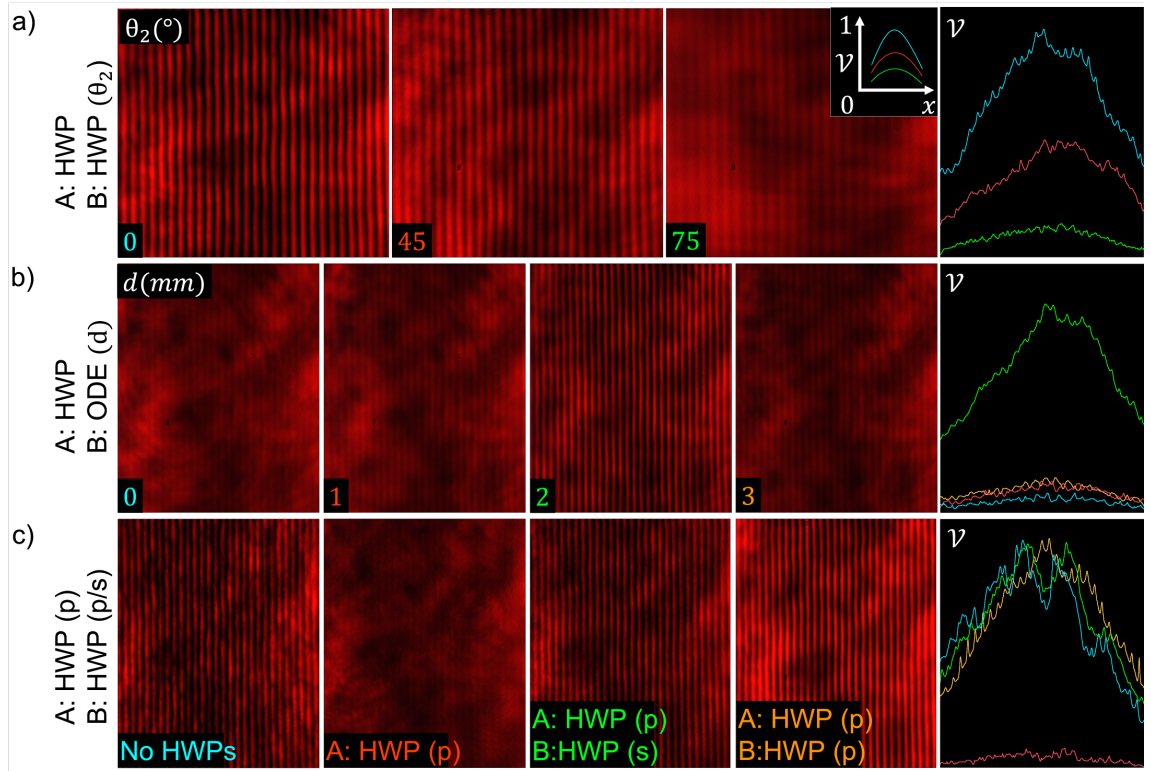


FIGURE 4.5: **Broadband interferograms in OPL matching test:** (a) When both beams pass through a HWP, the  $\Delta\text{OPL}$  is effectively zero – however, departure from normal incidence by rotating one HWP increases the optical path length,  $nd$ , reducing the fringe contrast (where  $n$  is the refractive index of the element). (b) A more substantial  $\Delta\text{OPL}$  is achieved by changing the medium thickness,  $d$ . (c) Combined path length and polarisation orientation matching achieves greater contrast still, as each beam contributes optimally with minimal stray light to wash out the fringes.

### 4.3 Broadband vector beams: experimental setup

The requirement for dynamic arbitrary control with dispersion compensation, as discussed in section 4.1, shows a precedent in using SLM pairs. I therefore chose to use two identical LC-SLMs – one to modulate the amplitude and phase (as performed by the DMD in chapter 3.5), and a second devoted to dispersion compensation to be placed in the image plane of the first. The process of combining orthogonal beams to allow for vector shaping is then an added complication which must be incorporated into this LC-SLM system.

As discussed in section 2.5.1, liquid crystal-based SLMs only modulate one axis of polarisation of an incident field. In the case of [165], beams made orthogonal and separated by a Wollaston prism are both modulated by strategic placement of a HWP. A double pass through the refracting optics before recombination suggests that there is no room for independent beam dispersion correction. We therefore opted to implement a *polarisation-invariant* second LC-SLM, which has been documented in [197, 198]: In short, an arbitrarily polarised beam incident on a polarising beamsplitter (PBS) is split into orthogonal p and s states – for an LC-SLM that modulates the s state only, the s state is passed straight to the modulator. The p state is instead reflected from a mirror through a HWP to be rotated into the s state before modulation.

The two paths form a Sagnac interferometer (see section 2.1.5); the net result is that two diffracted beams pass out of the same PBS face as the beam was originally incident upon, still orthogonal albeit with flipped polarisations. Several designs were considered to incorporate a dual-SLM Sagnac interferometer, which included the use of a double pass of a single LC-SLM with a split hologram for the two modulations. However, there were concerns over the proximity of the various beams to the optics in such a confined setup, and there was uncertainty over the impact of having markedly different angles of incidence between the first and second pass.

The following is an in-depth account of the features and operation of our eventual experimental setup for 100 nm broadband vector beam shaping, shown in figure 4.6. Firstly, a Fianium Femtopower 1060 (SC-400-6) Supercontinuum laser (SC) with a bandwidth spanning 1600 nm was used as a white light source. Bandpass filters were used to constrain the raw spectral range to 455-600 nm within the visible spectrum (as shown in figure 4.7).

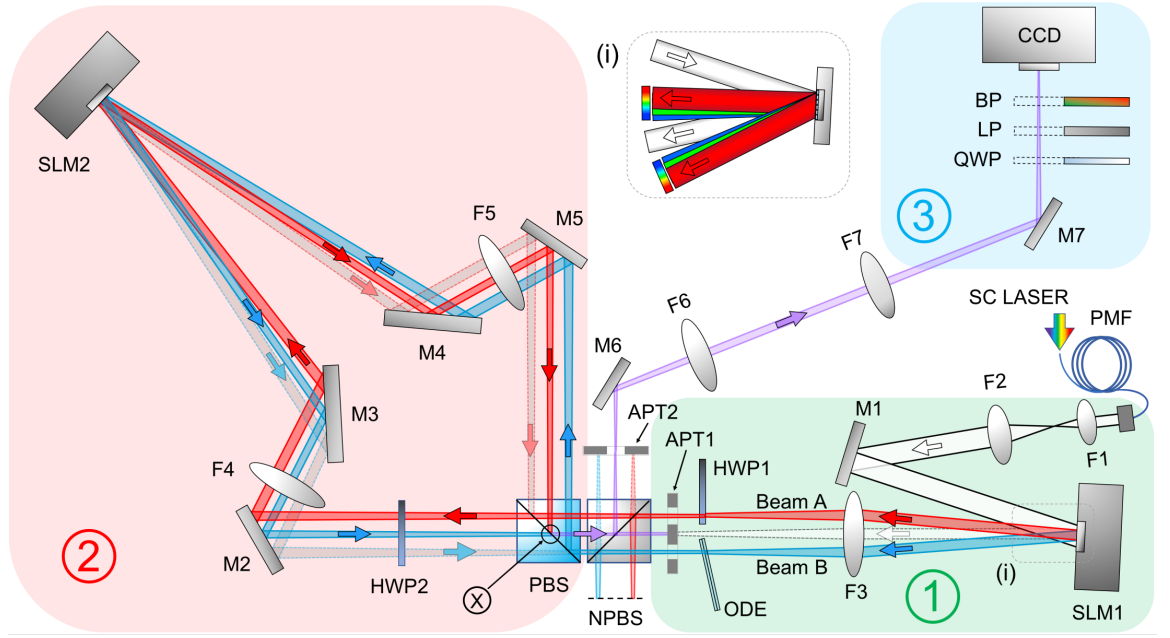


FIGURE 4.6: **Experimental setup:** From our publication, [185]. Stage 1: beam preparation and shaping, in the same operation as in chapter 3. Stage 2: a displaced Sagnac interferometer used to simultaneously correct the chromatic dispersion and recombine beams A and B at the PBS (purple). Stage 3: vector beam characterisation arm. The SC source enters the system via a polarisation-maintaining fibre (PMF). The beam expansion is performed by lenses F1 (20 mm) and F2 (100 mm). A pair of Boulder Nonlinear Systems P512-0635 LC-SLMs with  $512 \times 512$  resolution were used. HWP1 and HWP2 are achromatic and blue-centred half-wave plates respectively. NPBS and PBS are non-polarising and polarising beamsplitter cubes. Lenses F3-F5 share a 300 mm focal length for unity magnification in the 4F imaging of SLM1 onto SLM2. M1-M7 are visible dielectric mirrors. ODE is a custom made optical delay element. LP and QWP are a linear polariser and achromatic quarter-wave plate, respectively. BP is one of the four bandpass filters used to isolate the four wavebands measured. A Prosilica GC660 CCD with resolution  $656 \times 494$  is located in the FP of SLM1 and SLM2. Inset (i) depicts the white light chromatic dispersion from a simple vertical grating, with red dispersed the most and blue the least.

The operation of the setup is divided into three separate stages: in stage 1, the initial input beam is expanded and shaped into a +1 order of two beams using a liquid crystal spatial light modulator (LC-SLM). Stage 2 features a displaced Sagnac interferometer, which combines the diffracted beams whilst simultaneously compensating for the inherent chromatic dispersion. Lastly, the optional third stage is for analysing the resultant vector beam.

In stage 1, the SC beam is expanded and collimated using lenses F1 and F2, such that the beam overfills the first LC-SLM (SLM1) from a small angle of incidence

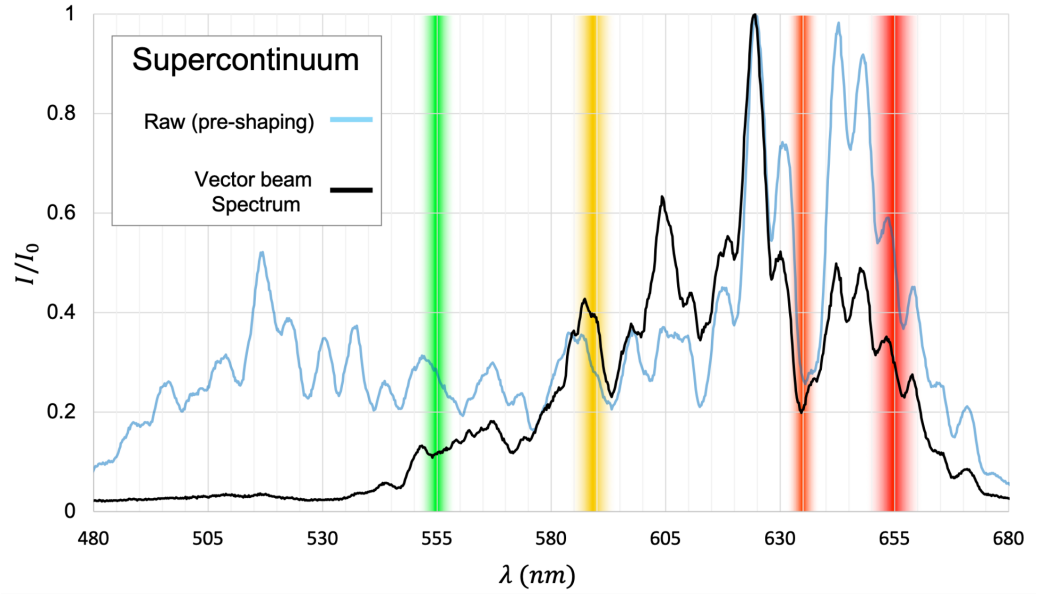


FIGURE 4.7: **Supercontinuum spectrum:** A comparison of the spectrum of the SC after passing through 455 to 655nm filters (blue), and the vector beam spectra incident on the CCD after beam shaping (black). The net contribution of the various wavelength-dependent components is to clip the full bandwidth – this is in part due to specific anti-reflection coatings found on e.g. the Boulder LC-SLMs. The wavebands ultimately measured are also superimposed from 555 to 655 nm.

( $\sim 5^\circ$ ). The 8-bit hologram sent to SLM1 then diffracts the input beam into two locations either side of the zero order in the Fourier plane, i.e. beams A and B (as in section 3.5). SLM1 only modulates the vertical polarisation component of the input beam, and so the diffracted modes are strongly vertically polarised. The hologram is also equipped with the same spatial control of the intensity and phase of A and B independently of one another. Lens F3 performs an FT on the field diffracted from SLM1, before aperture APT1 cuts off any undesired orders (notably the non-diffracting zero order shown in figure 4.6 as white). Only beam A passes through HWP1 to become orthogonal to beam B.

An optical delay element (ODE) was inserted into the path of beam B – shown in figure 4.8, this was a combination of glass cover slips and microscope slides, chosen to fully compensate the optical path length of the light through HWP1 on beam A. A further degree of freedom was added to fine-tune this delay: the angle of the ODE was pivoted away from normal to the beam axis, by up to  $\sim 10^\circ$  to increase the optical path by tens of  $\mu\text{m}$ . Ideally, the ODE should be perfectly normal to the passing beam to prevent any astigmatism, however this was ultimately not the limiting factor. Glass slides were used over a matching HWP because of the ease

of OPL matching by the pivoting method used, and the lack of any bezel or optical cement at the edges which would obstruct the beams.

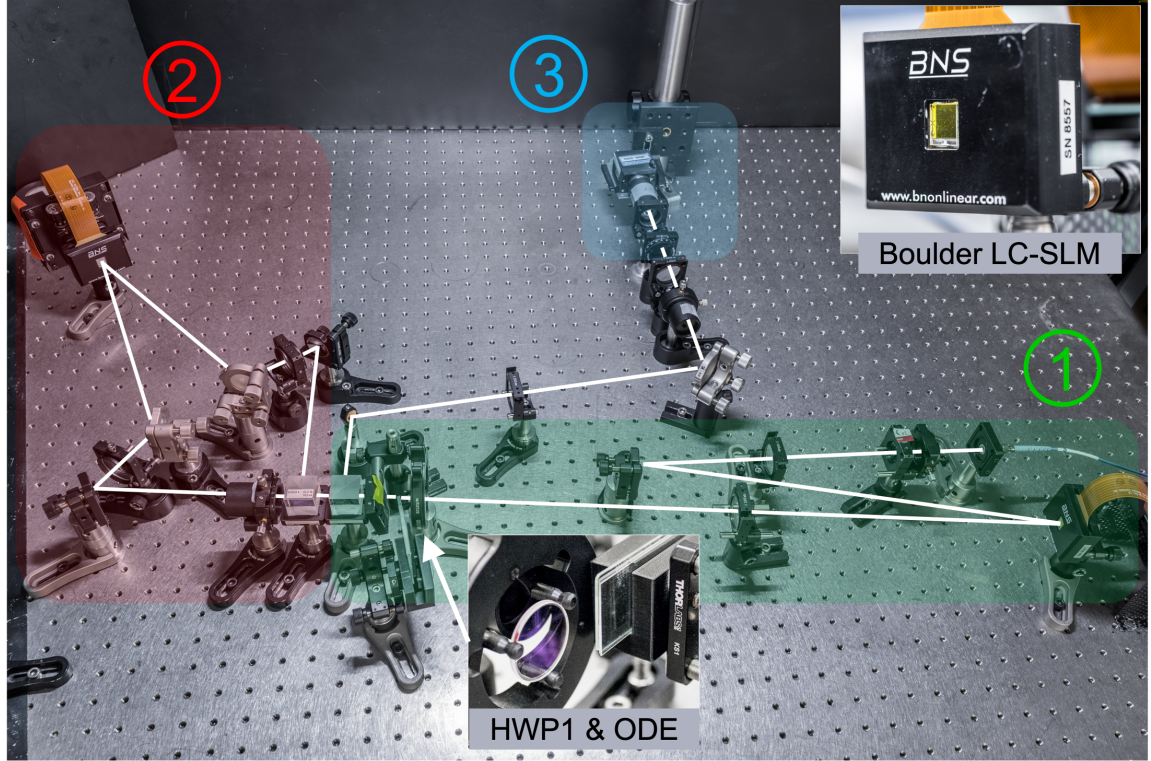


FIGURE 4.8: **DSLR photo of experimental setup:** A white line was superimposed onto the approximate zero-order beam paths for clarity. Inset, the Boulder LC-SLM used for SLM1 and SLM2; also, beams A and B pass through HWP1 and the optical delay element (ODE) respectively.

Stage 2 comprises a second LC-SLM, denoted SLM2. This is positioned at the far end of a “displaced” Sagnac interferometer, where original beams A and B travel through the interferometer in opposite directions, and do not interfere at the output. SLM2 is used to diffract these beams into directions which exactly counteract the chromatic dispersion introduced by SLM1. For simplicity, beams A and B are colour coded: consider beam A (red), which enters stage 2 horizontally polarised; after passing through unimpeded by a polarising beam splitter cube (PBS), beam A’s polarisation is rotated by  $90^\circ$  using HWP2 to prepare the beam for diffraction by SLM2, which also has a vertical modulation axis. Note that SLM2 is situated in the image plane of SLM1, with matching lenses  $F3, F4, F5 = 300$  mm forming a  $4F$  imaging system in between.

If SLM2 was replaced with a mirror, beam A would reflect off mirrors M2,M3 and propagate along the upper grey path to M4,M5 before reflecting from the PBS and returning along the same path from which it entered. However, with the introduction of a linear grating on SLM2, beam A is diffracted away from the zero order such that it instead crosses point X inside the PBS. The grating applied to SLM2 is in fact equal in magnitude but opposite in direction to the grating applied to SLM1 – this means that the first order beam born from beam A as the incident beam is now coincident and collinear with the path of the original (white) zero order of SLM1. This is critical because it is only along the original zero order path that the chromatic dispersion of both beams A and B is fully compensated.

At the same time, beam B (vertically polarised) reflects from the PBS along the opposite direction to beam A towards SLM2. Already vertically polarised, beam B needs no HWP. After diffracting from the same hologram on SLM2, the first order beam born from beam B is necessarily rotated  $90^\circ$  by HWP2 before also reaching point X inside the PBS. Thus the progeny of the original beams A and B overlap at X orthogonally polarised, with the chromatic dispersion theoretically eliminated. These beams are collinear, and combine to form a vector beam (purple) which leaves the PBS out the same facet that beam A and B originally enter. The previously passive non-polarising beamsplitter (NPBS) is then used to pass out the vector beam, before aperture APT2 (located at the FP of SLM1 and SLM2) blocks the original dispersive beams A and B.

Finally, the optional third stage is for analysis – for my investigation I used a pair of lenses ( $F6 = 200$  mm and  $F7 = 150$  mm) to demagnify the beam onto a CCD, which is also the re-imaged Fourier plane of both SLMs. Using a set of bandpass filters, an LP and QWP, the spatial and spectral properties of the resultant vector beams could be determined by their Stokes parameters.

## 4.4 Broadband vector beams: hologram design

The treatment of orthogonally polarised beams A and B to achieve vector vortex beams depends on the intensity, phase and polarisation of the vector beam to be generated, which was previously investigated in [165] and in my previous work [151] (chapter 3). My aim here was to produce arbitrary broadband vector beams centred around  $\lambda_0$  in the FP of both SLM1 and SLM2. That is, to generate beams defined by:

$$\mathbf{E}(x, y, \lambda_0) = \begin{bmatrix} E_A(x, y, \lambda_0)e^{i\phi_A(x, y, \lambda_0)} \\ E_B(x, y, \lambda_0)e^{i\phi_B(x, y, \lambda_0)} \end{bmatrix}. \quad (4.1)$$

Here,  $E_{A,B}$  is the amplitude of the E field, and  $\phi_{A,B}$  is the phase of the horizontally polarised beam A and vertically polarised beam B respectively. The  $(x, y)$  variables represent the Cartesian co-ordinates within the transverse plane of the target beam. The spatial modes encoded into beams A and B are then defined as  $\mathbb{E}_{A,B} = E_{A,B}e^{i\phi_{A,B}}$ .

As was the case in section 3.6, the role of SLM1 in stage 1 of the setup is to diffract light into the +1 order made of beams A and B, now at a selected central design wavelength  $\lambda_0$ . This can likewise be defined at the SLM1 plane as the complex field:

$$\begin{aligned} \mathbb{S}_{\text{dual}}(u, v, \lambda_0) &= W_{\text{rel}}e^{i\phi_{\text{global}}} \mathbb{A} + (1 - W_{\text{rel}})\mathbb{B} \\ &= S_{\text{dual}}(u, v, \lambda_0)e^{i\phi_{\text{S,dual}}(u, v, \lambda_0)}, \end{aligned} \quad (4.2)$$

$$\mathbb{A} = [\mathfrak{F}(E_A e^{i\phi_A})] e^{i(\phi_{A,\text{tilt}})}, \quad \mathbb{B} = [\mathfrak{F}(E_B e^{i\phi_B})] e^{i(\phi_{B,\text{tilt}})}. \quad (4.3)$$

Here  $(u, v)$  are the Cartesian co-ordinates in the SLM1 plane, and  $\mathfrak{F}$  is the Fourier transform to convert between the SLM1 plane and the Fourier plane where the target field lies. The same dynamic optimisation parameters from equation 3.16 –  $W_{\text{rel}}$  and  $\phi_{\text{global}}$  – return in equation 4.2 to allow the user to tune the relative global power and phase of beams A and B. Specifically,  $W_{\text{rel}} \in [0 : 1]$  is a real number which defines the fraction of power sent to A and B respectively; neglecting the envelope function of the grating, the powers are equal when  $W_{\text{rel}}$  is 0.5. Next,  $\phi_{\text{global}} \in [0 : 2\pi]$  is the relative phase between A and B whilst  $\phi_{A,\text{tilt}}$  and  $\phi_{B,\text{tilt}}$  are the wedge tilts used to diffract A and B into different spatial locations in the far field of SLM1.

The use of a phase-only LC-SLM over a DMD requires a different approach for complex modulation. There has been considerable work in this field to determine the optimal algorithm for modulation in a variety of environments – in fact they all

aim to tune the resulting intensity in a given location by spatial modulation of the efficiency of transmission in the desired diffraction order. The differing beam profiles produced result from where the unwanted light is dumped [72, 147]. I chose to utilise the method defined by Davis *et al.* (1999) [154]: whilst the phase on SLM1 is purely the target phase, the target amplitude is a spatial variation in the contrast of the diffraction gratings which direct the light into the target orders. It is this change in the contrast which modulates the efficiency of light into the target +1 order, and so the amplitude across the beam profile can be adjusted with these losses in efficiency. In the ideal case of the input beam having uniform intensity and phase, the phase hologram generated for SLM1 is defined as:

$$H(u, v, \lambda_0) = \left[ 1 - \frac{1}{\pi} \text{sinc}^{-1} \left( S_{\text{dual,norm}}(u, v, \lambda_0) \right) \right] \phi_{\text{S,dual}}(u, v, \lambda_0) \quad (4.4)$$

with  $S_{\text{dual,norm}}$  the normalised amplitude function  $S_{\text{dual}}$ . This equation gives total control of the phase and intensity of beams A and B respectively, whilst also allowing the fine tuning of their relative global power and phase.

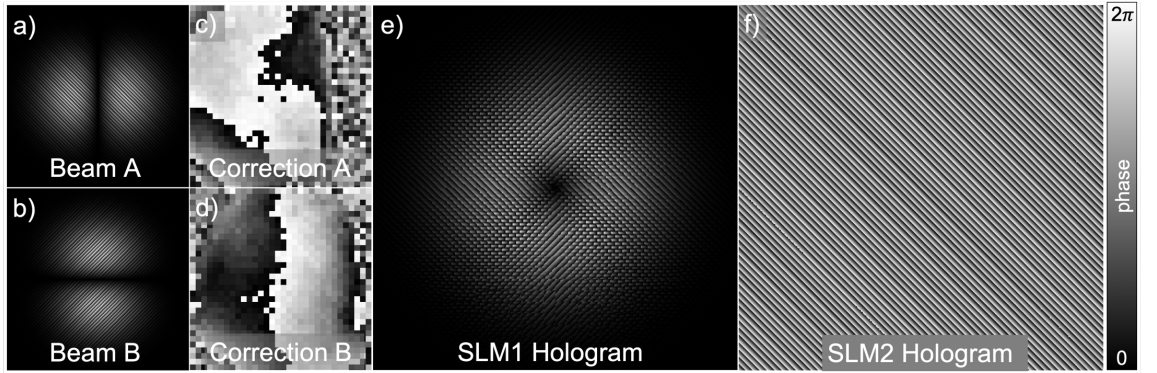


FIGURE 4.9: **Dual hologram design:** Adapted from our publication [185]. (a,b) Beams A and B are formed by the combination of the target complex field and separate linear tilt gratings, with an added corrective phase (c,d) using the method in section 4.4.2. The resultant hologram (e) is displayed on SLM1 to form a pair of modes in the +1 order ready for orthogonalisation. Figure 4.10 details the geometry that allows SLM2 to require only a simple linear grating (f) to both compensate for the chromatic dispersion and recombine the beams at the PBS.

The argument for the dispersion-compensating hologram on SLM2 is presented in figure 4.10: by considering the geometry of the chosen tilt angles of beams A (blue) and B (red) from the first SLM, it can be shown that the appropriate tilts required to redirect them both back onto the original zero order (green) axis can be achieved with the same single grating, rather than a combination of two different tilts. This













Beam operation	Beam A (H)	Beam B (V)	Beam operation	Beam A (H)	Beam B (V)
<b>1</b> In FP of SLM1 SLM1(Xcyc, Ycyc)	 (50, 50)	 (-50, 50)	<b>5</b> After M3,4 Lat. flip		
<b>2</b> After PBS Lateral flip for Hz			Net correction: From <b>5</b> to <b>1</b>		
<b>3</b> After M2,5 Lat. flip			Correction needed	Flip in V	Flip in H,V
<b>4</b> After Lenses F4,F5 Lat. & Long. flip			SLM1	(50, 50)	(-50, 50)
			Inverse SLM1	(-50,-50)	(50,-50)
			SLM2 (after Correction)	(-50,50) ←	(-50,50)

FIGURE 4.10: **SLM2 hologram argument:** A stepped explanation of the simple linear grating on SLM2, in spite of the opposing tilts on SLM1. By tracking the horizontal and vertical rotations performed by each component in the Sagnac interferometer, it is evident that an additional lateral flip of beam A leads to each beam requiring different sign changes for an exactly inverse grating: The tilted position of the beams (written here as number of phase cycles in each axis), after SLM1 (step 1) undergo various rotations with respect to the zero order position (green) through steps 2-5. In order to return the beam positions to step 1, the anticipated inverse of SLM1 must undergo a sign change of the vertical tilt for beam A (blue) and a vertical and horizontal tilt for beam B (red). This conveniently leads beam A and B to require the same tilt when inverting the grating of SLM1 to steer the beams back towards the axis of zero dispersion.

is only possible because the two beam paths towards SLM2 are not equivalent – beam B undergoes an additional lateral flip compared to beam A, by reflection off the PBS. This fortuitous discovery increases the final efficiency of generated vector beams. The phase tilts on SLM1 to create beams A and B (and shown in figure 4.9(a,b)) are defined as:

$$\phi_{A,\text{tilt}}(u, v) = \frac{2\pi}{\lambda_0 f_3}(ux + vy), \quad (4.5)$$

$$\phi_{B,\text{tilt}}(u, v) = \frac{2\pi}{\lambda_0 f_3}(-ux + vy). \quad (4.6)$$

As introduced earlier,  $\lambda_0$  is the central design wavelength of the broadband light source. The resulting +1 order is then located in the Fourier plane at the Cartesian

co-ordinates  $(x, y)$  and  $(-x, y)$  for beams A and B respectively. In these co-ordinates the zero order position is found at the origin, and  $f_3$  is simply the focal length of the Fourier lens F3. By using these co-ordinates for the phase tilts of A and B, both beams are then simultaneously diffracted back into the zero order position by a single grating on SLM2, defined as:

$$\phi_{\text{SLM2}}(u, v) = \frac{2\pi}{\lambda_0 f_3}(-ux - vy). \quad (4.7)$$

An example of the 8-bit greyscale holograms sent to SLM1 and SLM2 for the generation of dispersion-free radially polarised vector vortex beams is given by figure 4.9(e,f). Parts (c,d) show the phase correction maps used for beams A and B respectively, which is discussed further in section 4.4.2.

#### 4.4.1 Lookup table

LC-SLMs are calibrated for general use around  $\lambda_0$  – for complex beam modulation, control over the mapping of phase to greyscale across the hologram is another degree of optimisation. There are more elaborate methods to optimise the phase response of the device [199], however it is sufficient in this context to consider only the following: by choosing a set of 2D mapping co-ordinates as seen in figure 4.11, a continuous spline interpolation may be used to map the phase between a greyscale bit depth of  $[0 : 255]$ . Adjusting the shape of the spline amounts to adjusting the power sent to each of the diffraction orders which is key for +1 order efficiency.

#### 4.4.2 In situ wavefront correction

In an ideal scenario, the SLMs would be initially optically flat; all transmissive and reflective optical components would exactly relay the target amplitude and phase, and all components (including the detector) would be placed in the correct planes with no human error. In the absence of these conditions, we must correct real-world aberrations: these include any imperfections or dirt in the optics used, a departure from optical flatness in the LC-SLM pixel profile, and instances of beam defocus along the optic axis (particularly at the camera plane).

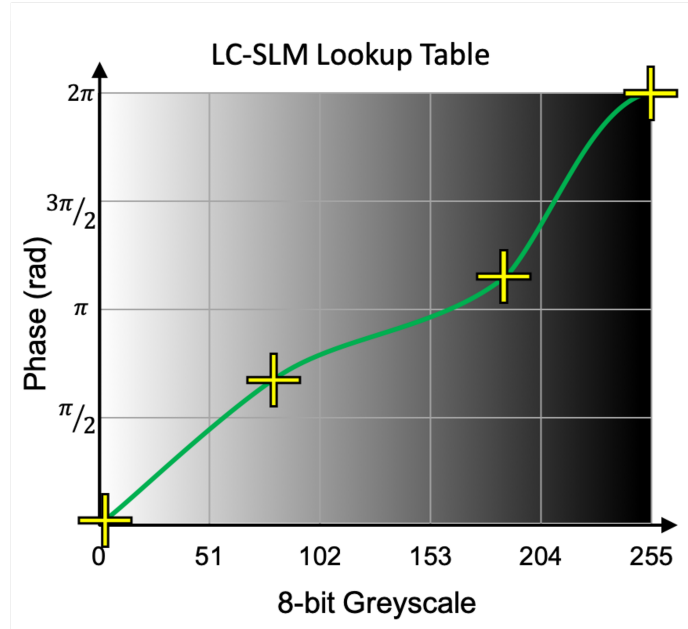


FIGURE 4.11: **LC-SLM Lookup table:** Commercial LC-SLMs are calibrated to perform in a specific diffractive regime with some central wavelength. One can adjust the mapping of the hologram phase to the 8-bit grey-scale that makes up the dynamic range of the modulator; this can be used to alter the efficiency of the complex beam shaping depending on the application. For example, to adjust the power into the zero/first orders.

Fortunately, such measures can be implemented using *wavefront correction*. One such example, presented by Čižmár *et al.* (2010) [200] uses orthogonal mode decomposition to determine the additional phase corrections that must be applied to every location on the wavefront – such that each location constructively interferes at a single diffraction limited spot in the camera plane.

By the theory of orthogonal mode decomposition, upon propagating, an optical field may be considered as being composed of orthogonal modes of some arbitrary basis. Whilst these orthogonal modes may be focused towards a common position in 3D space, full constructive interference between modes can only be achieved when phase aberrations are also taken into account. The technique is presented in figure 4.12(a,b), whereby a simple tilt hologram is encoded onto the modulator. [200] then uses the modes defined by the segmentation of the modulator array ( $512 \times 512$  for the Boulder Nonlinear Systems LC-SLM) into independent superpixels of equal dimension  $n$ , i.e. an orthogonal mode set of dimension  $\frac{512}{n} \times \frac{512}{n}$ .

The aim of the technique presented in [200] is to determine the phase correction required by each mode in the basis such that they will focus to the same 3D position

with the same phase. A central mode is selected as the reference, which is displayed throughout and whose phase remains fixed. For a given superpixel probe position, that superpixel and the reference superpixel alone are activated using a binary amplitude mask (figure 4.12(b)); by placing a camera in the FP of the modulator, we can then measure an interferogram in the +1 order position (figure 4.12(c)).

Next, a location within the interferogram on the camera was chosen as the pixel readout for the single measuring signal – the optimal readout pixel was determined by temporarily using the full grating and using the location of the +1 order. This prevented any unnecessary corrections – a readout pixel anywhere else in the FP would result in a correction map with an unnecessary linear phase tilt.

The following process was used to characterise an aberrated beam: for each probe superpixel position, the phase across the superpixel was shifted in increments of  $2\pi/m$  where  $m = 10$ , such that an entire  $2\pi$  phase cycle was scanned at a rate  $\nu$ . At each increment, the intensity at the pixel readout location at the centre of the interferogram was read, which results in an intensity signal defined by:

$$I(t) \propto |E_p|^2 + |E_r|^2 + 2|E_p||E_r|\cos(\psi_p - \psi_r + \nu t). \quad (4.8)$$

Here, the field of the probe and reference modes are  $E_{p,r}$  and their phases  $\psi_{p,r}$  respectively. Through all  $m$  phase increments, this resulted in a 1D periodic curve of intensity recorded by the camera. Since  $\cos(0) = 1$ , the harmonic cosine term in the above equation is maximal when the argument satisfies  $0 = \psi_p - \psi_r + \nu t$ , which implies that for optimal constructive interference between the probe and reference modes,  $\psi_p = \psi_r$  which is achieved when the probe mode receives an additional phase correction of  $\nu t$  [200]. These terms were recovered by performing an FT on the 1D array above. This procedure was repeated for every superpixel mode in the modulator array, before the individual phase corrections  $\nu t$  for each mode were combined within their superpixel locations to form a phase correction map. For the chosen linear diffraction grating this map will focus all modes down to the same point in phase, with only additive energy such that an optimal diffraction limited spot is formed.

The technique was applied to both the DMD holograms in figure 3.11 and SLM1 as depicted in figure 4.9(c,d); beams A and B were corrected individually for the same readout pixel location. To demonstrate both defocus and higher order corrections, the following examples are provided: firstly, a diffraction-limited spot is shown in

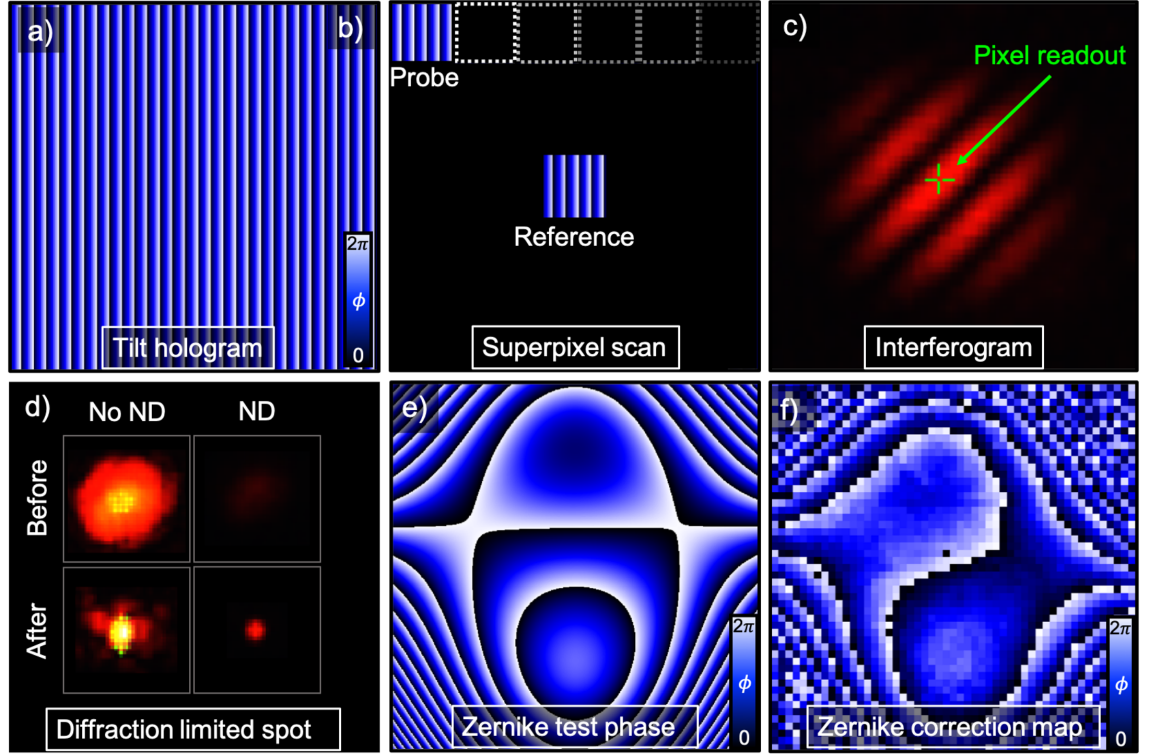


FIGURE 4.12: **In-situ wavefront correction:** The fundamentals of in situ wavefront correction, following the work presented in [200]. The target tilt hologram (a) is masked to show a reference superpixel and a probe superpixel (b) which raster scans the entire hologram. For each position of the probe, the two superpixels create an interferogram (c) – the probe superpixel scans a full cycle of phase, and records the phase value which returns the highest intensity. The full set of these phase values forms a 2D phase correction map, which can be applied to the original hologram tilt to optimally focus light into a single mode (d). (e,f) demonstrates that the correction can detect deliberately added higher order aberrations such as this combination of Zernike modes.

figure 4.12(d) filtered with and without a  $1000\times$  ND filter. Before correction, the beam is misshapen and its energy spread over a large area. After the correction phase is measured and applied, the beam is focused down into a spot. In a further test, a Gaussian mode was preloaded with a known aberration: a superposition of Zernike modes provided an asymmetric field with low and high frequency regions (figure 4.12(e)). The resulting correction (f) resolves an approximation of the aberration, albeit with less accuracy in the high frequency regions when the fringe spacing matched the superpixel resolution.

There are a few intricacies to mention for this procedure: firstly, there is a practical limit to the resolution of the phase map retrieved. For the LC-SLM used, a resolution  $\frac{512}{n} \times \frac{512}{n}$  with  $n = 10$  uses only 0.08% of the SLM during each measurement – the

smaller the superpixels, the larger the interferogram produced, and the lower the intensity per unit area. Thus at around  $n = 8$  the +1 order interferogram is at risk of being washed out by the zero order granular effect depicted in figure 4.3(a).

## 4.5 Broadband vector beams: results

The aim of this investigation was to present broadband vector beams with near-arbitrary polarisation control, which emulate the functionality of the beams presented in chapter 3, but usable across at least 100 nm. Using the third stage of the experimental setup, the beam polarisation states were again probed with a QWP and LP in order to generate the Stokes parameters, in accordance with [102, 151], (defined in section 2.2.6). However, in this investigation, the polarisation states should be maintained across the entire bandwidth. In order to determine the practicality of this, four wavelengths spanning 100 nm were selected for individual Stokes measurements using the following set of bandpass filters:  $555.6 \pm 4.05$  nm,  $589 \pm 5$  nm,  $635 \pm 3.5$  nm and  $655.6 \pm 6.05$  nm.

Firstly, beams A and B as Gaussian beams were combined to form beams of uniform polarisation: shown in figure 4.13 are two experimental beams, exhibiting  $45^\circ$  linear and circular polarisations across the beam profile. Note that the polarisation maps presented have been rendered with colours to match their measured wavelength. The ellipse parameters were chosen such that the semi-major axis  $\geq 0$ , whilst the inset intensity profiles ( $S_0$ ) were used as a transparency mask to convey the actual intensity across the polarisation map.

The results for  $45^\circ$  linear beams (a)-(d) show excellent uniformity with identical orientations, and a strong Gaussian profile. For the circularly polarised case (e)-(h), the beams are less accurately polarised, resembling a more elliptical polarisation state – note that in spite of careful alignment throughout the system, there remained a hidden misalignment which manifested as a shift in the relative amplitude and phase with wavelength. As such, it was only possible to generate a very accurate polarisation field in one of the four bands with any one alignment; the beams were ultimately aligned at the central wavelength  $\sim 605$  nm.

Figure 4.14 compares the ellipticity and orientation of the uniformly polarised beams from section 3.7.1 with the results achieved in this broadband setup. It is clear that the accuracy of these parameters varies with wavelength. For linear  $45^\circ$  beams (shown in a,b),  $(|P_{maj}/P_{min}|, \theta)$  values range from  $(0.048 - 0.16, 39.8 - 44.5)$ ; for circularly polarised beams (c), the ellipticity was found to be  $(0.65 - 0.77)$ . In terms of ellipticity, the 555 nm filtered beams far outperform the remaining bandwidth, on a par with the DMD vector modes (see section 3.7.5). As expected, any deviation

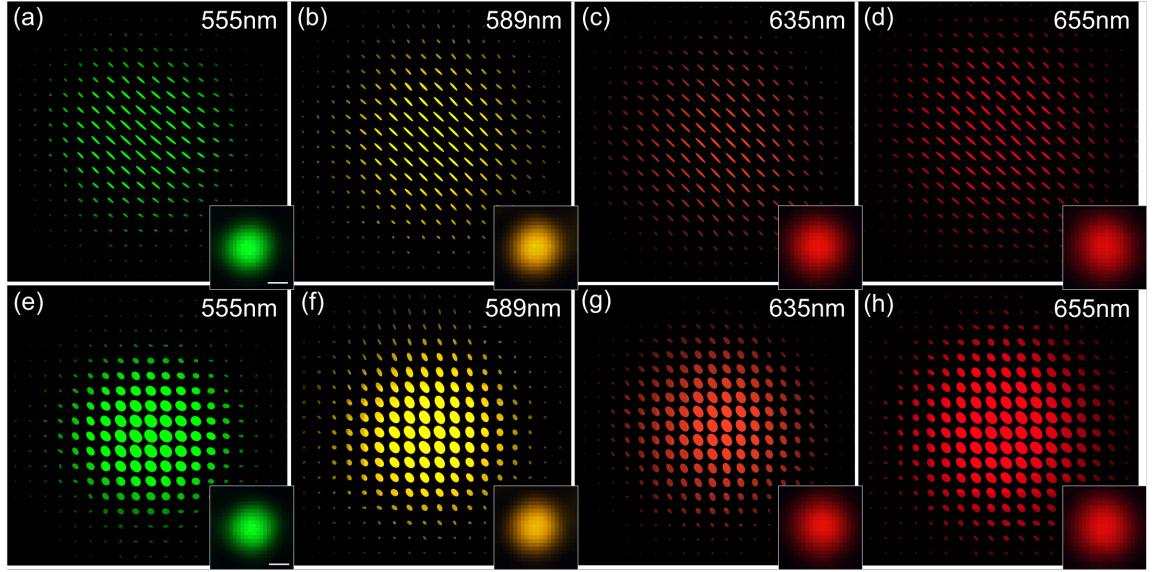


FIGURE 4.13: **Experimental vector beams of uniform polarisation:** From our publication, [185]. For each waveband, the Stokes measurements were recorded using a LP, QWP and bandpass filter before the CCD. When beams A and B are Gaussian with zero relative phase, the orthogonal polarisation components combine to produce linear  $45^\circ$  beams (a-d). When the phase difference is  $\pi/2$ , these beams tend towards circular polarisation. Each image is a polarisation map where each pixel in the raw CCD image (inset) is used to form a polarisation ellipse. A  $30\ \mu\text{m}$  scale bar is shown in (a) and (e).

from  $\lambda_0$  results in a shift in accuracy, however this shift is a positive one in ellipticity and negative in orientation.

Secondly, I present the generation of radially and azimuthally polarised vector vortex beams across a 100 nm bandwidth, shown in figure 4.15. The orientation, linearity and intensity of each beam shows a strong agreement with the simulated beam profile sent to SLM1. Note that the average radius of these vector beams increases with the waveband measured; this is due to the desired beams being imaged in the FP of SLM1, where the size of the object scales with the wavelength. For vector vortex beams, the relationship of the amplitude and phase components of beams A and B is exceptionally important. As such, any departure from ideal HG modes of purely orthogonal polarisation results in ‘lobeness’ – regions of the vortex beam which appear more elliptical than the target linear polarisations.

To illustrate the compensation achieved by using dual SLMs, the Fourier planes of both SLM1 and SLM2 were captured using a DSLR camera and CCD respectively, as shown in figure 4.16. In part (a) we see that each of the diffracted orders are dispersed

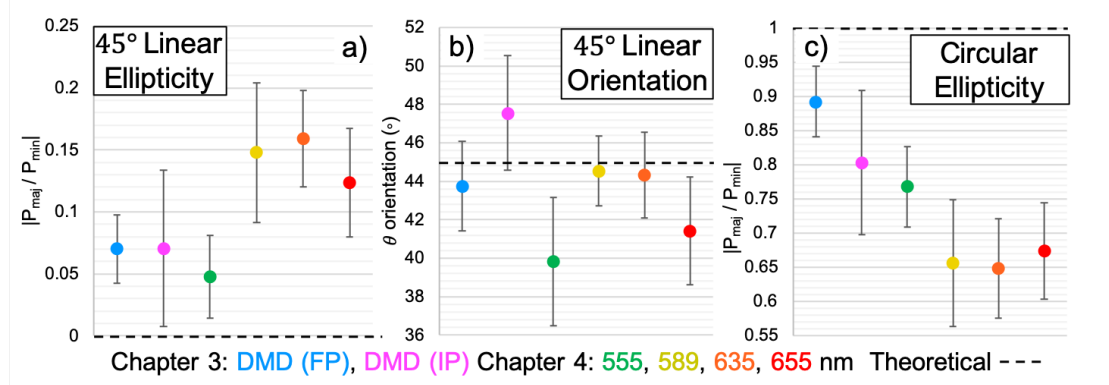


FIGURE 4.14: **Ellipticity and orientation of uniform beams:** Each polarisation ellipse map was made from 2D arrays of  $(P_{maj}, P_{min}, \theta, h)$ . We can use the average of  $(|P_{maj}/P_{min}|, \theta)$  across the beams to quantify the accuracy. Each array was thresholded at the full width half maximum of  $P_{maj}$  to avoid contributions from background regions with reduced beam intensity. The DMD vector beam results (blue, magenta) are included for reference.

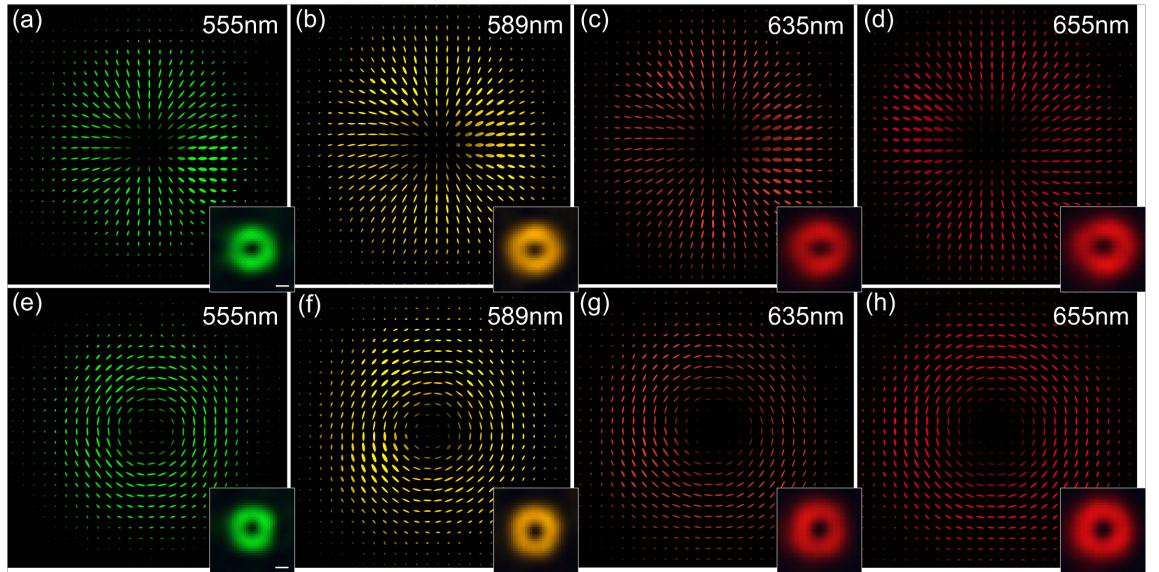


FIGURE 4.15: **Experimentally generated broadband radial and azimuthally polarised vector beams:** From our publication, [185]. By loading beam A and B with combinations of  $HG_{1,0}$  and  $HG_{0,1}$  and carefully weighted relative global amplitude and phases, the beams interfere to form vector vortex beams – specifically with radial (top row) and azimuthally (bottom row) polarised profiles. Inset of each polarisation ellipse map is the raw CCD image with no LP or QWP. A 30  $\mu m$  scale bar is shown in (a) and (e).

along the axis from the zero order, with the rate of dispersion angle increasing with order number. In the FP of SLM2 (b), all but the +1 order has been filtered out, and these beams become the new zero orders on SLM2; the secondary +1 beams born from these are diffracted onto a common axis as a dispersion-free vector vortex beam.

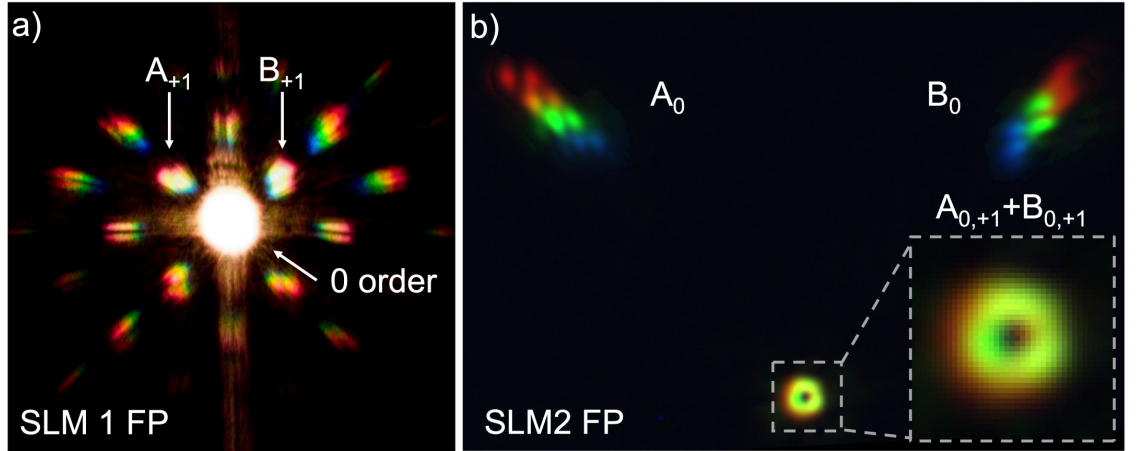


FIGURE 4.16: **Fourier planes:** (a) The FP of SLM1, taken with a DSLR, demonstrates the white light dispersion from a DOE. (b) The resultant CCD image of the FP of SLM2 with APT2 removed. The +1 orders from the SLM1 FP become zero orders reflected from SLM2, and the new diffracted +1 orders recombine in the same approximate transverse position as the original zero order – now dispersion-free.

Next, the generation of broadband “lemon” and “star” Poincaré beams is shown in figure 4.17. In general, the polarisation states achievable span most of the Poincaré sphere (section 2.2.5)[162, 182]. As was the case in figure 4.15, the beam waists scale with wavelength. Given that the Poincaré beams feature a radial transition of handedness, this is depicted as a transition from red (left) to blue (right). The inaccuracies in this vector beam manifest as non-linear states in the ring around the centre, as well as slight asymmetries in the handedness. The intensity profile of the inset CCD images resemble an aberrated Gaussian, due to the imperfections in the beam shape and misalignment that are exacerbated when interfering superpositions of LG beams with this particular setup.

In the second half of section 3.7.5, a method for quantifying the “likeness” of the Stokes measurements was introduced. The same strategy was applied to these equivalent broadband spatially varying vector beams: figure 4.18 presents the Fourier plane beam results. The black triangle data points demarcate the HeNe DMD vector

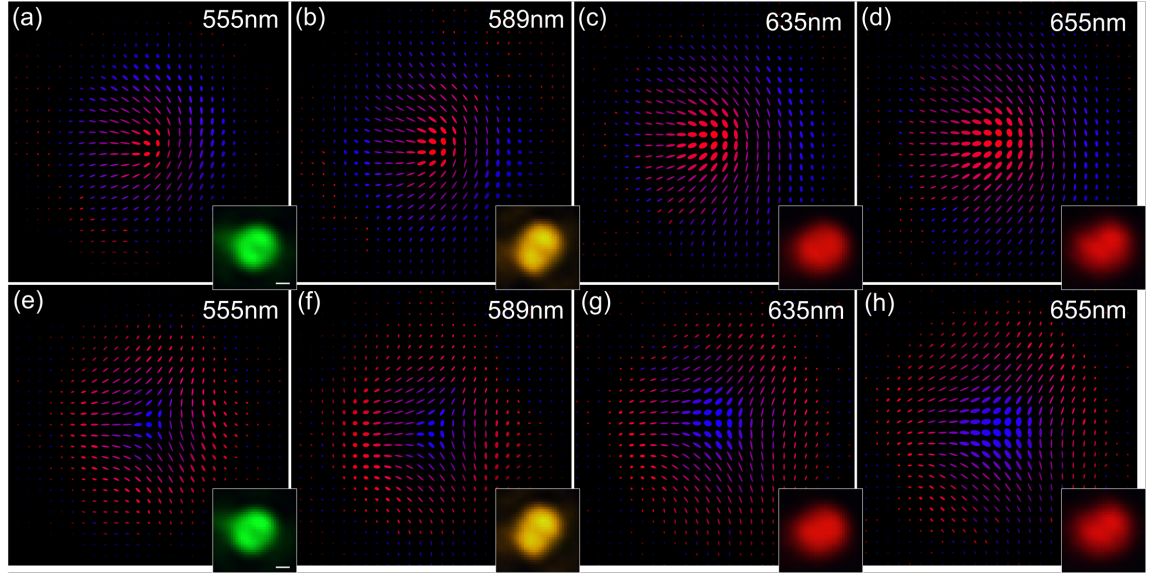


FIGURE 4.17: **Broadband Poincaré beams:** From our publication, [185]. Combinations of  $LG_{1,0}$  and  $LG_{0,0}$  combine to form the ‘lemon’ and ‘star’ Poincaré beams, whose polarisation states span virtually all of the Poincaré sphere. Here the polarisation handedness is shown as a gradient from red (left) to blue (right). Inset of each polarisation ellipse map is the raw CCD image with no LP or QWP.

A  $30\ \mu\text{m}$  scale bar is shown in (a) and (e).

beams from section 3.7.2; the remaining points are colour-matched with their respective filter. Whilst this is not a complete analysis, it indicates the relative quality in the two beam shaping methods, when also considering the different regimes used (monochromatic vs broadband).

Recall that for DMD radial and azimuthal beams (figure 4.18(a,b)), the raw beam likeness deviation and average across the measurements ( $L_{d,0}, L_{d,avg}$ ) was ( $< 0.01, 0.02$ ). In figure 4.18(a,b), we find a likeness deviation of ( $< 0.01 - 0.062, 0.03 - 0.085$ ) accounting for the 4 filter bandwidths across 100 nm. This suggests that  $L_{d,0}$  can be up to  $6\times$  worse to recreate the theoretical beam profile, whilst the average deviation  $L_{d,avg}$  is  $4\times$  worse. This sounds ominous, but amounts to full pixel deviations of (6%, 8%) from the theoretical, as opposed to the DMD case (1%, 2%) (when  $L_d = 0.01$  corresponds to 1% deviation).

In the case of DMD Poincaré beams (c,d), these same parameters ( $L_{d,0}, L_{d,avg}$ ) were found to be ( $0.017 - 0.035, 0.02$ ); in the broadband case we find that across the bandwidths measured, ( $0.01 - 0.16, 0.06 - 0.1$ ). This amounts to full pixel deviations of (3.5%, 2%) for the DMD experiment and (1.6%, 10%) in this broadband case. Clearly, the  $I_0$  Stokes images of each Poincaré beam is a strong match for the theory,

which is expected given its Gaussian profile. However, the deviations arise when recording the remaining Stokes measurements, which expose a difficulty in matching the theory. Recall that this was apparent in the Poincaré results of chapter 3 when compared to the vector vortex beams; in this case, the issues are magnified when using  $\lambda \neq \lambda_0$ .

Figure 4.19 presents a selection of vector beam superpositions to showcase the potential of the setup. The first and second columns show beams A and B on the CCD in the absence of APT2 – these are the chromatically dispersed beams of the SLM1 +1 order which become reflected zero orders from SLM2. As expected the dispersion of these beams is in the direction of the tilt hologram acting on each mode. The final column “A+B” is the compensated vector beam, where the diffracted progeny from beams A and B overlap along the zero dispersion axis (as in figure 4.16).

Parts 4.19(a)-(c) are comprised of lower order HG mode combinations, notably beams with/without a central optical vortex and the same  $\text{HG}_{4,3} + \text{HG}_{3,4}$  beam presented previously in figure 3.19. Also included is a superposition of  $\text{HG}_{10,9}$  and  $\text{HG}_{9,10}$  which exhibits a grid of many roughly defined vortices.

Figure 4.20 is included to demonstrate the challenges in extending the system (in its ultimate alignment) to capturing the image plane of the SLMs – here an amplitude mask of the letters “UoG” was applied to three regions of phase to produce a different polarisation within each letter when using the 635 nm filter ( $45^\circ$ , circular,  $-45^\circ$  polarisations). This test failed in part due to the aberrations and alignment which affected our ability to interfere beam A and B as successfully as the mode basis profiles, as well as spatial filtering of non-circular objects.

### 4.5.1 Coherence time of broadband vector beams

Given the vector beams presented are demonstrated to span at least  $\Delta\lambda = 100$  nm (centred on  $\lambda_0 = 605$  nm), we can approximate the coherence time  $\tau_c$ , the temporal length of the pulse used in ultrafast photonics. Using the equation from section 2.1.4 the coherence time is found to be  $\tau_c \sim 6$  fs. This length of pulse is applicable to the various ultrafast beam shaping examples given in section 1.3.6 which use the dispersion compensation methods described in section 4.1.

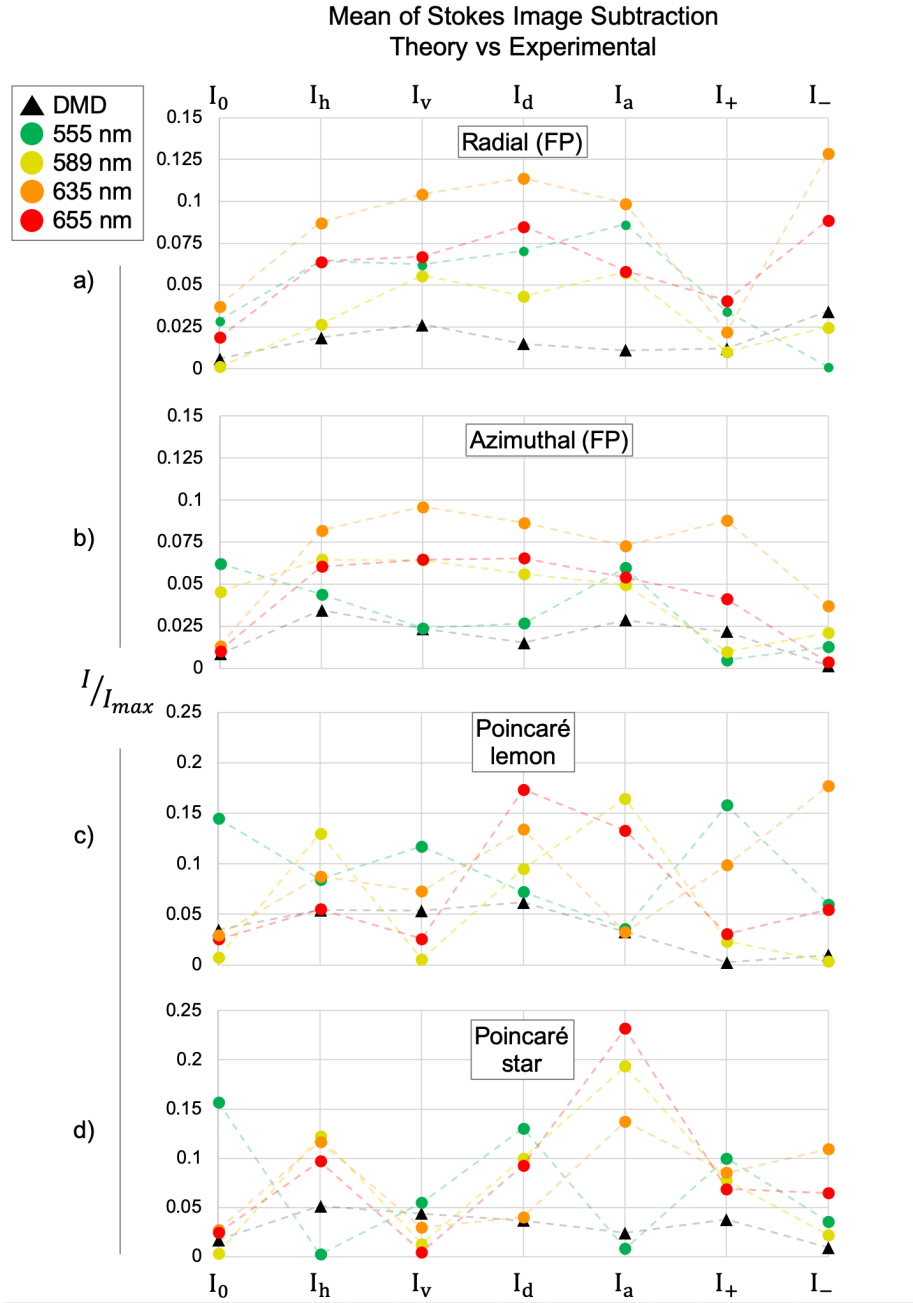


FIGURE 4.18: **Image subtraction in broadband vector beams:** As a continuation from figure 3.20, the likeness deviation from the theory (vertical) is plotted against the Stokes measurement (horizontal). The first column shows the raw beam intensity likeness deviation  $L_{d,0}$ , when no polariser is used-  $L_{d,avg}$  is then the average of all columns. The black triangle data points demarcate the associated DMD vector beam result from chapter 3.

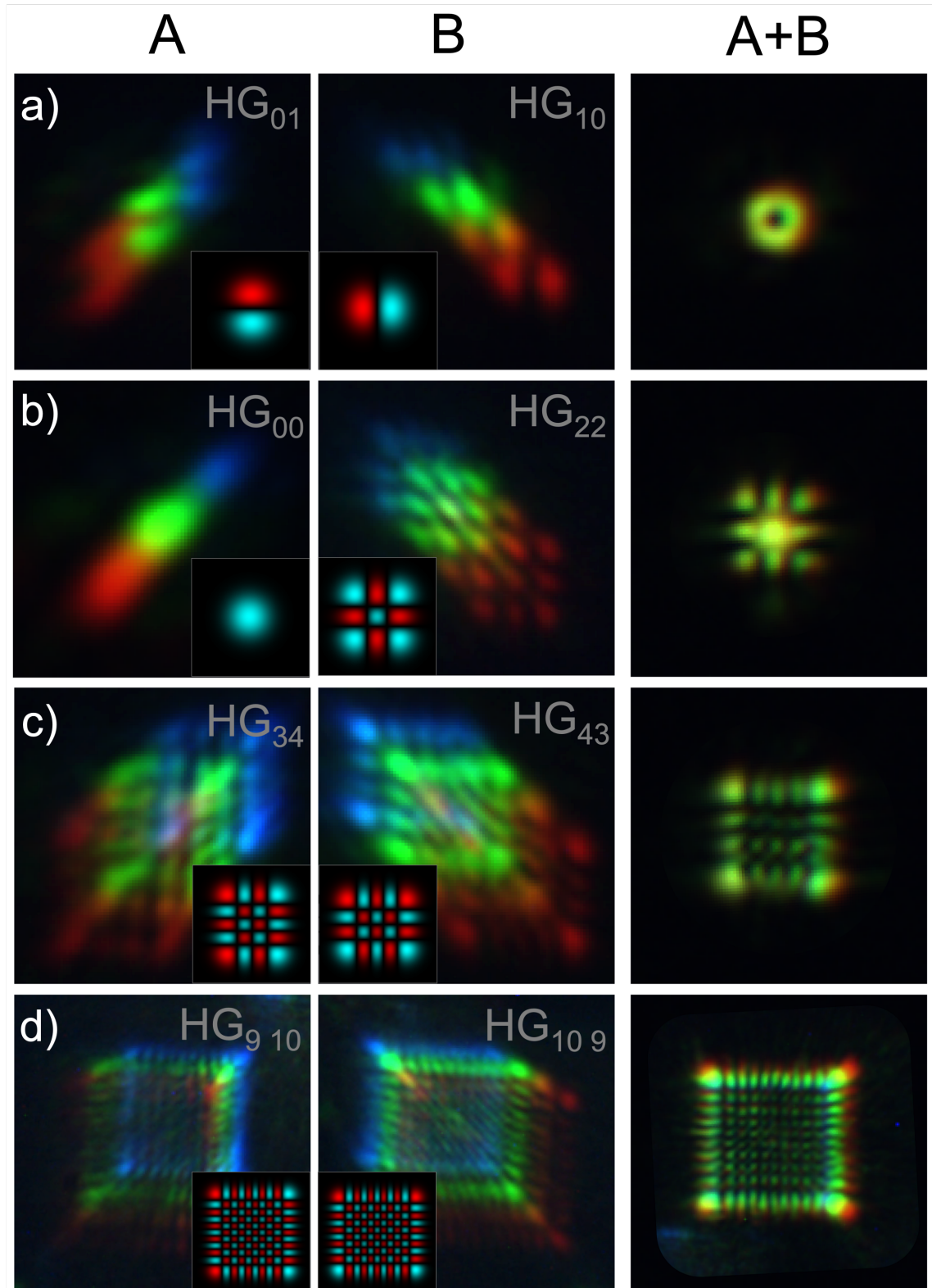


FIGURE 4.19: **Higher order vector beams:** Removal of APT2 allows the comparison of the diffracted orders of beam A and B from SLM1 and the combined A+B beam from SLM2. Due to the tilt hologram on SLM2 being the effective inverse of SLM1, the beams are dispersed in the opposite direction, which aligns all wavelengths to a significant accuracy. Inset are the theoretical HG mode orders, where areas of red are  $\pi$  out of phase from the blue areas.

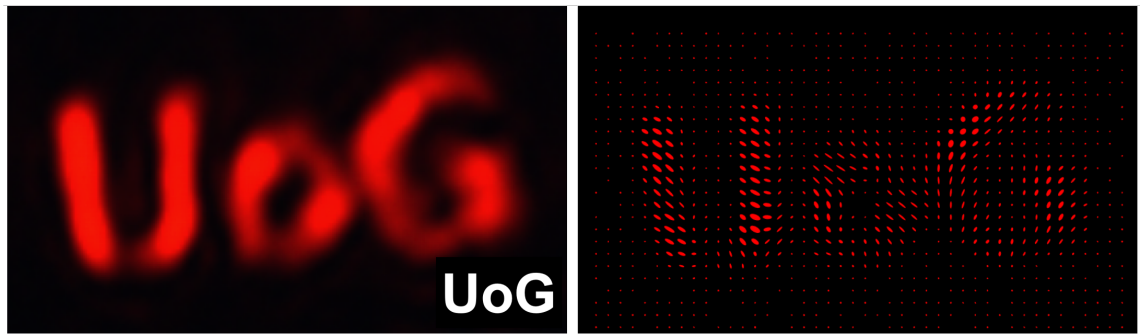


FIGURE 4.20: **Image plane test:** By placing an aperture in the FP of SLM1, the unwanted orders can be spatially filtered out such that the target complex field appears in the image plane. The phase of the tilt accompanying each of the letters in a binary amplitude mask was adjusted to produce ( $45^\circ$ , circular,  $-45^\circ$ ) polarisations in the U, O and G respectively. Residual misalignments in the system led to the combination of beams A and B failing to accurately produce the intended polarisations.

## 4.6 Broadband vector beams: discussion and conclusion

In order to gauge the success and viability of this investigation for future research and application, it is important to highlight the areas in which these results can be improved upon, and differentiate between those which are unavoidable due to the physics involved.

### 4.6.1 Evaluating the setup and design

The successful generation of vector beams with spatially varying polarisation is largely dependent on the intricacies of beam modulation and its ability to provide the optimum fidelity and efficiency; once this notion is compounded by using quasi-monochromatic bandwidths, great care must be taken to account for the numerous contributing factors.

Firstly, the complex modulation at SLM1 assumes that the incident beam has an approximately flat phase Gaussian profile; the incident beam is in fact coupled out from a polarisation-maintaining (PM) single mode fibre with an output coupler lens and expanded with a telescope with some Gaussian-like profile. Any discrepancy of assumed versus actual beam amplitude results in a drop in efficiency, and is due to the

fact that LC-SLMs are inherently phase-only modulators, and are lossy in amplitude shaping. This effect occurs across all wavelengths, and its impact on efficiency is dependent on the specific shaping chosen [154]. It is clear that this is one of the major contributors of inefficiency in this design, particularly with two LC-SLMs in tandem. In the case of a radially polarised vector beam, this effect would in theory limit the generation efficiency to  $\sim 30\%$ .

Another factor to consider when evaluating the efficiency of the optical setup is the wavelength rating of the various optics throughout the system – for instance, the phase retardance of the HWP and the transmission:reflection ratio of the BS used were wavelength dependent, and only some of these components were achromatic. Furthermore, an oversight was made in emulating [197] with the use of a 50:50 NPBS to pass out the combined vector beam from the Sagnac interferometer. This double-pass results in an unnecessary 75% loss in beam power. Since the incoming beams A,B and the outgoing vector beam are spatially separated by a few millimetres, a knife-edge mirror could still be used in place of the NPBS to prevent this loss in efficiency.

As this investigation was a proof of concept, the use of dynamically controlled commercial modulators was critical to discover the nature of dual SLM diffraction; in future, however, the single phase tilt on SLM2 may be replaced with a specially made DOE for even greater efficiency.

### 4.6.2 Operational bandwidth

The bandwidth of the SC output was chosen to match the specification of the optical components and the LC-SLMs themselves. Both SLM1 and SLM2 used anti-reflection coatings optimised for 635 nm. The bandwidth was also constrained by the stability of the system – any vibrations which cause the OPL of beams A and B to differ by more than the coherence length of the broadband source will result in a loss of coherence between beams A and B, and the combined polarisation state will not be tunable. Passing both beams around the same optics in a Sagnac configuration aids this as environmental vibrations affecting the optical table should be common for the entire system.

The experimental results detailing the various vector beam polarisation maps shows a satisfactory agreement with the target beams used in the holograms of SLM1, across the entire bandwidth tested. For the uniform polarisation beams,  $(|\frac{P_{maj}}{P_{min}}|, \theta)$  parameter values of  $(0.048 - 0.16, 39.8 - 44.5)$  were obtained for linear  $45^\circ$  beams, whilst  $|\frac{P_{maj}}{P_{min}}| : 0.65 - 0.77$  was found for circular beams. This clearly falls short of the accuracy obtained in the simpler (monochrome) DMD vector beam setup:  $(0.07 \pm 0.03, 43.74 \pm 2.3)$  and  $(0.89 \pm 0.05)$  respectively for the two polarisations.

The spatially varying vector beams, radial, azimuthal and Poincaré, were quantified by image subtraction in section 4.5. It was determined that the likeness deviation factor  $L_d$  was in general  $5\times$  worse in this case than in the previous monochromatic setup, with  $L_{d,avg}$  values indicating a maximum 8% and 10% deviation for vortex and Poincaré beams. This is equivalent to e.g. 10% of all pixels in the measurement image displaying a maximally inaccurate intensity; that this is also wavelength dependent underlines the importance of characterising the chromatic variations in beam shaping with the LC-SLMs.

It is speculated that the true limiting factor of polarisation accuracy was down to uncorrected opto-mechanical misalignments and aberrations which were present even after an attempt at wavefront correction on SLM1 for the central wavelength [200]. Whether it be from deviations in the angle of incidence or defocus, departure from the target beams resulted in local deviations in the polarisation ellipticity and orientation.

### 4.6.3 On correcting the angular dispersion

While using such a large bandwidth, it was prudent to use the central wavelength,  $(\lambda_0)$  of the incident beam when encoding the wavelength-dependent holograms. One must also then consider the effect this has on the remaining wavelengths in the beam. Some of these bandwidth effects can be compensated, whilst others will always work to reduce the efficiency. The primary source of wavelength dependent deformations in the beams diffracted from SLM1 is the chromatic dispersion which breaks up the incident broadband beam wavelengths by angle from the SLM. This angle  $\theta_m(\lambda)$  is defined by the grating equation 2.14,  $\theta_m(\lambda) = \sin^{-1}(m\lambda/d)$ , defining the diffraction angle for mode order  $m$ , where  $d$  is the grating period of the displayed grating. This is the angular dispersion which is corrected for with the introduction of SLM2 in the image plane of SLM1.

#### 4.6.4 Non-correctable wavelength dependence

The generated holograms (and their wavefront corrections) are tailored for a single wavelength,  $\lambda_0$ . This can be understood based on the LC-SLM geometric optics – the phase change in each pixel location  $\Delta\phi$  may be defined as  $\Delta\phi = \Delta\text{OPL}/\lambda$ . Here,  $\text{OPL} = (\text{Length through LC}) * n_{LC}$ , where  $n_{LC}$  is the crystal refractive index. On the assumption that the material dispersion is negligible, the components of the incident broadband beam of wavelength  $\lambda_0$  will interact with the correct phase hologram; however, the neighbouring wavelengths within the bandwidth will instead interact with a phase hologram which has been scaled by  $\lambda_0/\lambda$ .

Recall how phase-only LC-SLMs use pixel-by-pixel contrast to modulate the amplitude – as such, these remaining wavelengths interact with a grating displaying an incorrect contrast across the hologram. The effect, discussed further in the conclusion of our publication [185], was found to have minimal impact on the efficiency and fidelity of the beams simulated. Whilst this is not correctable, it was certainly not the limiting factor in the accuracy of the vector beams generated.

In summary, I have demonstrated a technique for generating dynamically reconfigurable broadband vector beams over a bandwidth of 100 nm, which corresponds to a coherence time of  $\sim 6$  fs. This optical design applies the recognised dispersion compensation methods of the field and combines a pair of LC-SLMs in an intricate Sagnac interferometer arrangement. This shared path design gives the optical setup added stability from environmental influence, and when coupled with 8-bit amplitude and phase modulation control, is very tolerant of slight misalignments. This design can be made more efficient and compact, which will further emphasise its appeal for applications in white-light and ultrafast beam shaping.

# Chapter 5

## Group velocity delay of structured light: Bessel beams

### 5.1 Structured light delay: introduction

The following chapter presents my own work, which aims to use the beam shaping skills and techniques acquired from the previous investigations to explore one more fundamental property of light – *velocity*. This chapter looks to verify the characteristics of group velocity delay in Bessel beams, once reported by (former colleagues of the University of Glasgow) Giovannini *et al.* (2015) [201]. The system presented in this chapter is a classical interpretation of a quantum correlation experiment, which uses a combined fibre and airspace interferometer to measure the delay between a Bessel beam and a collimated Gaussian beam. The project was led by my supervisor, Prof. Miles Padgett, with further supervision from Dr. Daan Stellinga. The experimental procedures, hologram design, testing and data acquisition were all performed by myself, with the subsequent data analysis a collaboration between myself and Dr. Stellinga.

The speed at which light propagates and the means to retard it have long been topics of interest within the research community. [10] explains that in the 17th century, Huygens became the first to recognise the apparent slowing of a light beam when propagating through a medium which is more dense than air, now established as the refractive index  $n$  such that  $v = c/n$ . Much later, Jean Bernard Léon Foucault (1819–1868) first quantified the slowing of light through water. Meanwhile, James

Clerk Maxwell (1831–1879) and his theoretical formalism of electromagnetism showed that the electric field could permeate as a transverse wave in the aether with a speed represented in terms of measurable quantities, namely the permittivity  $\epsilon_0$  and permeability  $\mu_0$  in a vacuum. Thus the speed of light in a vacuum was defined as

$$c = \frac{1}{\sqrt{\epsilon_0 \mu_0}} \quad (5.1)$$

Light is understood to be self-sustaining transverse waves of an electromagnetic field [10]. In the present day we refer to the speed of light as postulated by Albert Einstein – “that light is always propagated in empty space with a definite velocity  $c$  which is independent of the state of motion of the emitting body” [202].

### 5.1.1 Group velocity delay in a medium

In section 2.1.3 the definitions of the phase and group velocity were stated; specifically, in the case of quasi-monochromatic fields, a point of constant phase traverses at the phase velocity  $v_p$ . Furthermore, interfering neighbouring wavelengths form a superposition of harmonic waves, with a  $v_g$  envelope that modulates the average of the oscillation.

To fully appreciate the intricacies involved with light propagation in the real world, we must revisit these concepts. As described by Boyd and Gauthier (2009) [116], the propagation of light through media introduces frequency-dependent dispersions 2.1.6 which alter the beam shape in space and time. The phase velocity  $v_p$  applies to the speed of the wavefronts within the a pulse of, and is defined by  $v_p = c/n$ . A single pulse of light may be considered as the “superposition of an infinite number of monochromatic component waves” which interfere to give the aggregate pulse envelope [116]. On propagation through different media, the velocity of each component wave differs based on the refractive index. Specifically, that the pulse propagates with a group velocity  $v_g = \frac{c}{n_g}$  over sufficiently small distances, where  $n_g = n + \omega \frac{dn}{d\omega}$  is the group index. There are no constraints on this – if the dispersion encountered  $\frac{dn}{d\omega} > 0$ , we may achieve slow light ( $v_g < c$ ); if  $\frac{dn}{d\omega} < 0$ , we achieve fast light ( $v_g > c$ ).

From the above, it follows that  $v_g$  may exceed  $c$ , and there is a fundamental decoupling of the velocity of a pulse  $v_g$  and the velocity of any wavefront component  $v_p$  within the pulse [203]. As mentioned in section 2.1.3, this does not imply faster-than-light travel

that violates causality – for instance,  $v_p$  is the speed at which a point of constant phase moves for some *ideal monochromatic oscillation*. It would therefore need to be infinite in size with a constant amplitude, which rules out the possibility that it could carry information.

Several methods have been used to great effect to probe light propagation: this includes the demonstration of exceptionally low  $v_g$  (e.g.  $\sim 20\text{ms}^{-1}$ ) in non-linear and structured media such as crystals [204–207] and ultra-cold atomic gases [208, 209]. However, these approaches are not the only method for reducing the group velocity  $v_g$ .

### 5.1.2 Group velocity delay in free space

Consider the transmission of a plane wave through a hollow waveguide along direction  $z$ , such as a rectangular cavity. In general, the propagating field incident at some angle will internally reflect down the waveguide boundaries. Within the waveguide, the various propagating modes interfere with one another, creating a transverse standing wave with some lateral structure and, crucially, a transverse component of the wavevector:  $k_\perp$ . The associated phase fronts between incident and reflected wavevectors then also form nodes on the internal surface of the waveguide. In the 2D case, as shown in figure 5.1, the characteristic eigenmode of the waveguide is then the combination of constituent  $k$ -vectors (here  $k_{1,2}$ ), which in this case propagate as plane waves through the waveguide. Considering briefly the single photon case, in order to conserve the total wavevector, either the component along  $z$  must decrease, or the effective wavelength must increase. This leads to an observed increase in phase velocity, and in turn a drop in the group velocity. The consequence of this subtle behaviour is that photons in a vacuum with lateral structure will propagate at speeds less than  $c$  [210].

According to the supplementary material of Giovannini *et al.* (2015) [211], this phenomenon can be accounted for by considering the propagation of an arbitrary field. By integrating to find an effective  $v_g$  over an entire volume in which the velocity is changing, it can be shown that this group velocity with phase profile  $\Phi$ ,

$$v_{g,z} = \left( \frac{\partial^2 \Phi}{\partial z \partial \omega} \right)_{\omega_0}^{-1} \quad (5.2)$$

results in a nonplanar wave packet traversing the volume (from  $z_1$  to  $z_2$ ) in time

$$t = \left[ \frac{\partial}{\partial \omega} (\arg \langle \psi(z, \omega_0) | \psi(z, \omega) \rangle)_{\omega_0} \right]_{z_1}^{z_2}, \quad (5.3)$$

where  $\psi$  is the wavefunction. By use of the Paraxial approximation, the wavefunction  $\psi(x, y, z|k)$  progresses across the volume by  $\frac{\partial \psi}{\partial z} = \frac{i}{2k} \Delta_{\perp} \psi + ik\psi$ , when  $\Delta_{\perp} = (\frac{\partial}{\partial x})^2 + (\frac{\partial}{\partial y})^2$ . Notably, the author defines the term  $\hat{\mathbf{k}}_{\perp} = -i\Delta_{\perp}$  as the quantum mechanical operator of the transverse wavevector, such that  $\langle \hat{\mathbf{k}}_{\perp}^2 \rangle$  describes the mean square of the transverse vector component. Finally, the delay of a nonplanar wavefront may be described as

$$\delta z = -\frac{L}{2k_0^2} \Re \frac{\langle \psi(z_1, k_0) | \Delta_{\perp} | \psi(z_1, k_0) \rangle}{\langle \psi(z_1, k_0) | \psi(z_1, k_0) \rangle} = \frac{L}{2} \frac{\langle \hat{\mathbf{k}}_{\perp}^2 \rangle_{|\psi(z_1, k_0)}}{k_0^2}. \quad (5.4)$$

In the investigations that follow, it is sufficient to consider the simple ray optics model equivalent, however the principle remains the same: without a medium to delay the wavefront, the existence of a real, non-zero transverse wavevector  $\hat{\mathbf{k}}_{\perp}$  results in a reduction of the group velocity.

Let us consider the 3D geometric wave case: a propagating field of wavelength  $\lambda$  and wavenumber  $k_0 = 2\pi/\lambda$  can be decomposed into cartesian axes such that

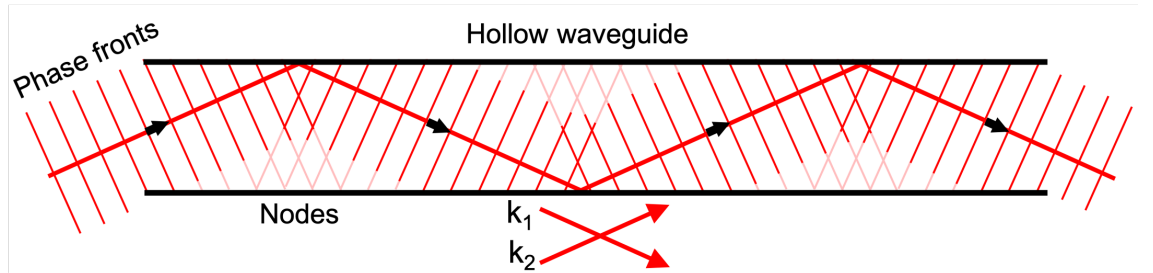


FIGURE 5.1: **Propagation down a hollow waveguide:** The  $\mathbf{k}$  vector directions formed by internal reflection off the boundaries of the waveguide imply non-zero transverse components. These  $\mathbf{k}$  vectors also combine along the boundaries as nodes. This leads to  $k_z < k_0$ , and in turn a decoupled group and phase velocity.

$$k_0^2 = k_x^2 + k_y^2 + k_z^2. \quad (5.5)$$

The practical eigenmodes applicable to this case must be finite in the transverse plane. Following the argument presented in [201]), we can therefore constrain the transverse

components  $k_{x,y} > 0$ . It follows that  $k_z < k_0$ : this component of the wavevector in the direction of propagation is inversely proportional to the phase velocity, indicating that in the  $z$  direction  $v_p > c$  and therefore  $v_g < c$  (based on  $v_p v_g = c^2$ , derived in appendix A). It is critical to note that this reduction of  $v_{g,z}$  is not due to the material composition of the waveguide, but the transverse boundary condition  $k_{x,y} > 0$ , and occurs in free space. This phenomenon is achievable by encoding a light field with structure, which acts to apply the associated boundary conditions, reducing the group velocity by such a degree that it can be readily observed. The delay in  $v_g$  compared to the non-structured field can be significantly larger than the wavelength  $\lambda$ , and so cannot be attributed solely to the Gouy phase shift ( $\pm\pi/2$ ) [212, 213].

In 2015 the work of Giovannini *et al.*, published in Science [201, 211, 214], used a quantum correlation system (Hong-Ou-Mandel interference [215]) to measure the group velocity delay of structured photons – specifically the relative delay between photons from a collimated Gaussian beam and a Bessel/focused beam. Note that this is a valid method because single photons propagate at  $v_g$  [216]. This chapter seeks to verify Bessel beam  $v_g$  delay by implementing this test within a classical interference system.

## 5.2 Structured light delay: theory

The following section introduces the Bessel beam structure to be used in subsequent  $v_g$  delay tests. Furthermore, a novel method to deduce the group delay from the classical interference of quasi-monochromatic light is also presented.

### 5.2.1 Group delay of Bessel beams

There exists a particular solution to the wave equation which is “non-diffracting” – a characteristic lack of divergence over some finite but workable distance. The fundamental *Bessel beam*, as defined by [10], propagates along  $z$  as an electric field which is proportional to the zero order Bessel function  $J_0$  such that

$$\tilde{E}(r, \theta, z, t) \propto J_0(k_y) e^{i(k_z z - \omega t)}, \quad (5.6)$$

in cylindrical co-ordinates. Here the radial wave vector is composed of  $k_y = k_0 \sin \alpha$  and  $k_z = k_0 \cos \alpha$  for some fixed  $\alpha \in [0 : \pi/2]$ . From the Fourier analysis in section 2.4 we may consider a Bessel beam as a field  $\tilde{E}(r, \theta, z, t)$  that can be defined as the superposition of infinite plane waves, whose wave vectors fall on a cone with a physical angle  $2\alpha$ . As a consequence, the intensity

$$I(r, \theta, t) \propto \tilde{E}\tilde{E}^* \propto J_0^2(k_y) \quad (5.7)$$

holds no dependence on the longitudinal position  $z$ , and so the transverse profile of the beam holds as it propagates. In practice, a Bessel beam can be viewed on camera as a “bullseye” – a well-defined central spot with concentric rings, all of which receive the same fraction of the total energy (shown in figure 5.3) [10]. Bessel beams are closely related to the modes associated with a circular waveguide, as demonstrated by their generation using a ring aperture [212, 217].

The primary method of Bessel beam generation is by use of an *axicon* lens – a glass prism with both planar and conical faces [218–220]. These lenses refract light according to Snell’s law:

$$n_{air} \sin(\alpha + \delta) = n_{glass} \sin(\delta). \quad (5.8)$$

Here  $n_{air, glass}$  are the respective refractive indices,  $\delta$  is the physical cone angle and  $\alpha$  is the angle between the resultant beam and optic axis. This lens refracts an incident plane wave into conical phase fronts such that they are all defined by a unique radial component of the wavevector,

$$k_r = \sqrt{k_x^2 + k_y^2} \quad (5.9)$$

This solution amounts to a single value of  $|\mathbf{k}_\perp| = k_r$ , and therefore a definite  $v_p$  and  $v_g$  [221].

As reported by [201], using refractive optics such as wedges, lenses and prisms (figure 5.2) introduces an added complication for the optical path – just 1 cm of glass amounts to  $\sim 10,000 \lambda$ , which must be accounted for. Instead, “zero-thickness” diffractive equivalents displayed on LC-SLMs have been used to impart the same phase on an incident beam, which will reflect and diffract an incident plane wave into diffraction orders [222] – as expected, the desired beams are found in the +1 diffraction order location. In the diffractive regime, the wavevector along the direction of propagation

is defined as  $k_z = k_0 - k_r^2/2k_0$ . This in turn produces the velocity components

$$v_p = c \left( 1 - \frac{k_r^2}{2k_0^2} \right)^{-1} \quad (5.10)$$

$$v_g = c \left( 1 - \frac{k_r^2}{2k_0^2} \right), \quad (5.11)$$

as stated by [201]. The relative shift in the  $v_{p,g}$  of these Bessel beams with respect to plane waves has previously been analysed in [223–226].

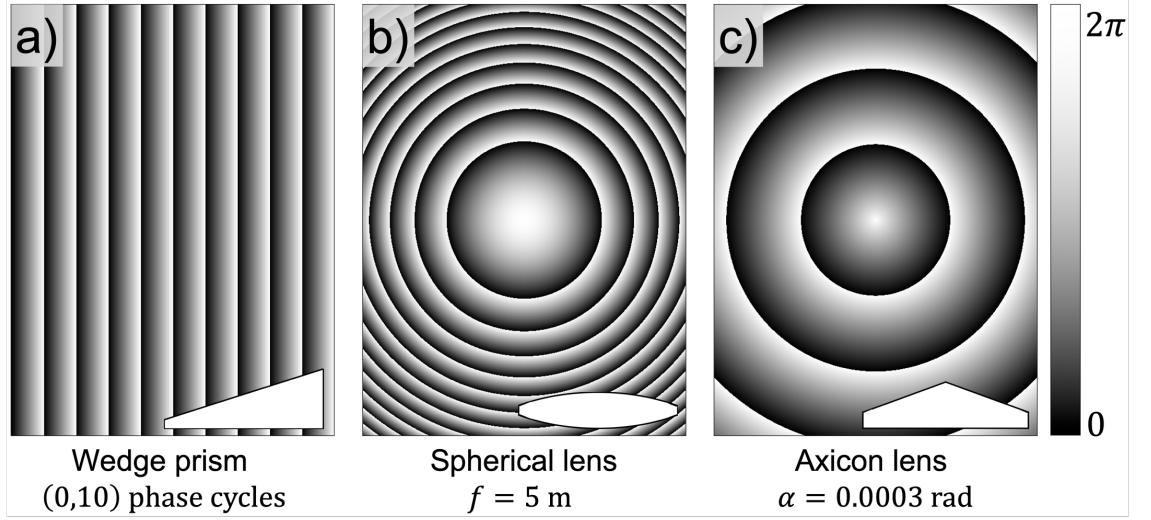


FIGURE 5.2: **Refractive vs diffractive optics:** Refractive optics common to the laboratory can be synthesised as holograms which are applied to reflective SLMs to impart the same phase with minimal medium thickness. This includes (a) a wedge tilt, (b) spherical and (c) axicon lenses, whose parameters can be changed dynamically.

By considering the length  $r$  travelled along the direction of wavevector  $k_0$  in figure 5.3, we may say that the shift in optical path length ( $\Delta\text{OPL}$ ) here between a planar-propagating beam and a Bessel beam is  $|r - L|$ , where  $r = L/\cos \alpha$ . By a Taylor expansion of  $1/\cos \alpha$ , we may then define the absolute propagation reduction  $\Delta z_{\text{Bessel}}$  of  $v_g$  along  $z$  as

$$\Delta z_{\text{Bessel}} \approx L \frac{k_r^2}{2k_0^2} = \frac{L\alpha^2}{2}. \quad (5.12)$$

That is, over a free space propagation of  $L = 0.8$  m, an axicon lens of strength  $\alpha = k_r/k_0 = 5 \times 10^{-3}$  radians should delay the light by  $10 \mu\text{m}$  (33.3 fs).

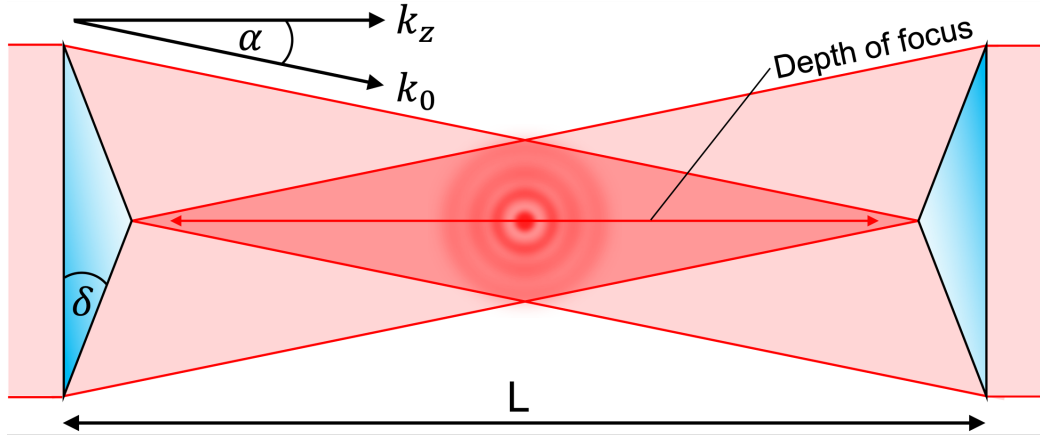


FIGURE 5.3: **Bessel beam delay:** Adapted from [201]. An incident plane wave exhibits a Bessel profile along a depth of focus after passing through an axicon lens – the rays exit at an angle of  $\alpha$  and invert. A second equal but opposite axicon returns the beam back to a plane wave after a Bessel propagation of  $L$  (m). The procedure is maximally efficient for this combination of  $L$  and  $\alpha$ , referred to later as  $\alpha_{opt}$  (optimised).

Consider again the setup depicted in figure 5.3: an incident plane wave encounters an axicon lens and is refracted radially over a distance of  $L$  to an equal but opposite axicon, which reverts the light into a plane wave once more. By dynamically varying the size of  $\alpha$  with a fixed  $L$ , it is possible to measure the characteristic  $v_g$  delay of Bessel beams.

### 5.2.2 Measuring the $v_g$ delay in interferometry

The treatment of the group velocity delay of light has thus far been theoretical; it is therefore necessary to introduce a means to measure it accurately under real-world conditions. In [201], time-correlated photon pairs were used in Hong-Ou-Mandel interference – a path delay was inferred from the characteristic dip in coincidence counts. In the classical case, we may consider a more straightforward approach using classical interference.

From the descriptions in section 2.1.3, two beams of the same source will interfere with fringes of some non-zero contrast for as long as the original wavetrains overlap, i.e. are spatially and temporally coherent. A measure of the degree of this coherence between the individual sources is known as the interferometric *visibility*,  $\mathcal{V}$ , which is

the contrast between the bright and dark regions in the superposition:

$$\mathcal{V} \equiv \frac{I_{max} - I_{min}}{I_{max} + I_{min}}, \quad (5.13)$$

where  $I_{max,min}$  are the intensities of neighbouring peaks and troughs in the fringe pattern observed, and  $\mathcal{V} \in [0 : 1]$ . As a relevant analogy, consider Young's double slit experiment (in section 2.1.5) with an extended low coherence source, as described in [10]: the flux-density distribution at the screen may be derived analytically, which considers the impact of the extended source length  $b$  and slit separation  $a$  on the subsequent distribution of visibility on the screen  $\mathcal{V}$ :

$$\mathcal{V} = \left| \text{sinc} \frac{a\pi b}{\ell\lambda} \right| \quad (5.14)$$

where  $\ell$  is the longitudinal distance between the source plane and slit plane. Note that this distribution of coherence is strictly the contrast of the fringes, and has no bearing on the transverse fringe locations. Calculating  $\mathcal{V}$  across a 1D transverse plane is a strong measure of the degree of coherence between the rays from the two slits.

This concept can be extended from slits to circular aperture sources, in which case the visibility distribution more resembles a first order Bessel function. Figure 5.4 adapted from [5] demonstrates the effect of increasing the length of the source  $b$  on the visibility distribution for a quasi-monochromatic source. A similar effect occurs when changing  $a$ , the separation of the apertures [227].

In our investigation, the concept of the visibility modulation envelope and its finite size can be exploited. Consider a quasi-monochromatic source split into two arms A and B and later recombined to form an interferogram. If the OPL of arm B is extended such that  $\Delta\text{OPL} < l_c$ , the periodicity of fringes remains fixed, whilst the visibility changes. In other words, it is a shift in the longitudinal alignment of the enveloping wavetrains. We characterise this as a relative shift in the  $v_g$  when compared to the case of  $\Delta\text{OPL} = 0$ . This technique is well understood using circular fringes in a Michelson interferometer, where a shift in mirror distance (in  $z$ ) results in a shift in contrast of the fringes.

Note that viewing circular fringes implies that the  $\Delta\text{OPL}$  of every spatial location in the interferogram is the same – as such, the visibility only has a single value at any one instant. In the case of interfering beams with an angle between them, the

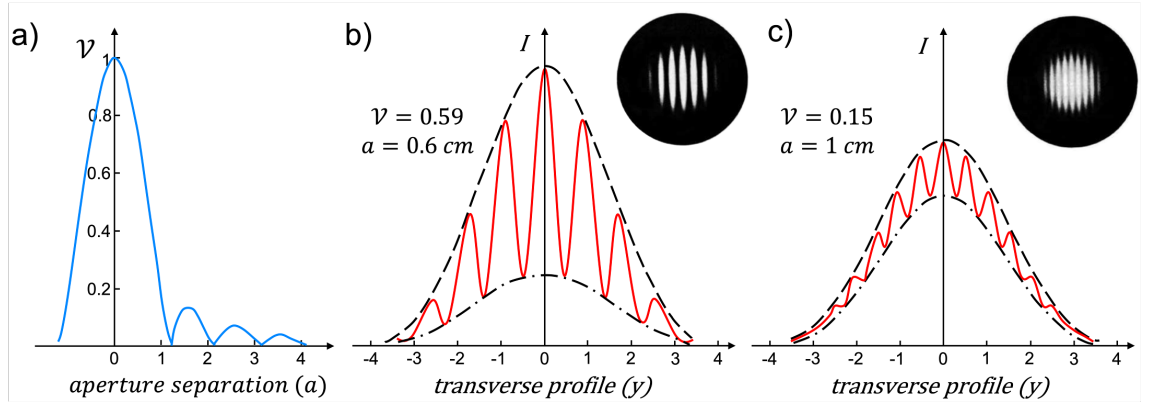


FIGURE 5.4: **Visibility in low coherence beams:** Adapted from [10] for reference only. (a) an example of the resultant visibility profile from the interference of beams from circular apertures. (b,c) a low coherence source will have a limited  $l_c$  over which the visibility  $\mathcal{V}$  is non-zero, which can be probed by changing the aperture separations or extending the source. In this example, reproduced from [5], an increase in aperture separation  $a$  results in the interference of mismatched wavetrains, which works to reduce the contrast in the fringes (see insets).

visibility varies across the interferogram, as the shortest-travelled components of one beam also interfere with the longest-travelled of the other. This is the source of the fundamental visibility profile seen in straight fringe interferograms.

It follows that by observing the shift in visibility in the interferogram, we can measure the  $v_g$  delay of a pair of beams A and B, should beam B undergo a lengthening due to receiving some structure over its OPL. The units of this measurement are interference fringes via camera pixels, i.e. wavelengths, which can be converted to a distance of delay or the time taken for both beams to propagate a given distance at velocity  $c$ . Instead of circular fringes, the following investigation uses an interferogram of many straight fringes, such that the entire range of visibility can be observed instantaneously across a camera sensor. By adding structure over a fixed length  $L$  of beam B, the peak of visibility shifts its lateral position by some pixel number, which is then converted to fringes/metres based on the detected periodicity of oscillating fringes.

### 5.3 Structured light delay: experimental setup

The following section describes in detail the experimental setup used to generate and analyse structured beams in terms of their respective group velocity delays when compared to a Gaussian beam. By virtue of the fact that this is a test to validate the results presented in [201], the initial structured and reference arms are intended to have an equal OPL. The back end of the system is then a classical interferometer, in order to capture the full envelope of coherence on a scientific CMOS camera.

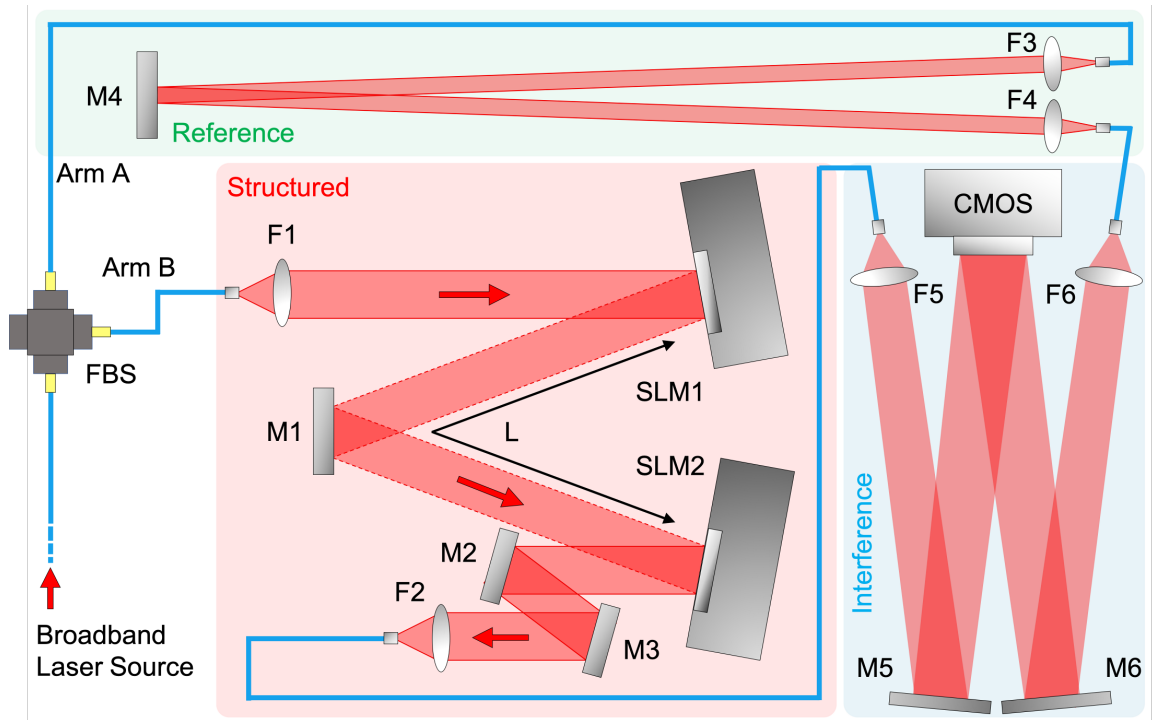
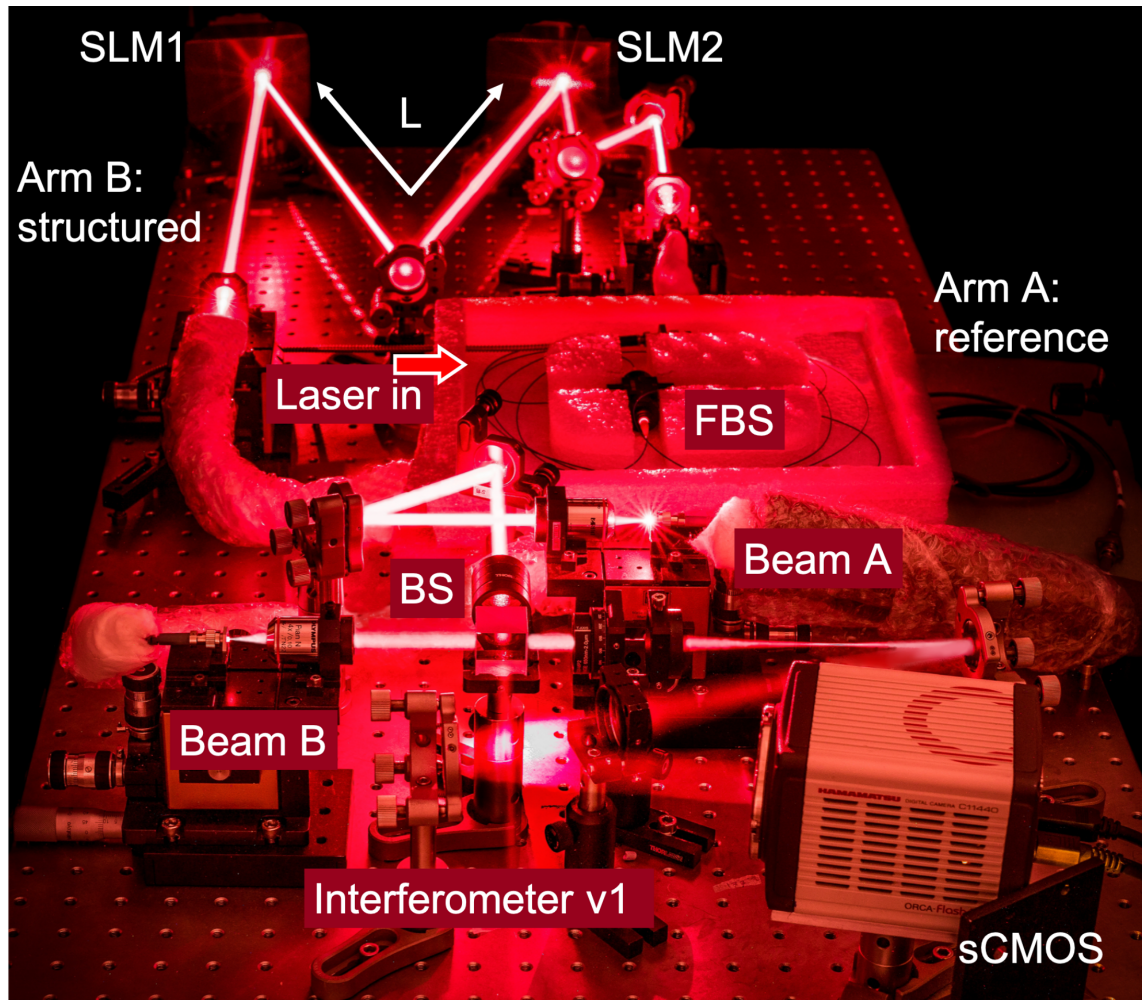


FIGURE 5.5: **Experimental setup:** The final iteration of the classical structured light interferometer used in this investigation. A broadband source is split into two arms – arm A consists of PM fibre and an airspace delay to act as a Gaussian reference beam (green), whilst arm B couples into a beam structuring section (red). An incident beam is modulated into the +1 order with a carrier grating and some structure. After propagating a distance  $L$ , a second SLM is used to destructure the light back into an approximate Gaussian for fibre coupling once more. The air and fibre propagation of each arm is matched such that when coupled out and expanded, the two arms combine as an interferogram overfilling the sCMOS detector (blue).

The completed setup is depicted in figure 5.5: firstly, a fibre-coupled broadband laser source is connected to an input arm of a polarisation-maintaining fibre beamsplitter (FBS). Note that the previously introduced Qioptiq and SLD sources were used

interchangeably during testing. The incident beam undergoes a division of amplitude inside the FBS, dividing the beam into two matching arms, labelled arm A and B. Arm A is the reference arm (green), which comprises of a length of polarisation-maintaining fibre (PMF) and free-space delay line, reflected by mirror M4. Lenses F3 and F4 are 20 $\times$  microscope objectives.



**FIGURE 5.6: Photo of experimental setup:** A 90 s long exposure image of a previous iteration of the optical setup, using a “laser tracing” method to reveal the beam path for reference. Specifically, this shows the Qioptiq source and its propagation through the structured arm, as well as the first iteration of the interferometer. This was also taken before the airspace delay was applied to arm A. The 4 fibre coupling stages with micrometer  $z$  translation stages can be seen. During full operation, all fibre optics were thermally insulated and blackout fabric was used to cover the entire bench. The final results reported were obtained with the second iteration of the interferometer; as such this image is for illustration only.

Arm B is the structured arm (red), which follows the same geometry as that introduced by [201]: beam B is output coupled from lens  $F1 = 40$  mm such that it enters

collimated and at the approximate size of the LC-SLM window. Beam B is then incident on SLM1 (Hamamatsu X10468-01) at a low angle of incidence, and diffracted with a simple vertical grating. This modulated +1 order beam (along with other orders) travels a distance  $L = 0.8$  m and is reflected by M1 onto SLM2. SLM2 is encoded with a simple horizontal grating to steer the +1 order of SLM1 into a new transverse location. Mirrors M2 and M3 then steer this new beam through lens F2 which couples the light into a length of PMF. The lengths were chosen such that in the case of SLM1 displaying a lens  $f = L/2 = 0.4$  m, the fibre facets were  $4F$  imaged onto one another via M1 and M2 i.e.  $(F1, F1 + f, f)$  (only in chapter 6). For Bessel beams, the diffracted light from SLM1,2 remain in the near field with some angular separation, so the optical spacing is merely to achieve symmetry between couplers F1 and F2 about mirror M1. The length of PMF used and the length of the free-space delay were chosen such that arm A and arm B have approximately the same amount of fibre and free space propagation (discussed further in section 5.3.5).

### 5.3.1 Structured light delay: interference system

In theory, beams A and B reach the interference section having travelled the same optical path length, however within beam B's path, a distance of  $L$  was traversed with whatever structure is applied by the SLMs. Figure 5.7 depicts two iterations of the classical interference performed – (a) a compact testing interferometer using a non-polarising beamsplitter (NPBS) and (b) the improved final airspace interferometer using large planar mirrors.

In the first iteration (a) (also featured in figure 5.6), arms A and B enter the interferometer via  $10\times$  microscope objectives coupled to a 3-axis fibre launch stage and a longitudinal translation stage with a micrometer. The path length of arm A could be adjusted several cm by repositioning mirror M4 and retuning the angles of mirrors M4 and M5. Beams A and B were incident on orthogonal faces of an NPBS, before the beams co-propagated through a magnifying telescope provided by lenses  $F5 = 80$  mm and  $F6 = 250$  mm. The resultant interferogram between beams A and B was detected by a high resolution sCMOS camera (Hamamatsu Orca). The aim here was to use the camera with the largest resolution, which could discern between the most number of interference fringes without encroaching on the Nyquist limit; this was imperative for instantaneous capture of the entire envelope of visibility.

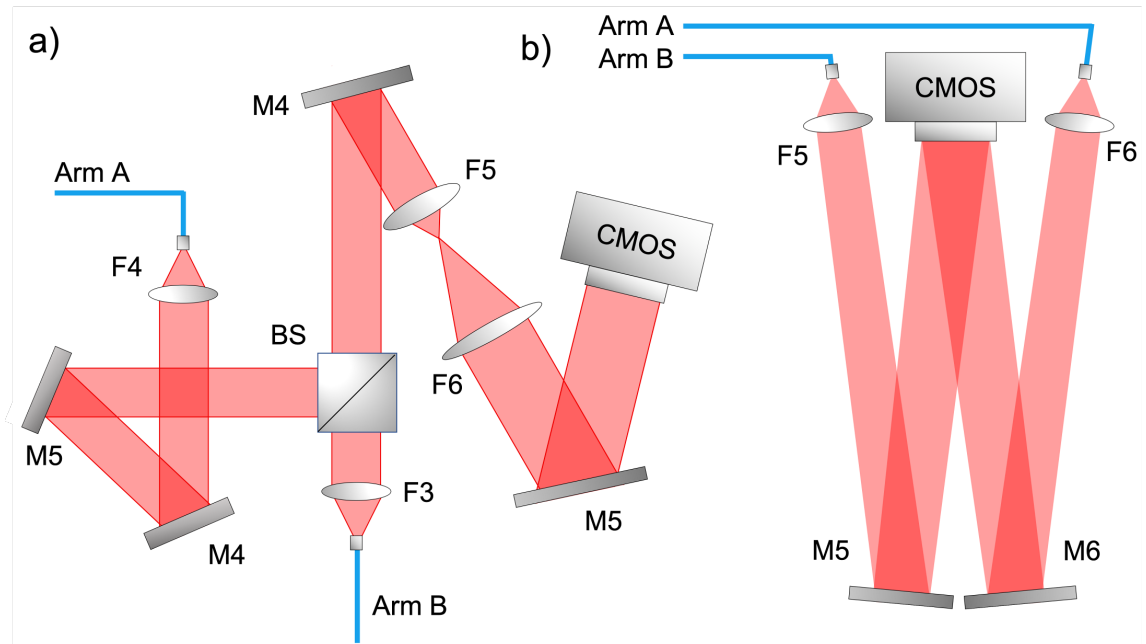


FIGURE 5.7: **Interferometer configurations:** (a) The first iteration of interferometer involved orthogonal beams A and B entering a beamsplitter, and using a 4F magnification telescope to expand the beams onto the camera. The number of fringes was varied by offsetting the angle of incidence of beam A into the BS. The final interferometer design (b) is a clean interference of two slowly-diverging beams from microscope objectives F5 and F6 after reflection from 2" planar mirrors M5 and M6. This design was used to aid beam alignment, increase the number of fringes and flatness of the interferogram, whilst also limiting optical aberrations. The mirror-camera distance is  $D = 1433$  mm, and the separation of the beams at mirrors M5,M6 is  $E = 40 - 70$  mm.

This interference system was initially suitable as a compact means to recombine the beams off-centre such that they interfere on camera with a beam size which fills the sensor. Specifically, the  $BS \rightarrow CCD$  distance was designed as a 4F imaging system, using  $(F5, F5 + F6, F6)$ , such that the NPBS plane was imaged onto the detector with a  $3\times$  magnification. However, difficulties arose when adjusting the number of fringes observed: small changes to the transverse position of the beams required “walking” the beams using mirrors M4, M5 and the x-axis of the output stage in arm B, which was an issue for long-term repeatability. Furthermore, with expanded beams the lenses acted as a hard aperture at the camera plane, preventing a more uniform interferogram profile.

The solution, presented in figure 5.7(b) was to extend the workspace and simplify the beams with a fundamental air-space interference system. In this configuration, arms A and B propagate from the same objective lenses as slowly diverging beams,

achieving a  $\sim 5\times$  expansion across 2.94 m. Beams A and B interfere and produce an interferogram after reflecting from a pair of 2" mirrors M5 and M6. This iteration was advantageous due to its simplicity, as fewer elements reduced the possibility of dirt, clipping and secondary interference effects. The number of fringes achieved is also only dependent on the separation of the mirrors, and so the system is far more robust for small alignments. It is also possible to increase either the distance of the objective lenses to the fibre output, or the overall propagation length to achieve a substantially overfilled detector, which produces interferograms with the most uniform intensity profiles.

### 5.3.2 Beam collimation

Our theoretical prediction of the  $v_g$  delay in Bessel beams rely on both arms having stable Gaussian beam profiles everywhere other than the structured path between the SLMs. In this regard, it was pertinent to consider the level of beam collimation achievable for the initial air-space propagation from the output of the FBS to SLM1.

Beam B before SLM1 is depicted in figure 5.8(a); the collimation of this beam was achieved by use of a shearing interferometer (recall section 4.2.2), as well as using a mirror to propagate the beam to the far field ( $\sim 7$  m here) in (b); the lens-fibre distance was adjusted until the beam full width half maxima (FWHM) were similar (labelled in each image). The same procedure was used in (d,e) by back-aligning the fibre output at F2 beyond SLM2. Note that if the beam is actually incident on a blank SLM window first (c,f), the non-flat phase across the SLM coupled with the hard-edged square aperture heavily aberrates the beam profile at the same plane – it is therefore not accurate to assume that a flat phase hologram sent to the SLM will impart a flat phase on the beam.

In order to improve the collimation succeeding SLM1, a further method was employed: a lens  $F = 300$  mm was placed beyond SLM1(2), such that the Fourier plane (FP) could be viewed on a CCD (as in figure 5.9(e)). Recall from section 2.4.1 that a collimated beam which passes through a lens of focal length  $F$  will focus to a diffraction limited spot in the back focal plane. It follows that any aberrations in the beam can be accounted for by applying low frequency correction holograms until a focused spot is achieved. Note that this technique relies on the accurate longitudinal position of the CCD, as any deviation from  $F$  will cause the beam to be defocused.

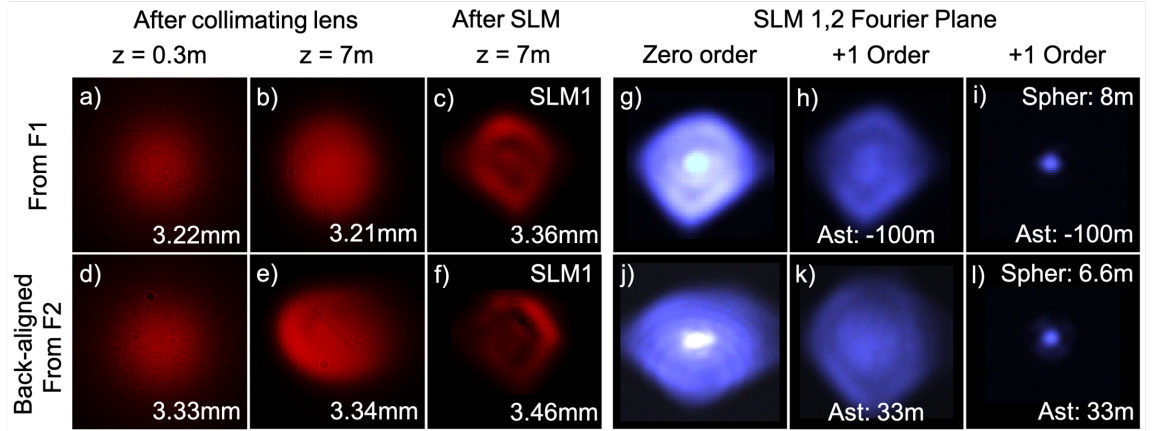


FIGURE 5.8: **Beam collimation and aberration correction:** (a,b,d,e) the beam incident on SLM1 and entering the fibre coupling at F2 were collimated by equalising the beam waist (FWHM labelled) in the near (L) and far (R) field. (c,f) The non-flat phase profile of the SLMs aberrated the beams. The beams were also observed in the back focal plane of lens  $F_{300} = 300$  mm and corrected using spherical and astigmatism (dual cylindrical) lens holograms.

A combination of cylindrical and spherical lens holograms were employed to de-skew and properly focus down the beams from each SLM respectively. These holograms are discussed further in section 5.4.

### 5.3.3 Beam alignment techniques

The accuracy and precision of beam structuring are important in all the investigations presented; in this case, however, they are absolutely critical to confirming the geometric theory. Within this investigation, the detected  $v_g$  of structured beams depends on factors such as i) the beam profile and divergence of the incident Gaussian beam, ii) the holographic phase encoded by the SLMs and iii) the components of the destructured beam which reach the interferometer. The first two factors combine when considering how centred the incident beam is on the SLM, and the third factor relates to how well the unshaped light from SLM2 couples into the output fibre at F2. The following is a brief description of the various methods I developed in achieving optimum alignment by mitigating these variables.

Firstly, the incident Gaussian beam was centred on the hologram of SLM1, as depicted in figure 5.9(e) – lens  $F_{300} = 300$  mm was again used to image the FP. In general, the energy distribution across the diffracted beam is dependent on the overlap of the

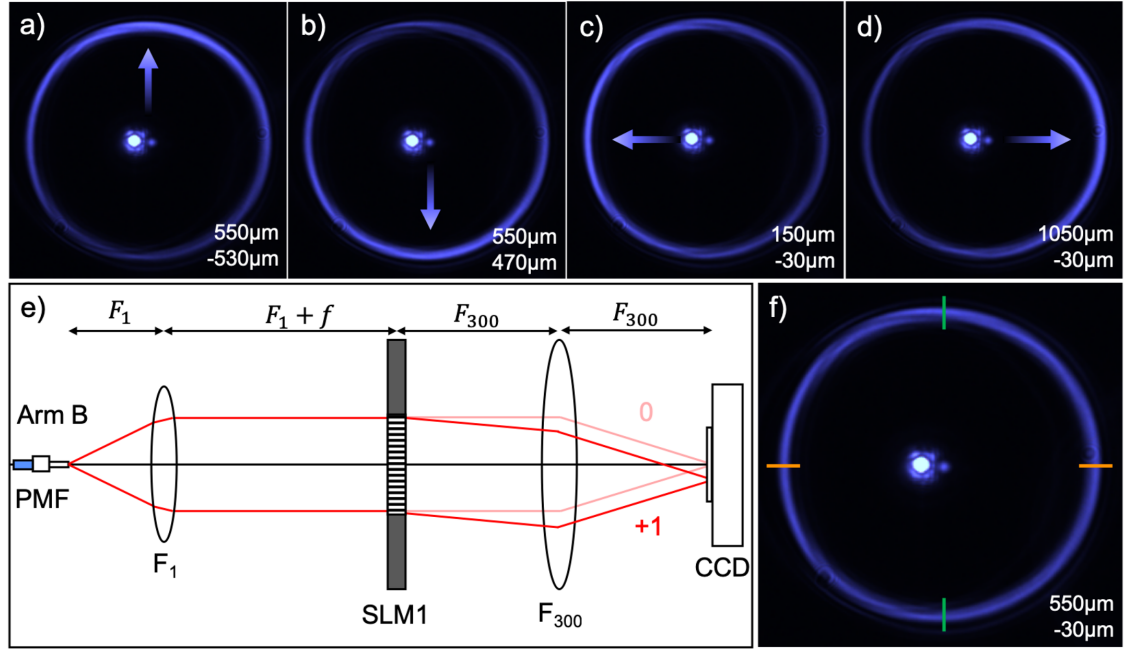


FIGURE 5.9: **Centering the beam on SLM1:**(a-d) Applying an axicon lens to SLM1 and observing it in the FP reveals the non-uniform distribution of energy across the intensity profile, which can be altered by changing the  $(u_{off}, v_{off})$  offset of the axicon hologram on the SLM window (shown in  $\mu\text{m}$ ). (e) shows the setup, where the camera is placed in the back focal plane of the temporary lens  $F_{300} = 300 \text{ mm}$ ; (f) shows a Bessel profile, successfully equalised in  $x$  and  $y$ . Note that the zero order is located at the centre of the images, and higher orders appear to overlap in regions of the ring-like intensity.

incident beam on the hologram – this distribution can be equalised in the horizontal and vertical axes either by fine-tuning the incident beam angle at lens  $F_1$  or by shifting the transverse location of the hologram on the SLM itself – the offsets labelled  $(u_{off}, v_{off})$ . For the case of a Bessel beam in the FP, figure 5.9(a-d) illustrates the power distribution with lateral shifts of  $\sim 1 \text{ mm}$  in various directions, whilst (f) shows the uniform distribution achieved with an optimal hologram offset of  $(550, -30) \mu\text{m}$ .

In the following descriptions, the use of a wedge tilt phase across the SLM is referred to as a *carrier* grating, denoted  $\phi_c$ , used to steer the target beam away from the zero (and higher) orders. Before considering the use of such a grating, it was worthwhile to ensure that the near-field plane of SLM1 approximately overlapped SLM2. To verify this, two distinct holograms were displayed on SLM1 and SLM2. By observing the resulting near-field overlap beyond SLM2 and adjusting the incident angle onto SLM2 via mirror M1, the near fields of each SLM can be overlapped to within a

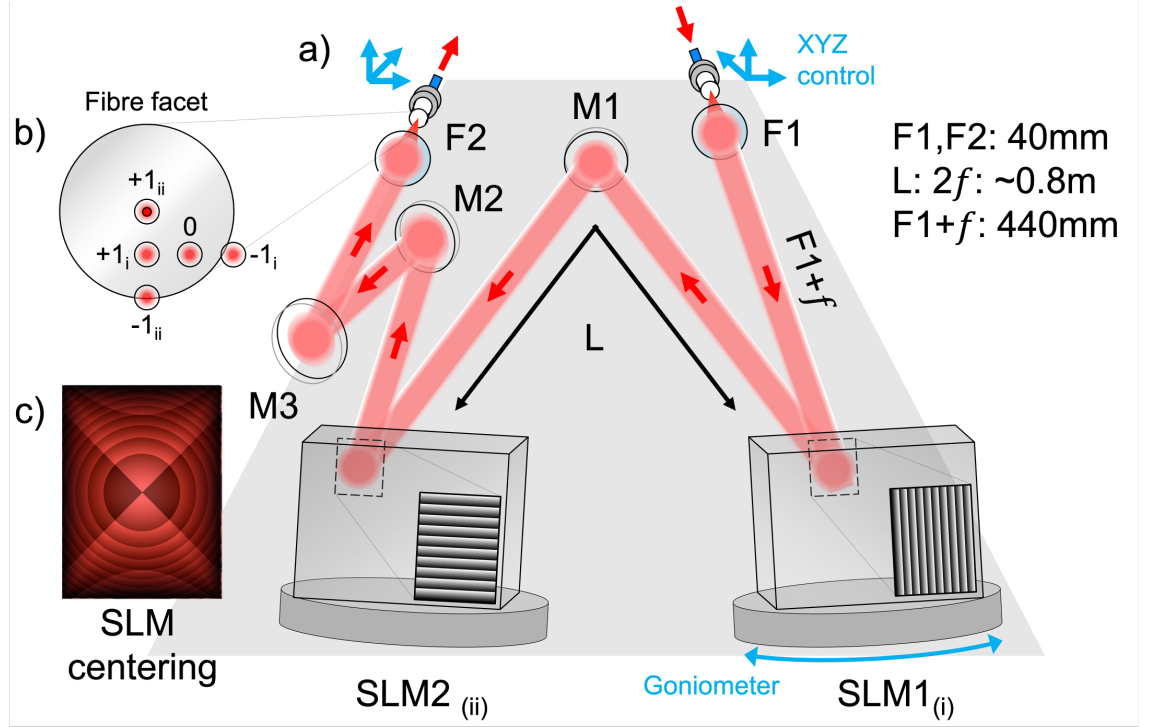


FIGURE 5.10: **Structured beam alignment:** (a) the incident beam is collimated by output coupler lens F1 before being incident on SLM1. A vertical grating is used to diffract the beam into the +1 order with some structure; after a distance  $L$ , SLM2 is used to both destructure the beam and tilt the beam in the horizontal. The mirrors M2, M3 are used to steer the destructured order down the fibre via lens F2. (b) depicts the arrangement of diffraction orders on the fibre facet – only the  $+1_{ii}$  order from SLM2 is coupled. (c) SLM1 is semi-aligned onto SLM2 by observing the near-field overlap of two distinct holograms on each SLM.

few hundred microns before further corrections lenses were used on SLM2. Figure 5.10(c) depicts a sketch of the overlap of the chosen low frequency spherical (SLM1) and astigmatism (SLM2) lenses.

Figure 5.10(a) portrays the structured beam section of arm B. The primary aims of this setup were to use SLM1 to structure an incident Gaussian beam from output coupling lens F1 and propagate this structure over a distance  $L$ ; SLM2 then destructures this beam before it is coupled into a fibre by lens F2. This final coupling dictates the available power in beam B for the interferometer; as such it was critical to develop a method of efficiently coupling the correct order down the single mode fibre.

Firstly, zero order coupling was achieved by using the SLMs as planar mirrors, ensuring the height of all the optics was similar, and employing a back-alignment of

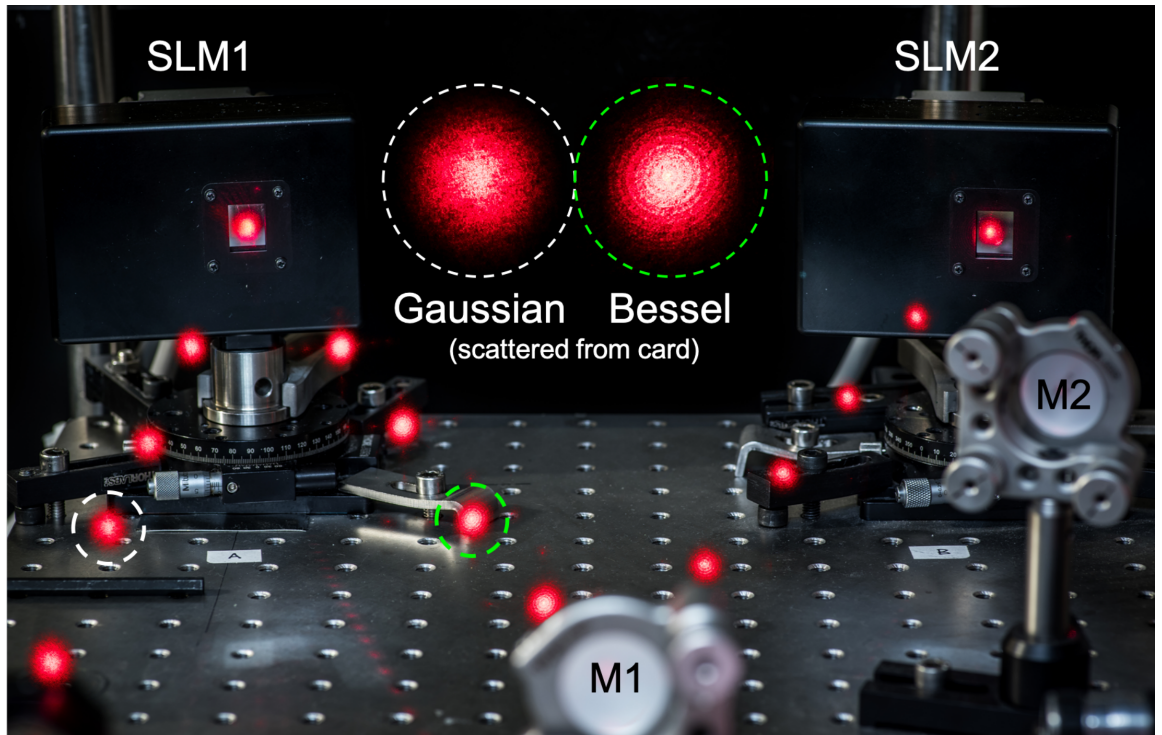


FIGURE 5.11: **Photo of LC-SLM beam structuring:** A photo composite of various planes throughout propagation from lens F1. The incident Gaussian beam is diffracted from SLM1 as the overlap of various orders. The blazed order  $+1_{ii}$  is diffracted as a Bessel beam which converges at lens M1, before inverting at SLM2. Note that the inset images of the beams appear grainy due to being taken through paper, and the first and zero order are unable to diverge within length  $L$ . Also pictured is the goniometer used to tilt SLM1 in the alignment procedure.

the output fibre back through the system to best position mirrors M2, M3 and the 3-axis coupling stage [228]. Next, a linear carrier grating was encoded onto SLM1 – a vertical grating of e.g. 20 cycles across the SLM window  $(20_x, 0_y)$ . This diffracted the incident beam into the fundamental  $\pm 1_i$  orders as seen in figure 5.10(b). SLM1 was mounted on a goniometer in order to rotate the coupling down the fibre from the zero order to the  $+1_i$  order. Next, SLM2 was encoded with a horizontal grating  $(0_x, 20_y)$ , which in turn diffracted the  $+1_i$  order into  $\pm 1_{ii}$  in the vertical direction. Fine adjustment of the fibre coupling stage and mirrors M2, M3 then allowed the coupling of the target  $+1_{ii}$  from SLM2 down the fibre.

The carrier gratings on the SLMs were chosen to be orthogonal and with a non-negligible number of cycles to maintain confidence in the exact orders being coupled, and to prevent the accidental overlap of the target beam and extraneous orders. Ultimately, either 20 cycles were used in the delay tests – using equation 2.14 and the geometry in figure 2.10, this corresponds to a  $y \approx 55.5 \mu\text{m}$  separation between

diffraction orders at the proximal facet of the fibre (compared to a  $3.5\ \mu\text{m}$  core diameter). Note that it was necessary to fine-tune the coupling at F2 at least once per day – this was perhaps due to gravitational drift, as well as temperature-dependent sub-micron changes in the opto-mechanics. Figure 5.11 shows the structuring arm in practice; both SLM1 and SLM2 display axicon lenses at some carrier tilt. The SLMs are both mounted on goniometers to allow for fine-tuning of the angle of incidence, and mirrors M1-M6 had 3-axis fine control.

### 5.3.4 Laser characteristics

The  $v_g$  delay between two beams borne of the same quasi-monochromatic source manifests as a shift in visibility when these beams are interfered. Upon traversing through the system independently, the coherence length  $l_c$  acts as a longitudinal constraint for path length matching arms A and B. The larger the bandwidth, the shorter the coherence length – considering the arguments in section 5.2.2, the challenge was to interfere a broadband source with enough fringes to observe the visibility envelope on a camera with a sufficient periodicity (*pixels/fringe*). By simple calculus we may estimate the number of fringes within the envelope, given that the speed of light  $c$  is defined by  $c = \nu\lambda_0$ , where  $\nu$  is the frequency. The spread of frequencies  $\Delta\nu = -c\Delta\lambda/\lambda_0^2$ . Given  $\Delta t \approx 1/\Delta\nu$  for some period  $\Delta t$ , we find that the distance propagated is  $\lambda_0 N_{\text{fringes}} \approx c\Delta t$ , i.e.

$$N_{\text{fringes}} \approx \frac{\lambda_0}{\Delta\lambda}. \quad (5.15)$$

The laser sources employed were the Qioptiq  $\lambda_{0,Qio} = 642.79\ \text{nm}$  and SLD  $\lambda_{0,SLD} = 832.36\ \text{nm}$  broadband sources – the former was more appropriate for alignment procedures and testing.

The SLD laser was used for its portability and significantly broad bandwidth  $\Delta\lambda_{SLD} = 18.5\ \text{nm}$ , which results in a predicted 45 fringes across the visibility envelope. Figure 5.12 demonstrates the achievable SLD spectra at the detector for beams A and B after propagation through all optics.

Multiple fibre-fibre couplings and a pair of LC-SLMs cut down the resultant power of arm B, and so two methods of power enhancements were considered: firstly, a “hybrid patch fibre cable” was recommended by the manufacturer to improve fibre

coupling. In practice this actually clipped the source bandwidth significantly (shown in grey). The diode laser driver could also be driven at a maximum of 200 mA, however this also clips the spectrum (shown in orange). In effect these methods produced a superposition of low and high coherence wavetrains, which manifests as an extended visibility profile with a poorly-defined peak. As such, these methods were not employed.

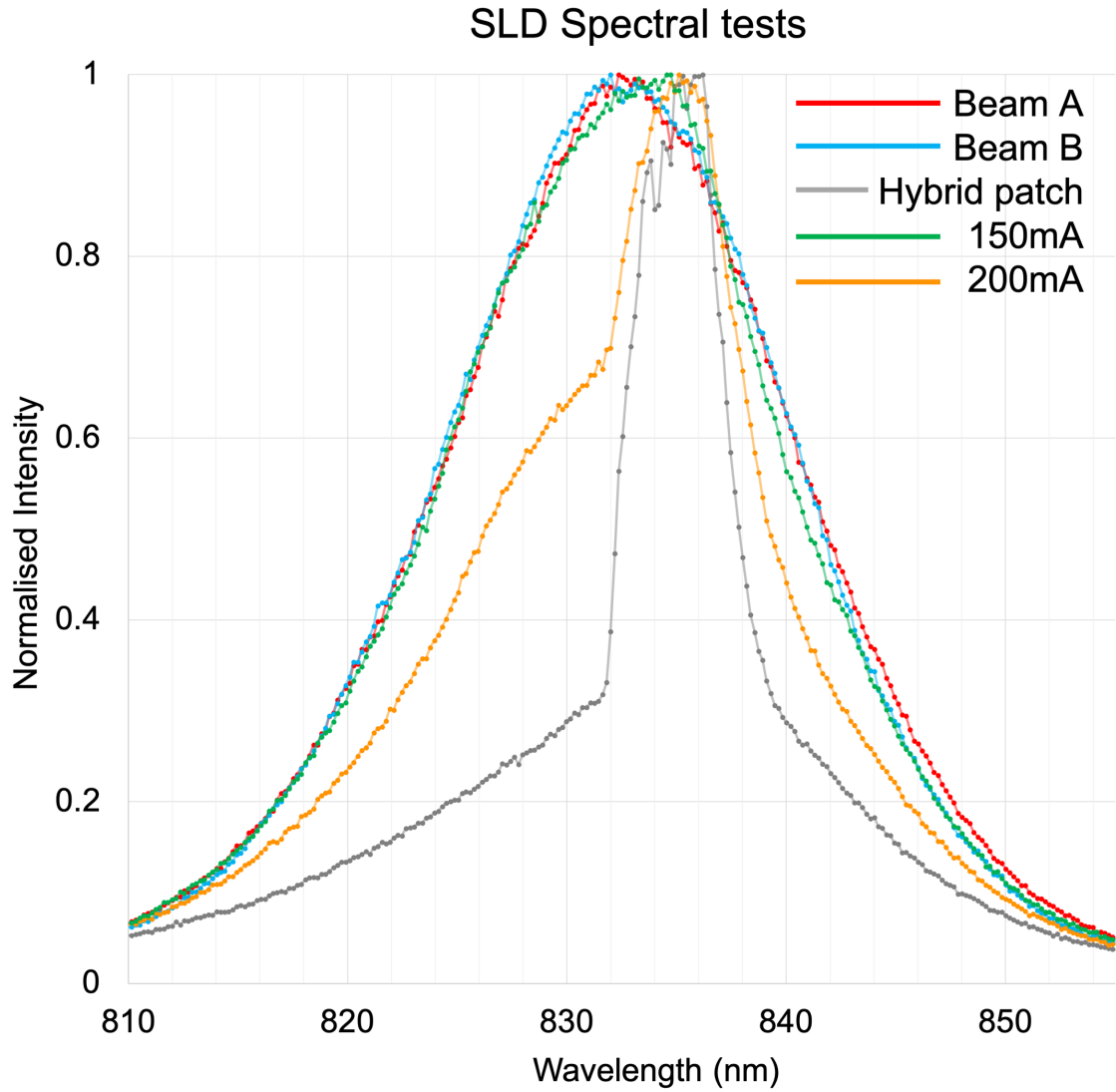


FIGURE 5.12: **Superluminescent diode spectra:** The spectral profile of the SLD source, where  $\lambda_0 = 832.36$  nm and  $\Delta\lambda_0 = 18.5$  nm (FWHM). The profiles in arm A (red), B (blue) whilst the source was driven at 150 mA (green) retain the original spectral components (figure 4.1). Attempts to boost the overall power for measurability, such as optimised coupling via a hybrid patch cable (grey) or maximising the operating current (orange) led to a significant clipping of the lower spectral components.

Given the fringe width of the visibility to be expected, we can estimate the number of fringes in the interferogram produced with the setup shown in figure 5.7(b). Consider the geometry of figure 5.13) – mirrors M5,M6 are centred  $E$  apart, with mirror-camera distance  $D$ . If we assume beams A and B have flat wavefronts, interfere at their beam centres and can simplify the argument such that one beam enters the camera plane perpendicularly. The full angle between interfering beams is

$$\phi = 2 \sin^{-1} \left( \frac{E}{2D} \right). \quad (5.16)$$

Adapting the diffraction equation 2.14, we find that the observable fringes of separation  $d$  on a detector of width  $w$  is

$$\text{no. of fringes} \approx \frac{w}{d} = \frac{w \sin \phi}{\lambda}. \quad (5.17)$$

For the current setup,  $D \sim 1430$  mm,  $w \sim 13.3$  mm and mirror separation  $E =$

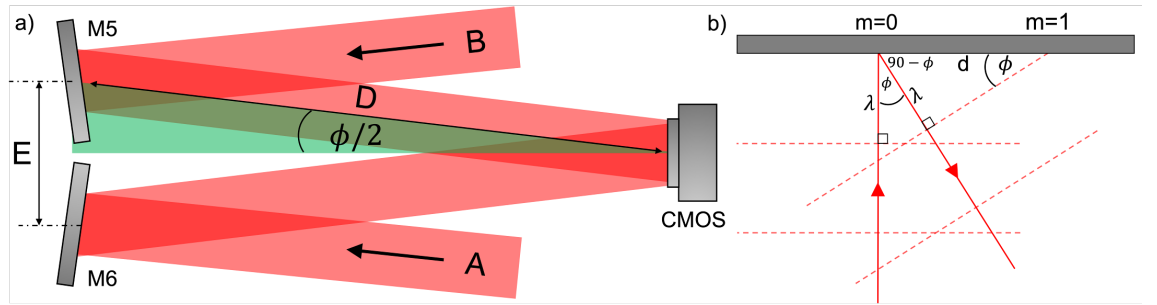


FIGURE 5.13: **Number of fringes in interferogram:** (a) A simplified geometric argument for determining the number of fringes which can be generated by interfering two beams from mirrors M5 and M6 with separation  $E$ .  $D$  is the mirror-camera distance, with full angle  $\phi$ . (b) the distance between fringes  $d$  can be determined from the grating equation, which when incident on a camera of width  $w$ , determines the total interference fringes from beams offset by angle  $\phi$ .

40 mm give an estimation of  $\sim 447$  fringes. The beam separation on the mirrors is therefore a direct means to vary the number of fringes within the interferogram, which in turn controls the proportion of the visibility envelope within the measurement window.

### 5.3.5 Interference visibility testing

A major source of issues arose when trying to identify the “primary” interference fringes when adjusting the optical path length (OPL) between the two arms. In this context, primary interference refers to the true recombination of wavetrains from the source; “secondary” interference refers to the coincidental interference arising from the recombination of one wavetrain with a secondary wavetrain, similar to the primary wavetrains but possibly generated from internal reflections within the optics. This was observed across an optical path difference which was much larger than the width of the *sinc* envelope of visibility expected, and so may not be attributed to the accidental use of secondary maxima within the *sinc* profile itself.

To begin with, the OPL of arms A and B were estimated by adding the  $n \times \text{length}$  of each medium in turn, where  $n$  is the refractive index. Using a typical value  $n_g \sim 1.5$  for the polarisation maintaining fibre (PMF) and fibre beamsplitter (FBS), the path lengths  $\text{OPL}_A \approx \text{OPL}_B$  compare as:

$$n_g(\text{FBS}_A + \text{PMF}_A) \approx n_g(\text{FBS}_B + \text{PMF}_B) + n_{air}(2F_1 + 2(F_1 + f) + L) + \mathcal{K}. \quad (5.18)$$

Here, the right hand side was simplified due to the symmetry in the structured arm, where  $F_2 = F_1$ ;  $\mathcal{K}$  is an offset which can be eliminated by using custom fibre lengths. Instead,  $\mathcal{K}$  was minimised by decreasing distance  $D$  for beam A, which in turn led to slightly curved interference fringes from mismatched beam waists (figure 5.14(c,d)). Such effects were mitigated by only using a subsection of rows from the centre of the interferogram.

Fine adjustment of the path lengths was achieved using fibre stages with micrometer  $z$  control at output lenses F5 and F6. This method of path length matching was found to locate strong interference fringes for the Qioptiq source, as shown in 5.14(a). Here, the visibility envelope peaks at 50-60% contrast over a width which extends beyond the 13.3 mm camera window. Note that the noise level in the data (red) was high enough that the polynomial fit (green) often gave erratic false peaks. As such, the Qioptiq source was only used in preliminary testing – only with  $\sim 900$  fringes across the camera could a well-defined envelope be obtained. However, this is beyond the Nyquist limit, and resulted in aliasing of the fringes.

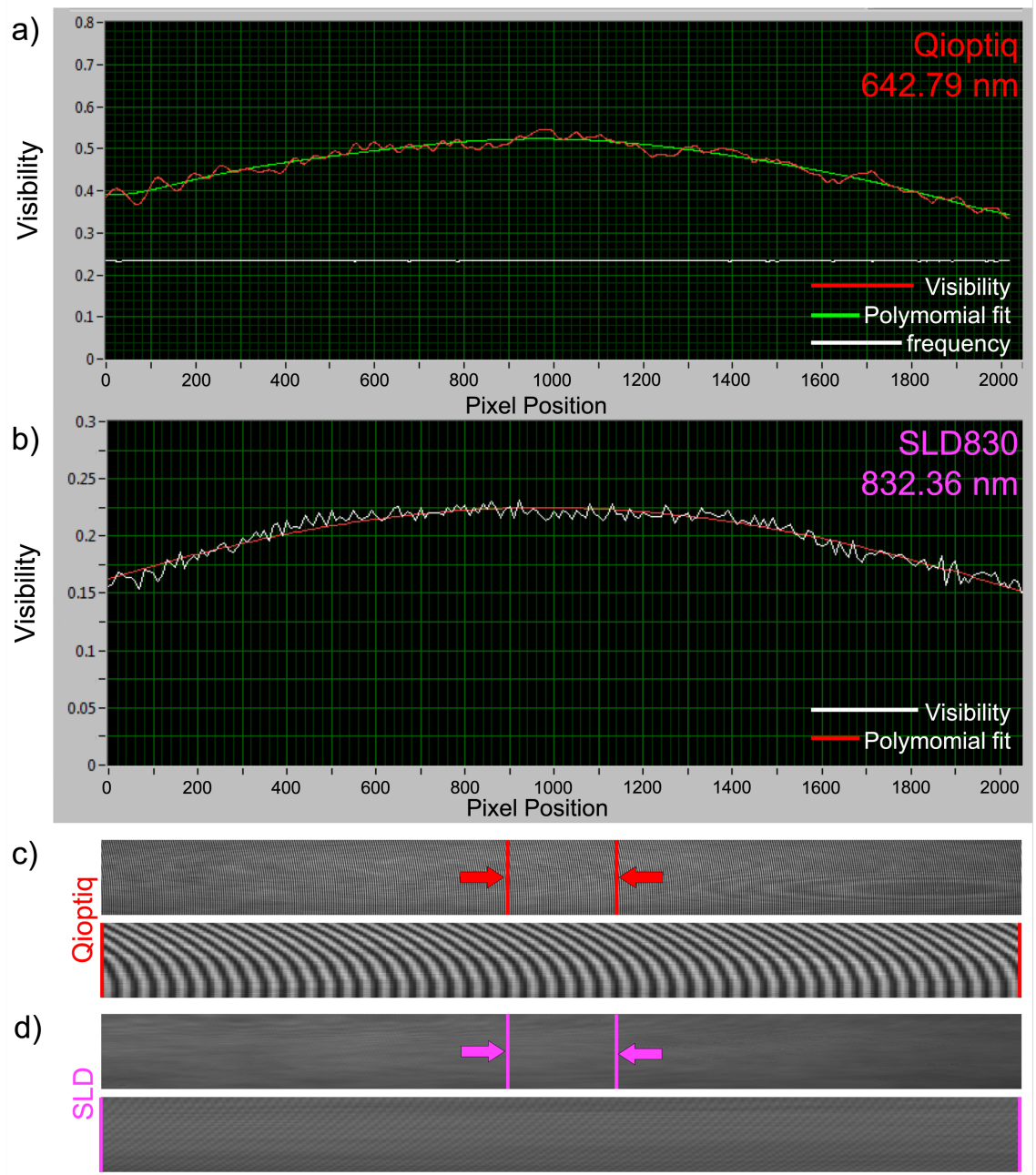


FIGURE 5.14: **Secondary interference visibility:** The setup with an unequal ratio of airspace and fibre in the OPLs of A and B led to unfavourable visibility envelopes in the (a) Qioptiq and (b) SLD sources. This is particularly detrimental in (b) where the profile is surprisingly flat with a very weak visibility. (c,d) (un)cropped examples of the interferogram with this path length matching regime – note that the curved fringes are as a result of mis-matched lengths  $D$  to account for  $\mathcal{K}$ . Generally, this was accounted for by extracting only a subsection of rows at any one time, which improved the visibility marginally.

A peculiarity arose when the Qioptiq source was switched over to the SLD broadband source. Consider figure 5.14(b) – the typical SLD interferogram using the above path length matching produced an extremely weak visibility envelope (max  $\sim 5\text{-}20\%$ ), with an extended width which continued well beyond that of the Qioptiq source (i.e. an envelope of  $> 600$  fringes when the camera window detects 200 fringes). This is in direct conflict with the bandwidth shown in figure 4.1 – recall that  $N_{\text{fringes},\text{SLD}} \approx 45$  fringes. This phenomenon persisted even when intensity and polarisation matching using linear polarisers (LP) in each arm of the interferometer. This suggested that the components which were interfering were narrowband and not of the same wavetrain, as shown by the width and contrast of the envelope.

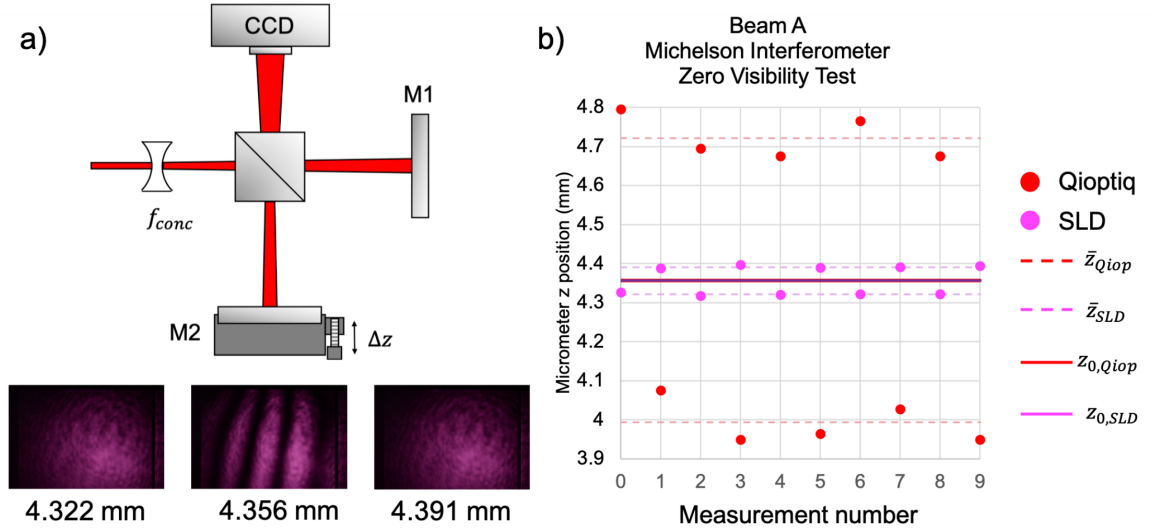


FIGURE 5.15: **Michelson interferometer coherence:** (a) The relative coherence lengths of each source were compared in a Michelson interferometer. The inset images define the  $z$  positions of mirror M2 with zero visibility for the SLD source. (b) repeated measurements of the positions of zero visibility confirm the bandwidth of the sources. Here  $\bar{z}$  denote the average positions of zero visibility, and  $z_0$  denote the deduced position of maximum visibility. Note that having travelled the same optical path, the positions of  $z_0$  overlap.

A convenient test of the coherence length was therefore conducted to verify the above spectra outside the optomechanics of the experimental setup. Figure 5.15(a) demonstrates a Michelson interferometer (recall section 2.1.5), which uses a concave lens  $f_{\text{conc}}$  to expand the incident beam, before an NPBS divides the beam into two arms. The path travelled to mirror M1 is fixed, whilst M2 is mounted on a translation stage. For both the Qioptiq and SLD source, the two  $z$  micrometer positions of M2 for zero visibility either side of the envelope of interference were recorded over 10

measurements. Here, zero visibility was determined by eye, which provides only the general behaviour of the coherence length for each source.

As depicted in figure 5.15(b), both sources have visibility maximum in the same average position, such that  $z_{0,Qiop} \approx z_{0,SLD}$ . The non-zero visibility range was measured to be  $\sim 727 \mu m$  for the Qioptiq source and  $\sim 69 \mu m$  for the SLD source; by equation 2.1.4, the latter corresponds to  $\ell_{c,SLD} \approx 18.70 \mu m$ . Although rough estimates, these results gave a degree of confidence to re-evaluate the behaviour of the SLD source, as in this test the visibility behaved as expected.

Given that the SLD source behaved more reasonable in isolation, a final test was conducted to probe the interferometric behaviour – particularly on propagation through each arm of the experimental setup itself. A second FBS was inserted into the fibre outputs of F5 and F6, and used to couple the light from arm A and arm B *separately*; this was used to self-interfere both beams in turn after their propagation through the system (e.g. after propagation through arm A(B), beam A(B) interferes with itself on camera). The motive behind this test was to determine if there was a component within either of the arms which would cause them to misbehave in such a way as to cause issues when self-interfering in the interferometer.

The results for arm B, shown in figure 5.16, revealed that (a) the SLD laser source was in fact capable of producing a compact visibility envelope in line with the theory ( $\Delta\lambda = 18.5 \text{ nm}$ ), whilst the Qioptiq source confirmed a wider envelope appropriate for its bandwidth. The results for arm A showed the same behaviour.

From these results, it was postulated that whilst the beams interfering at the camera were of the same original source in terms of  $\lambda$  and  $\Delta\lambda$ , there remained a mismatch in terms of the mediums traversed in each OPL. As such, there was a possibility that the interference observed was not via the primary wavetrains, and was perhaps due to unforeseen back-reflections between the fibre facets. Interestingly, there were no other regions of non-zero visibility within  $\Delta\text{OPL} \approx 50 \text{ cm}$  of the results shown, which makes the risk of having fundamentally incorrect OPLs in each arm unlikely. The need for matching fibre and airspace in each arm was debated, and led to the introduction of an “airspace delay” within the reference arm in figure 5.5. Fortunately, this immediately improved the SLD visibility envelope drastically in peak visibility, width and quality of fit (shown later in figure 5.24) in line with self-interference.

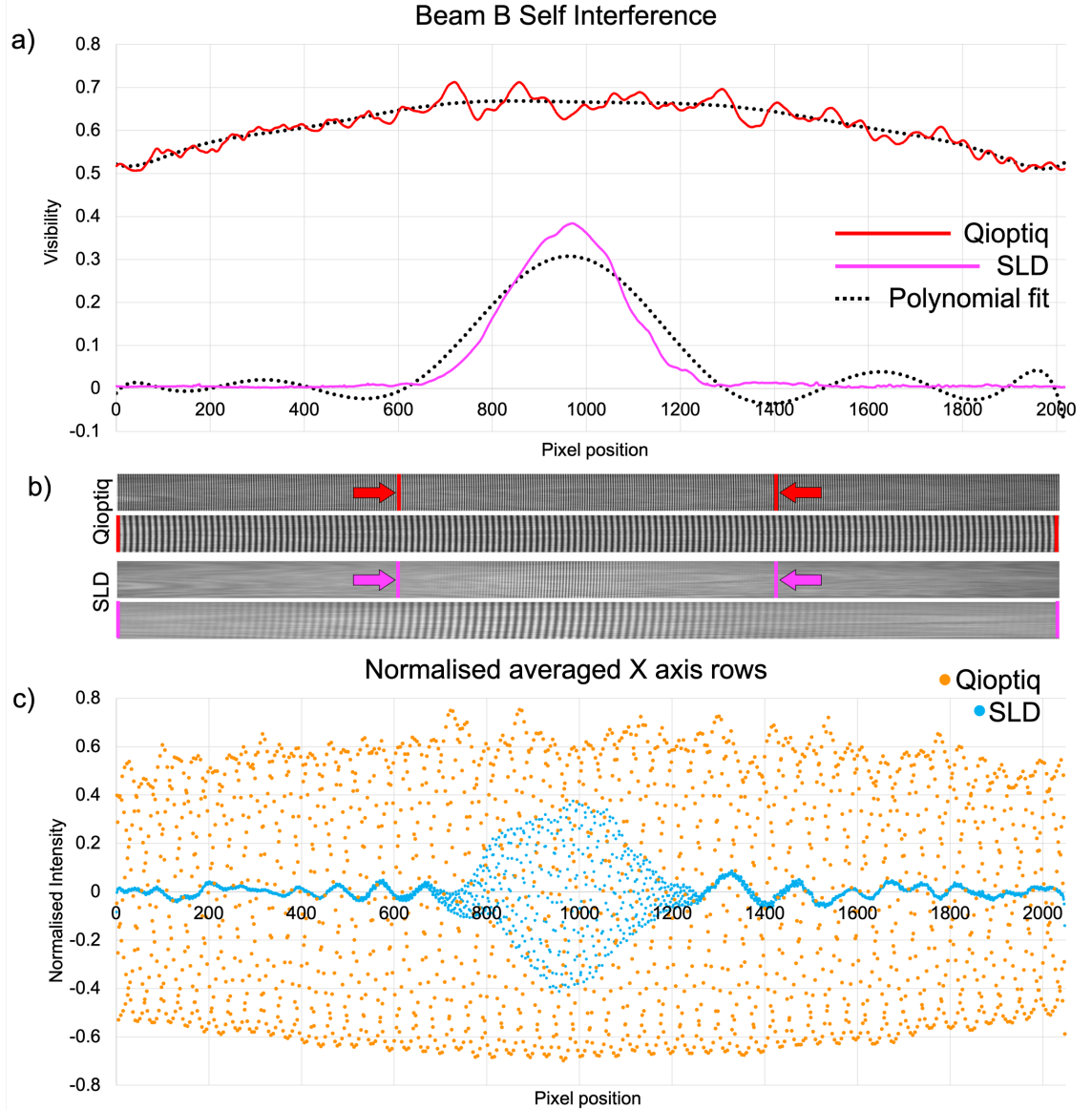


FIGURE 5.16: **Arm B self interference:** Arm B was connected to a FBS, which in turn was connected to output objective lenses F5 and F6 to self interfere at the camera. (a) the visibility envelope of the Qioptiq remains similar, whilst the SLD shows a marked improvement. (b) camera images of each interferogram were compressed and cropped to portray the drop-off in visibility. (c) An average over the rows demonstrates the relative envelopes of the bright and dark fringes, normalised to 0 – in both cases the profile of the dark fringes is cleaner than the bright fringes, which may make a more stable fit.

It must be stressed that this revelation was made at the end of the time allotted for this project, and only preliminary experimental data was recorded with the airspace included. This will be stated where applicable in section [5.5](#).

## 5.4 Structured light delay: hologram design

The aim of this investigation was to use a classical interference system to observe the relative  $v_g$  delay between Gaussian and Bessel beams. The following section focuses on the holograms used to structure and destructure the Bessel profiles within arm B.

In the first instance, Beam B propagates as the fundamental Gaussian mode along a single mode fibre. In order to structure this as a Bessel beam, the phase of an axicon lens was added to the conventional linear carrier grating of SLM1; after Bessel-type propagation along a free space length  $L$ , SLM2 was also encoded with an axicon lens to undo the first. In theory this reverts a sizeable amount of the original Gaussian beam energy to a Gaussian profile once more, which is optimal for recoupling and transmitting along a PMF towards the interference section.

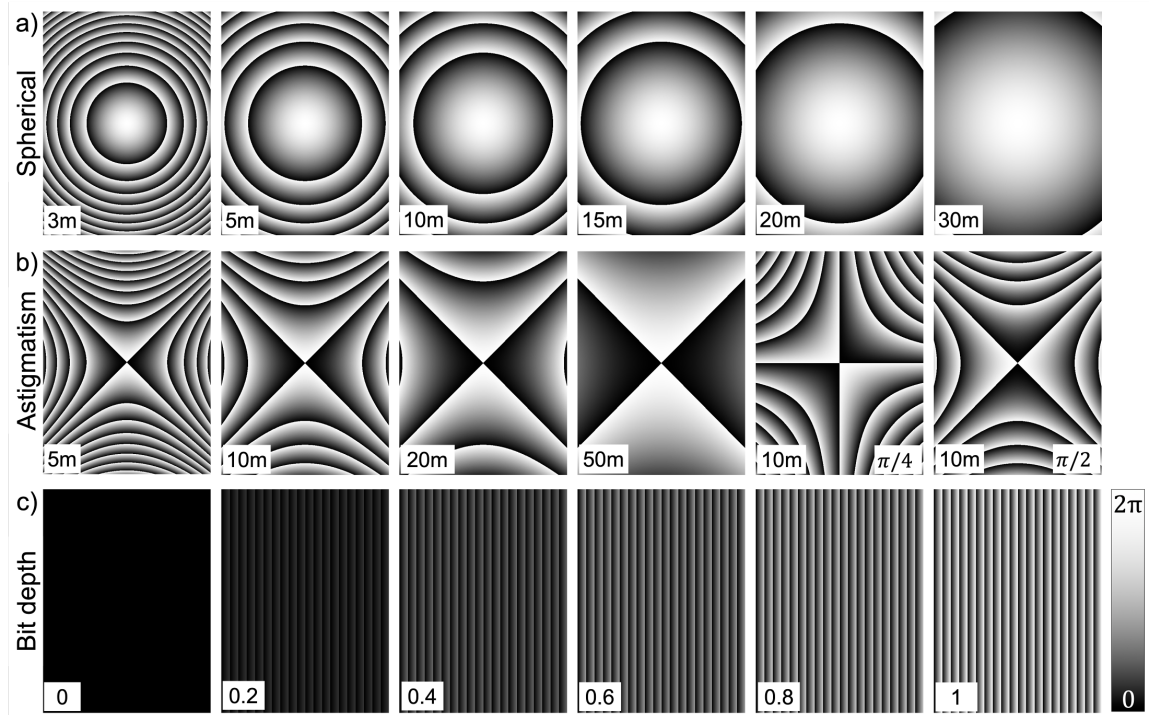


FIGURE 5.17: **Holographic aberration correction:** (A) spherical lenses were used to correct for varying amounts of defocus in the beam. (b) a pair of rotatable cylindrical lenses (with one inverted) can also be used to correct any astigmatism of the beam. (c) the bit depth of the entire hologram can be altered to provide a phase-independent amplitude modulation which reduces the total power in the beam by adjusting the originally 8-bit [0:255] range of the hologram phase depth.

The carrier hologram is a linear tilt grating, whose phase is defined as

$$\phi_c(u, v) = \frac{2\pi}{d_x}u + \frac{2\pi}{d_y}v \quad (5.19)$$

In this formalism,  $(u, v)$  and  $(x, y)$  represent Cartesian co-ordinates in the SLM and Fourier plane respectively;  $d_{x,y} = W_{x,y}/N_{x,y}$  are the slit separations, resulting in  $(N_x, N_y)$  phase cycles across each SLM width  $W_{x,y}$ . Typically this was encoded with  $(20, 0)$  phase cycles across SLM1 and  $(0, 20)$  across SLM2; as seen in figure 5.10 (b), this was deemed a suitable deviation from neighbouring orders whilst preserving coupling efficiency. Also, SLM2 diffracted the beams in an orthogonal direction to SLM1 to better distinguish between the various diffraction orders.

The programmable spherical correction phase applied to this carrier grating, as depicted in figure 5.17(top) is:

$$\phi_{spher}(u, v) = \exp \left[ -ik_0 \left( \frac{(u - u_{off})^2 + (v - v_{off})^2}{2f_{spher}} \right) \right]; \quad (5.20)$$

here  $f_{spher}$  is the focal length of the lens and  $(u_{off}, v_{off})$  is the offset from the centre of the SLM (featured in figure 5.9). As discussed in 5.3.2, this is used for correcting longitudinal defocus.

The accompanying astigmatism correction is the sum of a pair of cylindrical lenses of focal length  $f_{cyl}$ ,

$$\phi_{ast}(u, v) = \exp \left[ -ik_0 \frac{u^2}{2f_{cyl}} \right] + \exp \left[ -ik_0 \frac{v^2}{-2f_{cyl}} \right]. \quad (5.21)$$

which is useful for correcting aberrations in the transverse plane (5.17(middle)).

In the primary investigation of  $v_g$  delay in structured light, the structure is an additional phase  $\phi_{struct}$  added to the above carrier and correction phases. For an axicon lens, the phase applied is defined as:

$$\phi_{struct} = \phi_{axicon}(u, v) = k_0 \cos(\alpha)r \quad (5.22)$$

where  $r = \sqrt{u^2 + v^2}$  and  $\alpha$  is the angle the conical waves make with the optic axis. Therefore, the total phase hologram encoded onto each SLM is defined as

$$\phi_{SLM}(u, v) = \left| \phi_c(u, v) + \phi_{spher}(u, v) + \phi_{ast}(u, v) + \phi_{struct}(u, v) \right| \bmod 2\pi, \quad (5.23)$$

which is phase wrapped by modulo  $2\pi$ , the bit depth of the LC-SLM. Note that in addition to this hologram, SLM1 was eventually encoded with a bit depth control as a means to equalise the coupling power across the full set of axicon strengths used in measurements (figure 5.17(bottom)). For example, given a weak axicon strength coupling power  $P$  ( $\mu\text{W}$ ) at maximum  $\alpha = 0.005$  rad, the bit depth was adjusted for each axicon strength in the range  $\alpha \in [0 : 0.005]$  until all strengths coupled into the fibre with  $P$ . Arm A was then also reduced in power to match  $P$ .

### 5.4.1 Axicon lens optimisation

In the ray optics theory, we assume that the field either side of the structured section  $L$  is collimated, with evenly matched axicons on each SLM to achieve coupling down the fibre at F2. During the alignment procedures outlined in section 5.3.3, it was found that a stronger-than-anticipated spherical correction on SLM2 was required to couple the diffracted light down the fibre, as determined from its independent aberration correction. Secondly, it was found that the strength of axicon lens on SLM2,  $\alpha_2$ , required to be offset from  $\alpha_1$  by a factor of  $\sim 0.88$  to provide the best coupling at lens F2. Shown in figure 5.18(a) are the optimum power values of  $\alpha_2$  vs  $\alpha_1$ , which follow a linear offset. The resultant power increase is shown in part (b), compared to the original case where  $\alpha_2 = \alpha_1$ . The linearity of this axicon offset is indicative of a systematic defocus in the system; under ideal conditions, the beams either side of the structured path  $L$  are collimated. In this system, the offsets apply to each axicon strength equally, which should allow the delay recorded for each strength to be correct relative to one another. Clearly this is a discrepancy which must be accounted for in order to validate the theory, however in the first instance this strategy was adopted to test the relative behaviours of the setup.

The process of aligning the hologram of SLM1 onto SLM2 requires high precision beyond the initial overlap method described in section 5.3.3 – specifically, it requires an understanding of the focusing behaviour of various axicon strengths. The distance

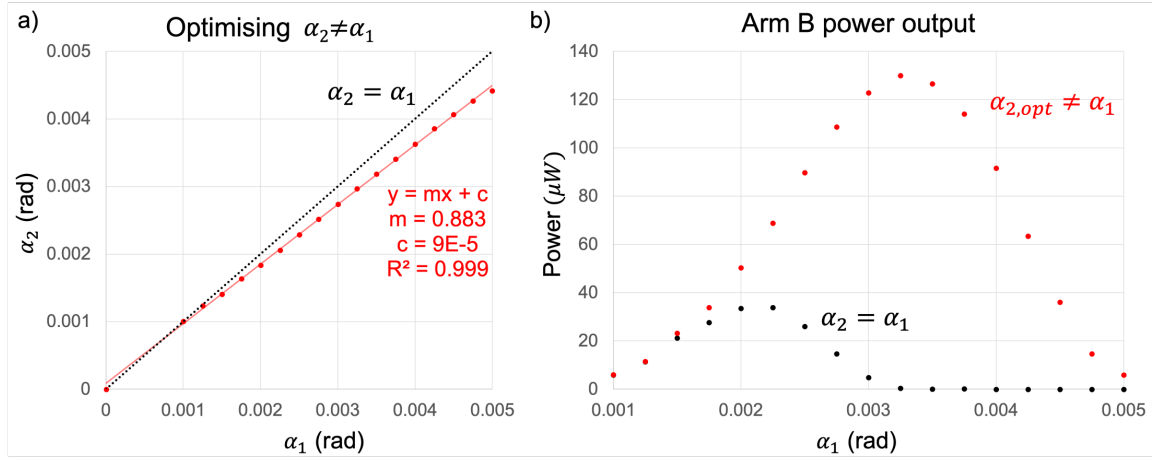


FIGURE 5.18:  $\alpha_2$  **optimisation**: (a) residual misalignments in  $z$  required  $\alpha_2 \neq \alpha_1$  – the optimal value was found to be a fixed linear offset from  $\alpha_1$ . (b) the resultant improvement in coupling power through the distal end of the fibre at F5 proved vital for detectable interference at large  $\alpha$ .

between SLMs is a constant,  $L = 0.8$  m. From the geometry in section 5.2.1, there is an optimum axicon pair with angle  $\alpha_{1,2} = \alpha_{opt}$  which fully inverts within  $L$  such that the maximum power is retained in the destructured beam. Determining the  $(u_{off}, v_{off})$  offset of the axicon lens on SLM2 was an iterative process which required adjusting the sign for  $\alpha_2$  for optimal iterative alignment.

Figure 5.19 presents the geometric argument: in case 1, it was found that for weak axicons  $\alpha_1 < \alpha_{opt}$ , SLM2 should display the opposite sign for best coupling – this is due to the wavefronts converging as they enter axicon 2. However, there exists a *flip point* where the rays neither diverge nor converge, the preferred sign flips, and  $\alpha_2 = (0.88)\alpha_1$  is then the optimum signage (case 2). A note of caution- the switching of weak axicon sense was strictly used for coupling iterative alignment only, and the forthcoming delay measurements in section 5.5 were obtained with *identical* same-sign axicons to accurately emulate fixed refractive lenses.

The optimal axicon  $\alpha_{opt}$  (case 3) for this system can be estimated by considering the geometry in figure 5.3: across the distance  $L$ , it is expected that a given portion of the beam will be steered by half of the size of the axicon lens in use,  $r$  i.e.  $\alpha_{opt} \approx \tan^{-1}(r/L)$ . For  $r = 3$  mm, we find that  $\alpha_{opt} \approx 0.0037$  rad. This is similar to what we see in practice; figure 5.18(b) shows that the peak power output from arm B occurs at  $\alpha \approx 0.0033$  rad with the flip point at  $\alpha \approx 0.0017$  rad. This indicates the appropriate set of Bessel beams for measurement as being about the region  $\sim \alpha = 0.0035$  rad.

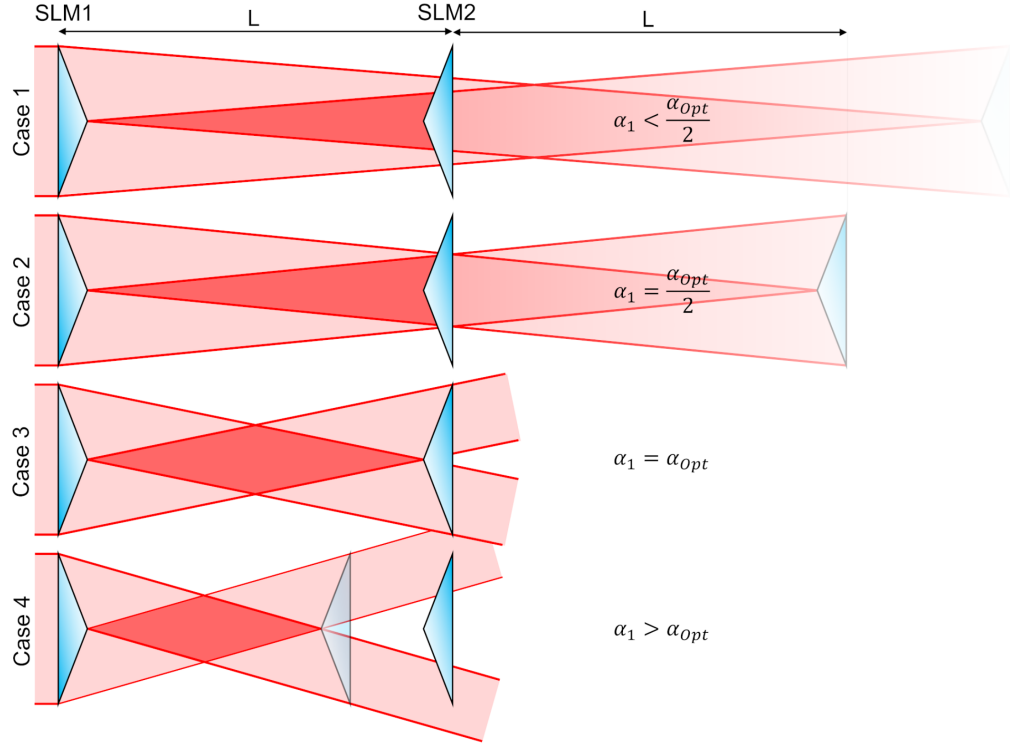


FIGURE 5.19: **Axicon strength at a fixed distance:** Within the fixed distance  $L$ , the strength of axicon  $\alpha$  dictates the convergence of rays and in turn the coupling behaviour. In the first case, weak axicons on SLM1 produce converging rays at SLM2, which indicates very poor coupling using opposite axicons. The flip point occurs when  $\alpha_1 = \alpha_{opt}/2$ . When  $\alpha_1 > \alpha_{opt}$ , the rays begin to diverge away from the centre of SLM2 and the coupling potential reduces considerably.

## 5.5 Structured light delay: results

The system was subject to an extended run of measurement testing throughout the investigation, in order to answer several questions: firstly, does this classical regime of the system validate the theoretical argument, and in turn the results in Giovannini *et al.* (2015) [201]? Secondly, how do the variables and intricacies outlined in previous sections impact the ability of the system to produce accurate and repeatable results? The following section presents an overview of the key findings of this experiment within ongoing developments in optimising the setup.

To probe the characteristic delay of Bessel beams, a range of axicon strengths  $\alpha \in [0 : 0.005]$  rad was displayed on both LC-SLMs. Figure 5.20(top) depicts several of the final holograms on SLM1, complete with carrier grating and correction phases (a); (bottom) shows the corresponding SLM2 holograms.

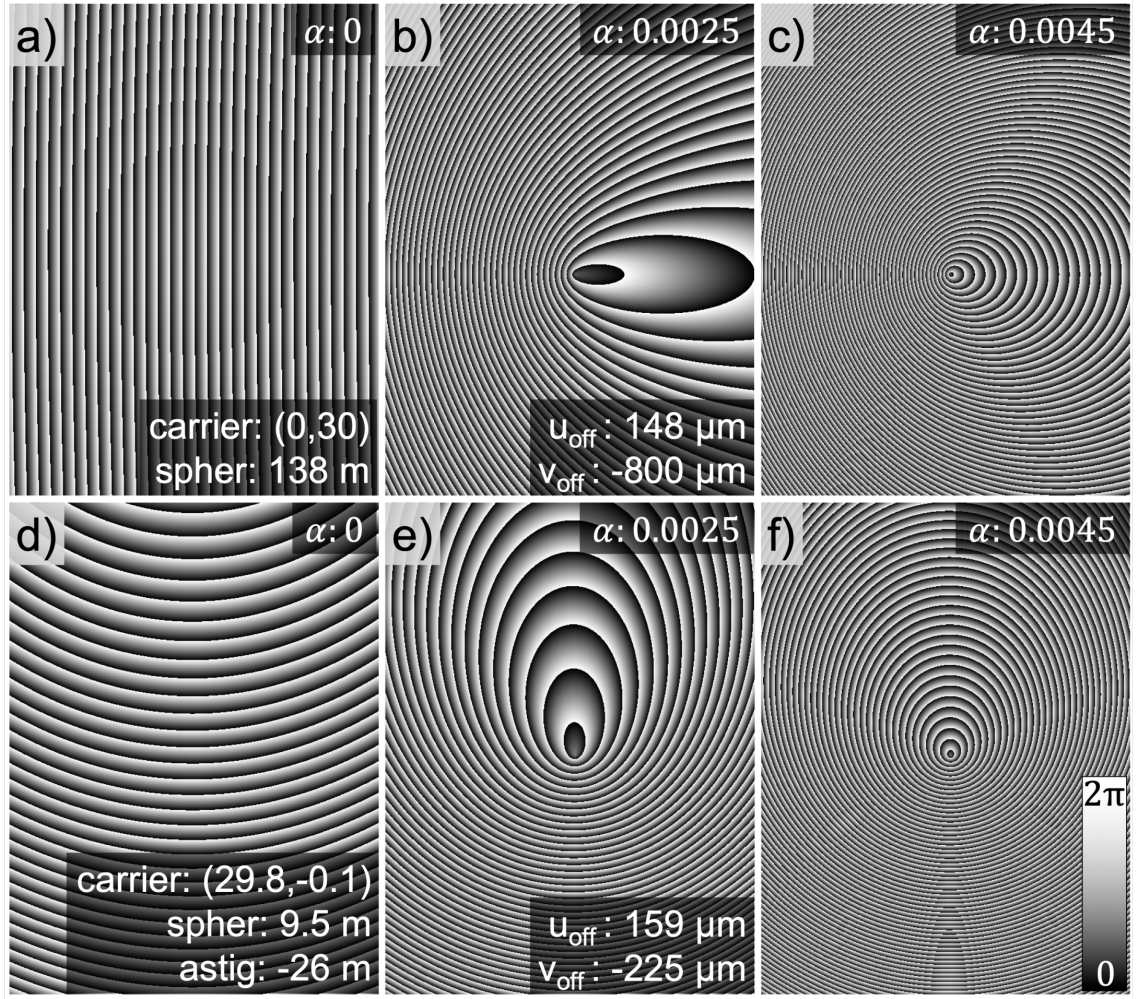


FIGURE 5.20: **Axicon lens delay holograms:** The holograms used for SLM1 (top) and SLM2 (bottom) in measuring Bessel beam  $v_g$  delay, complete with carrier and correction holograms with lateral offsets. (a,d) are the base holograms when  $\alpha = 0$ . (b,c,e,f) show weak and strong axicon holograms for Bessel delay.

### 5.5.1 Qioptiq source delay testing

The vast majority of testing was completed using the Qioptiq source – although the bandwidth was comparatively small, the coupling power, visibility maximum and operating wavelength were all favourable for fine-tuning the system. Using a source of  $\Delta\lambda_{Qio} > 0.08$  nm required a great number of interferogram fringes to reveal a slowly-varying visibility envelope: generally between 405-760 fringes were used, which translates to 2.69-5.06 pixels per fringe – approaching the Nyquist limit.

On any given test day, the variables  $\alpha$  and  $(u_{\text{off}}, v_{\text{off}})$  encoded onto SLM2 were tuned for the optimum coupling of each axicon strength around the optimum  $\alpha_{\text{opt}}$ -

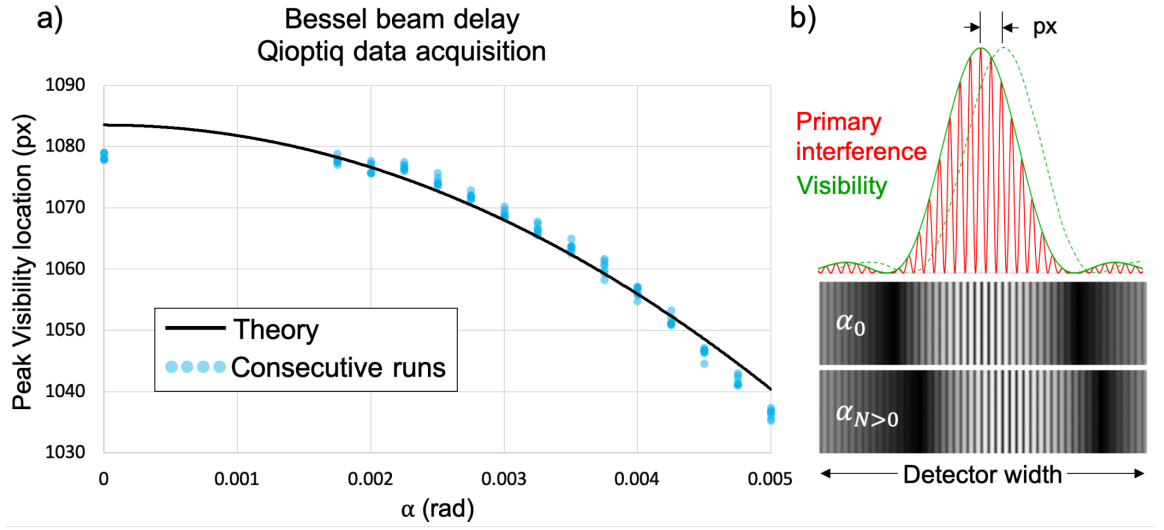


FIGURE 5.21: **Bessel beam visibility pixel shift:** The data acquisition involved recording the lateral pixel position of peak visibility on the camera, from  $\alpha \in [0 : 0.005]$  rad. The best agreement to the theoretical fit (black) occurs around  $\alpha_{opt}$  where there is maximal coupling of beam B. Here, the theory has been offset to determine if the data points follow a trend. (b) a simulated sketch of the shift in the visibility envelope, and its effect on the position of the peak (green) – the extent of the envelope drop off has been exaggerated for clarity.

necessary to couple in sufficient light into Arm B. The holograms were displayed in turn at a rate of  $\sim 0.5$  Hz, and repeated a maximum of 20 times in a given session. The lateral pixel shift of the detected visibility envelope maximum was recorded and plotted against the axicon strength, in radians.

Figure 5.21(a) demonstrates one such data set of  $N = 6$  consecutive runs, where the black line is the theoretical trend of  $L\alpha^2/2$ . Recall that there was a near-zero coupling of the light at lower  $\alpha$  (figure 5.18), which causes a noise-affected visibility and unreliable measurements – therefore only axicon strengths above  $\alpha_{opt}/2$  were deemed reliable. The high sensitivity and residual stability issues of this interferometer also caused a flicker of the peak value. This can be observed in the spread of values for repeated measurements. In general, there is a correlation with the theoretical parabolic curve, although the  $\alpha = 0$  position did not match up in this instance – probably due to residual transverse structure in the plane wave reference. Part (b) shows a sketch of the effect varying  $\alpha$  has on the visibility envelope position with respect to the primary interference of beams A and B.

The bulk of the investigation was spent attempting to achieve viable interferograms with visibility envelopes which agreed with the measured bandwidths of the sources.

Considerable time was also spent optimising the alignment and stability of the setup, as well as expanding on the capabilities of the system (see chapter 6). Preceding the employment of the airspace delay in arm A, the Qioptiq source was relied upon, with mixed results.

Recall from figure 5.14(a) that the Qioptiq source bandwidth (estimated as  $> 0.08$  nm) would necessarily require many more fringes on the detector to reveal an envelope which could be well-defined. Furthermore, this visibility profile had a noise level which risked providing false peaks for the polynomial fit used. Figure 5.22 depicts 4 unrelated data acquisitions, acquired separately across a 6 month period. Each data set was therefore using a different alignment under distinct conditions – this data is included to portray the wide variety of delay curves observed compared to the theory (black), in spite of any confidence in the alignment by optimising the power down the fibre.

The pixel delay shown has been converted to  $\mu\text{m}$  by

$$\overline{\Delta z} = \frac{1}{N} \sum \frac{\lambda \Delta z_{px}}{P}, \quad (5.24)$$

where  $\Delta z_{px}$  is the pixel shift observed,  $P$  is the pixels per fringe detected across the interferogram and  $N$  is the number of consecutive iterations. The theoretical delay is  $L\alpha^2/2$  where  $L = 0.8$  m and is plotted in  $\mu\text{m}$ . One common characteristic of the Qioptiq delay curves measured was that the data tended to be a strong match with theory around  $\alpha_{opt}$ , before a stronger than anticipated delay was observed at  $\alpha > \alpha_{opt}$ . Note that in the region of  $\alpha_{opt}$  the full width at half maximum (FWHM) of the envelope is at its maximum and remains stable; either side of this region, the loss of power in arm B resulted in a reduced FWHM, and consequently reduced reliability in the fit.

Much of section 5.3 concerned the procedures used for optimal coupling of the system, from manual alignment to hologram offsets. To validate the need for these measures, figure 5.23 illustrates the profound effect of sub-optimal axicon offsets ( $u_{off}, v_{off}$ ) on SLM2. Part (a) and (b) demonstrate the deviation from theory when the hologram is shifted in the  $x$  axis over  $\sim 1$  mm, whilst (b) shows that for  $y$ . From this we can say that with increasing  $\alpha$  comes a much stronger reliance on the hologram offsets, which is expected due to the angles of convergence of strong axicons; this effect is also seen in figure 5.22. Thus the alignment procedure from day to day was necessary to

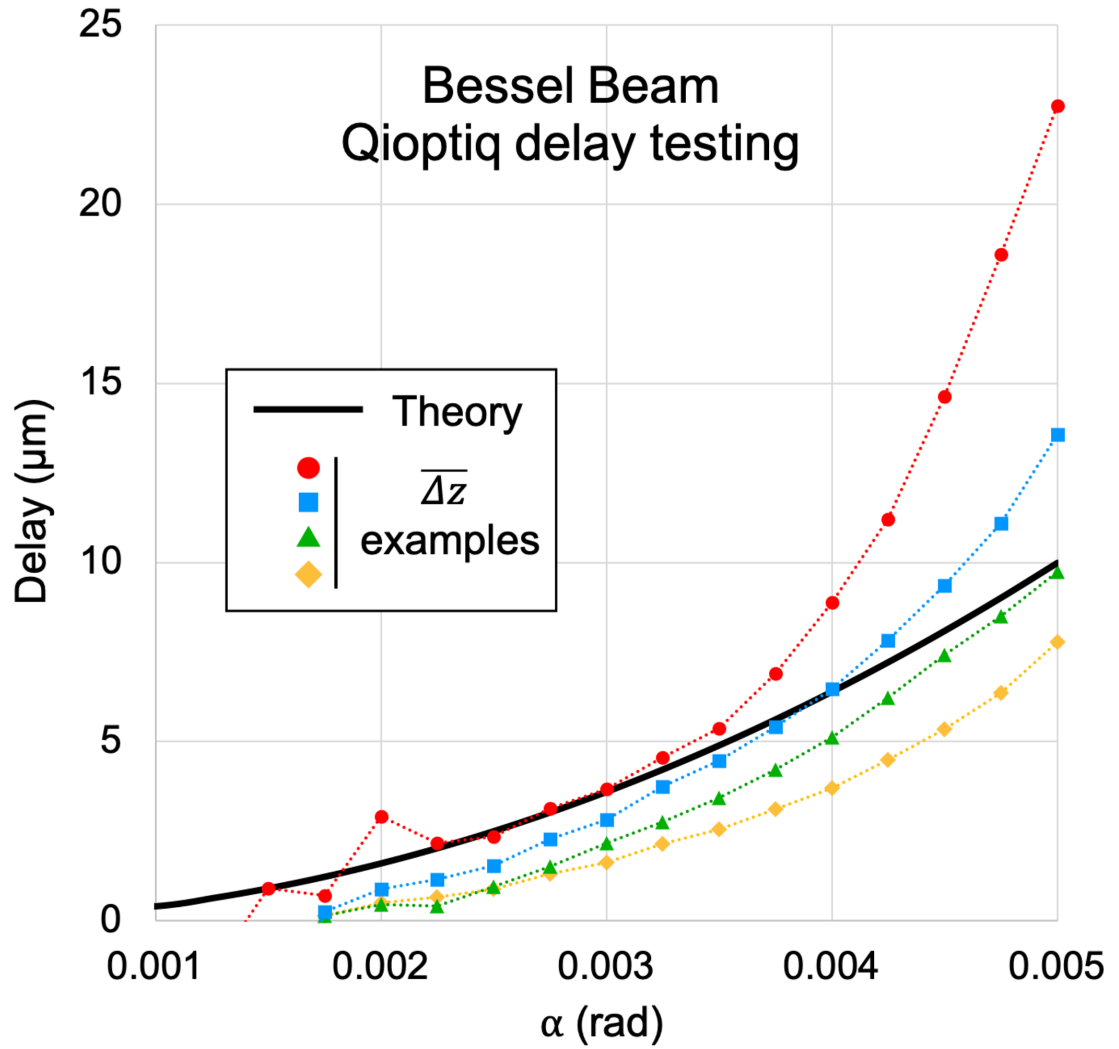


FIGURE 5.22: **Qioptiq Bessel beam  $v_g$  delay:** A typical example of the delay observed for the relatively narrowband Qioptiq source, in  $\mu\text{m}$  – note that the poor coupling at  $\alpha < 0.002$  rad reduced the visibility of the interferogram, resulting in unreliable data points. However, the overall trend shows good agreement until larger  $\alpha$ . In general, the Qioptiq source  $v_g$  delay observed was higher than anticipated beyond  $\alpha_{opt}$  – this may be due to a systematic alignment issue, or highlights an error with the envelope and its ability to be fit to accurately.

determine the optimal coupling, and correct any drift in the alignment. We expect a delay of between  $[0-10]\mu\text{m}$  across the range – interestingly, a change in the  $x$  offset on the SLM caused almost twice as much deviation as the  $y$  offset – this could perhaps be due to the order of the carrier gratings (SLM1 has horizontal gratings, SLM2 has vertical), or indicative of the initial coupling angle down the fibre in arm B. Note that the same effect was observed for SLM1. Given the extreme delays present and the poor fit of even small deviations in the hologram position, this testing was only conducted to observe the behaviour when adjusting the digital parameters when the physical parameters are fixed.

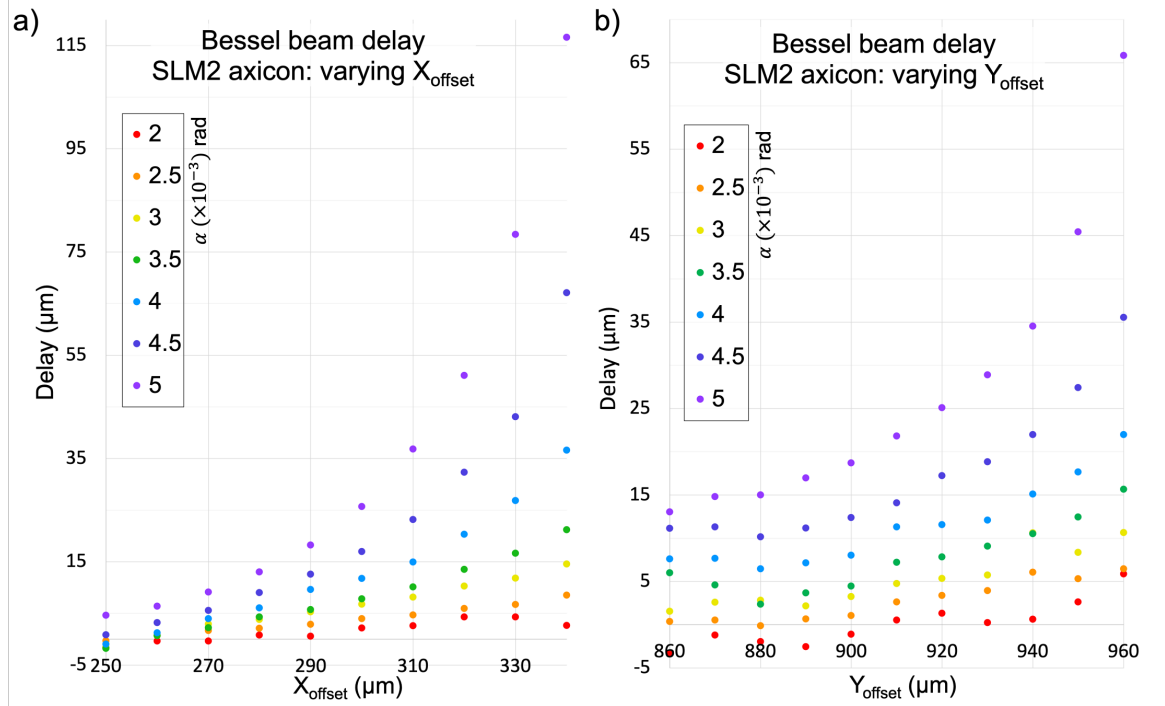


FIGURE 5.23: **Bessel beam delay versus axicon alignment:** Consecutive data runs with varying  $(u_{\text{off}}, v_{\text{off}})$  offsets of the axicon on SLM2 revealed a high dependence of delay on beam alignment. (a) a shift of the axicon hologram in the  $x$  direction was around twice as strong as in the  $y$  direction (b). The same characteristics were observed across both SLMs separately.

### 5.5.2 Broadband $v_g$ delay in Bessel beams

The SLD source of bandwidth  $\sim 18.5\text{ nm}$  provided no sensible results until the airspace and fibre lengths in the OPLs were matched at the very end of the laboratory time allotted. Figure 5.24(a) presents the resulting visibility envelope achieved,

complete with the polynomial fit used to determine the envelope maximum pixel location. This visibility profile is similar in width and shape to those found in the self-interference tests (figure 5.16), and a maximum visibility of  $\mathcal{V} = 0.73$  indicates that this is likely the interference of the two primary wavetrains from arms A and B. The camera image in (b) was compressed and cropped to show the fringes. (c) shows the average of the x-axis rows, normalised to zero. Specifically, we can see the modulating envelopes of the bright fringes (above) and dark fringes (below).

A number of improvements were also made to the measurement operation for this test. Firstly, the bit depth control shown in figure 5.17 was applied to each axicon on SLM1, to equalise the power in stronger and weaker coupling Bessel beams; this resulted in a similar envelope FWHM across most of the  $\alpha$  range. Secondly, the residual flicker in the system was better accounted for by taking differential measurements – each value was immediately compared to a consecutive  $\alpha = 0$  base value, and subtracted. These base values taken either side of the data points shown were successful in improving the consistency over more lengthy data runs, however improvements to the speed of the data acquisition would contribute even more to the stability in such a time-sensitive interferometric system.

Figure 5.25 presents the Bessel beam  $v_g$  delay achieved with the SLD source with this improved visibility envelope, over  $N = 9$  measurement iterations. In order to establish what kind of trend was measured, the data was fitted with several trends based on the general equation

$$\Delta z_{g,Bes}(\alpha) = \frac{L}{2}\alpha^B + C; \quad (5.25)$$

here,  $L$  is the structured path length,  $B$  is the polynomial order and  $C$  is a vertical offset. In practice,  $L$  was measured with an accuracy of  $\pm 5$  mm, however its impact on the delay accuracy is not the limiting factor.

From the theory we expect to observe an  $\alpha^2$  relationship, with  $C = 0$  ( $\mu\text{m}$ ). In figure 5.25, the trends are plotted with variables  $[L, B, C]$ ; the theory is therefore plotted with  $[0.8, 2, 0]$ . In an attempt to better interpret the measurements, further trends of unconstrained  $C$  giving  $[0.8, 2, 0.681]$  (dotted) and a best fit  $[0.794, 2.036, 1.42]$  (dashed) are also included. From the  $R^2$  values in the figure, it is clear that there is a systematic offset in the measured delay of Bessel beams; furthermore, the delay varies as  $\alpha^{2.036}$  and not  $\alpha^2$ . Of particular interest is how this trend somewhat resembles that

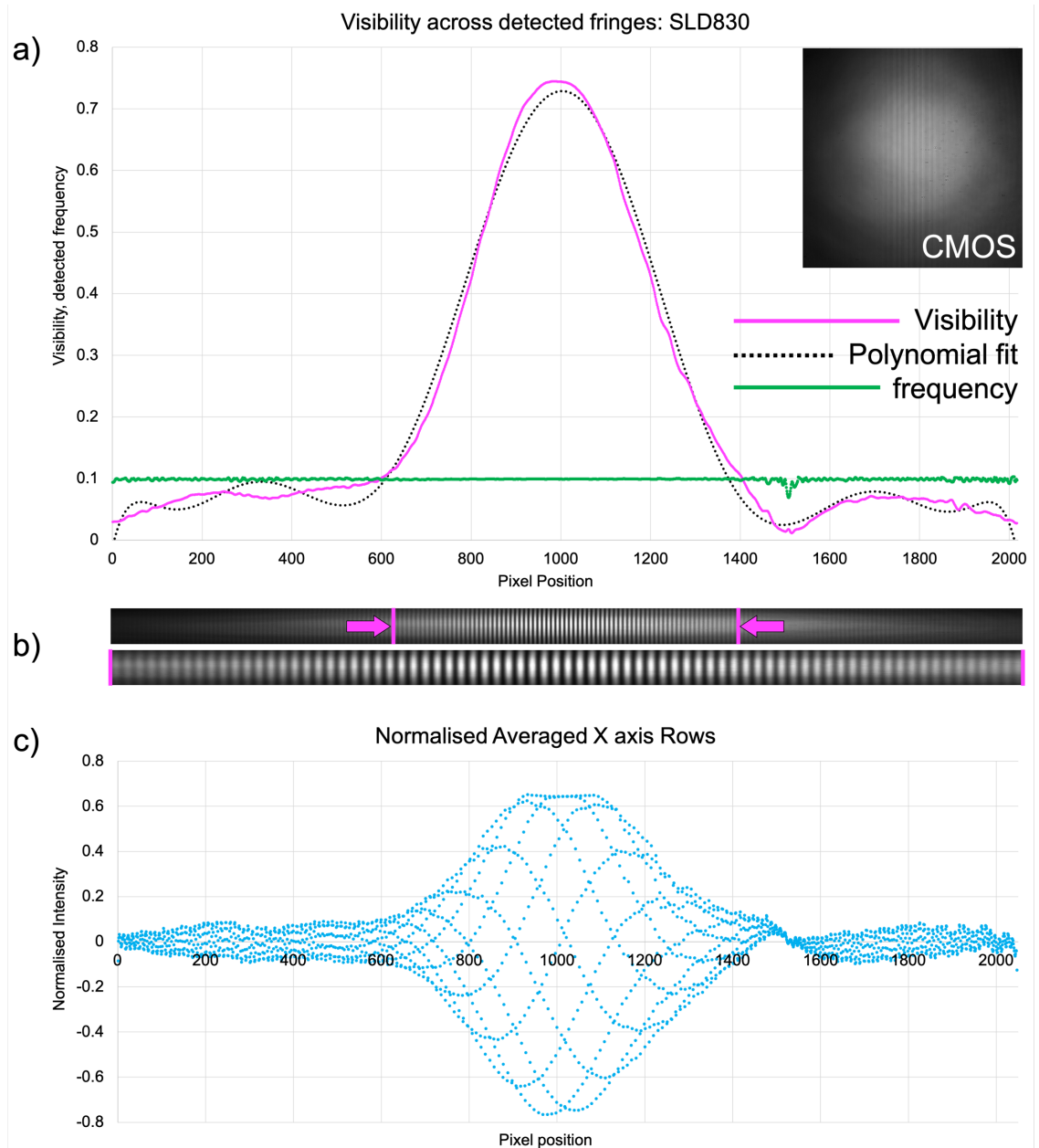


FIGURE 5.24: **Adjusted SLD visibility envelope:** (a) the latest visibility profile, after the airspace and fibre OPLs were matched in each arm. The interferogram (inset) achieved on the CMOS detector shows a well-defined sinc profile and a markedly higher  $\mathcal{V}$ . (b) the interferogram (top) compressed and (bottom) cropped to show the actual fringes and their visibility drop-off. (c) the normalised rows of the interferogram show the profile of the bright and dark fringes on the top and bottom curve respectively. In this figure the bright fringes look to be clipped in intensity – this was later resolved by reducing the camera exposure slightly (both the average and maximum pixel intensity should be monitored for maximal yet unsaturated measurements).

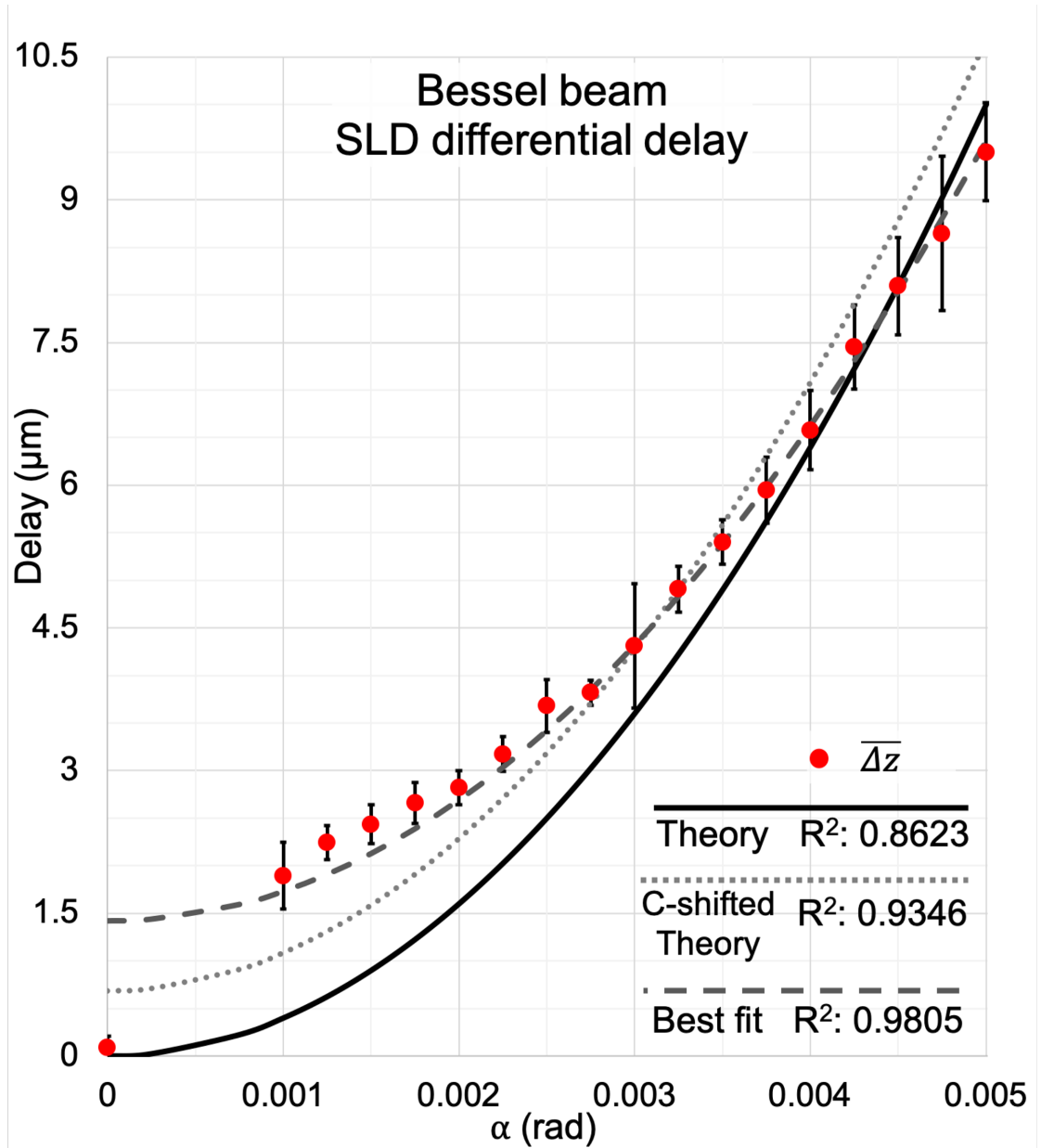


FIGURE 5.25: **SLD Bessel beam  $v_g$  delay:** The most current Bessel delay result at the time of writing; the averages of 9 consecutive measurements are marked in red, with an error bar of 1 standard deviation ( $\sigma$ ) from the spread of delays across each  $\alpha$  measured. The trends plotted reveal that shifting the  $C$  intercept of the purely theoretical delay (dotted line) is not enough to adequately describe the trend measured – instead, an offset  $\alpha^{2.036}$  fit (dashed line) was found to be a better fit.

reported in [201] with the same structured arm (via Hong-Ou-Mandel interference of quantum correlated photons).

The results presented are from the initial stages of probing the system with a well-contained visibility envelope; as such the source(s) of these discrepancies can only be speculated. The experiment itself presents a formidable challenge in beam structuring, which can be summarised as follows: firstly, what are the necessary adjustments needed to correctly collimate/structure the various optical elements in arm B? Secondly, what is the coupling behaviour of the system when these supposedly accurate adjustments are applied simultaneously? It was discovered early on that these problems are difficult to reconcile at the same time, especially with such a sensitive system.

Perhaps naively, correction lenses applied to SLM2 and the distance between lens F2 and the fibre facet were both adjusted until maximum power was achieved. This is in spite of collimation testing, and was wholly necessary to produce interferograms with sufficient signal to acquire reliable datasets. As such, it is possible that the beams in the structured arm deviate slightly from collimated Gaussian and Bessel beams of angle  $\alpha$ . It remains to be seen if these deviations can be characterised sufficiently to be included in the theoretical model.

It may also be the case that the visibility maximum detected at  $\alpha = 0$  becomes a neighbouring near-maximal peak for  $\alpha > 0$  – this would result in the data being offset equally across the range. From figure 5.23 it is clear that alignment inaccuracies of only tens of  $\mu\text{m}$  can result in a very different delay trend.

For a measured  $L = 0.794 \pm 0.005$  m average delay compared to a non-structured beam for  $\alpha = 0.00225$  rad was measured as  $\Delta z_{g,Bes} = 3.174 \pm 0.18 \mu\text{m}$ , compared to the theoretical case  $\Delta z_{g,Bes} = 2.025 \mu\text{m}$ . For the case  $\alpha = 0.0045$  rad, the delay measured was  $\Delta z_{g,Bes} = 8.093 \pm 0.51 \mu\text{m}$ , compared to the theoretical case  $\Delta z_{g,Bes} = 8.1 \mu\text{m}$ . Only at higher axicon strengths does this correlate well with the theory; regardless, the delay observed follows a definite trend which deviates only slightly from the theoretical variables [L,B,C] with a characteristic offset.

As mentioned previously, only preliminary results were obtained before the submission of this thesis for examination. In the intervening months before publication, attempts were made to better align the system to realise the trend seen in the theory. Firstly, the structured arm was re-collimated by minimising the beam divergence in the near (30 cm) and far field (7.5 m) of the collimating lenses and SLM planes

as before. However, this simple collimation strategy was employed with both the Qioptiq (643 nm) and the SLD (833 nm) sources; it was found that when the fibre output stage at F1 was collimated for the SLD source, the Qioptiq source produced a beam waist in the far field which was  $\sim 4\times$  smaller. This amounts to a subtle change in the distance between the fibre facet and the collimating lens between sources, due to a wavelength dependent deviation in the numerical aperture of the optics. It is believed this was at least partially responsible for the systematic offset in the measurements obtained with the SLD source previously, and would have a knock-on effect on the required SLM correction lenses needed, which altogether offset the collimated/structured states.

Furthermore, 3" mirrors were used in this instance to remove the risk of clipping the beam profiles. The resultant SLM correction lenses, combined with the adjusted collimation of the fibre ports at lens F1 and F2, resulted in a markedly different axicon coupling behaviour, as depicted in appendix C. Compared to the previous trends, shown in 5.18, I found that the optimal  $\alpha_2$  was found to be closer to  $\alpha_1$  on any given alignment attempt, which reduced the offset across the range. More importantly, there was found to be sufficient power across the range to disregard this optimisation altogether, such that  $\alpha_2 = \alpha_1$ .

The resulting differential  $v_g$  delay obtained, also in C, shows a clear improvement on the previous attempts, and is a reasonably strong  $L/2 * \alpha^2$  fit with  $R^2 = 0.9881$  for  $L = 0.782$  m. The precision in this measurement is also improved, with smaller error bars  $\sigma$ , and passes through the origin (plane wave reference point).

## 5.6 Structured light delay: discussion and conclusion

The investigation into the  $v_g$  delay of Bessel beams using classical interference incorporates the beam shaping and alignment techniques of chapters 3 and 4 and introduces an additional level of complexity in both the alignment and analysis stages. As such, the experiment underwent a great number of iterations which either enhanced or degraded the stability and accuracy of the results obtained. This section will reflect on the main features of the current setup and their impact in achieving a system which can reproduce sensible results which are indicative of the geometry. I will then outline the possible next steps in improving the setup, and suggest more investigations which can be undertaken in future.

### 5.6.1 Evaluating the setup and design

From the comparison tests between the two laser sources available, as expected the  $\Delta\lambda = 18.5$  nm of the SLD outperforms the  $> 0.08$  nm width of the Qioptiq source for creating a well-defined visibility envelope on interference. Our confidence in being able to apply a polynomial fit to measure the shift in the peak was directly due to this bandwidth and its envelope width, first evidenced by the Michelson test. The SLD source did however provide some issues; at  $\lambda = 832.36$  nm it can only be aligned using an infrared IR-viewer, and was not optimised for the LC-SLMs nor the PM fibres used (visible, 630 nm respectively). In future it may be more appropriate to re-introduce the SC source from chapter 4, and use a bandpass filter of width  $> 20$  nm to equal or improve upon the short coherence length of the SLD.

During the setup phase of the experiment, the two arms consisting of PM fibres and an airspace structuring section were all measured by hand, and the approximate OPLs were matched. This resulted in a defined length of interference along  $z$ , with no other traces of interference observed. Our understanding at the time was that this had to be the primary position of matched optical paths. However, the visibility profile observed using the SLD source and this setup (see figure 5.14) spanned far too many fringes and with such a low contrast that its veracity was questioned. As a consequence, the Qioptiq source was used for the majority of the investigation; meanwhile, prolonged efforts to reconcile the discrepancies included changing the

FBS and optical fibres, including various polarisers, trying different interferogram profiles and adjusting the SLD power and coupling.

Towards the end of the investigation, the use of self-interference both independent of the setup (figure 5.15) and within the setup (figure 5.16) led to a breakthrough in proving the coherence length of the SLD source. In the final stages of the investigation, an airspace delay was added to arm A to equalise the OPL of air and silica fibre lengths in each arm. The resultant interference, shown in figure 5.24, transformed the reliability of the setup, and led to the final results depicted. The importance of matching the media in which light propagates, beyond merely matching the total OPLs, cannot be understated, and in future could also be probed in a separate investigation using high precision measurements of fibre lengths via time-of-flight.

### 5.6.2 Sources of error

The results presented for the  $v_g$  delay of Bessel beams were obtained using a system whose sensitivity is by virtue of its complexity; to improve upon the stability and accuracy of the results, it is necessary to discuss the sources of error within the experimental setup.

In the ideal case, the beam incident on SLM1 from output coupling lens F1 should be a collimated Gaussian beam; in the absence of highly structured holograms, it should remain collimated upon reflection from SLM1 and SLM2, before coupling once more down the fibre, (where F1 and F2 are identical). Any departure from this caused by the non-flat phase profile of the SLMs introduces a significant defocus and transverse aberration in the beam which had to be corrected by non-negligible focal lengths of correction lenses. It would be pertinent to fully probe the collimation of the beams either side of the SLMs with new techniques; this should lead to a more accurate geometry in figure 5.3, and optimise the coupling efficiency. Re-collimating the stages using the SLD source (originally the Qioptiq source) appears to have made a significant difference to the collimation achieved either side of the structured region  $L$ .

Given the dependence of Bessel beam delay on the position of the axicon lens holograms on the SLMs depicted in figure 5.23, it is clear that the accuracy of the values obtained is influenced greatly by the alignment of the beam on the SLM windows.

By offsetting the holograms on each SLM on the order of 10s of  $\mu\text{m}$ , the coupling efficiency with which a given part of the structured beam from SLM1 was successfully optimised to couple back into a fibre. Great care was taken to ensure the correct diffraction orders and locations of the target beam were matched up correctly. Nevertheless, it may be appropriate to convert this alignment stage from an indirect measurement (of power) to a direct measurement of correlation.

During the interference testing and subsequent delay runs, it was found that the position of the peak visibility fluctuated with a flicker of  $\sim 2\text{-}10$  pixels at a rate of  $\sim 1$  Hz, with an encompassing drift of the interferogram over time. A number of steps were taken to minimise this effect, including using isolator legs on the bench, insulating the fibre optics and using blackout materials in a “lights off” environment. By its very nature, an interferometer is sensitive to external vibrations, including those outside the laboratory and high frequency vibrations/heat from nearby technology. Whilst averaging over many data runs has helped to reveal the trends of the data captured, future experimentation should also consider the time-dependent behaviours of the laser source, e.g. polarisation and power oscillations, particularly when using PM fibres. Furthermore, the setup of the bench could be further optimised by total isolation of the SLM drivers from the optical table.

### 5.6.3 Future work

Over the course of this investigation, the technical challenges involved in measuring  $v_g$  with an assortment of beams have all been addressed. The system currently shows promising functionality by way of the Bessel beam delay tests presented above, the accuracy of which can be increased by further optimisation of the alignment and measuring process. The SLMs within the beam shaping system provide a degree of control on the scale of microns which ought to be sufficient compared with the size of the incident beam, and can be used with high precision to couple a sizeable portion of destructured light. The interferometer now has a stable design which removes any extraneous optics and can provide a uniform interferogram at a wide range of distances and angles.

In accordance with the original work which provided the motivation of this investigation [201], the next stage was to consider beam structures whose  $v_g$  delay is more

difficult to quantify: a focused beam, for example, is wholly reliant on accurate characterisation of the incident beam. My long term objective was to demonstrate these results classically to verify the behaviour of structured light, in the hopes that there may be opportunity to explore more exotic structures, such as varying degrees of optical speckle.

# Chapter 6

## Group velocity of structured light: further studies

### 6.1 Further studies: introduction

The following chapter is a continuation of the work in chapter 5 by way of measuring the  $v_g$  delay of a confocal telescope, as well as employing the wavefront correction methods from chapter 4 to investigate optical speckle (de)structuring and coupling down a fibre. This is in anticipation of potential future investigations into the  $v_g$  delay of varying degrees of optical speckle.

The investigation presented in chapter 5 involved the use of a fibre-based interferometer, in which the propagation of a beam of Gaussian profile (A) was compared with that of a Bessel beam (B). A pair of LC-SLMs were used to (de)structure the beam using a combination of tilt, correction and axicon lens holograms. Beams A and B were classically interfered; using a low coherence source, the envelope of visibility could be observed across the interferogram. A shift in the OPL of beam B, achieved by modulating with various strengths of axicon lens, corresponded to a shift in the fringe position of the visibility envelope; by extension, this is the  $v_g$  delay of a Bessel beam.

## 6.2 $v_g$ delay of a confocal telescope

To compliment the results presented in section 5.5, there remained the opportunity to further verify the work of Giovannini *et al.* (2015) [201], by investigating the  $v_g$  delay of a *confocal* (same foci) telescope. That is, instead of a pair of axicon lenses of strength  $\alpha_{opt}$ , both SLMs display an additional spherical lens hologram  $\phi_{struct} = \phi_{spher}(u, v)$ . The phase of this hologram was previously defined in equation 5.20; here,  $f = 0.397$  m and hologram offsets  $(u_{off}, v_{off})$  remain unchanged from the Bessel beam measurements.

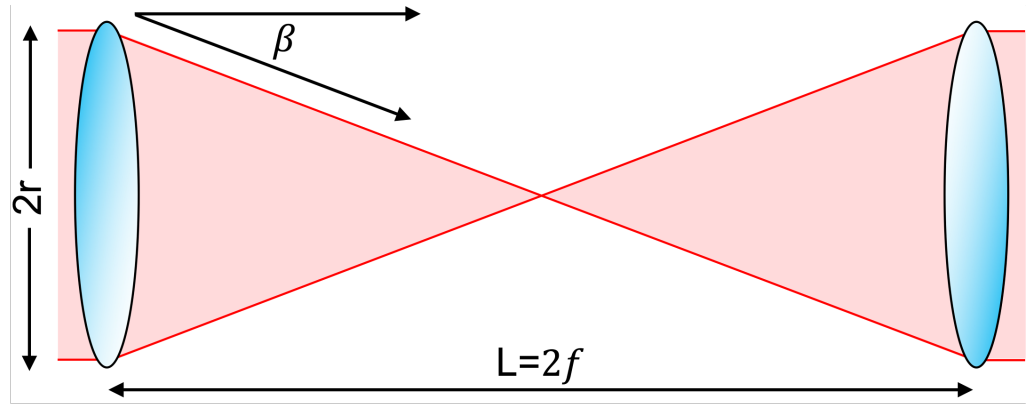


FIGURE 6.1: **Confocal telescope delay:** Adapted from [201]. An incident plane wave of radius  $r$  is focused down to a spot in the back focal plane of a spherical lens of focal length  $f$  with an angle  $\beta$ . The beam inverts and diverges such that at a second identical lens  $L = 2f$  from the first, the beam exits as a collimated beam once more.

Consider the geometry depicted in figure 6.1, recreated from [201]: a pair of lenses separated by  $L$  form a confocal telescope; for maximum coupling efficiency, each lens has a focal length of  $f = L/2$ . For an incident beam of radius  $r$ , the converging beam leaving the first lens will propagate along the distance  $L/\cos\beta$  until it reaches the second lens in an inverted position. This corresponds to a delay from the optical axis of  $\Delta z = L/\cos\beta - L$ . By using the similar triangle with  $\cos\beta = f/\sqrt{r^2 + f^2}$  and a Taylor expansion, we find that  $\Delta z \approx r^2/f$ . In the ideal case of an incident Gaussian profile with  $1/e^2$  beam radius  $w$ , the expectation value  $\langle r^2 \rangle = w^2/2$  (derived in appendix B). It follows that for a beam of  $1/e^2$  radius  $w$ , the predicted delay over a distance  $L = 2f$  is

$$\Delta z = \frac{w^2}{2f} = \left(\frac{w}{f}\right)^2 \times \frac{f}{2}. \quad (6.1)$$

The term  $w/f$  is a measure of the beam divergence which is controlled by the numerical aperture of the lenses. Despite the simplicity of the geometric arguments, the predictions for the delay of Bessel beams and focusing beams are backed up by more in-depth theoretical models, which are explained in [211, 229]; specifically, that the transverse wavevector  $\langle \hat{\mathbf{k}}_{\perp}^2 \rangle = \frac{2}{w_f^2}$  where  $w_f = \frac{2f}{k_0 w_0}$  is the focusing waist of an initial beam waist  $w_0$ .

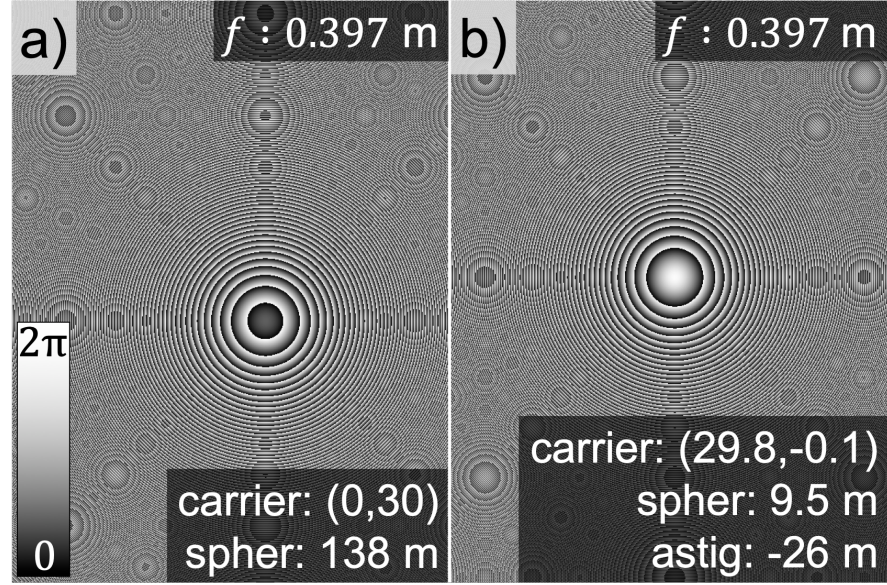


FIGURE 6.2: **Confocal lens phase holograms:** (a) SLM1 and (b) SLM2 display a combination of the spherical lens hologram of  $f = 0.397$  m, and the same carrier grating and correction lenses as in figure 5.20.

The resultant SLM phase holograms  $\phi_{SLM}(u, v)$ , which also incorporate the carrier gratings and correction phases, are shown in figure 6.2. During the  $v_g$  delay measurement acquisition, the holograms were switched to spherical lenses of either  $f = 0.397$  m or  $f = 1 \times 10^6$  m and a set of differential measurements were recorded. The latter focal length is effectively infinite, and allows for easier programming of the SLMs – the base  $\alpha = 0$  holograms in 5.20(a,d) are equivalent to the holograms with  $f = 1 \times 10^6$  m, when there is effectively no structure and the beam diffracts with an approximately Gaussian profile.

During the confocal lens  $v_g$  delay data acquisition, differential measurements of the above focal lengths were used. The pixel delay was determined as the average of the

difference between the visibility maximum when  $f = 0.397$  m ( $x_i$ ) and the neighbouring non-focused cases  $f = 1 \times 10^6$  m ( $x_{i\pm 1}$ ) such that

$$\overline{\Delta z_{lens}} = \frac{1}{N} \sum_{i=1}^N \left| \frac{1}{2} \left( (x_{i-1} - x_i) + (x_{i+1} - x_i) \right) \right|, \quad (6.2)$$

where  $N$  is the total number of measurements.

Figure 6.3(a) demonstrates a typical  $\Delta z_{px}$  delay in terms of lateral pixel shift between the two cases, whilst (b) shows the absolute pixel differential between nearest neighbours, with an average pixel shift across 200 measurements found to be 105.68 pixels. Inset shows the interferogram profile; in this instance there is secondary interference occurring due to surface oxidation in the gold coated mirrors M5,6 – this in turn manifested in the visibility envelope as a higher order envelope disrupting the expected sinc profile.

Figure 6.4(a) demonstrates the lens delay after replacing said mirrors, i.e. the visibility became that shown in figure 5.24. In this test an average pixel delay of 89.73 was recorded across 500 measurements over an acquisition time of  $\sim 600$  s. Over this time frame we can clearly see an overriding drift in the position of the visibility maximum, however with differential measurements this should not affect the final result.

Recall from equation 6.1 that the theoretical delay achievable by a confocal lens system  $\Delta z_{g,lens}$  over a length of  $L = 2f$  is  $w^2/2f$ , compared to that for a Gaussian beam. In this case,  $w$  is the half width of the beam profile at  $1/e^2$  the maximum of the Gaussian profile. It was therefore necessary to measure the true  $w$  of the beam exiting output coupling lens  $F1$ , and before SLM1. It was imperative that this value be measured with the utmost accuracy, due to its role in determining the delay measured – what follows is a description of the logic behind the value obtained. A series of beam profiles were measured using a DSLR camera (based on its sensor size, portability and availability at the time).

In order to best fit to the beam profiles measured, a few Gaussian distributions were considered. Firstly, in the ideal case

$$f(x) = Ae^{-2\left(\frac{x-\mu}{w}\right)^2}, \quad (6.3)$$

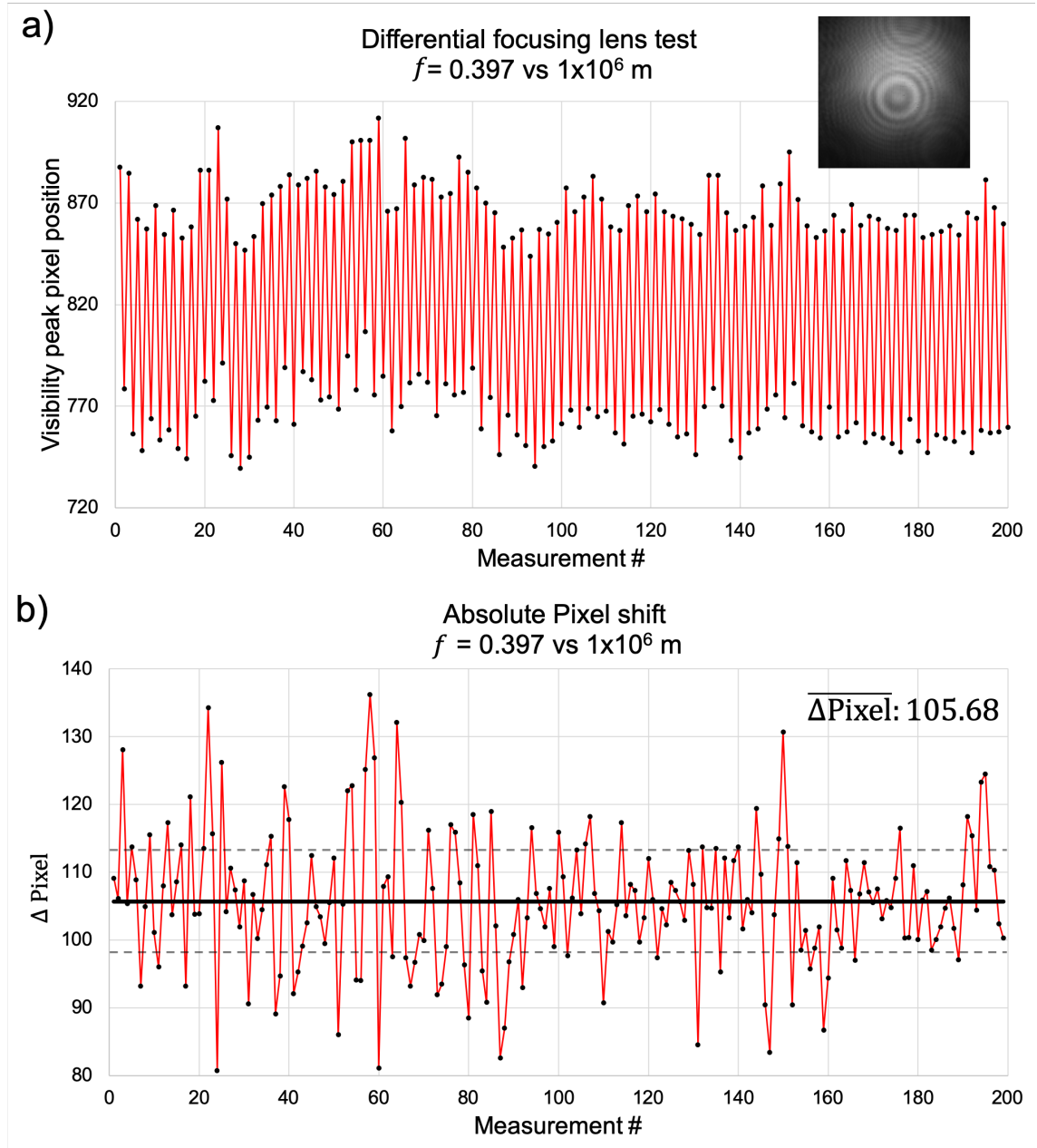


FIGURE 6.3: **Confocal lens delay test 1:** The first confocal lens test after an improved visibility envelope was obtained. This test, spanning 200 measurements, shows a relatively consistent delay between  $f = 0.397 \text{ m}$  and an effectively infinite lens ( $f = 1 \times 10^6 \text{ m}$ ). Note that the mirrors M5,M6 were inspected and found to have microscopic surface damage, resulting in secondary interference fringes (inset). (b) the differential pixel shift plotted about the average of 105.68 pixels, with one  $\sigma$  error lines (dashed), reveal a well behaved delay.

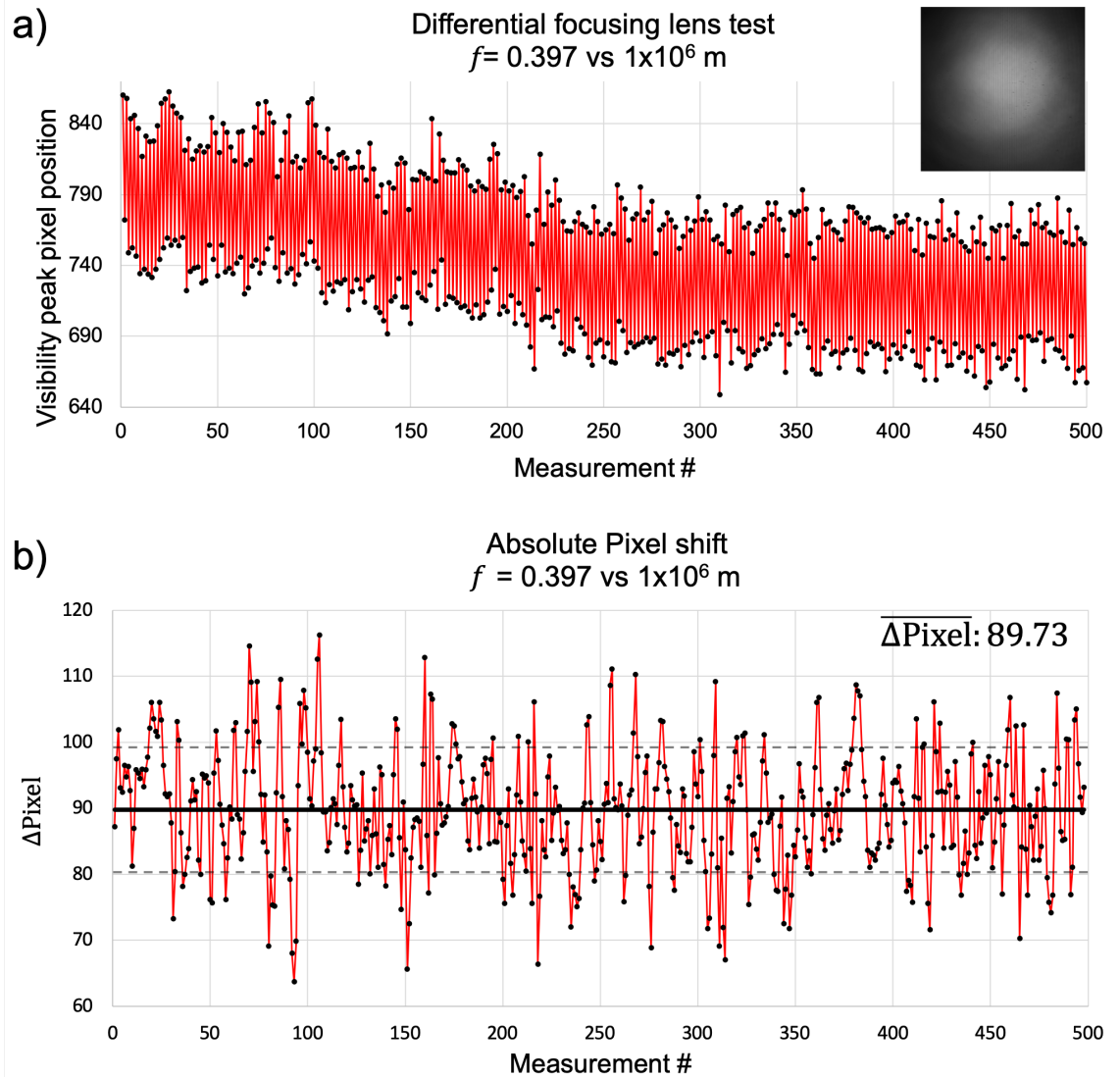


FIGURE 6.4: **Confocal lens delay test 2:** (a) (inset) replacing the large mirrors M5,M6 resulted in a much improved visibility envelope profile (shown in 5.24). With this particular alignment, extended lens delay testing across 500 measurements produced an 89.73 pixel shift. Note that the peak of the visibility envelope drifts  $\sim 80$  pixels over 10 minutes. (b) the one  $\sigma$  standard deviation of values halves (dashed) is plotted on top of the average pixel shift in the differential measurements. In the absence of any obvious alignment errors, further testing is required to verify whether test 1 or test 2 (or neither) may be considered characteristic of the system.

where  $A$  is the amplitude,  $w$  is the half width at  $1/e^2$  and  $\mu$  is the mean of the distribution. Shown in figure 6.5(a,b) (green), this fit was deemed insufficient to accurately define the beam profile (red). Instead, a fit of

$$f(x) = Ae^{-2\left(\frac{x-\mu}{w}\right)^2} + Bx + C, \quad (6.4)$$

provides a tilt  $B$  and offset  $C$ ; this was found to fit the profiles much better. In (c), several beam profiles are illustrated – the profile was extracted from the red plane of the original image (top). (below) are the three different polarisation states recorded: clearly the beam at lens F1 remains unpolarised, with more power coupled into the horizontal state – this is only a source of inefficiency which can be corrected in future by employing a linear polariser after F1.

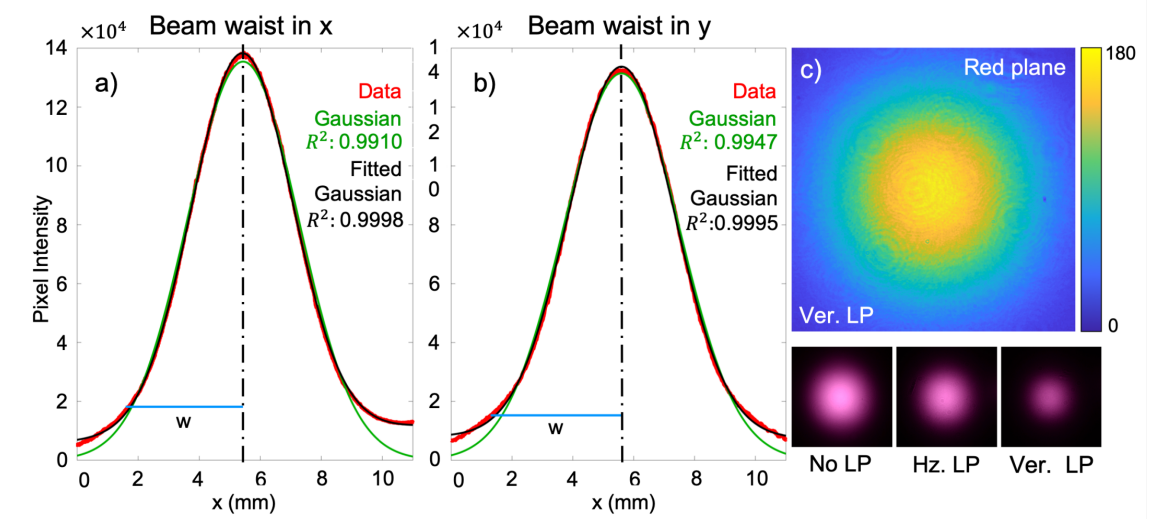


FIGURE 6.5: **Gaussian fitting to extract beam waist** A selection of beam profiles taken by a DSLR camera were analysed to determine  $w$ . Each image was loaded into Matlab, where a fitting tool was used to fit a Gaussian distribution along both the (a)  $x$ -axis and (b)  $y$ -axis. The data (red) was tested against a simple Gaussian (green) and offset tilted Gaussian (black); the latter was used to extract  $w$  (blue). (c) shows a heat map of the red plane from the original image – (below) photos included to show the 3 polarisation states analysed for reference.

Several beam profiles like those shown were recorded by placing the camera between lens F1 and SLM1 at two planes in  $z$  – 87 mm and 320 mm from SLM1. Furthermore, a linear polariser (LP) was placed at lens F1, in order to filter the incident beam in several polarisation states.

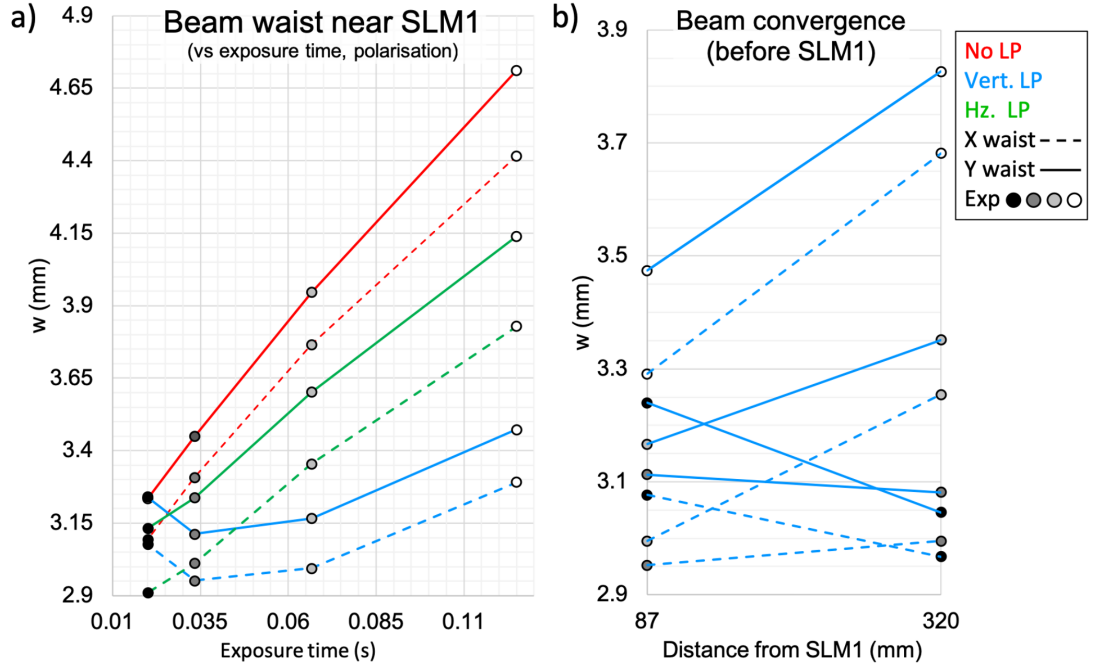


FIGURE 6.6: **Non-linear exposure effects and beam convergence** (a) to illustrate the intricacies of beam waist characterisation, the  $w$  recovered from several beam profiles with different polarisations/exposures is shown. In particular, an LP was placed before the camera in the vertical (blue), horizontal (green) and removed completely (red). In fact, we need only consider the vertical component, which is the only one which SLM1 can modulate. A non-linear sensor sensitivity may also be responsible for the exposure-based trend seen; we can choose the lowest width observed to mitigate background broadening effects. (b) considering beam profiles extracted from two different  $z$  planes before SLM1 reveals a slight convergence of the beam – this in turn can be factored in by extending the trend to the plane at 0 mm from the SLM i.e. the actual beam waist incident on SLM1.

The SLD source is unpolarised; coupling through the PM FBS and PM fibres, it was apparent that both polarisations enter the airspace structuring arm to contribute to the overall beam waist. However, since the LC-SLMs used have a vertical modulation axis, we can expect that only the component of polarisation will reach the fibre coupling at lens F2. Figure 6.6(a) shows the effect of polarisation and DSLR exposure time on  $w$ , for a plane 87 mm from the SLM. Plotted in red is the beam waist with no polarisation filter – the contribution from both polarisations. In green and blue are with an LP in the horizontal and vertical state respectively. The beam profiles were taken along both axes, where dashed lines indicate the  $x$ -axis. From this graph we can clearly see that the beam waist measured increases with exposure – this may be due to a non-linear CMOS sensor sensitivity at relatively large exposures.

Furthermore, the waist along the  $y$ -axis is consistently larger than that in  $x$ ; in a

practical sense, measuring with a manually aligned camera on the optical bench runs the risk of being skewed in the horizontal direction (whereas the vertical is aligned by using opto-mechanical mounts on the bench itself). Therefore, it may be more sensible to only consider the beam waist in the vertical direction.

On top of this analysis, figure 6.6(b) depicts a simple convergence test of the beam before SLM1. The collimation testing in section 5.3.2 concluded that the beam was well-collimated before SLM1, however by recording beam profiles in two  $z$  planes, we can determine directly any convergence of the beam before it reaches SLM1. Shown is the detected convergence of the beam in the  $x, y$ -axes across all four exposures recorded. By calculating the trend of each exposure, we may determine the  $C$  intercept at the SLM plane – the true original beam waist – without removing SLM1.

When considering the above analysis, we need only consider the vertical beam profiles projected onto the SLM1 plane, and may factor in the non-linearity of the sensor by careful selection of the exposures included. There is also the risk of waist broadening due to ambient light detected – in this case, the lowest  $w$  measured in the vertical polarisation will be used, i.e.  $w = 3.098$  mm. For completeness, using all vertical profile exposures yields a similar result ( $w = 3.219 \pm 0.126$  mm to one  $\sigma$ ).

The expected  $v_g$  delay for a confocal lens pair of focal length  $f = 0.397$  m using equation 6.1 is  $\Delta z_{g,lens} = 12.02$   $\mu\text{m}$  using the chosen measured half width,  $w = 3.098$  mm.

Given the variability in the Bessel beam testing for much of the project (figure 5.22), the measurement of confocal lens delays was sporadic. That said, the measurements in figures 6.3 and 6.4 represent the latest findings; the former was acquired after introduction of the airspace delay in arm A, and the latter was acquired after the mirrors M5,6 were replaced when it became clear that surface defects were causing misleading secondary interference fringes (figure 6.3 inset).

To determine the experimental lens delay obtained, we may simply convert the measured pixel delay into metres. In test 1, we found that  $\Delta z_{px} = 105.68 \pm 7.49$  px; in test 2 (with replaced mirrors), we found that  $\Delta z_{px} = 89.73 \pm 9.15$  px. With a detected periodicity of fringes  $px/fringe = 10.269$  and source of  $\lambda = 832.36$  nm, this results in a measured delay of  $\Delta z_{lens,exp} = 8.57 \pm 0.61$   $\mu\text{m}$  in test 1 and  $\Delta z_{lens,exp} = 7.27 \pm 0.74$   $\mu\text{m}$  in test 2.

There are several elements to consider when trying to account for the differences here. Firstly, the original work of [201] used the same apparatus and reported a considerably smaller beam waist of  $w = 2.32 \pm 0.09$  mm. The results reported in that work concur with a beam of this size, which in theory would be  $\Delta z = 6.7 \mu\text{m}$ . This is closer to what we observe in the current system, albeit with a larger measured  $w$ .

The dependence on  $w$  clearly dominates the delay measured – the question remains as to what proportion of the beam which receives this delay is coupled down the fibre at F2 towards the interferogram, and to what extent suboptimal hologram offsets ( $u_{off}, v_{off}$ ) affect this delay. In future, these variables will be studied in more detail.

Given the results presented above were preliminary findings during the final laboratory time before the submission of this thesis, there was a window of opportunity to continue this testing thereafter, presented in appendix D. Whilst the results above suggest a degree of instability in the  $k$  vectors coupled down the fibre day to day, the work to be emulated [201] pointed to a measuring strategy that did not wholly rely on empirical measurement of a single  $w$  to find  $\Delta z_{g,lens}$ . Introducing a Gaussian amplitude mask on both SLMs, of radius  $w_1$  is a means by which the beam waist  $w$  can be artificially constrained between the SLMs; this has the effect of reducing the strength of perpendicular  $k$  vectors reaching the interferometer in a controlled manner.

Figure D.1 depicts the experimental measurement of confocal lens delay versus Gaussian aperture radius  $w_1$ . A Gaussian fit on both SLMs leads to an altered expectation value, such that the theoretical trend from section 6.2 becomes  $\Delta z_{g,lens} = \frac{w_1^2}{4f}$ . The result then shows a strong fit for  $w_1 < w$  where  $w = 2.32 \pm 0.09$  mm as measured above. It can therefore be said that due to residual misalignments in the system, the group velocity delay of a focused beam is highly dependent on the three dimensional coupling strength into the interferometer, and more work could be done to better understand the constraints of this coupling.

### 6.3 (De)structuring optical speckle

The previous investigations into the  $v_g$  delay of beams with Bessel (chapter 5) and focused beam structuring (6.2) illustrate the free space delay of light when applying well-documented boundary conditions on a Gaussian beam. Given the potential of the experimental setup to probe any number of beam structures that are capable of being (de)structured to propagate down a fibre, discussions with my supervisors led to the proposal of a novel investigation into a very different but pervasive beam structure – *optical speckle*.

In section 2.1.7, the behaviour and methods for the creation of optical speckle were briefly stated. Its fine structure suggests there is a more involved mechanism to accurately theorise the effect on  $v_g$ , however we can approximate it based on its variables. Consider again the axicon pair in figure 5.3: an axicon of strength  $\alpha_{opt}$  and of spatial extent  $a$  is characterised by  $\tan \alpha_{opt} \approx \alpha_{opt} \approx a/2L$  such that  $\Delta z_{Bessel,opt} = a^2/8L$ . We may exploit this simple geometry, and determine the expectation of  $\alpha$  aggregated for optical speckle, based on the spread of plane waves combined to generate such speckle. For a single randomised plane wave on the SLM, we may define the grating fringe separation  $d = w/N$  where  $N$  is the number of cycles and  $w$  is the side length of the SLM. The resultant transverse components  $k_{x,y}$  can then be represented by  $(2\pi/d_x, 2\pi/d_y)$ . In the same way an axicon lens has a single  $\mathbf{k}$  vector, the same radial component can be produced for any one tilt hologram, where  $|k_x + ik_y| = k_r$ . By trigonometry, this radial component is offset from  $k_0$  by  $\alpha_r = \arcsin(k_r/k_0)$ , such that across many randomised plane waves, the total observed speckle delay is

$$\Delta z_{Speckle} \approx \frac{L}{2} \frac{\langle \hat{\mathbf{k}}_{\perp, speckle}^2 \rangle_{|\psi(z_1, k_0)}}{k_0^2} = \frac{L}{2} \langle \alpha_r^2 \rangle. \quad (6.5)$$

The holographic generation of speckle as it appears in nature would require an unfeasibly large number of overlapping wavevectors with exceptional resolution; furthermore, destructuring and fibre-coupling such a field would prove difficult. Instead, it was decided that an approximation of speckle could be generated by SLM1 with a known finite set of random wavevectors, which could be generated quickly and destructured in several ways. The following method for programmable optical speckle on an LC-SLM was devised by Dr. Stellinga in collaboration with myself using the National Instruments LabVIEW software.

In the first instance we want to generate a set of  $N$  wedge phase gratings within a certain range of the ideal coupling, which when combined, diffract a plane wave into an approximate optical speckle upon propagation along length  $L$ . In general, we define the resultant speckle field as a superposition of three or more constituent wavevectors, where each phase component  $\phi$  contains the wavevector magnitude  $k$  for each constituent plane wave.

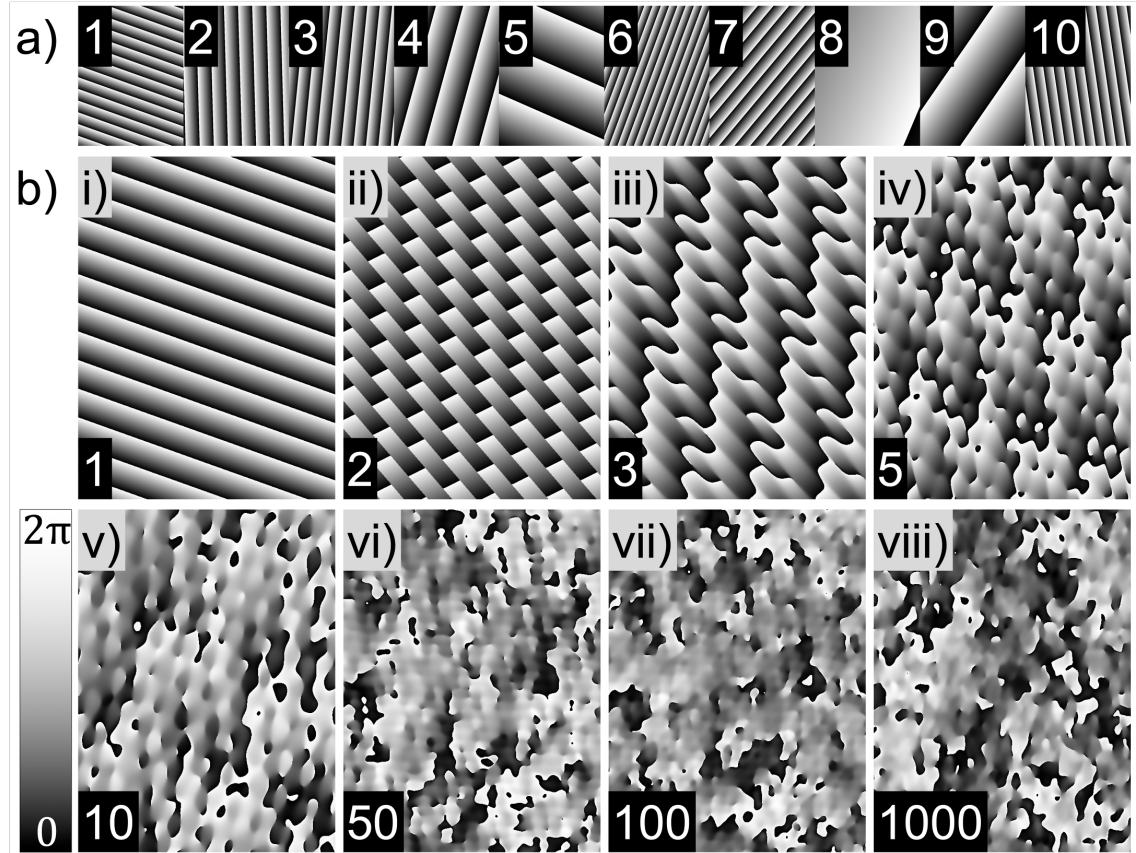


FIGURE 6.7: **Generating holographic optical speckle:**(a) the first  $n = [0 : 10]$  plane waves with random  $k$  vectors. (b) the summation of  $n$   $k$  vectors for i)  $N = 1, 2, 3 \dots 1000$ ] for the same seed value gradually approximates an optical speckle.

The following procedure for holographic speckle generation was designed to ensure a thoroughly randomised field whilst remaining programmable. Firstly, a uniform white noise generator was used to create a set of three pseudorandom values, using a chosen random seed of 1. These values were then used as independent seeds for the three grating variables to be assigned to each of the  $N$  holograms: the polar angle, azimuthal angle and additional phase offset  $\phi_{off}$ . The latter was used to ensure that the plane waves were totally independent from one another. The polar angles

were formed as noise with a Gaussian profile and some standard deviation  $\sigma$ . The azimuthal angle and phase offset were both uniform noises with an amplitude of  $\pi$ . These values were then converted to randomised  $(N_{cyc,x}, N_{cyc,y}, \phi_{off})$  variables for each plane wave, where  $\phi_{off} \in [0 : 2\pi]$ . Here,  $(N_x, N_y)$  are the number of phase cycles across the SLM in each axis.

With a uniform amplitude of 1, the phase hologram sent to SLM1 comprised the speckle wavevectors with phase cycles  $(N_{cyc,x}, N_{cyc,y})$ , combined with the carrier grating  $(N_{c,x}, N_{c,y})$  and the appropriate correction lenses (spherical and astigmatism):

$$\phi_{speck,hol}(u, v) = \left| \phi_c(u, v) + \phi_{spher,ast}(u, v) + \phi_{speck,tot}(u, v) \right| \bmod 2\pi. \quad (6.6)$$

Here, the total phase component of the speckle contribution is extracted from the resultant field after combining the complex fields from all plane waves:

$$E_{speck,tot}(z, t) = E e^{i\phi_{speck,tot}} = \sum_{n=0}^{N-1} E_n e^{i(\phi_n + \phi_{off,n})}, \quad (6.7)$$

where  $\phi_{off,n}$  is the additional phase offset. The hologram of each plane wave is the same form as that used for the carrier grating in equation 5.19 with slit separations  $d_{x,y}$  (such that  $d_{x,y} = W_{x,y}/N_{cyc,x,y}$ ). Note that  $E_n$  may also be randomised, however in this instance was set to 1 for all plane waves. Figure 6.7(a) portrays the pseudorandom generation of the first 10 phase gratings. Part (b) portrays the given superposition of a set of wavevectors when  $n = [1 : 1000]$ ; note that when  $n = [1 : 5]$  the superposition of so few wavevectors maintains a periodic grating structure, whilst  $n > 10$  begins to take on a more randomised phase distribution.

The first column of figure 6.8(a-d) demonstrates different strengths of speckle field which arrive at SLM2 for  $N = 1000$  wavevectors with  $\sigma = 5, 10, 20, 40$  cycles from the carrier tilt. The second column shows the phase addition of speckle, carrier tilt and aberration correction holograms displayed on SLM1. Finally, the last column is a set of camera images of the plane at SLM2, which shows the overlap of the undiffracted Gaussian zero order from SLM1 with the desired speckle field- it is required that the carrier tilts on each SLM combined are enough to diffract the (de)structured speckle away from the unwanted orders on the fibre facet.

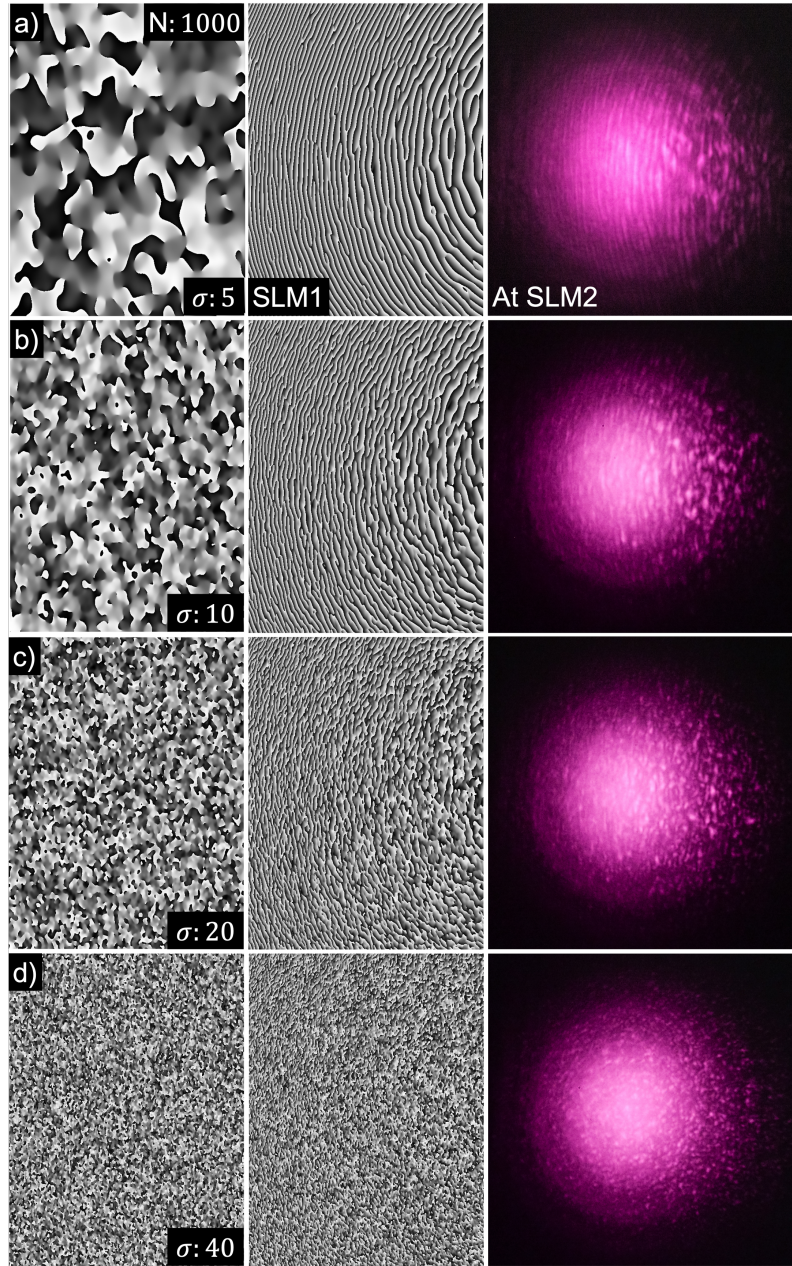


FIGURE 6.8: **Diffractive speckle fields using an LC-SLM:**(Column 1) the generation of speckle fields made up of  $N$  plane waves of some spread  $\sigma$  (cycles or mdeg) from the original carrier grating. (Column 2) the resultant holograms when combining the speckle field, carrier grating and aberration correction lenses. (Column 3) photographs of the speckle field largely overlapping the zero order at the plane of SLM2; a large enough carrier grating tilt is required on both SLMs to avoid coupling any 1st order into the single mode fibre. The degree of speckleness increases as the spread of wavevectors used to construct the speckle  $\sigma$  increases.

### 6.3.1 In-situ wavefront correction revisited

Fundamentally, the role of the hologram on SLM2 is to encode the most appropriate phase mask on the structured light to best couple it down a single mode PMF towards the interference section. As it happens, the optimal coupling down such a fibre is a focused Gaussian profile. The second stage of this investigation of optical speckle was to probe the feasibility of using SLM2 to destructure the light from SLM1. This final section concerns the adaptation of the wavefront correction algorithm discussed in section 4.4.2 for use in this setup, and gives a clear route forward for future work in characterising the propagation behaviour of optical speckle.

The algorithm in section 4.4.2 describes the use of an SLM to determine the 2D phase map required to best focus all of the available light in a wavefront down to a single spot [200]. Recall that the measurements were based on the intensity fluctuations of a single point within an interferogram, formed by the combination of reference and raster scanned superpixels. Within the structured arm of the setup here, the wavefront algorithm remains the same, however the point of convergence is no longer a chosen pixel of an interferogram on camera, but the proximal end of the fibre at lens F2. In this regime, the target phase for each superpixel is that which couples the highest power down the fibre.

To measure the intensity of the wavefronts, a camera was placed at the distal facet of the fibre beyond lens F5, and the measurement was the sum over all pixels. This concept was tested by attempting to retrieve the corrections originally applied to SLM2 to best couple the diffraction order  $+1_{ii}$  down the fibre (i.e. those illustrated in the top rows of figure 5.17). The test, presented in figure 6.9, was performed as follows: SLM1 was encoded with carrier and correction holograms  $\phi_{c,1} + \phi_{correct,1}$  (a), and SLM2 was encoded with only the carrier grating  $\phi_{c,2}$  (b). In the first instance,  $\phi_{correct,2}$  (c) was added to SLM2 which couples 100% of some baseline power  $P$  through the fibre.

The wavefront correction algorithm was then conducted with SLM1 displaying hologram (a) and SLM2 displaying hologram (c). Parts (d) to (i) show a range of phase correction masks which, when combined with  $(\phi_{c,2})$  (b), couple a fraction of  $P$  with varying success. The phase steps  $m$ , superpixel size  $n$  and size of the beam on the camera were adjusted to determine the optimal correction achievable. For low frequency corrections like the lens in (c),  $m = 8$  and  $n = 10$  were found to couple the

most light; furthermore, a focused beam with a higher signal per pixel at the detector was found to couple more power than even the holographic lens (c) ( $P = 103\%$ ).

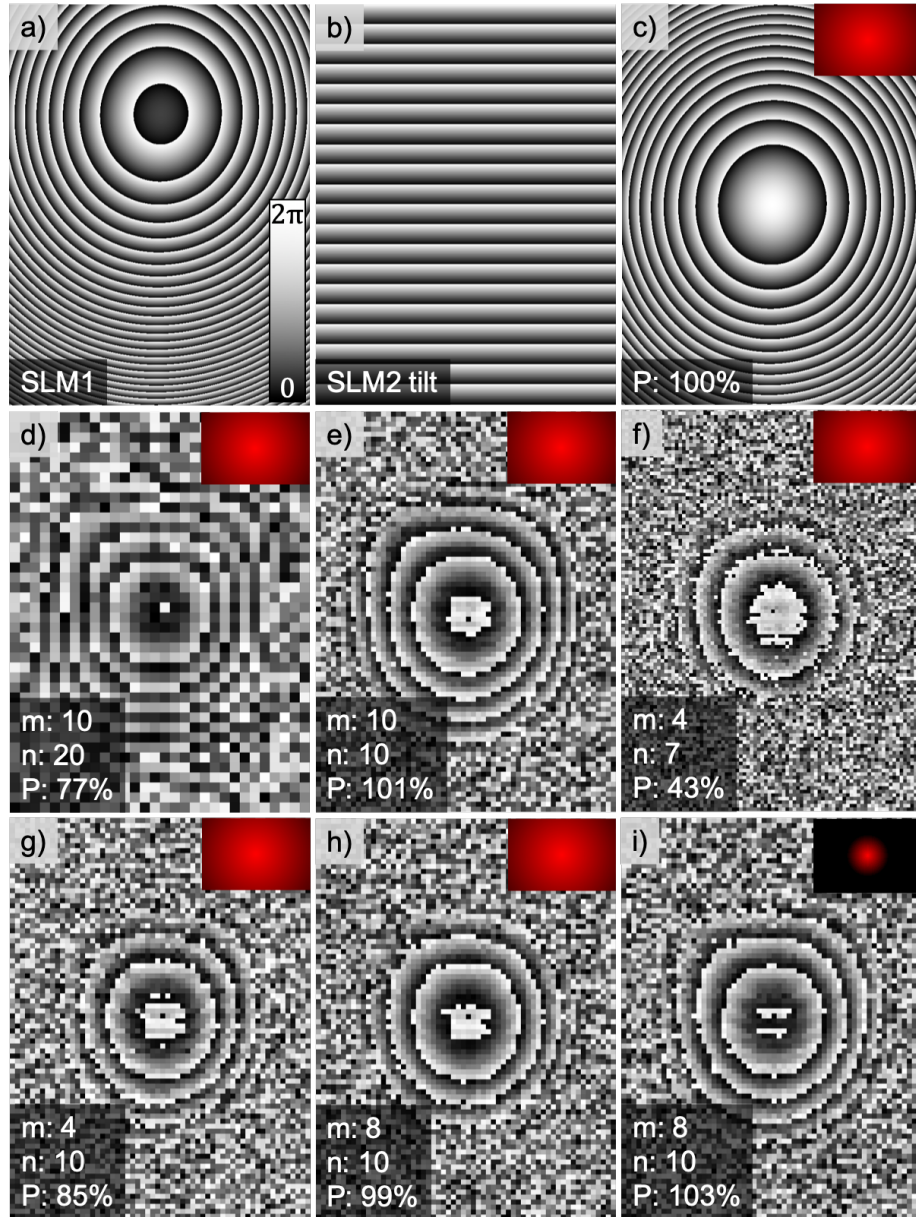


FIGURE 6.9: **Spherical wavefront correction:** Given the (a) corrected carrier grating on SLM1 and (b) original carrier grating on SLM2, in-situ wavefront correction was performed to recover (c) the expected spherical correction on SLM2. (d-i) illustrates the relative coupling power  $P$  achievable as a percentage of (c), when varying the number of phase steps  $m$  and superpixel size  $n$ . Inset within each phase correction map is the size of the beam on the camera.

### 6.3.2 Microscanning wavefront correction

Inherent to this wavefront correction algorithm is the reduction in measuring signal with superpixel size. We may require a higher resolution correction map to unlock more structured fields, however there is a limit to the superpixel size  $n$  with which the phase can be accurately probed, due to a “washout effect” when the signal approaches the ambient light level. In practice this was found to be around  $n = 7$  for a correction map resolution of  $< 10,000$  pixels. In order to circumvent this lack of light, a *microscanning* capability was incorporated: figure 6.10(a) introduces the concept in relation to this application. By defining an additional 2D array whose positions are separated by a new variable, step size  $t$ , we can decouple the superpixel size  $n$  from the correction map resolution. Consecutive locations of the SLM being probed overlap to form a higher resolution correction phase map using more of the SLM window for each measurement.

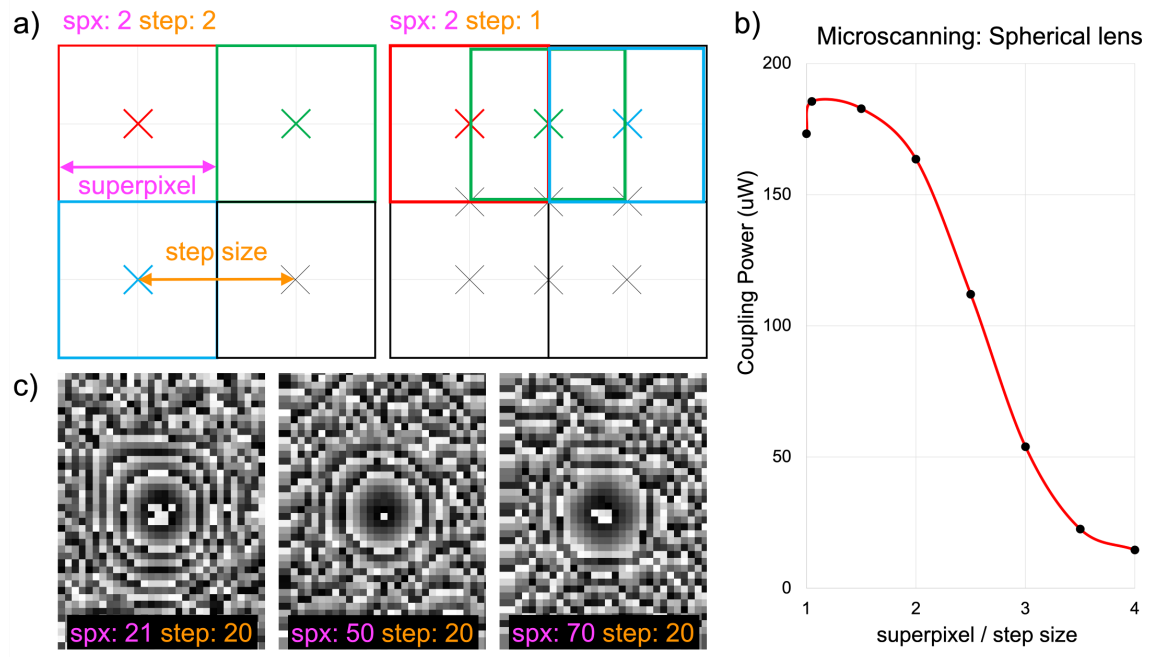


FIGURE 6.10: **Microscanning wavefront correction:** (a) By decoupling the superpixel (spx) size  $n$  from the number of measurements made by introducing a step size  $t$ , we can overlap successive superpixels – this results in more of the SLM hologram being used per measurement, and therefore higher resolution correction maps. (b) the technique allows us to double the resolution using the same superpixel size, although interpolation effects limit the accuracy when the  $n/t > 3$  (as illustrated in (c)).

Whilst this technique improves the maximum resolution achievable by making more light available per  $n$ , there is a limit to its use. Figure 6.10(b,c) demonstrates the effect of increasing the ratio between superpixels and step size: the accuracy with which the correction phase can be retrieved diminishes, leading to a loss in coupling efficiency down the fibre. However, using this method, both lens and speckle correction maps with 30,000 and 19,200 pixels respectively were achieved, which is a considerable resolution improvement for such highly structured fields (shown in figure 6.11). Note that the correction maps were either upsampled or 2D interpolated by nearest neighbour method to rescale the map to the size of the SLM.

### 6.3.3 Optical speckle down a single mode fibre

The primary justification of implementing wavefront correction in this system was to be able to destructure and fibre-couple any structured beam that arrives at SLM2. This in turn opens the possibility of destructuring optical speckle of varying degrees of “speckleness”.

Figure 6.11 presents the holograms and correction maps used to successfully destructure and fibre-couple optical speckle (and focused beams for reference). A random speckle field of  $N = 50$  phase cycles,  $\sigma = 8$  shown in (b) was applied to the carrier grating on SLM1 (a) to form optical speckle about the +1 diffraction order (c). A microscanning wavefront correction algorithm was then applied, given SLM2 displayed only the carrier and correction lenses (d), to form a speckle phase correction map (e). Notably, the resultant hologram pairing of (c) and (f) coupled as much as 73% of the original power  $P$  of the non-structured gratings (a,d).

To compare this correction technique to the programmed holograms from section 6.2, the method was used to determine the correction required for an  $f = 0.4$  m lens. Part (g,h) shows the holograms used in the confocal lens test (i.e. figure 6.2), whilst (i) shows the hologram correction that equates to a spherical lens (h). Here, the correction phase hologram slightly outperformed the previously programmed hologram in coupling efficiency; note that a linear correction can be seen in the outer regions of the correction hologram due to an unforeseen aberration (i).

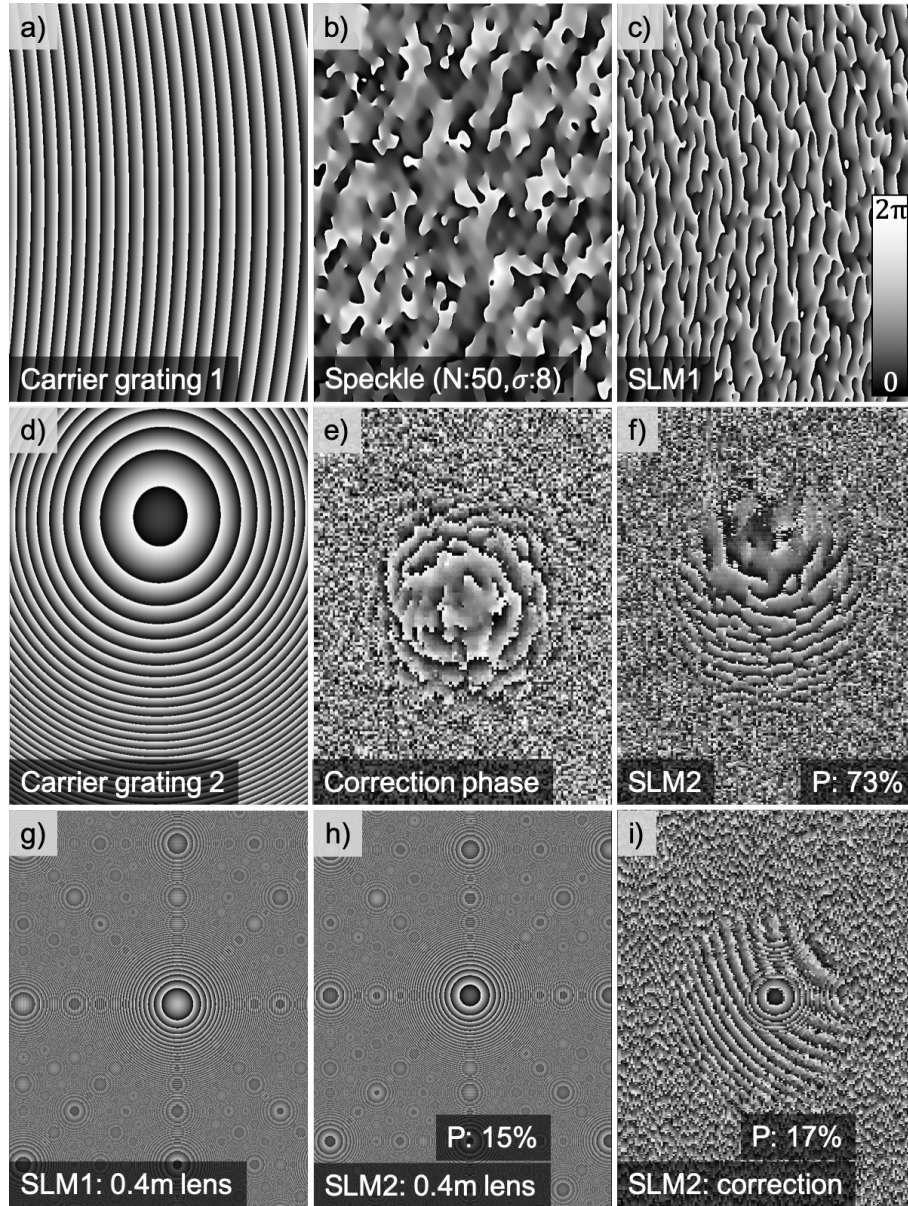


**FIGURE 6.11: Wavefront correction for optical speckle and focusing lens:** Applying the (b) randomised speckle field to (a) an SLM1 carrier grating produces (c) a speckle field about the +1 order location. When (c) and (d) are used in a microscanning wavefront correction measurement, the correction phase map (e) is obtained, resulting in a 73% coupling c.f. carrier-only gratings. (g-i) for illustration, the same process for a focused beam of  $f = 0.397$  m, where the corrected phase (i) outperforms the programmed hologram (h) from figure 6.2.

### 6.3.4 High order optical speckle destructuring using a speckle basis

The degree of optical speckle is determined by the number of  $k$  vectors  $N$  and the standard deviation  $\sigma$ ; as such there is flexibility to generate optical speckle of widely-varying degrees of speckleness. In coupling tests it was found that  $\sigma$  was the limiting factor in coupling the destructured speckle beam into the fibre. Furthermore, it was clear that with higher spatial frequencies in the speckle, the efficiency of the correction maps was greatly reduced. To prepare for higher-ordered speckle correction, a second regime of wavefront correction was considered, defined here as *speckle basis correction*.

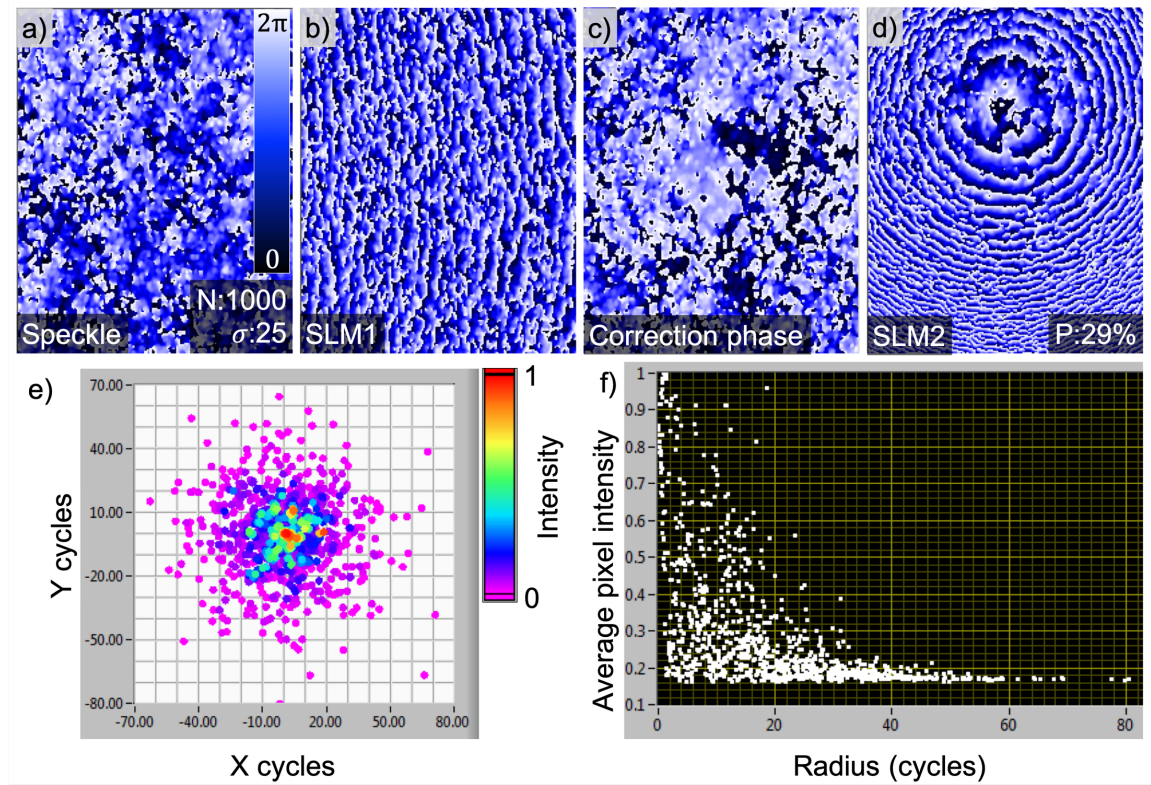


FIGURE 6.12: **Speckle basis correction:** the speckle hologram (a) applied to SLM1 (b) can be wavefront-corrected based on the known  $k$  vectors that make up the original speckle. The algorithm uses the entirety of the SLM for each measurement, and the correction map (c) on SLM2 (d) displays higher spatial frequencies than can be achieved by using superpixels. (e,f) the  $k$  vectors within the original speckle can be graphed based on their contribution to the coupling power, in terms of  $(N_{cyc,x}, N_{cyc,y})$  phase cycles from the carrier grating.

The algorithm, developed in collaboration with Dr. Stellinga, makes use of the set of known random  $k$  vectors used to produce the original speckle hologram, defined in equation 6.6. It works similarly to that introduced in section 4.4.2, however instead of scanning through  $m = 10$  offset phases at every superpixel position, the offset is applied iteratively to each  $k$  vector displayed in full. This is beneficial because the entire SLM2 window is in use for each measurement, such that the number of measurements becomes  $m \times N$ . For each  $k$  vector component within the speckle field,  $m$  different phase offsets were applied.

For each measurement step in the speckle basis correction data acquisition, the SLM2 phase hologram is

$$\phi_{SLM2,step}(u, v) = \phi_c(u, v) + \phi_{spher,ast}(u, v) + \phi_{measure}(u, v) \quad (6.8)$$

Here  $\phi_c$ ,  $\phi_{spher,ast}$  are the carrier grating and programmed lens corrections respectively, whilst  $\phi_{measure}(u, v)$  is the phase to be measured. Specifically,

$$\phi_{measure}(u, v) = \arg(1 + e^{i(\phi_{probe}(u,v) + \phi_{shift}(u,v))}), \quad (6.9)$$

where  $\phi_{shift} = 2\pi i/m$  is the phase shift applied to each  $k$  vector component of the original speckle  $\phi_{probe,n}(u, v) = \phi_n + \phi_{off,n}$ . The total data acquisition is performed over  $[0:i:m-1]$  for  $\phi_{measure}(u, v)$ , and over  $[0:n:N-1]$  for all  $N$   $k$  vector contributions  $\phi_n$  from equation 6.7. The 1 in the argument is the reference plane wave, which remains fixed. For every probe plane wave, a sine wave of intensity is measured, which is a function of the shifted phase  $\phi_{shift}$ . The phase of this sine wave is then the reconstruction phase associated with that plane wave.

The average intensity across all pixels,  $E_i^2$ , is then measured and used as a weighting factor for each phase offset  $m$ , before combining these into a complex term for all phase offsets of *each*  $k$  vector  $\phi_{k,j}$ :

$$Ee^{i\phi_{recon}} = \sum_{i=0}^{m-1} \left( E_i \exp\left(\frac{2i\pi}{m}\right) \right). \quad (6.10)$$

Here  $\phi_{recon}$  is the reconstructed phase correction contributed by a single  $k$  vector. It follows that the total calculated speckle correction to be displayed on SLM2 is the combination of original carrier and correction phases with the corrected speckle  $k$

vector phases, namely

$$\phi_{SLM2,corrected}(u, v) = \phi_c(u, v) + \phi_{spher,ast}(u, v) + \arg\left(\sum_{j=0}^{N-1} e^{i(\phi_{probe,j}(u,v) + \phi_{recon}(u,v))}\right). \quad (6.11)$$

Figure 6.12 depicts the speckle basis correction for a high order speckle ( $N = 1000$ ,  $\sigma = 25$ ): the generated speckle field (a) was applied to the carrier grating of SLM1 (b). By definition, the resultant correction phase map (c) matches the high resolution of the original field, and utilises the entire SLM window. (d) shows the addition of the correction map and the carrier grating (including correction lenses). This speckle basis correction was compared to the original raster scanning method by testing the coupling efficiency when deconstructing and fibre coupling a speckle beam of  $N = 1000$ ,  $\sigma = 25$ ; the result was an improvement in the power output from  $P = 10.34\%$  to  $P = 28.59\%$ , which demonstrates its usefulness in future speckle beam measurements. The associated graphs illustrate the contribution of each  $k$  vector to the speckle, in terms of  $(N_{cyc,x}, N_{cyc,y})$  phase cycles, plotted as (e) an intensity colour map and (f) a radius from the carrier grating location at (0,0).

## 6.4 Further studies: conclusion

The investigation presented within this chapter is a continuation of the work in chapter 5, concerned with expanding the scope of  $v_g$  delay in structured beams by considering that for a confocal lens pair and optical speckle. The theoretical geometry of both beam structures were characterised, and preliminary results for the group delay in lenses of  $f = 0.397$  m were reported.

It is clear that when optimising the system for Bessel beam delay, the effect can be readily observed as a polynomial trend. This is a luxury not afforded to confocal lens delay measurements, which rely on the empirical measurement of  $w$  and the correct coupling of (de)focused light from the SLMs. Between the two tests presented, there is sufficient stability across several hundred measurements to be confident that statistical noise has been suppressed. An additional result has also been included in appendix D, which introduces a Gaussian aperture to both SLMs- it was discovered that with apertures smaller than the original beam waist, a strong fit with the theory

is achievable. However, there remains more work to be done to accurately quantify  $w$ , and (similar to the Bessel delay tests) to develop an independent test of coupling efficiency of the (de)structured light down the fibre at F2, which may require imaging the fibre facet.

Given time constraints, the investigation into optical speckle is ongoing; thus far, I have demonstrated the holographic generation of various orders of optical speckle, as well as presented two methods with which to destructure optical speckle in order to couple down a single mode fibre.

The continuation of this work will aim to make use of the focused beams, speckle generation and wavefront correction algorithms, given the results for the Bessel tests prove to definitively match the theory and are repeatable beyond doubt. Early testing has shown promise for the use of a diffusor before the coupling lens F2, in order to scatter the low and high angle  $k$  vectors more uniformly- in this configuration, SLM2 may be removed, such that the speckle structure region extends to  $L \sim 1.4$  m. Such tests have revealed that the predicted delay for any given speckle pattern is dependent on its random seed number, and so the delay must be a statistical average of many seeds. There also remains the opportunity to automate the beam preparation stages – removing the human element in alignment may improve the time efficiency and accuracy of the alignment.

Finally, successful measurement of the delay of optical speckle could lead to in-situ analysis of the propagation behaviour of optical speckle where it occurs naturally and not as a holographic approximation, in an effort to gain new insights into the propagation characteristics of natural sources of speckled light.

# Chapter 7

## Conclusion

Optical beam shaping is an exciting and ever-evolving field in optics, with a global community marrying research and industry to exploit its potential. Command of both scalar and vector-based beam shaping regimes allows us to manipulate the fundamental properties of light in a diverse array of applications, which grows year upon year. The primary objectives of this thesis have been to use the foundations of classical optical wave theory and the state of the art in structuring practices to introduce two novel beam shaping techniques: high-speed DMD and broadband dual-SLM vector beam shaping. Furthermore, the skills developed were then applied to probe the fundamental propagation of structured light in free space, specifically the group delay of broadband Bessel and focused beams.

The following summaries aim to provide a brief retrospective on the work as a whole and highlight key findings which may be of interest to the beam shaping community. I will also use this opportunity to gauge the success of each project, and justify the actions taken. Lastly, I will contextualise this work by making recommendations on its future direction and application.

### 7.1 Chapters 1 and 2

In chapter [1](#), I presented the general definition of vector beam shaping, and its relation to historical forms of scalar beam shaping in amplitude and phase. I then provided the motivation for this thesis, in the form of a wide variety of applications

in research and industry. Most notably, structured light is intrinsic to the fields of air/fibre-space optical communication, micro-manipulation and microscopy. Vector beam shaping is credited with introducing a new degree of freedom to exploit; to increase data bandwidth in optical data channels, and maximise the efficiency and resolution of optical traps and probes. Furthermore, advancement of conventional beam shaping operations with the latest in spatial light modulation technology has opened new doors: high speed adaptive optics and imaging through turbid media, computational imaging and probing the nature of light in quantum systems.

Chapter 2 was used to present the prerequisite mechanisms of beam shaping from first principles – this included the description of interference and the wavelength-dependent nature of coherence and dispersion. Key to the characterisation of structured vector beams was the discussion on polarisation, including the optics, systems and metrology used to manipulate and quantify polarised light. Finally, the chapter introduced the principles and state of the art in spatial light modulation technology to be used in this work.

## 7.2 Chapter 3

In chapter 3, the objective was to evaluate the prospect of the DMD as a low-cost high-speed alternative to industry-standard liquid crystal modulators for shaping vector beams. The current options in scalar and vector beam shaping techniques were discussed, as well as the gap in the market for high speed switching rates. Also described were the intricacies of the mirror-based DMD when used as a diffractive optical element, as a cautionary guide for future users. On publication of this work, it was understood to be the first use of a DMD in the diffractive regime to generate arbitrary vector beams. The switching rate of top of the line DMDs is several orders of magnitude faster than LC-SLMs of a similar price and resolution.

The system described makes use of a relatively cheap TI Lightcrafter DMD and an array of birefringent optics to diffract and overlap monochromatic optical modes with orthogonal polarisations, resulting in the generation of beams with arbitrary amplitude, phase and polarisation. The use of Stokes parameters allowed for the characterisation of the various transverse polarisations achieved with polarisation ellipse maps. The role of the DMD as a high-speed modulator was demonstrated by

exploiting the onboard memory of the device, which culminated in the experimental  $\sim 4$  kHz switching of vector vortex beams – a rate which is limited only by the price level, and not the fundamental technology.

I believe the system presented in chapter 3 makes a compelling case for the incorporation of DMDs in a variety of beam shaping systems, as a scalar and vector beam shaper and for high speed wavefront control. I provide a rigorous analysis of the use of such devices in the laboratory, including the implications of binary amplitude modulation, blazing and their impact on diffraction efficiency. In my tests I was encouraged by the ease with which the TI development module could be used in the diffractive regime, and was surprised at its optical flatness. The device can be addressed in largely the same way as an LC-SLM, however its innate relative inefficiency remains an inescapable trade off. For monochromatic sources, my setup generated vector beams with an excellent agreement to the theory; in particular, well-defined and almost aberration-free optical modes were combined with  $\mu\text{m}$  precision of amplitude and phase, to generate beams whose polarisation state was within 5% of the theory throughout the transverse profile, based on the Stokes parameters and intensity likeness.

Based on the evidence provided, I wholly recommend consideration of the DMD as a diffractive optical element for arbitrary monochromatic vector beam shaping. The super-fast maximum switching rates make this device of immediate use to the characterisation of propagation through dynamic turbid media, which relies on real-time beam shaping to be effective. Provided there are viable workarounds for the loss in efficiency, the DMD can be advantageous in both research and real-world environments over the more established LC-SLMs. My investigation reaffirms the growing sentiment that when in need of a beam shaping solution, there is no outright winner – only by considering the specific application and its needs will the optimum device be known. The table in figure 7.1 outlines the key findings of this chapter, in the wider context of the beam shaping community.

### 7.3 Chapter 4

The investigation of chapter 4 arose from a simple question: given the successful implementation of monochromatic vector beams in chapter 3, what is required to

Attribute	LC-SLM	DMD
Cost	<ul style="list-style-type: none"> <li>Basic devices for scientific use ~£1000.</li> <li>&gt;£10k for increased bit depth, switching rate and AR coating.</li> </ul>	<ul style="list-style-type: none"> <li>&lt;£200 for cheap commercial digital projectors, &lt;£1000 for standard TI DMDs</li> <li>&lt;£10,000 for superfast DMD (more RAM)</li> </ul>
Resolution	<ul style="list-style-type: none"> <li>Typically side length ~256-1024 pixels w/ 3.5-20 <math>\mu\text{m}</math> pitch</li> <li>4K UHD (Holoeye)</li> </ul>	<ul style="list-style-type: none"> <li>Similar, also with standard display sizes (VGA, XGA, HD, 4K UHD)</li> <li>Reduced by Binary amplitude modulation</li> </ul>
Polarisation	<ul style="list-style-type: none"> <li>Phase modulation for only 1 axis (Ver/Hz)</li> </ul>	<ul style="list-style-type: none"> <li>Polarisation insensitive</li> </ul>
Switching Rate	<ul style="list-style-type: none"> <li>Via HDMI, standard monitor rate (60-200 Hz)</li> <li>High cost devices up to ~1kHz with reduced stability, bit-depth</li> </ul>	<ul style="list-style-type: none"> <li>Via HDMI, standard monitor rate (60-200 Hz)</li> <li>Binary patterns preloaded onto RAM for 4-32.5kHz</li> </ul>
Diffraction Efficiency	<ul style="list-style-type: none"> <li>(+1) Up to 95% with AR coatings</li> <li>(+1) Radial vector beam: &lt;80%</li> </ul>	<ul style="list-style-type: none"> <li>Array diff. eff. 86% (all on)</li> <li>(+1) Radial vector beam: &lt;5%</li> </ul>
Bandwidth	<ul style="list-style-type: none"> <li>Rated for 400-700 nm with gradual drop in efficiency, Custom AR coatings available</li> </ul>	<ul style="list-style-type: none"> <li>Rated for 400-700 nm, mirrors reflective beyond visible, only limited by (pitch <math>\gg \lambda</math>)</li> </ul>
White Light Diffraction	<ul style="list-style-type: none"> <li>Requires chromatic dispersion compensation</li> <li>Successful shaping at <math>\Delta\lambda = 100</math> nm</li> </ul>	<ul style="list-style-type: none"> <li>Fixed Mirror tilt (<math>\pm 12^\circ</math>) causes extreme levels of dispersion</li> <li>Aberrations occur even for <math>\Delta\lambda = 0.1</math> nm</li> </ul>
Spatial Modes	<ul style="list-style-type: none"> <li># independent focused spots in FP <math>\propto</math> # pixels</li> </ul>	<ul style="list-style-type: none"> <li>Less than LC-SLM, max diff. angle limited by binary shaping, unwanted orders</li> </ul>
Fidelity	<ul style="list-style-type: none"> <li>Random scattering from LC subdomains on scale of overall scatter- reduces corrected power ratio of diffraction modes, performance deteriorates with # modes</li> </ul>	<ul style="list-style-type: none"> <li>DMDs suffer no random scattering, typically outperform LC-SLMs in power ratio (mode vs background)) fidelity by 10-15%</li> </ul>
Applications	<ul style="list-style-type: none"> <li>Industry-standardized diffractive optical elements with large knowledge base</li> <li>Well established in micromanipulation, microscopy, quantum optics &amp; others</li> <li>High efficiency diffractive beam shaping with suppressed unwanted orders.</li> <li>Various application-specific complex amplitude modulation methods</li> <li>White light arbitrary vector beam shaping</li> <li>Low voltage, compact micro-displays</li> </ul>	<ul style="list-style-type: none"> <li>High fidelity raster scan imaging through complex media, in vivo imaging, MMF</li> <li>High speed Mode Division Multiplexing through fibres &amp; airspace</li> <li>High speed optical trapping, SIM, STED microscopy</li> <li>Compressive sensing with structured light, LiDAR</li> <li>Low cost, dynamic and repeatable beam modulation or pattern projection.</li> </ul>

FIGURE 7.1: **General findings on DMDs vs LC-SLMs:** The general attributes listed aim to inform future users on the pros and cons of using each technology. Relatively cheap options exist for both, whilst top tier products are available for a higher price. The number of LC cells/micromirror pixels is comparable, however recall that binary amplitude modulation uses multiple adjacent mirrors to achieve complex modulation, which also limits the number of independent spatial modes achievable. LC-SLMs are lauded for their efficiency, whilst DMDs can achieve super-fast switching rates. Whilst the efficiency per  $\lambda$  of DMDs is more achromatic, they suffer from extreme dispersion with non-monochromatic light, and compensation may be compromised. The  $\text{sinc}^4$  profile of diffraction from a DMD results in higher fidelity modes, compared to the random scattering of liquid crystals in LC-SLMs [176]. The key attributes of each technology may then be exploited for specific applications in the shaping of light.

extend such a beam shaping capability to white light sources? As is often the case, a search for the answer raised even more questions: how well do wavelength-dependent SLMs diffract quasi-monochromatic sources? What is the impact of laser coherence? Finally, what geometries of orthogonal beam overlapping are feasible given the above constraints?

I began this chapter by conducting feasibility studies to probe SLM diffractive behaviour and dispersion correction using broadband light. I was taken aback at the extreme skew of the angular dispersion observed with a DMD, which may only be attributable to its tilted mirror array. Ultimately this forced the use of LC-SLMs instead. A clever optical geometry using a pair of LC-SLMs within a Sagnac interferometer resulted in a system which, although more complex, used the same holographic beam shaping algorithms as before. The combination of incorporating an optical delay element and utilising in-situ wavefront correction proved crucial to interfering orthogonal modes with a workable path length, and an accurate transverse spatial profile. The final system was a proof-of-concept to experimentally generate beams of near-arbitrary polarisation, such as vector vortex and Poincaré beams, across a chosen bandwidth of 100 nm.

The results obtained in this investigation accurately portray the increased difficulty in the alignment process over that in chapter 3. Great care was taken to implement the 4F imaging system between SLMs, and correctly overlap the two arms throughout the Sagnac interferometer. Nevertheless, there was a limit of precision on both the dispersion compensation and alignment procedure, which manifested as a loss in the range of polarisation states achievable. The Stokes parameters measured indicate that the orientation and ellipticity of modes is wavelength dependent, with spatially varying mode combinations achieving an image subtraction likeness which deviates from the theory by 10%. I believe this work serves as a fascinating study into the wavelength dependence of SLMs and dispersion compensation, providing meaningful advice for would-be users of such devices for ultrafast and even white light beam shaping.

In future, this work may be emulated by customisation of the bench optics; using optimised coatings, a more precise delay element, replacing the SLMs with a static DOE and replacing the beamsplitter with a knife-edge mirror should increase the efficiency dramatically. The system was arranged in stages with an emphasis on being able to track the relevant diffraction orders for dispersion-compensated vector

beam shaping – as such, its applicability in white light beam shaping could improve with miniaturisation of the optical setup. Lastly, the vector beams may be probed with time-of-flight detection to demonstrate their direct application as a source of ultrafast structured light.

## 7.4 Chapters 5 and 6

The investigation introduced in chapter 5, and extended in chapter 6, aimed to incorporate the beam shaping and alignment techniques acquired from the previous investigations to probe the fundamental  $v_g$  delay of structured light. The experiment was proposed as a classical interpretation of previous works which probed the behaviour of structured photons; as such, several iterations of classical interferometry were investigated. A broadband source was split into two beams; one beam received scalar beam (de)structuring over a finite path length, whilst the other propagated with a Gaussian profile. Interference of these beams after a similar propagation distance resulted in a visibility-modulated interferogram; the associated  $v_g$  delay of Bessel and focused beams manifested as a lateral shift in the visibility envelope, and could be predicted by simple geometry.

The result presented for the Bessel beam case using the improved visibility profile marks a significant step in demonstrating a system which is both accurate and stable. Despite featuring systematic offsets from the theoretical model, the first SLD Bessel test behaves in the same manner as the work which precedes it [201]. A post-submission overhaul of the original alignment and collimation was found to reduce these offsets considerably, however further testing and refinement of alignment principles into a fool-proof repeatable procedure are deemed necessary to advance this project.

In chapter 6, the longstanding issues with the visibility profile hindered any meaningful delay testing for confocal and speckle structures. A post-submission introduction of SLM Gaussian aperture masks in D was found to give a strong fit at smaller beam waists. In light of the visibility issues, a significant effort was made to prepare both structure regimes; this included probing the beam waist width of the incident beam on SLM1, and investigating the generation and de-structuring of optical speckle. The latter was necessary to establish whether the components within speckle could

be coupled through an optical fibre after appropriate modulation. The preliminary results presented for confocal lens delay show promise – although highly dependent on  $w$  and  $(u_{off}, v_{off})$ , the system is clearly sensitive enough to detect the subtle delays created. It remains a matter of improving the alignment strategy and bolstering our confidence with the theoretical model used.

Throughout this final project, a significant attention to optimum optical alignment strategies ensured an experiment whose behaviour was well characterised. This in turn aided the degree of accuracy which could be attached to the measurements recorded, in spite of the numerous difficulties to ensure precision. The nature of interference and coherence of quasi-monochromatic light was studied in multiple testing environments, which upheld the theoretical arguments for the behaviour I expected. The breakthrough of matching the propagation arms (beyond just OPL) to include equal media and lens elements was a major turning point in achieving well-defined low coherence interferograms suitable for delay measurements.

The results depicted in chapters 5 and 6 have now been supplemented by the appendices C and D. I am confident that the final  $v_g$  delay behaviour reported for Bessel beams is sufficiently stable and an accurate account of the physical propagation, within my system in particular. Further analysis is required to confirm the repeatability of this dataset. In chapter 6, the focused beam results presented are more ambiguous due to the significant role of beam waist characterisation; further testing, such as applying both centre and edge stop holographic apertures and beam profiling throughout the system may be required. Given the above are found to be reliable measures of known structured beams, the necessary preparations have now been made to attempt  $v_g$  delay of optical speckle; the (de)structuring of holographic optical speckle down a fibre has been demonstrated using several regimes of wavefront correction.

I believe the work presented in these final chapters demonstrate a conscientious approach to optical alignment within a challenging experimental setup; the level of scrutiny applied to every step was necessary to successfully analyse the optical effects in a meaningful way, and maintain sufficient confidence to report on minute interferometric behaviours. The apparatus proved to be temperamental under such sensitive analysis, however a combination of routine alignment and various stability enhancements throughout the project mitigated most problems. After a lengthy and rigorous investigation to achieve the interferograms first predicted, the system

is now well-behaved and able to probe the propagation behaviour of any number of structured light profiles.

Future work in this investigation therefore ought to confirm the delay trends reported thus far; it should also identify and incorporate the physical discrepancies observed, to update the theory. The optical speckle structuring technique is now primed for delay analysis; there remains questions about which components of the original optical speckle successfully couple into the fibre. This may require time-of-flight analysis, to determine the spread of wavelengths and  $k$  vectors which enter the interferometer; indeed, the use of a diffuser promises to provide unbiased low-level coupling down the fibre. This investigation has been a success as an exercise in advanced beam structuring and alignment procedures; furthermore, it confirms the propagation behaviour of structured light with a direct and intuitive measurement. There is now a clear route forward to investigate the peculiar propagation of optical speckle.

## 7.5 Final remarks

Our curiosity with the nature of light and its fundamental properties is innate, and the extent of its potential has only begun to be realised in many applications across many fields. This study marks a humble but well-informed contribution to this global endeavour, by demonstrating the use of spatial light modulation in new and exciting ways. Furthermore, this study presents the findings of a personal pursuit to engage with the laws of nature at the forefront of scientific knowledge – to couple established optical theory with innovative new technologies in order to advance our collective understanding. It is my hope that this body of work serves to inform and motivate my peers in the beam shaping community, and that the field continues to thrive as the real-world potential of structured light approaches unprecedented new heights in the years to come.

# Appendix A

## Relating phase and group velocities in a waveguide

In a waveguide, we may generalise the propagation of light using the propagation constant: specifically, we define  $v_p = \omega/\beta$  and  $v_g = d\omega/d\beta$ , where

$$\beta = \sqrt{k_0^2 - k_c^2}, \quad (\text{A.1})$$

is the guided propagation constant. Note that here,  $k_0 = \omega/c$  and  $k_c$  are the free space and cut-off wavenumbers; the latter is a constant, dependent on the boundary conditions of the waveguide being considered.

It follows that for a general waveguide,

$$\frac{d\beta}{d\omega} = \frac{d}{d\omega} \left( \frac{\omega^2}{c^2} - k_c^2 \right)^{\frac{1}{2}} = \frac{\omega}{\beta c^2}. \quad (\text{A.2})$$

Finally, we can see that

$$v_p v_g = \frac{\omega}{\beta} \frac{\beta c^2}{\omega} = c^2. \quad (\text{A.3})$$

## Appendix B

### Expectation value of $r^2$ for a Gaussian beam

The following is a derivation of the expectation value of  $r^2$  for a Gaussian beam, used in chapter 6 to theorise the  $v_g$  delay of a confocal telescope.

A Gaussian intensity distribution of  $1/e^2$  radius  $w$  may be defined as:

$$I(r, w) = A * e^{-2\left(\frac{r}{w}\right)^2}, \quad (\text{B.1})$$

where  $r$  is the axial distance and  $A$  is the amplitude of the beam. The expectation value of some function  $g$  weighted by an arbitrary intensity distribution  $I$  is written as

$$\langle g \rangle = \frac{\int_0^{2\pi} d\theta \int_0^\infty dr (r * g * I)}{\int_0^{2\pi} d\theta \int_0^\infty dr (r * I)}. \quad (\text{B.2})$$

In our specific case,  $g = r^2$  and  $I = I(r, w)$  as stated above, which leads to

$$\langle r^2 \rangle = \frac{\int_0^{2\pi} d\theta \int_0^\infty dr \left( r^3 * A * e^{-2\left(\frac{r}{w}\right)^2} \right)}{\int_0^{2\pi} d\theta \int_0^\infty dr \left( r * A * e^{-2\left(\frac{r}{w}\right)^2} \right)}. \quad (\text{B.3})$$

Without dependence on  $\theta$  and at a constant amplitude  $A$ , this simplifies to:

$$\langle r^2 \rangle = \frac{\int_0^\infty dr \left( r^3 * e^{-2(\frac{r}{w})^2} \right)}{\int_0^\infty dr \left( r * e^{-2(\frac{r}{w})^2} \right)}. \quad (\text{B.4})$$

Using the standard solutions of the definite integral of a Gaussian function, we find that:

$$\int_0^\infty dr e^{-2(\frac{r}{w})^2} = \frac{w}{2} \sqrt{\frac{\pi}{2}}, \quad (\text{B.5})$$

$$\int_0^\infty dr r e^{-2(\frac{r}{w})^2} = \frac{w^2}{4}, \quad (\text{B.6})$$

$$\int_0^\infty dr r^2 e^{-2(\frac{r}{w})^2} = \frac{w^3}{8} \sqrt{\frac{\pi}{2}}, \quad (\text{B.7})$$

$$\int_0^\infty dr r^3 e^{-2(\frac{r}{w})^2} = \frac{w^4}{8}. \quad (\text{B.8})$$

Using the second and fourth forms, we may define the expectation value of  $r^2$  for a Gaussian beam:

$$\langle r^2 \rangle = \left( \frac{w^4}{8} \right) / \left( \frac{w^2}{4} \right) = \frac{w^2}{2}. \quad (\text{B.9})$$

# Appendix C

## SLD Bessel beam delay with improved alignment

The following results related to [5](#) were obtained after the original submission of this thesis, and are included here to better inform the reader of the subtleties in the system alignment and collimation procedures. The trends in figure [C.1](#) and [C.2](#) are a noteworthy improvement over those first presented, indicating that great care must be taken in preparing the experimental setup- this includes correctly measuring the aberrations present in the structured arm, and fine-tuning the destructuring and coupling alignment.

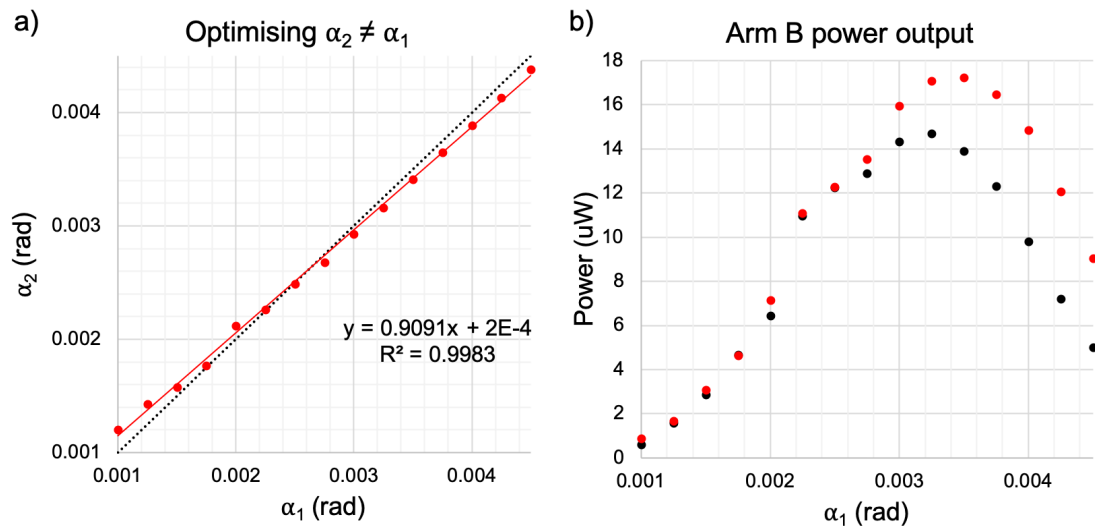


FIGURE C.1: **Optimising  $\alpha_2$  in an improved alignment:**(a) In a repeat of the previous test shown in 5.18, the strength of  $\alpha_2$  was optimised for power down the fibre; what we find is a linear trend which more closely matches the ideal  $\alpha_2 = \alpha_1$ . (b) This manifests as an improved coupling strength throughout the axicon range, such that there is sufficient power to disregard the optimisation entirely, and retain the ideal lenses on each SLM.

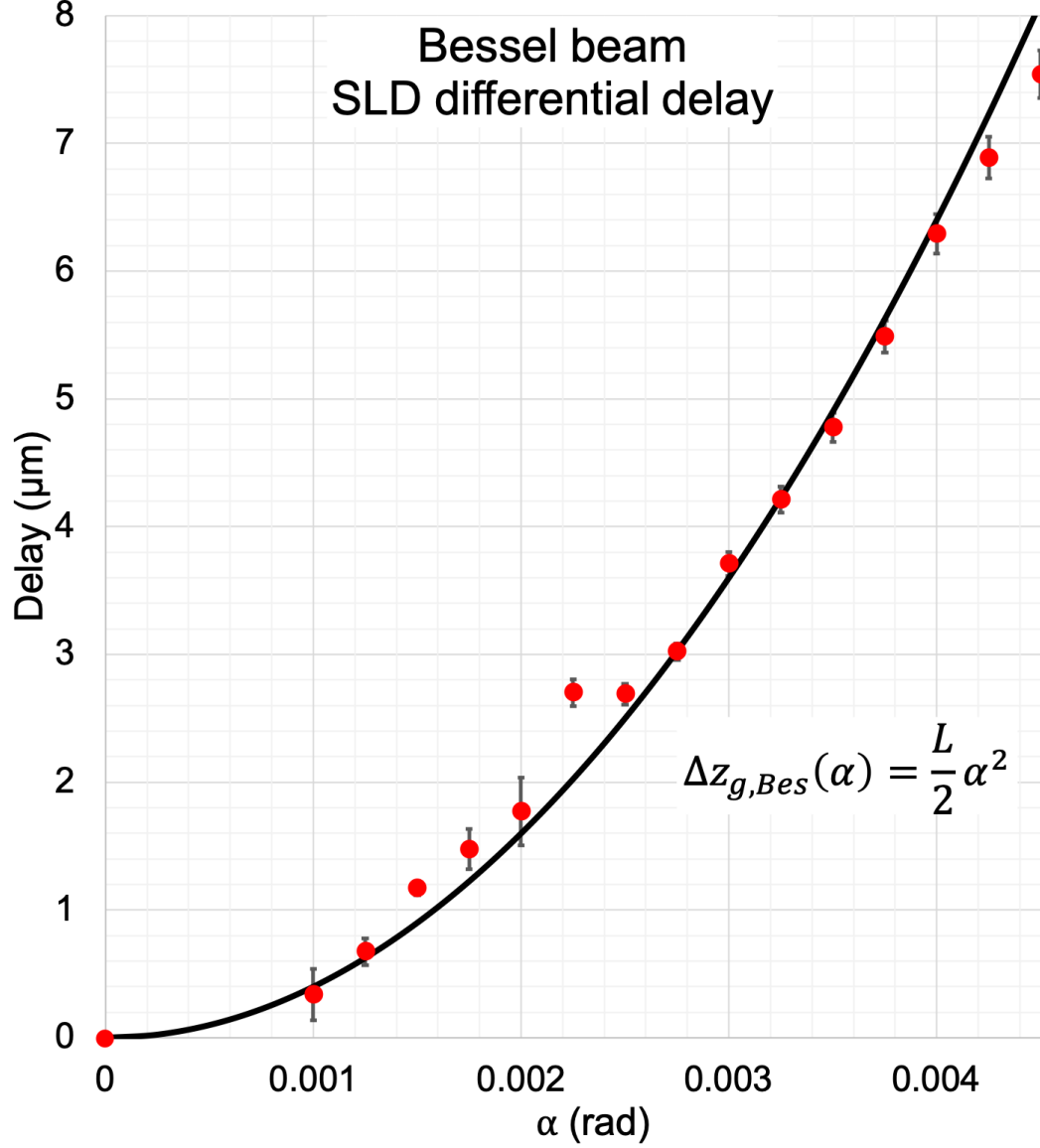


FIGURE C.2: **SLD Bessel beam delay with equal  $\alpha$** : This result was obtained after the re-collimation of fibre coupling lenses F1 and F2, and a re-evaluating the aberrations on the LC-SLMs. As such, no optimisation was used in the axicon strengths, such that  $\alpha_2 = \alpha_1$ . The resulting measurements depicted show an improved fit with the predicted  $\alpha^2$  theory. Note that an outlier “kink” in the curve was observed at different  $\alpha$  for differing carrier tilts (here at  $\alpha = 0.00225$ ). This is perhaps due to a characteristic bleeding of an unwanted order which happens to overlap the Bessel profile when considering that specific tilt and  $\alpha$  together.

# Appendix D

## SLD lens delay with Gaussian apertures

The following result for the group velocity delay of a beam within a confocal lens setup was obtained after the initial submission of this thesis; as discussed in section 6.2, a Gaussian aperture amplitude mask was applied to both SLMs, which constrained the perpendicular  $k$  vector components in use. Figure D.1 depicts the impact of decreasing the aperture radius  $w_1$  on the experimental delay trend. In short, a smaller beam waist necessarily results in a lower group velocity delay detected, whilst at the same time the overall fit to the theory also improves.

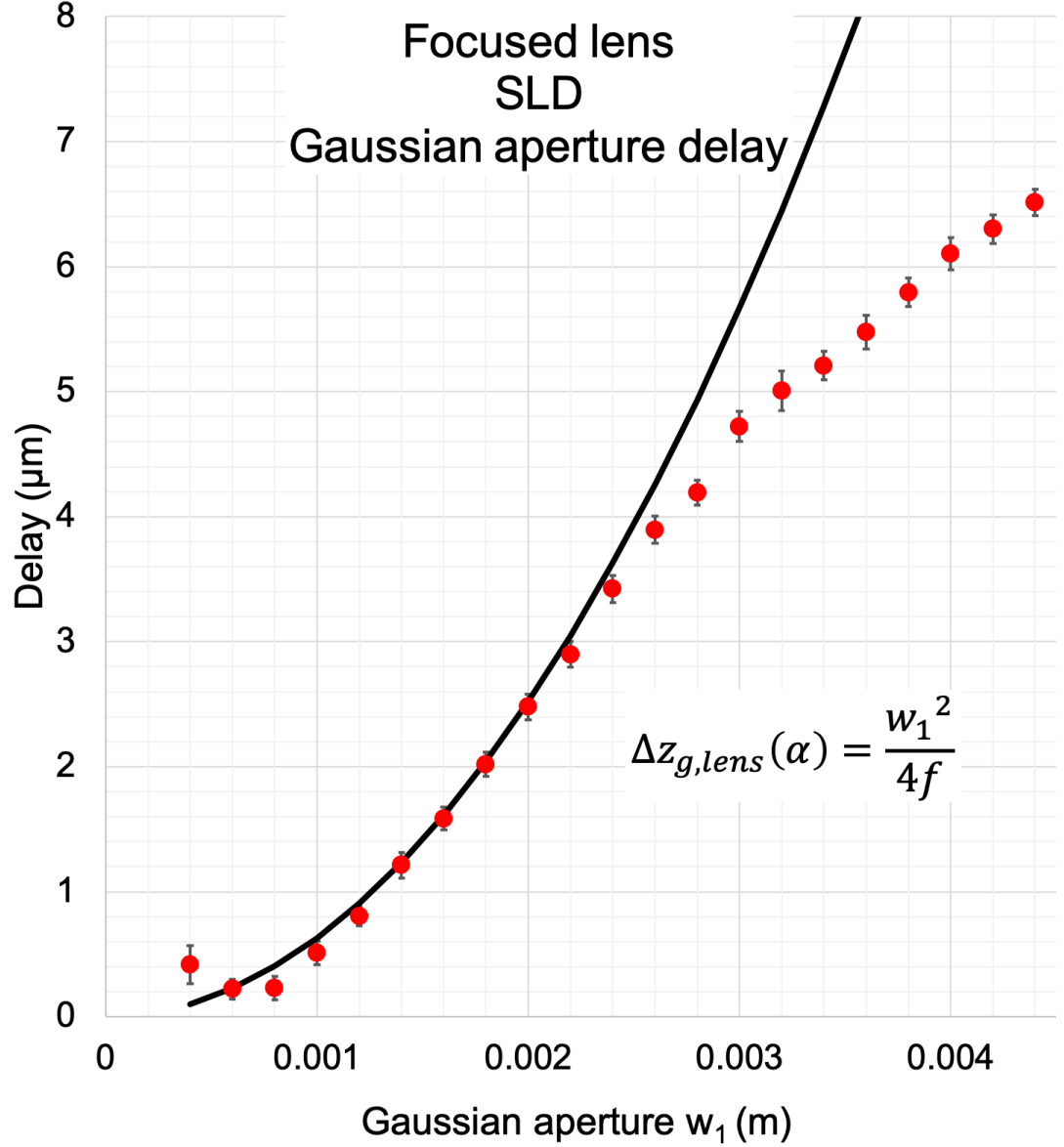


FIGURE D.1: **Confocal lens delay with Gaussian apertures:** This result was obtained by applying identical Gaussian apertures of radius  $w_1$  onto both SLM1 and SLM2. In the probable event that not all of the higher order components of structured light are coupled down the fibre, applying an aperture on the SLMs is a means to constrain the beam waist. This result suggests an agreement with the theory (adapted for concurrent Gaussian expectations) at beam waists smaller than the previously measured  $w$ , but also the increased loss of higher structure components as  $w_1$  increases to the half width of the SLM.

# Bibliography

- [1] S. Turtaev, I. T. Leite, T. Altwegg-Boussac, J. M. Pakan, N. L. Rochefort, and T. Čížmár, “High-fidelity multimode fibre-based endoscopy for deep brain in vivo imaging,” *Light: Science & Applications*, vol. 7, no. 1, p. 92, 2018.
- [2] M. P. Edgar, G. M. Gibson, R. W. Bowman, B. Sun, N. Radwell, K. J. Mitchell, S. S. Welsh, and M. J. Padgett, “Simultaneous real-time visible and infrared video with single-pixel detectors,” *Scientific reports*, vol. 5, p. 10669, 2015.
- [3] K. O’Holleran, M. R. Dennis, F. Flossmann, and M. J. Padgett, “Fractality of light’s darkness,” *Physical review letters*, vol. 100, no. 5, p. 053902, 2008.
- [4] M. Mignardi. (2016) The pioneering work that led to the dmd. [Online]. Available: [http://e2e.ti.com/blogs\\_/b/enlightened/archive/2016/10/06/the-pioneering-work-that-led-to-the-dmd](http://e2e.ti.com/blogs_/b/enlightened/archive/2016/10/06/the-pioneering-work-that-led-to-the-dmd)
- [5] L. MANDEL and E. WOLF, “Coherence properties of optical fields,” *Rev. Mod. Phys.*, vol. 37, pp. 231–287, Apr 1965. [Online]. Available: <https://link.aps.org/doi/10.1103/RevModPhys.37.231>
- [6] H. Rubinsztein-Dunlop, A. Forbes, M. V. Berry, M. R. Dennis, D. L. Andrews, M. Mansuripur, C. Denz, C. Alpmann, P. Banzer, T. Bauer *et al.*, “Roadmap on structured light,” *Journal of Optics*, vol. 19, no. 1, p. 013001, 2016.
- [7] J. Hecht, *Fibre optics calls up the past*. New Scientist, January 1984, vol. 101, no. 1392.
- [8] C. Rosales-Guzmán, B. Ndagano, and A. Forbes, “A review of complex vector light fields and their applications,” *Journal of Optics*, vol. 20, no. 12, p. 123001, 2018.

- 
- [9] A. Forbes, A. Dudley, and M. McLaren, “Creation and detection of optical modes with spatial light modulators,” *Advances in Optics and Photonics*, vol. 8, no. 2, pp. 200–227, 2016. [Online]. Available: <http://aop.osa.org/abstract.cfm?URI=aop-8-2-200>
  - [10] E. Hecht, *Optics*, 4th ed., A. Black, Ed. Addison Wesley, 2002.
  - [11] S. N. Khonina and S. V. Karpeev, “Grating-based optical scheme for the universal generation of inhomogeneously polarized laser beams,” *Applied Optics*, vol. 49, no. 10, pp. 1734–1738, 2010. [Online]. Available: <http://ao.osa.org/abstract.cfm?URI=ao-49-10-1734>
  - [12] S. S. Stafeev, V. V. Kotlyar, A. G. Nalimov, M. V. Kotlyar, and L. O’Faolain, “Subwavelength gratings for polarization conversion and focusing of laser light,” *Photonics and Nanostructures - Fundamentals and Applications*, vol. 27, pp. 32–41, 2017. [Online]. Available: <http://www.sciencedirect.com/science/article/pii/S1569441017301530>
  - [13] M. V. Berry, M. R. Jeffrey, and E. Wolf, *Chapter 2 Conical diffraction: Hamilton’s diabolical point at the heart of crystal optics*. Elsevier, 2007, vol. 50, pp. 13–50. [Online]. Available: <http://www.sciencedirect.com/science/article/pii/S0079663807500028>
  - [14] S. N. Khonina, S. V. Karpeev, S. V. Alferov, and V. A. Soifer, “Generation of cylindrical vector beams of high orders using uniaxial crystals,” vol. 17, no. 6, p. 065001, 2015. [Online]. Available: <http://dx.doi.org/10.1088/2040-8978/17/6/065001>
  - [15] N. M. Massa, *Fundamentals of Photonics: Fibre Optic Telecommunication*, isbn: 9781628412710 ed., C. Roychoudhuri, Ed. <https://doi.org/10.1117/3.784938>: SPIE Digital Library, 2008, vol. 1, no. 1.8.
  - [16] M. Hilbert and P. López, “The world’s technological capacity to store, communicate, and compute information,” *Science*, vol. 332, no. 6025, pp. 60–65, 2011. [Online]. Available: <https://science.sciencemag.org/content/332/6025/60>
  - [17] A. D. Ellis, N. M. Suibhne, D. Saad, and D. N. Payne, “Communication networks beyond the capacity crunch,” *Philosophical Transactions of*

- the Royal Society A: Mathematical, Physical and Engineering Sciences*, vol. 374, no. 2062, p. 20150191, 2019/04/25 2016. [Online]. Available: <https://doi.org/10.1098/rsta.2015.0191>
- [18] M. Pope and J. Shim, *The Looming Bandwidth Crunch - Legitimate Crisis, or Cyberspace Chicken Little?*, 01 2010, vol. 27.
- [19] C. A. Brackett, “Dense wavelength division multiplexing networks: principles and applications,” *IEEE Journal on Selected Areas in Communications*, vol. 8, no. 6, pp. 948–964, 1990.
- [20] D. J. Richardson, J. M. Fini, and L. E. Nelson, “Space-division multiplexing in optical fibres,” *Nature Photonics*, vol. 7, pp. 354 EP –, 04 2013. [Online]. Available: <https://doi.org/10.1038/nphoton.2013.94>
- [21] B. Ndagano, R. Brüning, M. McLaren, M. Duparré, and A. Forbes, “Fiber propagation of vector modes,” *Opt. Express*, vol. 23, no. 13, pp. 17 330–17 336, Jun 2015. [Online]. Available: <http://www.opticsexpress.org/abstract.cfm?URI=oe-23-13-17330>
- [22] J. Carpenter, B. J. Eggleton, and J. Schröder, “110x110 optical mode transfer matrix inversion,” *Opt. Express*, vol. 22, no. 1, pp. 96–101, Jan 2014. [Online]. Available: <http://www.opticsexpress.org/abstract.cfm?URI=oe-22-1-96>
- [23] A. E. Willner, “Vector-mode multiplexing brings an additional approach for capacity growth in optical fibers,” *Light: Science & Applications*, vol. 7, p. 18002 EP, March 2018. [Online]. Available: <https://doi.org/10.1038/lsa.2018.2>
- [24] J. Liu, S.-M. Li, L. Zhu, A.-D. Wang, S. Chen, C. Klitis, C. Du, Q. Mo, M. Sorel, S.-Y. Yu, X.-L. Cai, and J. Wang, “Direct fiber vector eigenmode multiplexing transmission seeded by integrated optical vortex emitters,” *Light: Science & Applications*, vol. 7, pp. 17 148 EP –, 03 2018. [Online]. Available: <https://doi.org/10.1038/lsa.2017.148>
- [25] L. Wang, R. M. Nejad, A. Corsi, J. Lin, Y. Messaddeq, L. Rusch, and S. LaRochelle, “Linearly polarized vector modes: enabling mimo-free mode-division multiplexing,” *Opt. Express*, vol. 25, no. 10, pp. 11 736–11 749, May 2017. [Online]. Available: <http://www.opticsexpress.org/abstract.cfm?URI=oe-25-10-11736>

- 
- [26] Z. Bouchal and R. Celechovský, “Mixed vortex states of light as information carriers,” *New Journal of Physics*, vol. 6, no. 1, p. 131, 2004.
  - [27] G. Rademacher, R. S. Luis, B. J. Puttnam, T. A. Eriksson, E. Agrell, R. Maruyama, K. Aikawa, H. Furukawa, Y. Awaji, and N. Wada, “159 tbit/s c+l band transmission over 1045 km 3-mode graded-index few-mode fiber,” in *2018 Optical Fiber Communications Conference and Exposition (OFC)*, 2018, pp. 1–3.
  - [28] P. J. Winzer, D. T. Neilson, and A. R. Chraplyvy, “Fiber-optic transmission and networking: the previous 20 and the next 20 years (invited),” *Opt. Express*, vol. 26, no. 18, pp. 24 190–24 239, Sep 2018. [Online]. Available: <http://www.opticsexpress.org/abstract.cfm?URI=oe-26-18-24190>
  - [29] N. Bozinovic, Y. Yue, Y. Ren, M. Tur, P. Kristensen, H. Huang, A. E. Willner, and S. Ramachandran, “Terabit-scale orbital angular momentum mode division multiplexing in fibers,” *Science*, vol. 340, no. 6140, pp. 1545–1548, 2013. [Online]. Available: <https://science.sciencemag.org/content/340/6140/1545>
  - [30] B. J. Puttnam, G. Rademacher, R. S. Luís, T. A. Eriksson, W. Klaus, Y. Awaji, N. Wada, K. Maeda, S. Takasaka, and R. Sugizaki, “0.715 pb/s transmission over 2,009.6 km in 19-core cladding pumped edfa amplified mcf link,” in *Optical Fiber Communication Conference Postdeadline Papers 2019*. Optical Society of America, 2019, p. Th4B.1. [Online]. Available: <http://www.osapublishing.org/abstract.cfm?URI=OFC-2019-Th4B.1>
  - [31] G. Milione, M. P. Lavery, H. Huang, Y. Ren, G. Xie, T. A. Nguyen, E. Karimi, L. Marrucci, D. A. Nolan, R. R. Alfano *et al.*, “4× 20 gbit/s mode division multiplexing over free space using vector modes and a q-plate mode (de) multiplexer,” *Optics letters*, vol. 40, no. 9, pp. 1980–1983, 2015.
  - [32] G. Gibson, J. Courtial, M. J. Padgett, M. Vasnetsov, V. Pas’ko, S. M. Barnett, and S. Franke-Arnold, “Free-space information transfer using light beams carrying orbital angular momentum,” *Opt. Express*, vol. 12, no. 22, pp. 5448–5456, Nov 2004. [Online]. Available: <http://www.opticsexpress.org/abstract.cfm?URI=oe-12-22-5448>
  - [33] M. Krenn, R. Fickler, M. Fink, J. Handsteiner, M. Malik, T. Scheidl, R. Ursin, and A. Zeilinger, “Communication with spatially modulated

- light through turbulent air across vienna,” *New Journal of Physics*, vol. 16, no. 11, p. 113028, nov 2014. [Online]. Available: <https://doi.org/10.1088%2F1367-2630%2F16%2F11%2F113028>
- [34] J. Wang, J.-Y. Yang, I. M. Fazal, N. Ahmed, Y. Yan, H. Huang, Y. Ren, Y. Yue, S. Dolinar, M. Tur *et al.*, “Terabit free-space data transmission employing orbital angular momentum multiplexing,” *Nature photonics*, vol. 6, no. 7, p. 488, 2012.
- [35] J. B. Sampsel, “Digital micromirror device and its application to projection displays,” *Journal of Vacuum Science & Technology B: Microelectronics and Nanometer Structures Processing, Measurement, and Phenomena*, vol. 12, no. 6, pp. 3242–3246, 1994.
- [36] K. I. Willig, B. Harke, R. Medda, and S. W. Hell, “Sted microscopy with continuous wave beams,” *Nature Methods*, vol. 4, pp. 915 EP –, 10 2007. [Online]. Available: <https://doi.org/10.1038/nmeth1108>
- [37] P. Török and P. Munro, “The use of gauss-laguerre vector beams in sted microscopy,” *Optics express*, vol. 12, no. 15, pp. 3605–3617, 2004.
- [38] S. W. Hell and J. Wichmann, “Breaking the diffraction resolution limit by stimulated emission: stimulated-emission-depletion fluorescence microscopy,” *Opt. Lett.*, vol. 19, no. 11, pp. 780–782, Jun 1994. [Online]. Available: <http://ol.osa.org/abstract.cfm?URI=ol-19-11-780>
- [39] X. Hao, C. Kuang, T. Wang, and X. Liu, “Effects of polarization on the de-excitation dark focal spot in sted microscopy,” *Journal of Optics*, vol. 12, no. 11, p. 115707, 2010.
- [40] S. Segawa, Y. Kozawa, and S. Sato, “Resolution enhancement of confocal microscopy by subtraction method with vector beams,” *Opt. Lett.*, vol. 39, no. 11, pp. 3118–3121, Jun 2014. [Online]. Available: <http://ol.osa.org/abstract.cfm?URI=ol-39-11-3118>
- [41] M. G. L. Gustafsson, “Nonlinear structured-illumination microscopy: Wide-field fluorescence imaging with theoretically unlimited resolution,” *Proceedings of the National Academy of Sciences*, vol. 102, no. 37, pp. 13 081–13 086, 2005. [Online]. Available: <https://www.pnas.org/content/102/37/13081>

- 
- [42] M. A. A. Neil, R. Juškaitis, and T. Wilson, “Method of obtaining optical sectioning by using structured light in a conventional microscope,” *Opt. Lett.*, vol. 22, no. 24, pp. 1905–1907, Dec 1997. [Online]. Available: <http://ol.osa.org/abstract.cfm?URI=ol-22-24-1905>
  - [43] R. Fiolka, L. Shao, E. H. Rego, M. W. Davidson, and M. G. L. Gustafsson, “Time-lapse two-color 3d imaging of live cells with doubled resolution using structured illumination,” *Proceedings of the National Academy of Sciences*, vol. 109, no. 14, pp. 5311–5315, 2012. [Online]. Available: <https://www.pnas.org/content/109/14/5311>
  - [44] M. G. L. Gustafsson, “Surpassing the lateral resolution limit by a factor of two using structured illumination microscopy,” *Journal of Microscopy*, vol. 198, no. 2, pp. 82–87, 2019/04/19 2000. [Online]. Available: <https://doi.org/10.1046/j.1365-2818.2000.00710.x>
  - [45] C. Maurer, A. Jesacher, S. Bernet, and M. Ritsch-Marte, “What spatial light modulators can do for optical microscopy,” *Laser & Photonics Reviews*, vol. 5, no. 1, pp. 81–101, 2011.
  - [46] M. M. Qureshi, J. Brake, H.-J. Jeon, H. Ruan, Y. Liu, A. M. Safi, T. J. Eom, C. Yang, and E. Chung, “In vivo study of optical speckle decorrelation time across depths in the mouse brain,” *Biomedical optics express*, vol. 8, no. 11, pp. 4855–4864, 10 2017. [Online]. Available: <https://www.ncbi.nlm.nih.gov/pubmed/29188086>
  - [47] D. Stellinga, D. B. Phillips, M. Edgar, S. Turtaev, T. Čižmár, and M. J. Padgett, “Imaging beyond a multimode fibre with time of flight depth information,” in *Conference on Lasers and Electro-Optics*. San Jose, California: Optical Society of America, 2018, p. STh3K.3. [Online]. Available: [http://www.osapublishing.org/abstract.cfm?URI=CLEO\\_SI-2018-STh3K.3](http://www.osapublishing.org/abstract.cfm?URI=CLEO_SI-2018-STh3K.3)
  - [48] D. B. Conkey, A. M. Caravaca-Aguirre, and R. Piestun, “High-speed scattering medium characterization with application to focusing light through turbid media,” *Optics express*, vol. 20, no. 2, pp. 1733–1740, 2012.
  - [49] T. Čižmár and K. Dholakia, “Exploiting multimode waveguides for pure fibre-based imaging,” *Nature communications*, vol. 3, p. 1027, 2012.

- 
- [50] S. Popoff, G. Lerosey, M. Fink, A. C. Boccara, and S. Gigan, “Image transmission through an opaque material,” *Nature communications*, vol. 1, p. 81, 2010.
  - [51] S. Popoff, G. Lerosey, R. Carminati, M. Fink, A. Boccara, and S. Gigan, “Measuring the transmission matrix in optics: an approach to the study and control of light propagation in disordered media,” *Physical review letters*, vol. 104, no. 10, p. 100601, 2010.
  - [52] S. Bianchi and R. Di Leonardo, “A multi-mode fiber probe for holographic micromanipulation and microscopy,” *Lab on a Chip*, vol. 12, no. 3, pp. 635–639, 2012.
  - [53] S. A. Vasquez-Lopez, R. Turcotte, V. Koren, M. Plöschner, Z. Padamsey, M. J. Booth, T. Čižmár, and N. J. Emptage, “Subcellular spatial resolution achieved for deep-brain imaging in vivo using a minimally invasive multimode fiber,” *Light: Science & Applications*, vol. 7, no. 1, p. 110, 2018.
  - [54] M. Plöschner, T. Tyc, and T. Čižmár, “Seeing through chaos in multimode fibres,” *Nature Photonics*, vol. 9, no. 8, p. 529, 2015.
  - [55] N. Radwell, A. Selyem, L. Mertens, M. P. Edgar, and M. J. Padgett, “Hybrid 3d ranging and velocity tracking system combining multi-view cameras and simple lidar,” *Scientific Reports*, vol. 9, no. 1, p. 5241, 2019. [Online]. Available: <https://doi.org/10.1038/s41598-019-41598-z>
  - [56] J. H. Shapiro and R. W. Boyd, “The physics of ghost imaging,” *Quantum Information Processing*, vol. 11, no. 4, pp. 949–93, 2012.
  - [57] R. S. Aspden, D. S. Tasca, R. W. Boyd, and M. J. Padgett, “EPR-based ghost imaging using a single-photon-sensitive camera,” *New Journal of Physics*, vol. 15, no. 7, p. 073032, jul 2013. [Online]. Available: <https://doi.org/10.1088%2F1367-2630%2F15%2F7%2F073032>
  - [58] P. A. Morris, R. S. Aspden, J. E. C. Bell, R. W. Boyd, and M. J. Padgett, “Imaging with a small number of photons,” *Nature Communications*, vol. 6, pp. 5913 EP –, 01 2015. [Online]. Available: <https://doi.org/10.1038/ncomms6913>

- 
- [59] J. H. Shapiro, “Computational ghost imaging,” *Phys. Rev. A*, vol. 78, p. 061802, Dec 2008. [Online]. Available: <https://link.aps.org/doi/10.1103/PhysRevA.78.061802>
  - [60] B. Sun, M. P. Edgar, R. Bowman, L. E. Vittert, S. Welsh, A. Bowman, and M. J. Padgett, “3d computational imaging with single-pixel detectors,” *Science*, vol. 340, no. 6134, p. 844, 05 2013. [Online]. Available: <http://science.sciencemag.org/content/340/6134/844.abstract>
  - [61] N. Radwell, K. J. Mitchell, G. M. Gibson, M. P. Edgar, R. Bowman, and M. J. Padgett, “Single-pixel infrared and visible microscope,” *Optica*, vol. 1, no. 5, pp. 285–289, 2014. [Online]. Available: <http://www.osapublishing.org/optica/abstract.cfm?URI=optica-1-5-285>
  - [62] M. F. Duarte, M. A. Davenport, D. Takhar, J. N. Laska, T. Sun, K. F. Kelly, and R. G. Baraniuk, “Single-pixel imaging via compressive sampling,” *IEEE Signal Processing Magazine*, vol. 25, no. 2, pp. 83–91, 2008.
  - [63] L. J. Hornbeck, “Multi-level digital micromirror device,” Dec. 10 1996, uS Patent 5,583,688.
  - [64] D. Dudley, W. M. Duncan, and J. Slaughter, “Emerging digital micromirror device (dmd) applications,” in *MOEMS display and imaging systems*, vol. 4985. International Society for Optics and Photonics, 2003, pp. 14–26.
  - [65] C. H. R. M.-S. Matthew P. Edgar, Miles J. Padgett, “Real-time photon-counting lidar enhanced with deep-learning (conference presentation),” *Proc.SPIE*, vol. 10799, 2018.
  - [66] S. D. Johnson, D. B. Phillips, Z. Ma, S. Ramachandran, and M. J. Padgett, “A light-in-flight single-pixel camera for use in the visible and short-wave infrared,” *Opt. Express*, vol. 27, no. 7, pp. 9829–9837, Apr 2019. [Online]. Available: <http://www.opticsexpress.org/abstract.cfm?URI=oe-27-7-9829>
  - [67] J. Liang, L. Zhu, and L. V. Wang, “Single-shot real-time femtosecond imaging of temporal focusing,” *Light: Science & Applications*, vol. 7, no. 1, p. 42, 2018. [Online]. Available: <https://doi.org/10.1038/s41377-018-0044-7>

- 
- [68] A. Ashkin, “Acceleration and trapping of particles by radiation pressure,” *Physical Review Letters*, vol. 24, no. 4, pp. 156–159, 01 1970. [Online]. Available: <https://link.aps.org/doi/10.1103/PhysRevLett.24.156>
  - [69] J. E. Curtis, B. A. Koss, and D. G. Grier, “Dynamic holographic optical tweezers,” *Optics communications*, vol. 207, no. 1-6, pp. 169–175, 2002.
  - [70] M. Padgett and R. Bowman, “Tweezers with a twist,” *Nature Photonics*, vol. 5, pp. 343 EP –, 05 2011. [Online]. Available: <https://doi.org/10.1038/nphoton.2011.81>
  - [71] N. B. Simpson, K. Dholakia, L. Allen, and M. J. Padgett, “Mechanical equivalence of spin and orbital angular momentum of light: an optical spanner,” *Opt. Lett.*, vol. 22, no. 1, pp. 52–54, Jan 1997. [Online]. Available: <http://ol.osa.org/abstract.cfm?URI=ol-22-1-52>
  - [72] R. W. Bowman, G. M. Gibson, A. Linnenberger, D. B. Phillips, J. A. Grieve, D. M. Carberry, S. Serati, M. J. Miles, and M. J. Padgett, ““red tweezers”: Fast, customisable hologram generation for optical tweezers,” *Computer Physics Communications*, vol. 185, no. 1, pp. 268–273, 2014.
  - [73] M. Friese, T. Nieminen, N. Heckenberg, and H. Rubinsztein-Dunlop, “Optical alignment and spinning of laser-trapped microscopic particles,” *Nature*, vol. 394, no. 6691, p. 348, 1998.
  - [74] Q. Zhan, “Trapping metallic rayleigh particles with radial polarization,” *Optics express*, vol. 12, no. 15, pp. 3377–3382, 2004.
  - [75] S. Franke-Arnold, J. Leach, M. J. Padgett, V. E. Lembessis, D. Ellinas, A. J. Wright, J. M. Girkin, P. Öhberg, and A. S. Arnold, “Optical ferris wheel for ultracold atoms,” *Optics Express*, vol. 15, no. 14, pp. 8619–8625, 2007. [Online]. Available: <http://www.opticsexpress.org/abstract.cfm?URI=oe-15-14-8619>
  - [76] H. Kawauchi, K. Yonezawa, Y. Kozawa, and S. Sato, “Calculation of optical trapping forces on a dielectric sphere in the ray optics regime produced by a radially polarized laser beam,” *Opt. Lett.*, vol. 32, no. 13, pp. 1839–1841, Jul 2007. [Online]. Available: <http://ol.osa.org/abstract.cfm?URI=ol-32-13-1839>
  - [77] G. Chryssolouris and M. (MIT, Cambridge, *Laser machining - Theory and practice*. United States: Research supported by NSF; Ford Motor Co.,

- 
- Cross Co., et al. New York, Springer-Verlag, 1991. [Online]. Available: <https://www.osti.gov/servlets/purl/5565766>
- [78] V. Niziev and A. Nesterov, “Influence of beam polarization on laser cutting efficiency,” *Journal of Physics D: Applied Physics*, vol. 32, no. 13, p. 1455, 1999.
- [79] S. Pereira and A. Van de Nes, “Superresolution by means of polarisation, phase and amplitude pupil masks,” *Optics communications*, vol. 234, no. 1-6, pp. 119–124, 2004.
- [80] R. Drevinskas, J. Zhang, M. Beresna, M. Gecevičius, A. G. Kazanskii, Y. P. Svirko, and P. G. Kazansky, “Laser material processing with tightly focused cylindrical vector beams,” *Applied Physics Letters*, vol. 108, no. 22, p. 221107, 2016. [Online]. Available: <https://doi.org/10.1063/1.4953455>
- [81] M. Meier, V. Romano, and T. Feurer, “Material processing with pulsed radially and azimuthally polarized laser radiation,” *Applied Physics A*, vol. 86, no. 3, pp. 329–334, Mar 2007. [Online]. Available: <https://doi.org/10.1007/s00339-006-3784-9>
- [82] Q. Zhan, “Cylindrical vector beams: from mathematical concepts to applications,” *Advances in Optics and Photonics*, vol. 1, no. 1, pp. 1–57, 2009.
- [83] K. S. Youngworth and T. G. Brown, “Focusing of high numerical aperture cylindrical-vector beams,” *Opt. Express*, vol. 7, no. 2, pp. 77–87, Jul 2000. [Online]. Available: <http://www.opticsexpress.org/abstract.cfm?URI=oe-7-2-77>
- [84] Q. Zhan and J. R. Leger, “Focus shaping using cylindrical vector beams,” *Opt. Express*, vol. 10, no. 7, pp. 324–331, Apr 2002. [Online]. Available: <http://www.opticsexpress.org/abstract.cfm?URI=oe-10-7-324>
- [85] X. Li, T.-H. Lan, C.-H. Tien, and M. Gu, “Three-dimensional orientation-unlimited polarization encryption by a single optically configured vectorial beam,” *Nature Communications*, vol. 3, pp. 998 EP –, 08 2012. [Online]. Available: <https://doi.org/10.1038/ncomms2006>
- [86] T. B. Pittman, Y. H. Shih, D. V. Strekalov, and A. V. Sergienko, “Optical imaging by means of two-photon quantum entanglement,” *Physical*

- 
- Review A*, vol. 52, no. 5, pp. R3429–R3432, 11 1995. [Online]. Available: <https://link.aps.org/doi/10.1103/PhysRevA.52.R3429>
- [87] J. Leach, B. Jack, J. Romero, M. Ritsch-Marte, R. Boyd, A. Jha, S. Barnett, S. Franke-Arnold, and M. Padgett, “Violation of a bell inequality in two-dimensional orbital angular momentum state-spaces,” *Optics express*, vol. 17, no. 10, pp. 8287–8293, 2009.
- [88] A. C. Dada, J. Leach, G. S. Buller, M. J. Padgett, and E. Andersson, “Experimental high-dimensional two-photon entanglement and violations of generalized bell inequalities,” *Nature Physics*, vol. 7, pp. 677 EP –, 05 2011. [Online]. Available: <https://doi.org/10.1038/nphys1996>
- [89] T. Chapuran, P. Toliver, N. Peters, J. Jackel, M. Goodman, R. Runser, S. McNown, N. Dallmann, R. Hughes, K. McCabe *et al.*, “Optical networking for quantum key distribution and quantum communications,” *New Journal of Physics*, vol. 11, no. 10, p. 105001, 2009.
- [90] B. Ndagano, I. Nape, M. A. Cox, C. Rosales-Guzman, and A. Forbes, “Creation and characterization of vector vortex modes for classical and quantum communication,” *arXiv preprint arXiv:1709.00736*, 2017.
- [91] V. Parigi, V. D’Ambrosio, C. Arnold, L. Marrucci, F. Sciarrino, and J. Laurat, “Storage and retrieval of vector beams of light in a multiple-degree-of-freedom quantum memory,” *Nature communications*, vol. 6, pp. 7706; 7706–7706, 07 2015. [Online]. Available: <https://www.ncbi.nlm.nih.gov/pubmed/26166257>
- [92] T. Feurer, J. C. Vaughan, R. M. Koehl, and K. A. Nelson, “Multidimensional control of femtosecond pulses by use of a programmable liquid-crystal matrix,” *Opt. Lett.*, vol. 27, no. 8, pp. 652–654, Apr 2002. [Online]. Available: <http://ol.osa.org/abstract.cfm?URI=ol-27-8-652>
- [93] J. C. Vaughan, T. Feurer, and K. A. Nelson, “Automated two-dimensional femtosecond pulse shaping,” *J. Opt. Soc. Am. B*, vol. 19, no. 10, pp. 2489–2495, Oct 2002. [Online]. Available: <http://josab.osa.org/abstract.cfm?URI=josab-19-10-2489>
- [94] T. Brixner, G. Krampert, T. Pfeifer, R. Selle, G. Gerber, M. Wollenhaupt, O. Graefe, C. Horn, D. Liese, and T. Baumert, “Quantum control by ultrafast polarization shaping,” *Physical review letters*, vol. 92, no. 20, p. 208301, 2004.

- 
- [95] J. C. Vaughan, T. Hornung, T. Feurer, and K. A. Nelson, “Diffraction-based femtosecond pulse shaping with a two-dimensional spatial light modulator,” *Opt. Lett.*, vol. 30, no. 3, pp. 323–325, Feb 2005. [Online]. Available: <http://ol.osa.org/abstract.cfm?URI=ol-30-3-323>
  - [96] E. Frumker and Y. Silberberg, “Femtosecond pulse shaping using a two-dimensional liquid-crystal spatial light modulator,” *Opt. Lett.*, vol. 32, no. 11, pp. 1384–1386, Jun 2007. [Online]. Available: <http://ol.osa.org/abstract.cfm?URI=ol-32-11-1384>
  - [97] J. M. Donohue, J. Lavoie, and K. J. Resch, “Ultrafast time-division demultiplexing of polarization-entangled photons,” *Physical Review Letters*, vol. 113, no. 16, pp. 163602–, 10 2014. [Online]. Available: <https://link.aps.org/doi/10.1103/PhysRevLett.113.163602>
  - [98] X. Wang and N. Wada, “Spectral phase encoding of ultra-short optical pulse in time domain for ocdma application,” *Optics Express*, vol. 15, no. 12, pp. 7319–7326, 2007. [Online]. Available: <http://www.opticsexpress.org/abstract.cfm?URI=oe-15-12-7319>
  - [99] A. M. Weiner, “Femtosecond pulse shaping using spatial light modulators,” *Review of Scientific Instruments*, vol. 71, no. 5, pp. 1929–1960, 2000. [Online]. Available: <https://doi.org/10.1063/1.1150614>
  - [100] J. Vučić, C. Kottke, S. Nerreter, K.-D. Langer, and J. W. Walewski, “513 mbit/s visible light communications link based on dmt-modulation of a white led,” *Journal of lightwave technology*, vol. 28, no. 24, pp. 3512–3518, 2010.
  - [101] A. Forbes, F. Dickey, M. DeGama, and A. du Plessis, “Wavelength tunable laser beam shaping,” *Opt. Lett.*, vol. 37, no. 1, pp. 49–51, Jan 2012. [Online]. Available: <http://ol.osa.org/abstract.cfm?URI=ol-37-1-49>
  - [102] N. Radwell, R. Hawley, J. Götte, and S. Franke-Arnold, “Achromatic vector vortex beams from a glass cone,” *Nature communications*, vol. 7, p. 10564, 2016.
  - [103] C. Canavesi, F. Morichetti, A. Canciamilla, F. Persia, and A. Melloni, “Polarization- and phase-sensitive low-coherence interferometry setup for the characterization of integrated optical components,” *Journal of Lightwave*

- 
- Technology*, vol. 27, no. 15, pp. 3062–3074, 2009. [Online]. Available: <http://jlt.osa.org/abstract.cfm?URI=jlt-27-15-3062>
- [104] K. Lindfors, T. Kalkbrenner, P. Stoller, and V. Sandoghdar, “Detection and spectroscopy of gold nanoparticles using supercontinuum white light confocal microscopy,” *Physical review letters*, vol. 93, no. 3, p. 037401, 2004.
- [105] D. N. Naik, N. A. Saad, D. N. Rao, and N. K. Viswanathan, “Ultrashort vortex from a gaussian pulse –an achromatic-interferometric approach,” *Scientific Reports*, vol. 7, no. 1, p. 2395, 2017. [Online]. Available: <https://doi.org/10.1038/s41598-017-02613-3>
- [106] R. D. Hawley, J. Cork, N. Radwell, and S. Franke-Arnold, “Passive broadband full stokes polarimeter using a fresnel cone,” *Scientific Reports*, vol. 9, no. 1, p. 2688, 2019. [Online]. Available: <https://doi.org/10.1038/s41598-019-39118-0>
- [107] D. Huang, E. Swanson, C. Lin, J. Schuman, W. Stinson, W. Chang, M. Hee, T. Flotte, K. Gregory, C. Puliafito, and a. et, “Optical coherence tomography,” *Science*, vol. 254, no. 5035, p. 1178, 11 1991. [Online]. Available: <http://science.sciencemag.org/content/254/5035/1178.abstract>
- [108] E. Whittaker, *A history of the theories of aether and electricity : from the age of Descartes to the close of the nineteenth century*. Longmans, Green, 1910.
- [109] C. Huygens, *Treatise on light (translation)*. London: Macmillan, 1912.
- [110] T. Young, “The bakerian lecture: Experiments and calculations relative to physical optics,” in *Philosophical Transactions of the Royal Society of London*, vol. 94, 1804, pp. 1–16.
- [111] E. Collett, *Field Guide to Polarization*, ser. Field Guide Series. SPIE Press, 2005. [Online]. Available: <https://books.google.co.uk/books?id=5lJwcCsLbLsC>
- [112] H. J. Pain, *The Physics of Vibrations and Waves*, 6th ed., ser. ISBN-13: 978-0470012963. Wiley-Blackwell, 2005.
- [113] R. A. F. Hugh D. Young, *University Physics with Modern Physics, 14th Edition*, 14th ed., ser. ISBN-13 9780321973610. Pearson, 2016.

- 
- [114] A. Chapanis, “Fundamentals of optics. francis a. jenkins , harvey e. white,” *The Quarterly Review of Biology*, vol. 27, no. 1, pp. 115–115, 1952. [Online]. Available: <https://doi.org/10.1086/398796>
  - [115] D. T. Reid, “Ultrafast photonics,” Scottish Universities Physics Alliance (SUPA) postgraduate lecture series, 2016.
  - [116] R. W. Boyd and D. J. Gauthier, “Controlling the velocity of light pulses,” *Science*, vol. 326, no. 5956, pp. 1074–1077, 2009. [Online]. Available: <https://science.sciencemag.org/content/326/5956/1074>
  - [117] C. Akcay, P. Parrein, and J. P. Rolland, “Estimation of longitudinal resolution in optical coherence imaging,” *Applied Optics*, vol. 41, no. 25, pp. 5256–5262, 2002. [Online]. Available: <http://ao.osa.org/abstract.cfm?URI=ao-41-25-5256>
  - [118] G. Sagnac, “L’éther lumineux démontré par l’effet du vent relatif d’éther dans un interféromètre en rotation uniforme,” *Comptes Rendus*, vol. 157, pp. 708–710, 1913.
  - [119] C. G. L. Robert R. Thomson, Derryck T. Reid, *Ultrafast Nonlinear Optics*. Springer, 2013.
  - [120] R. Fork, O. Martinez, and J. Gordon, “Negative dispersion using pairs of prisms,” *Optics letters*, vol. 9, no. 5, pp. 150–152, 1984.
  - [121] L. I. Goldfischer, “Autocorrelation function and power spectral density of laser-produced speckle patterns,” *Journal of the Optical Society of America*, vol. 55, no. 3, pp. 247–253, 1965. [Online]. Available: <http://www.osapublishing.org/abstract.cfm?URI=josa-55-3-247>
  - [122] M. V. B. John Frederick Nye, “Dislocations in wave trains,” *Proceedings of the Royal Society of London. A. Mathematical and Physical Sciences*, vol. 336, no. 1605, pp. 165–190, 2019/05/07 1974. [Online]. Available: <https://doi.org/10.1098/rspa.1974.0012>
  - [123] A. M. Yao and M. J. Padgett, “Orbital angular momentum: origins, behavior and applications,” *Adv. Opt. Photon.*, vol. 3, no. 2, pp. 161–204, Jun 2011. [Online]. Available: <http://aop.osa.org/abstract.cfm?URI=aop-3-2-161>
  - [124] M. Optics. Catalog: Retarder principles whitepaper.

- 
- [125] Thorlabs. Mounted calcite beam displacers. [Online]. Available: [https://www.thorlabs.com/newgrouppage9.cfm?objectgroup\\_id=745&pn=BD27](https://www.thorlabs.com/newgrouppage9.cfm?objectgroup_id=745&pn=BD27)
  - [126] E. Hecht, “Note on an operational definition of the stokes parameters,” *American Journal of Physics*, vol. 38, no. 9, pp. 1156–1158, 1970.
  - [127] C. W. Simon Hooker, *Laser Physics*. Oxford University Press, 2010.
  - [128] A. Siegman, *Lasers*. University Science Books, 1986.
  - [129] M. Padgett, J. Arlt, N. Simpson, and L. Allen, “An experiment to observe the intensity and phase structure of laguerre–gaussian laser modes,” *American Journal of Physics*, vol. 64, no. 1, pp. 77–82, 2019/08/06 1996. [Online]. Available: <https://doi.org/10.1119/1.18283>
  - [130] L. Allen, M. Padgett, and M. Babiker, “The orbital angular momentum of light,” ser. Progress in Optics, E. Wolf, Ed. Elsevier, 1999, vol. 39, pp. 291 – 372. [Online]. Available: <http://www.sciencedirect.com/science/article/pii/S0079663808703913>
  - [131] P. Coullet, L. Gil, and F. Rocca, “Optical vortices,” *Optics Communications*, vol. 73, no. 5, pp. 403 – 408, 1989. [Online]. Available: <http://www.sciencedirect.com/science/article/pii/0030401889901806>
  - [132] M. C. T. Bahaa E. A. Saleh, *Fundamentals of Photonics*. Wiley-Interscience, 1991.
  - [133] D. GABOR, “A new microscopic principle,” *Nature*, vol. 161, no. 4098, pp. 777–778, 1948. [Online]. Available: <https://doi.org/10.1038/161777a0>
  - [134] E. N. Leith and J. Upatnieks, “Reconstructed wavefronts and communication theory,” *J. Opt. Soc. Am.*, vol. 52, no. 10, pp. 1123–1130, Oct 1962. [Online]. Available: <http://www.osapublishing.org/abstract.cfm?URI=josa-52-10-1123>
  - [135] M. Born, E. Wolf, A. B. Bhatia, P. C. Clemmow, D. Gabor, A. R. Stokes, A. M. Taylor, P. A. Wayman, and W. L. Wilcock, *Principles of Optics: Electromagnetic Theory of Propagation, Interference and Diffraction of Light*, 7th ed. Cambridge University Press, 1999.

- 
- [136] Meadowlark, “Meadowlark optics: spatial light modulator - 512 x 512,” 2019. [Online]. Available: [https://www.meadowlark.com/store/data\\_sheet/SLM-Small\\_512x512.pdf](https://www.meadowlark.com/store/data_sheet/SLM-Small_512x512.pdf)
  - [137] G. W. Gray, K. J. Harrison, and J. A. Nash, “New family of nematic liquid crystals for displays,” *Electronics Letters*, vol. 9, no. 6, pp. 130–131, 1973.
  - [138] HamamatsuPhotonics, “Opto-semiconductor handbook,” <https://www.hamamatsu-news.de/>, 2014.
  - [139] L. J. Hornbeck, “Current status of the digital micromirror device (dmd) for projection television applications,” in *Proceedings of IEEE International Electron Devices Meeting*. IEEE, 1993, pp. 381–384.
  - [140] B. Lee, *Introduction to  $\pm 12$  Degree Orthogonal Digital Micromirror Devices (DMDs)*, dlpa008b ed., Texas Instruments, [www.ti.com/lit/an/dlpa008b/dlpa008b.pdf](http://www.ti.com/lit/an/dlpa008b/dlpa008b.pdf), February 2018.
  - [141] T. Instruments. (2008, September) Tidn2509927: Using lasers with dlp dmd technology. [Online]. Available: <http://www.ti.com/lit/wp/dlpa037/dlpa037.pdf>
  - [142] M. K. Sheeja, A. Kumar, F. N. Saidalavi, and A. S. Nair, “Conversion of an 84- $\times$ 48-pixel mobile phone display to a liquid crystal spatial light modulator,” *Optical Engineering*, vol. 47, no. 2, pp. 1 – 4, 2008. [Online]. Available: <https://doi.org/10.1117/1.2844877>
  - [143] X. Yu, A. Todi, and H. Tang, “Bessel beam generation using a segmented deformable mirror,” *Applied Optics*, vol. 57, no. 16, pp. 4677–4682, 2018. [Online]. Available: <http://ao.osa.org/abstract.cfm?URI=ao-57-16-4677>
  - [144] J. P. Gardner, J. C. Mather, M. Clampin, R. Doyon, M. A. Greenhouse, H. B. Hammel, J. B. Hutchings, P. Jakobsen, S. J. Lilly, K. S. Long, J. I. Lunine, M. J. Mccaughrean, M. Mountain, J. Nella, G. H. Rieke, M. J. Rieke, H.-W. Rix, E. P. Smith, G. Sonneborn, M. Stiavelli, H. S. Stockman, R. A. Windhorst, and G. S. Wright, “The james webb space telescope,” *Space Science Reviews*, vol. 123, no. 4, pp. 485–606, Apr 2006. [Online]. Available: <https://doi.org/10.1007/s11214-006-8315-7>

- 
- [145] C. Day. Miniaturized adaptive optics at spie photonics west. [Online]. Available: <https://physicstoday.scitation.org/doi/10.1063/PT.5.010075/full/>
  - [146] M. D. P. et al., “James webb space telescope optical simulation testbed i: overview and first results,” vol. Space Telescopes and Instrumentation 2014: Optical, Infrared, and Millimeter Wave, 914309, <https://doi.org/10.1117/12.2056936>, 2014.
  - [147] T. W. Clark, R. F. Offer, S. Franke-Arnold, A. S. Arnold, and N. Radwell, “Comparison of beam generation techniques using a phase only spatial light modulator,” *Optics express*, vol. 24, no. 6, pp. 6249–6264, 2016.
  - [148] E. G. Loewen, M. Nevière, and D. Maystre, “Grating efficiency theory as it applies to blazed and holographic gratings,” *Applied Optics*, vol. 16, no. 10, pp. 2711–2721, 1977. [Online]. Available: <http://ao.osa.org/abstract.cfm?URI=ao-16-10-2711>
  - [149] C. Palmer, *Diffraction Grating Handbook*, 6th ed. Newport Corporation, 2005.
  - [150] M. Mirhosseini, O. S. Magana-Loaiza, C. Chen, B. Rodenburg, M. Malik, and R. W. Boyd, “Rapid generation of light beams carrying orbital angular momentum,” *Optics express*, vol. 21, no. 25, pp. 30 196–30 203, 2013.
  - [151] K. J. Mitchell, S. Turtaev, M. J. Padgett, T. Čížmár, and D. B. Phillips, “High-speed spatial control of the intensity, phase and polarisation of vector beams using a digital micro-mirror device,” *Opt. Express*, vol. 24, no. 25, pp. 29 269–29 282, Dec 2016. [Online]. Available: <http://www.opticsexpress.org/abstract.cfm?URI=oe-24-25-29269>
  - [152] —, “High-speed polarisation shaping of arbitrary vector beams using a digital micro-mirror device,” *Conference on Lasers and Electro-Optics*, vol. STu4O.2, 2017. [Online]. Available: [http://www.osapublishing.org/abstract.cfm?URI=CLEO\\_SI-2017-STu4O.2](http://www.osapublishing.org/abstract.cfm?URI=CLEO_SI-2017-STu4O.2)
  - [153] J. Romero, D. Giovannini, S. Franke-Arnold, S. M. Barnett, and M. J. Padgett, “Increasing the dimension in high-dimensional two-photon orbital angular momentum entanglement,” *Physical Review A*, vol. 86, no. 1, pp. 012 334–, 07 2012. [Online]. Available: <https://link.aps.org/doi/10.1103/PhysRevA.86.012334>

- 
- [154] J. A. Davis, D. M. Cottrell, J. Campos, M. J. Yzuel, and I. Moreno, “Encoding amplitude information onto phase-only filters,” *Applied optics*, vol. 38, no. 23, pp. 5004–5013, 1999.
  - [155] R. Di Leonardo, F. Ianni, and G. Ruocco, “Computer generation of optimal holograms for optical trap arrays,” *Optics Express*, vol. 15, no. 4, pp. 1913–1922, 2007.
  - [156] J. P. Kirk and A. L. Jones, “Phase-only complex-valued spatial filter,” *Journal of the Optical Society of America*, vol. 61, no. 8, pp. 1023–1028, 1971. [Online]. Available: <http://www.osapublishing.org/abstract.cfm?URI=josa-61-8-1023>
  - [157] B. Jack, A. M. Yao, J. Leach, J. Romero, S. Franke-Arnold, D. G. Ireland, S. M. Barnett, and M. J. Padgett, “Entanglement of arbitrary superpositions of modes within two-dimensional orbital angular momentum state spaces,” *Physical Review A*, vol. 81, no. 4, pp. 043844–, 04 2010. [Online]. Available: <https://link.aps.org/doi/10.1103/PhysRevA.81.043844>
  - [158] A. Jesacher, C. Maurer, A. Schwaighofer, S. Bernet, and M. Ritsch-Marte, “Near-perfect hologram reconstruction with a spatial light modulator,” *Opt. Express*, vol. 16, no. 4, pp. 2597–2603, Feb 2008. [Online]. Available: <http://www.opticsexpress.org/abstract.cfm?URI=oe-16-4-2597>
  - [159] W. S. R.W. Gerchberg, “Practical algorithm for determination of phase from image and diffraction plane pictures,” *Optik*, vol. 35, pp. 237–246, 1972.
  - [160] L. Marrucci, C. Manzo, and D. Paparo, “Optical spin-to-orbital angular momentum conversion in inhomogeneous anisotropic media,” *Physical review letters*, vol. 96, no. 16, p. 163905, 2006.
  - [161] A. Rubano, F. Cardano, B. Piccirillo, and L. Marrucci, “Q-plate technology: a progress review,” *J. Opt. Soc. Am. B*, vol. 36, no. 5, pp. D70–D87, May 2019. [Online]. Available: <http://josab.osa.org/abstract.cfm?URI=josab-36-5-D70>
  - [162] D. Naidoo, F. S. Roux, A. Dudley, I. Litvin, B. Piccirillo, L. Marrucci, and A. Forbes, “Controlled generation of higher-order poincaré sphere beams from a laser,” *Nature Photonics*, vol. 10, no. 5, p. 327, 2016.

- 
- [163] S. C. Tidwell, D. H. Ford, and W. D. Kimura, "Generating radially polarized beams interferometrically," *Appl. Opt.*, vol. 29, no. 15, pp. 2234–2239, May 1990. [Online]. Available: <http://ao.osa.org/abstract.cfm?URI=ao-29-15-2234>
- [164] M. A. A. Neil, F. Massoumian, R. Juškaitis, and T. Wilson, "Method for the generation of arbitrary complex vector wave fronts," *Opt. Lett.*, vol. 27, no. 21, pp. 1929–1931, Nov 2002. [Online]. Available: <http://ol.osa.org/abstract.cfm?URI=ol-27-21-1929>
- [165] C. Maurer, A. Jesacher, S. Fürhapter, S. Bernet, and M. Ritsch-Marte, "Tailoring of arbitrary optical vector beams," *New Journal of Physics*, vol. 9, no. 3, p. 78, 2007.
- [166] S. Liu, S. Qi, Y. Zhang, P. Li, D. Wu, L. Han, and J. Zhao, "Highly efficient generation of arbitrary vector beams with tunable polarization, phase, and amplitude," *Photonics Research*, vol. 6, no. 4, pp. 228–233, 2018.
- [167] X.-L. Wang, J. Ding, W.-J. Ni, C.-S. Guo, and H.-T. Wang, "Generation of arbitrary vector beams with a spatial light modulator and a common path interferometric arrangement," *Optics letters*, vol. 32, no. 24, pp. 3549–3551, 2007.
- [168] B. R. Brown and A. W. Lohmann, "Complex spatial filtering with binary masks," *Applied Optics*, vol. 5, no. 6, pp. 967–969, 1966.
- [169] Y.-X. Ren, M. Li, K. Huang, J.-G. Wu, H.-F. Gao, Z.-Q. Wang, and Y.-M. Li, "Experimental generation of laguerre-gaussian beam using digital micromirror device," *Applied optics*, vol. 49, no. 10, pp. 1838–1844, 2010.
- [170] V. Lerner, D. Shwa, Y. Drori, and N. Katz, "Shaping laguerre–gaussian laser modes with binary gratings using a digital micromirror device," *Optics letters*, vol. 37, no. 23, pp. 4826–4828, 2012.
- [171] D. Stuart, O. Barter, and A. Kuhn, "Fast algorithms for generating binary holograms," *arXiv preprint arXiv:1409.1841*, 2014.
- [172] S. A. Goorden, J. Bertolotti, and A. P. Mosk, "Superpixel-based spatial amplitude and phase modulation using a digital micromirror device," *Optics express*, vol. 22, no. 15, pp. 17 999–18 009, 2014.

- 
- [173] A. B. Stilgoe, A. V. Kashchuk, D. Preece, and H. Rubinsztein-Dunlop, “An interpretation and guide to single-pass beam shaping methods using slms and dmds,” *Journal of Optics*, vol. 18, no. 6, p. 065609, 2016.
  - [174] K. J. M. M. J. P. D. B. P. T. Č. Sergey Turtaev, Ivo T. Leite, “Exploiting digital micromirror device for holographic micro-endoscopy,” 2019. [Online]. Available: <https://doi.org/10.1117/12.2509429>
  - [175] T. Instruments, “Dlp lightcommander development kit: Extending the connection between the controller board and the dmd board- white paper dlpa028,” TI, white paper, December 2011.
  - [176] S. Turtaev, I. T. Leite, K. J. Mitchell, M. J. Padgett, D. B. Phillips, and T. Čižmár, “Comparison of nematic liquid-crystal and dmd based spatial light modulation in complex photonics,” *Optics express*, vol. 25, no. 24, pp. 29 874–29 884, 2017.
  - [177] W.-H. Lee, “Binary computer-generated holograms,” *Applied Optics*, vol. 18, no. 21, pp. 3661–3669, 1979.
  - [178] J. Courtial, “Self-imaging beams and the guoy effect,” *Optics communications*, vol. 151, no. 1-3, pp. 1–4, 1998.
  - [179] R. Dorn, S. Quabis, and G. Leuchs, “Sharper focus for a radially polarized light beam,” *Physical review letters*, vol. 91, no. 23, p. 233901, 2003.
  - [180] E. Galvez, P. Crawford, H. Sztul, M. Pysher, P. Haglin, and R. Williams, “Geometric phase associated with mode transformations of optical beams bearing orbital angular momentum,” *Physical review letters*, vol. 90, no. 20, p. 203901, 2003.
  - [181] J. Dymnt, “Hermite-gaussian mode patterns in gaas junction lasers,” *Applied Physics Letters*, vol. 10, no. 3, pp. 84–86, 1967.
  - [182] A. M. Beckley, T. G. Brown, and M. A. Alonso, “Full poincaré beams,” *Optics express*, vol. 18, no. 10, pp. 10 777–10 785, 2010.
  - [183] E. J. Galvez, S. Khadka, W. H. Schubert, and S. Nomoto, “Poincaré-beam patterns produced by nonseparable superpositions of laguerre–gauss and polarization modes of light,” *Applied optics*, vol. 51, no. 15, pp. 2925–2934, 2012.

- 
- [184] R. Liu, F. Li, M. Padgett, and D. Phillips, “Generalized photon sieves: fine control of complex fields with simple pinhole arrays,” *Optica*, vol. 2, no. 12, pp. 1028–1036, 2015.
  - [185] K. J. Mitchell, N. Radwell, S. Franke-Arnold, M. J. Padgett, and D. B. Phillips, “Polarisation structuring of broadband light,” *Opt. Express*, vol. 25, no. 21, pp. 25 079–25 089, Oct 2017. [Online]. Available: <http://www.opticsexpress.org/abstract.cfm?URI=oe-25-21-25079>
  - [186] D. Preece, S. Keen, E. Botvinick, R. Bowman, M. Padgett, and J. Leach, “Independent polarisation control of multiple optical traps,” *Optics express*, vol. 16, no. 20, pp. 15 897–15 902, 2008.
  - [187] F. Kenny, D. Lara, O. Rodríguez-Herrera, and C. Dainty, “Complete polarization and phase control for focus-shaping in high-na microscopy,” *Optics express*, vol. 20, no. 13, pp. 14 015–14 029, 2012.
  - [188] Z. Chen, T. Zeng, B. Qian, and J. Ding, “Complete shaping of optical vector beams,” *Optics express*, vol. 23, no. 14, pp. 17 701–17 710, 2015.
  - [189] V. Niziev, R. Chang, and A. Nesterov, “Generation of inhomogeneously polarized laser beams by use of a sagnac interferometer,” *Applied optics*, vol. 45, no. 33, pp. 8393–8399, 2006.
  - [190] P. Fischer, C. Brown, J. Morris, C. López-Mariscal, E. Wright, W. Sibbett, and K. Dholakia, “White light propagation invariant beams,” *Opt. Express*, vol. 13, no. 17, pp. 6657–6666, Aug 2005. [Online]. Available: <http://www.opticsexpress.org/abstract.cfm?URI=oe-13-17-6657>
  - [191] P. Fischer, H. Little, R. L. Smith, C. Lopez-Mariscal, C. T. A. Brown, W. Sibbett, and K. Dholakia, “Wavelength dependent propagation and reconstruction of white light bessel beams,” *Journal of Optics A: Pure and Applied Optics*, vol. 8, no. 5, pp. 477–482, apr 2006. [Online]. Available: <https://doi.org/10.1088%2F1464-4258%2F8%2F5%2F018>
  - [192] M. Gecevicius, M. Ivanov, M. Beresna, A. Matijosius, V. Tamuliene, T. Gertus, A. Cerkauskaite, K. Redekas, M. Vengris, V. Smilgevicius *et al.*, “Toward the generation of broadband optical vortices: extending the spectral range of a q-plate by polarization-selective filtering,” *JOSA B*, vol. 35, no. 1, pp. 190–196, 2018.

- 
- [193] Y. S. Rumala, G. Milione, T. A. Nguyen, S. ao Pratavieira, Z. Hossain, D. Nolan, S. Slussarenko, E. Karimi, L. Marrucci, and R. R. Alfano, “Tunable supercontinuum light vector vortex beam generator using a q-plate,” *Opt. Lett.*, vol. 38, no. 23, pp. 5083–5086, Dec 2013. [Online]. Available: <http://ol.osa.org/abstract.cfm?URI=ol-38-23-5083>
  - [194] K. Yamane, Y. Toda, and R. Morita, “Ultrashort optical-vortex pulse generation in few-cycle regime,” *Optics express*, vol. 20, no. 17, pp. 18 986–18 993, 2012.
  - [195] J. Leach and M. Padgett, “Observation of chromatic effects near a white-light vortex,” *New Journal of Physics*, vol. 5, no. 1, p. 154, 2003.
  - [196] D.-M. Spangenberg, A. Dudley, P. H. Neethling, E. G. Rohwer, and A. Forbes, “White light wavefront control with a spatial light modulator,” *Optics express*, vol. 22, no. 11, pp. 13 870–13 879, 2014.
  - [197] J. Liu and J. Wang, “Demonstration of polarization-insensitive spatial light modulation using a single polarization-sensitive spatial light modulator,” *Scientific reports*, vol. 5, p. 9959, 2015.
  - [198] M. A. Cox, C. Rosales-Guzmán, M. P. Lavery, D. J. Versfeld, and A. Forbes, “On the resilience of scalar and vector vortex modes in turbulence,” *Optics express*, vol. 24, no. 16, pp. 18 105–18 113, 2016.
  - [199] C. Rosales-Guzmán and A. Forbes, *How to Shape Light with Spatial Light Modulators*. SPIE Digital Library, 2017.
  - [200] T. Čižmár, M. Mazilu, and K. Dholakia, “In situ wavefront correction and its application to micromanipulation,” *Nature Photonics*, vol. 4, no. 6, p. 388, 2010.
  - [201] D. Giovannini, J. Romero, V. Potoček, G. Ferenczi, F. Speirits, S. M. Barnett, D. Faccio, and M. J. Padgett, “Spatially structured photons that travel in free space slower than the speed of light,” *Science*, vol. 347, no. 6224, pp. 857–860, 2015. [Online]. Available: <https://science.sciencemag.org/content/347/6224/857>
  - [202] A. Einstein, “On the electrodynamics of moving bodies,” *Annalen Phys.*, vol. 17, no. 10, pp. 891–921, 1905.

- 
- [203] W. R. P. I.S. Grant, *Electromagnetism*. Wiley, 1980, vol. 2nd edition.
  - [204] M. S. Bigelow, N. N. Lepeshkin, and R. W. Boyd, “Superluminal and slow light propagation in a room-temperature solid,” *Science*, vol. 301, no. 5630, pp. 200–202, 2003. [Online]. Available: <https://science.sciencemag.org/content/301/5630/200>
  - [205] T. Baba, “Slow light in photonic crystals,” *Nature Photonics*, vol. 2, pp. 465 EP –, 08 2008. [Online]. Available: <https://doi.org/10.1038/nphoton.2008.146>
  - [206] R. W. B. Joseph E. Vornehm. (2009) Tutorials in complex photonic media.
  - [207] E. Wisniewski-Barker, G. M. Gibson, S. Franke-Arnold, Z. Shi, P. Narum, R. W. Boyd, and M. J. Padgett, “Experimental investigation of the transient dynamics of slow light in ruby,” *New Journal of Physics*, vol. 16, no. 12, p. 123054, dec 2014. [Online]. Available: <https://doi.org/10.1088%2F1367-2630%2F16%2F12%2F123054>
  - [208] L. V. Hau, S. E. Harris, Z. Dutton, and C. H. Behroozi, “Light speed reduction to 17 metres per second in an ultracold atomic gas,” *Nature*, vol. 397, no. 6720, pp. 594–598, 1999. [Online]. Available: <https://doi.org/10.1038/17561>
  - [209] H. H. Jen, B. Xiong, I. A. Yu, and D.-W. Wang, “Electromagnetically induced transparency and slow light in quantum degenerate atomic gases,” *Journal of the Optical Society of America B*, vol. 30, no. 11, pp. 2855–2863, 2013. [Online]. Available: <http://josab.osa.org/abstract.cfm?URI=josab-30-11-2855>
  - [210] J. R. Sambles, “Structured photons take it slow,” *Science*, vol. 347, no. 6224, pp. 828–828, 2015. [Online]. Available: <https://science.sciencemag.org/content/347/6224/828>
  - [211] D. Giovannini, J. Romero, V. Potoček, G. Ferenczi, F. Speirits, S. M. Barnett, D. Faccio, and M. J. Padgett. (2015) Supplementary materials for spatially structured photons that travel in free space slower than the speed of light. [Online]. Available: [www.sciencemag.org/cgi/content/full/science.aaa3035/DC1](http://www.sciencemag.org/cgi/content/full/science.aaa3035/DC1)
  - [212] A. Yariv, *Quantum Electronics*. Wiley, November 1988, vol. 3rd Edition, no. ISBN: 978-0-471-60997-1.

- 
- [213] S. Feng and H. G. Winful, “Physical origin of the gouy phase shift,” *Opt. Lett.*, vol. 26, no. 8, pp. 485–487, Apr 2001. [Online]. Available: <http://ol.osa.org/abstract.cfm?URI=ol-26-8-485>
  - [214] I. S. Osborne, “Slowing down light with added structure,” *Science*, vol. 347, no. 6224, pp. 836–836, 2015. [Online]. Available: <https://science.sciencemag.org/content/347/6224/836.5>
  - [215] C. K. Hong, Z. Y. Ou, and L. Mandel, “Measurement of subpicosecond time intervals between two photons by interference,” *Phys. Rev. Lett.*, vol. 59, pp. 2044–2046, Nov 1987. [Online]. Available: <https://link.aps.org/doi/10.1103/PhysRevLett.59.2044>
  - [216] A. M. Steinberg, P. G. Kwiat, and R. Y. Chiao, “Dispersion cancellation in a measurement of the single-photon propagation velocity in glass,” *Physical Review Letters*, vol. 68, no. 16, pp. 2421–2424, 04 1992. [Online]. Available: <https://link.aps.org/doi/10.1103/PhysRevLett.68.2421>
  - [217] E. R. Nagelberg and J. Shefer, “Mode conversion in circular waveguides,” *The Bell System Technical Journal*, vol. 44, no. 7, pp. 1321–1338, 1965.
  - [218] R. M. Herman and T. A. Wiggins, “Production and uses of diffractionless beams,” *Journal of the Optical Society of America A*, vol. 8, no. 6, pp. 932–942, 1991. [Online]. Available: <http://josaa.osa.org/abstract.cfm?URI=josaa-8-6-932>
  - [219] J. H. McLeod, “The axicon: A new type of optical element,” *Journal of the Optical Society of America*, vol. 44, no. 8, pp. 592–597, 1954. [Online]. Available: <http://www.osapublishing.org/abstract.cfm?URI=josa-44-8-592>
  - [220] A. Vasara, J. Turunen, and A. T. Friberg, “Realization of general nondiffracting beams with computer-generated holograms,” *Journal of the Optical Society of America A*, vol. 6, no. 11, pp. 1748–1754, 1989. [Online]. Available: <http://josaa.osa.org/abstract.cfm?URI=josaa-6-11-1748>
  - [221] J. T. Lunardi, “Remarks on besell beams, signals and superluminality,” *Physics Letters A*, vol. 291, no. 2, pp. 66–72, 2001. [Online]. Available: <http://www.sciencedirect.com/science/article/pii/S0375960101007149>

- 
- [222] S. Klewitz, S. Sogomonian, M. Woerner, and S. Herminghaus, “Stimulated raman scattering of femtosecond bessel pulses,” *Optics Communications*, vol. 154, no. 4, pp. 186–190, 1998. [Online]. Available: <http://www.sciencedirect.com/science/article/pii/S0030401898003174>
  - [223] D. Mugnai, A. Ranfagni, and R. Ruggeri, “Observation of superluminal behaviors in wave propagation,” *Physical Review Letters*, vol. 84, no. 21, pp. 4830–4833, 05 2000. [Online]. Available: <https://link.aps.org/doi/10.1103/PhysRevLett.84.4830>
  - [224] K. B. Kuntz, B. Braverman, S. H. Youn, M. Lobino, E. M. Pessina, and A. I. Lvovsky, “Spatial and temporal characterization of a bessel beam produced using a conical mirror,” *Physical Review A*, vol. 79, no. 4, pp. 043 802–, 04 2009. [Online]. Available: <https://link.aps.org/doi/10.1103/PhysRevA.79.043802>
  - [225] I. Alexeev, K. Y. Kim, and H. M. Milchberg, “Measurement of the superluminal group velocity of an ultrashort bessel beam pulse.” *Phys Rev Lett*, vol. 88, no. 7, p. 073901, Feb 2002.
  - [226] P. W. Milonni, “Controlling the speed of light pulses,” vol. 35, no. 6, pp. R31–R56, 2002. [Online]. Available: <http://dx.doi.org/10.1088/0953-4075/35/6/201>
  - [227] B. J. Thompson and E. Wolf, “Two-beam interference with partially coherent light,” *J. Opt. Soc. Am.*, vol. 47, no. 10, pp. 895–902, Oct 1957. [Online]. Available: <http://www.osapublishing.org/abstract.cfm?URI=josa-47-10-895>
  - [228] M. McLaren, J. Romero, M. J. Padgett, F. S. Roux, and A. Forbes, “Two-photon optics of bessel-gaussian modes,” *Physical Review A*, vol. 88, no. 3, pp. 033 818–, 09 2013. [Online]. Available: <https://link.aps.org/doi/10.1103/PhysRevA.88.033818>
  - [229] Z. L. Horváth, J. Vinkó, Z. Bor, and D. von der Linde, “Acceleration of femtosecond pulses to superluminal velocities by gouy phase shift,” *Applied Physics B*, vol. 63, no. 5, pp. 481–484, 1996. [Online]. Available: <https://doi.org/10.1007/BF01828944>